Caractérisation Physico-chimique et adhérence de couches d'oxydes thermiques sur des aciers recyclés.

Thanasak Nilsonthi

UNIVERSITÉ DE GRENOBLE

THÈSE

Pour obtenir le grade de

DOCTEUR DE L'UNIVERSITÉ DE GRENOBLE

Spécialité : **Matériaux, Mécanique, Génie Civil, Electrochimie**

Arrêté ministériel : 7 août 2006

Et de

DOCTEUR DE L'UNIVERSITÉ DE TECHNOLOGIE KING MONKUT DE BANGKOK

Spécialité : **Materials Engineering**

Présentée par

Thanasak NILSONTHI

Thèse dirigée par **Alain GALERIE** et **Yves WOUTERS** en France et par **Somrerk CHANDRA-AMBHORN** en Thaïlande,

Préparée au **Laboratoire SIMaP (Ecole Doctorale I-MEP2)** de Grenoble et au département **MPTE** de Bangkok

CARACTERISATION PHYSICO-CHIMIQUE ET ADHÉRENCE DES COUCHES D'OXYDES THERMIQUES FORMÉES SUR ACIERS RECYCLÉS

Thèse soutenue publiquement le **18 09 2013**
devant le jury composé de :

M. Patrick MASSET
Directeur de Recherches, Fraunhofer Institute Sulzbach-Rosenberg, Président
M. Jérôme FAVERGEON
Professeur, Université de Technologie de Compiègne, Rapporteur
M. Panyawat WANGYAO
Directeur de Recherches, Chulalongkorn University Bangkok, Rapporteur
M. Alain GALERIE
Professeur Émérite, Grenoble INP, Directeur de thèse
M. Somrerk CHANDRA-AMBHORN
Associate Professor, KMUTNB, Bangkok, Directeur de thèse en Thaïlande
M. Yves WOUTERS
Professeur, Université Joseph Fourier, Grenoble, Co-directeur de thèse

ACKNOWLEDGMENTS

I give my heartfelt thanks to Institut polytechnique de Grenoble (Grenoble INP, France), Université Joseph Fourier (UJF, France) and King Mongkut's University of Technology North Bangkok (KMUTNB, Thailand). Their support knowledge and facility are important for the completion of Ph.D. thesis.

I am greatly indebted to my thesis supervisor, Professor emeritus Alain Galerie (Grenoble INP, France), Professor Yves Wouters (UJF, France) and Associate Professor Dr.Somrerk Chandra-ambhorn (KMUTNB, Thailand), for his excellent guidance, advice and support. I wish to thank extended to Associate Professor Dr.Somrerk Chandra-ambhorn who was mainly responsible international thesis co-supervision for initiating the project and for his early guidance.

I would like to thank Frédéric Charlot of Consortium des Moyens Technologiques Communs (CMTC), Grenoble INP, France, for helpful instruction, advice and interest of the micro-tensile test in the chamber of scanning electron microscope. I would also like to thank Komsan Ngamkum of Rajamangala University of Technology Suwannabhumi, Suphanburi campus, Thailand, where the macro-tensile test was conducted.

I appreciate the Iron and Steel Institute of Thailand (ISIT) for granting this research. I also gratefully acknowledge funding award of the "Thai-French Innovation Institute (TFII) Excellent Scholarship" (2010-2012) from the French embassy in Thailand. Thanks for faculty of engineering and funding research for a thesis from graduate school, King Mongkut's University of Technology North Bangkok, Thailand, during the course of this study.

I would like to gratefully and sincerely thank Dr.Patrick Masset of the Fraunhofer Institute Sulzbach-Rosenberg, Germany as the president of jury and also Professor Jérôme Favergeon of the Université de Technologie de Compiègne, France and Dr.Panyawat Wangyao of the Chulalongkorn University (CU), Thailand as the rapporteur for their valuable comments as the reviewers of the thesis manuscript.

Thanks are also extended to Sahaviriya Steel Industries public company limited is acknowledged for providing the conventional steel and G Steel public company limited for providing the recycled steel. Acknowledgement is also given to ArcelorMittal for providing the silicon and copper-containing model steels.

I give my honest thanks to doctoral group, Youcef Madi, Evangéline Ahtoy, Minh-Thi Tran, Piyorose Promdirek, Ludovic Couture, Jéroôme Issartel, Abdelhalim Loucif, Anusara Srisrual and Ismaël Guillotte of Surface Interfaces Réactivité (SIR), Science et Ingénierie des Matériaux et Procédés (SIMaP), École Doctorale Ingénierie-Matériaux Mécanique Energétique Environnement Procédés Production (I-MEP2), Grenoble INP, Université de Grenoble. As well as the kind Uncle Pierre Chollat and Guy Espagnac as the engineers in SIMaP Laboratory, and also Jacqueline Cuoq as the SIR secretary, for bring their happiness in Grenoble.

Finally, I wish to thank you ten thousand times my parent and sister for their necessities support and continuous encouragement in the course of my study. This thesis is devoted to my dad, mum and sister, as well as my past teachers and my future students.

ABSTRACT

Physico-chemical characterisation and adhesion behaviour of thermal oxide scales formed on recycled steels

The purpose of this study was first to develop in Thailand a “macroscopic” adhesion test using a conventional tensile machine, to compare it to the micro-tensile test used in Grenoble and sitting in the SEM chamber, and to use it for measuring adhesion of scales grown during processing on industrial steels. Parameters affecting the test, i.e. strain rate and Si content of steels were investigated. The results showed that spallation of scales during straining increased with increasing tensile strain rate. A higher strain rate resulted in lower strain initiating the first spallation and lower mechanical adhesion of scales, which could be explained by a relaxation effect. Oxide containing Si existed at the steel-scale interface and promoted adhesion of scales. Oxidation studies were also performed, and the behaviour in water vapour of steels with different contents of Si and Cu was investigated. Increasing Si content tended to decrease oxidation rate. It also resulted in the thickening of the wüstite and fayalite layers which formed by internal oxidation. When Si in steel increased, the intermediate ($FeO + Fe_3O_4$) and outermost (Fe_2O_3 sitting on Fe_3O_4) layers formed by external oxidation were thinner. For Cu containing steel, increasing Cu content tended to decrease the oxidation rate. It also decreased the innermost and intermediate layers and resulted in more Cu precipitates along steel-scale interface.

Keywords: Oxide scale, Adhesion, Tensile test, Oxidation kinetics, Hot-rolled steels, Recycled steels, Silicon-containing steel, Copper-containing steel.

RÉSUMÉ

Caractérisation physico-chimique et adhérence des couches d'oxydes thermiques formées sur aciers recyclés

L'objectif de cette étude était, en premier lieu, de mettre en place en Thaïlande un test d'adhésion par traction-écaillage sur une machine de traction classique (test « macroscopique »), de le comparer au test « microscopique » Grenoblois fonctionnant dans la chambre du MEB et de l'utiliser pour évaluer l'adhérence des calamines de process sur des aciers industriels. Deux paramètres ont été étudiés, la vitesse de déformation et la teneur des aciers en silicium. Il apparaît que l'écaillage des calamines au cours du test augmente quand augmente la vitesse de déformation. Une vitesse de déformation élevée entraîne une déformation au premier écaillage plus faible, donc une adhérence mesurée plus faible. Cet effet est lié aux phénomènes de relaxation. On a pu alors montrer que la présence d'oxyde(s) contenant Si, situé(s) à l'interface avec le métal, augmentait l'adhérence. Les études d'oxydation dans la vapeur d'eau qui ont aussi été réalisées ont révélé que la présence de silicium réduisait la vitesse d'oxydation. En augmentant la teneur en Si, les couches de fayalite et de wüstite s'épaississent ; par contre, les couches externes s'amincissent. Pour les aciers contenant du cuivre, la vitesse d'oxydation est réduite quand la teneur en Cu est augmentée. De la même façon, les couches internes sont plus épaisses et on observe une augmentation du nombre de précipités de Cu quand la teneur en cet élément augmente.

Mots-clés: Couches d'oxyde, Adhérence, Test de traction, Cinétique d'oxydation, Aciers au carbone, Aciers recyclés, Aciers au silicium, Aciers au cuivre.

CONTENTS

INTRODUCTION

1. Steelmaking process in Thailand

Moving towards 2015 ASEAN Economic Community, Thailand has its ambition to be one of the regional steel producing leaders with green sustainability concept. This is achievable since nowadays the blast furnace (BF) route is not the main line to produce steels in Thailand, but the recycled or electric-arc-furnace (EAF) one gains market parts. In the latter route, steel scraps as main raw materials are used to produce the steels [ISIT (2006)]. Slabs produced by those processes might be classified by their thickness. ***The conventional slab*** produced from the BF route has a typical thickness of ca. 200 mm. For the EAF route, ***the recycled slab*** can be either ***a medium slab*** in case that its thickness is ca. 80 to 100 mm, or ***a thin slab*** in case that its thickness is ca. 50 mm [Ghosh (2008)]. The slab shapes are shown in Figure 1.

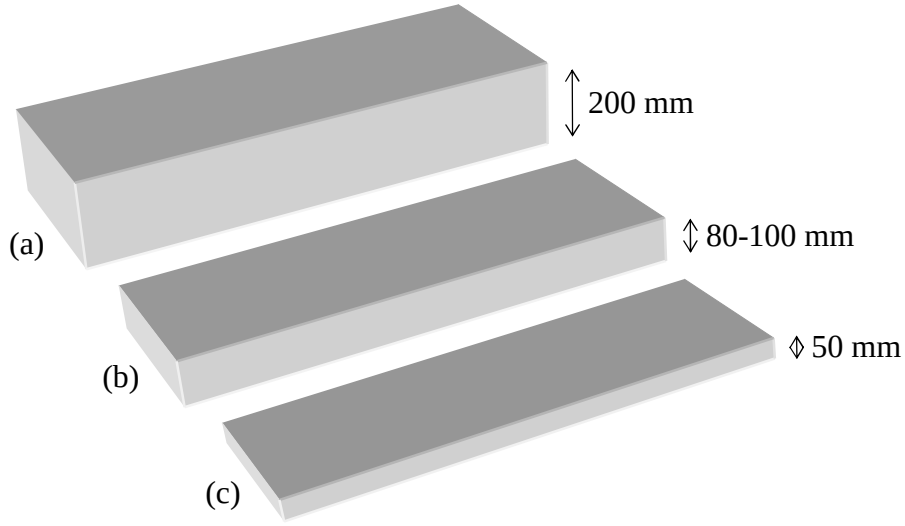

Figure 1: Typical thickness of conventional slab (a), medium slab (b), and thin slab (c).

The slab produced from the EAF route contains principally metallic iron and carbon. Si and Al are used as de-oxidants in the steelmaking process. As a result, Si may exist in steel slab in the range of 0.03 to 0.25 wt% [Thai steelmakers (2009)]. Some elements contaminated in scraps are difficult to be oxidised and removed during steelmaking process, particularly Cu, Sn, Pb, As, Ni, Cr, Mo, and W. In case of copper, the acceptable content is in the range of 0.12 to 0.20 wt%. [Ghosh (2008), Thai steelmakers (2009)]. The produced slab is typically conveyed to be rolled in the hot rolling line. The product of this process is a hot-rolled coil covered by thermal oxide scale, and it is this oxide scale that plays the important role on the final surface quality of the product. For example, in case that the hot-rolled steel is further delivered for cold rolling, the thermal oxide scale must be completely removed before cold rolling. This can be done by mechanical or chemical means, typically scale breaking and/or pickling. Existence of alloying elements, particularly Si and tramp elements, affect the formation of thermal oxide scale and also the adhesion of scale on its substrate. They can finally influence the mechanical and chemical de-scaling processes. The basic understanding of the role of such elements is then of importance to help control adhesion and pickling ability of scale on steel substrate.

For the thermal oxide actually formed in the hot rolling line, extensive works have been reported on characterisation of scale on the BF-type steel where the effect of tramp elements is less significant [Chattopadhyay (2005), Raman (2006), Suárez (2007), Zhang (2007), Jatuphaksamphan (2010)]. On the contrary, studies on formation of scale on the EAF-type recycled steel are very limited. The reports are mainly made in the studies of model alloys, for example the study on the effect of Si on the formation of scale on steel substrate in dry air [Taniguchi (2001), Yang (2008)]. As for adhesion, the study in this aspect has been conventionally made by chemical methods, e.g. the immersion test [Chattopadhyay (2005), Zhang (2007), Chattopadhyay (2008), Jatuphaksamphan (2010)]. There is no report on the adhesion of scale investigated by the mechanical technique, e.g. the in-situ tensile test, at room temperature for the hot-rolled low carbon steel.

2. Ph.D. thesis objectives

The main objectives of this work are as follows.

For ***the academic objective***, it is to study the effects of the alloying elements present in steel particularly Si and Cu on the formation, oxidation kinetics, mechanical adhesion and picklability of oxide scale formed on the steel strips. The adhesion of scale on steel substrate investigated using micro and macro tensile tests is extensively studied. The advantages and disadvantages of each testing method are comparatively evaluated for proposing the idea in selecting the testing method suitable with the problem in hand. The values of the adhesion energies and parameters that affect the value will also be addressed. These can be further used for the comparison with the determined adhesion energy by the other methods.

For ***the industrial objective***s, the first aim is at studying the characteristics, mechanical adhesion and picklability of oxide scale on the recycled steel strip produced from slabs made from the EAF route. The comparative study of that scale with scale on steel strip produced from slabs made from the BF route is also made.

3. Structure of the manuscript

Chapter 1 presents literature review. The main content consists of general steel production, evolution of iron oxide scale and effect of alloying elements particularly Si and Cu on scale formation. Mechanism and kinetics of scale formation at high temperature are reviewed, followed by the review on scale adhesion and pickling tests is also reviewed.

Chapter 2 presents the experimental methods. The main contents consist of materials and apparatus for oxidation kinetics study and physico-chemical characterisation. The adhesion of scale investigated by the tensile and pickling tests is also presented.

Chapter 3 presents the evaluation of the process route on scale structure. The studied materials in that part are as-received hot-rolled conventional and recycled steels. The adhesion of scale on the as-received materials investigated by the micro- and macro-tensile tests is later discussed, followed by pickling results of scale on the as-received materials.

Chapter 4 presents the role of silicon content on scale structure of the as-received hot-rolled 0.026-wt% Si and 0.193-wt% Si steels. Adhesion of scale on as-received and polished steels is later presented, pickling results of scale on the steel substrate is also described.

Chapter 5 presents the roles of silicon in silicon-containing model steels on scale formation and oxidation kinetics.

Chapter 6 presents the roles of copper in copper-containing model steels on scale formation and oxidation kinetics.

Chapter 7 presents the conclusions and perspectives. This chapter consists of the conclusions for the adhesion of scale on steels produced by different process routes (chapter 3), for the adhesion of scale on hot-rolled steels with different silicon contents (chapter 4), for the oxidation of silicon-containing model steels (chapter 5), and for the oxidation of copper-containing model steels (chapter 6). Perspective on the work is finally presented.

Appendix I on X-ray diffraction presents the reference data for phase identification.

Appendix II on Raman spectroscopy presents the reference data in identifying the nature of the oxides. The data received from several the literature reviews.

Appendix III is about parameters of oxide. It presents the reference data for calculating mechanical adhesion energy, and another important data of oxides found in this work.

Resume in French presents the summary in French.

CHAPTER 1

LITERATURE REVIEW

1.1 General steel production

1.1.1 Steelmaking process

The raw material used in a hot rolling process is a slab which can be produced by different routes [Fruehan (1998), Ghosh (2008)], as depicted in Figure 1.1. A slab can be produced by a blast-furnace route starting from iron ore, coal and limestone. The iron produced by a blast furnace is called “pig iron”. The pig iron is further refined in a steelmaking process resulting in a slab called in the present work “conventional steel”.

A slab can also be produced by an electric-arc-furnace route, and called in the present work “recycled steel”. In this path, a slab is made of recycled steels, or scraps, using an electric-arc-furnace and secondary refining process. Because the scraps are used as main raw material, some elements exist in the steel with the higher content than the one produced using the blast-furnace route, e.g. Si, Cu, Sn, Pb or As [Ghosh (2008), Thai steelmakers (2009)]. Table 1.1 exemplifies chemical compositions of the conventional and recycled low carbon steels.

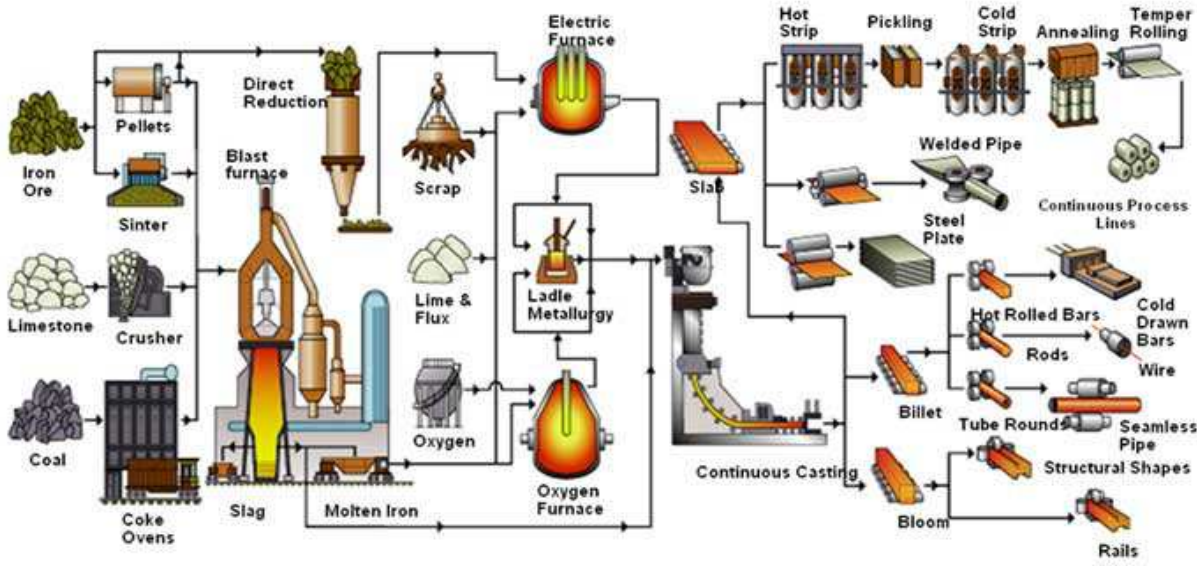

Figure 1.1: Two common methods for making steel [http://hytechcontrols.com (2012)].

Table 1.1: Typical chemical compositions of the conventional and recycled steels (wt.%) [Thai steelmakers (2009), http://ssi-steel.com (2012)].

Steel	Si	Cu	S	P	Mn
Conventional	1.0 max	1.0 max	0.5 max	0.5 max	2.0 max
Recycled	0.25 max	0.12 – 0.2	0.015 – 0.05	0.02 – 0.05	0.3 – 1.0

1.1.2 Hot rolling process

A steel strip can be produced from the conventional steel by a hot rolling process as shown in Fig. 1.2.

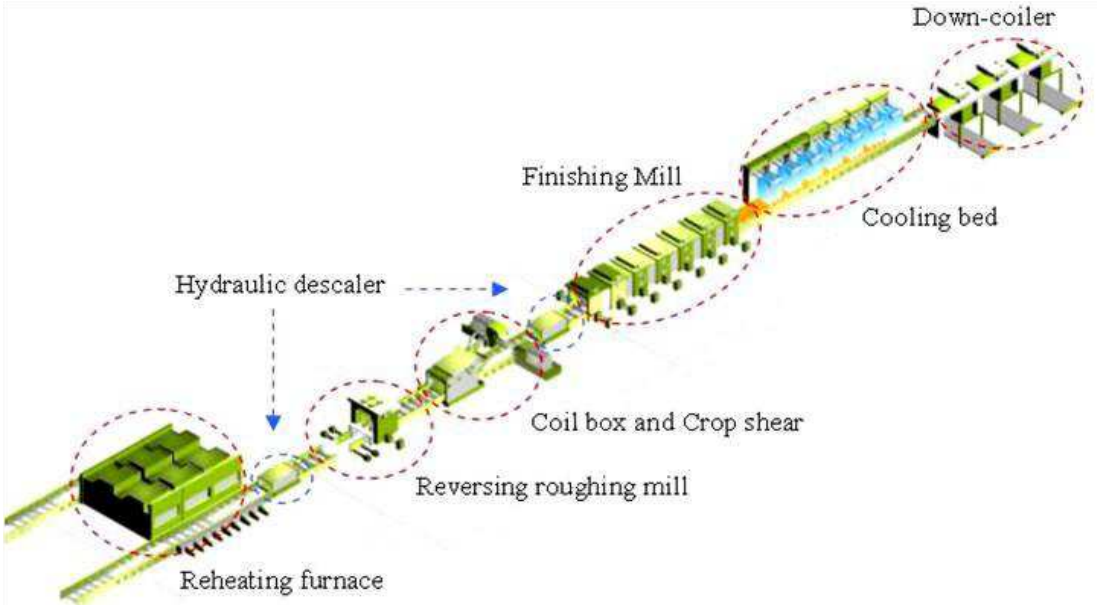

Figure 1.2: Hot rolling process view of the hot-rolled steel strip and facilities [http://ssi-steel.com (2012)].

Main steps of the hot rolling process are as followed [http://ssi-steel.com (2012)].

Slab

A slab as main raw material used in the process is weight and measured before being a pick up by a walking beam into a furnace.

Walking beam reheating furnace

Slab is heated in a reheating furnace with a temperature in the range approximately 1250 to 1300°C during 3 to 4 hours.

High pressure de-scaling box

After the reheating furnace, the slab is de-scaled by a high pressure water jet with the pressure of 160 bars. High pressure of water removes the oxides formed during reheating. This is for preparing a clean surface without scale for the next rolling in the roughing stands.

Reversing roughing mill and vertical edger

A slab with a surface cleaned enters a reversing roughing mill with a vertical edger for control its desired width. A roughing mill can reduce its thickness from 160 – 250 mm to 26 – 40 mm. The machines work by passing forward and backward for 5 to 7 times until the desired thickness and width are obtained.

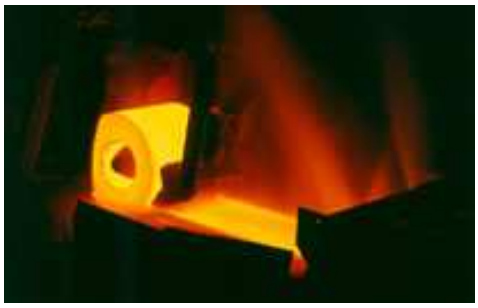

Coil box and crop shear

After rolling in a roughing mill, the slab is elongated where its surface is exposed to humid air atmosphere. For conserving heat and store temperature in a slab, the transfer bar is coiled in a coil box before entering the finishing mill.

Finishing mill

The transfer bar is sent to the 7 finishing stands for reducing the thickness of slab to the required value. Finishing temperature is in the range approximately of 820 to 1000°C.

Cooling bed

After finishing mill, the steel strip is delivered across a cooling bed for decreasing a temperature from 1000°C to approximately 650°C. This process can control metallurgical properties.

Down-coiler

The finished hot-rolled steel strips are coiled in a down-coiler with a temperature in the range approximately 500 to 760°C. The hot-rolled product is attracted with a strapping band, weighed, and given a product number. Samples are taken to measure the output quality.

Hot-rolled coil

The coils with 15 to 31 tonnes in weight, 750 to 1550 mm in width and 1.0 to 19.0 mm in thickness are stored until a steel cooled down to room temperature. Finally, the coiled hot-rolled steel strips can be delivered to customer or further processing, e.g. cold rolling.

The Hot Finishing Line (HFL) is an additional process to increase the quality of the hot-rolled steel strips. Machinery on this line comprises as follows.

Skin-pass machine

A surface quality of steel strips can be improved by a skin-pass machine using rollers to press the steel strips. It can also be used to cut the strips as a customer's weight specifications.

Shearing line machine

The main purpose of a shearing line machine is to cut large sections of steel strips into smaller coils as specified by the customer, or to reshape these coils.

Also, steel strips can be produced from the recycled steel using scrap as raw materials. The process is shown in Fig. 1.3. Production process comprises 3 basic steps as follows.

1. Steel making
The first step of the production process is to melt a scraps and pig iron with coke. This process is carried out in the Electric Arc Furnaces (EAF). Chemical composition can be controlled as customer's requirement at a ladle furnace.

2. Continuous slab casting
In the second step, the steel as liquid form is carried out to medium thickness by sing the continuous slab caster.

3. Hot rolling process
In the last step, the slab from caster is started in reheating furnace at required rolling temperature. The hot slab is fed through a roughing mill, and then slab is rolled at coil box before fed to finishing stands with shape control.

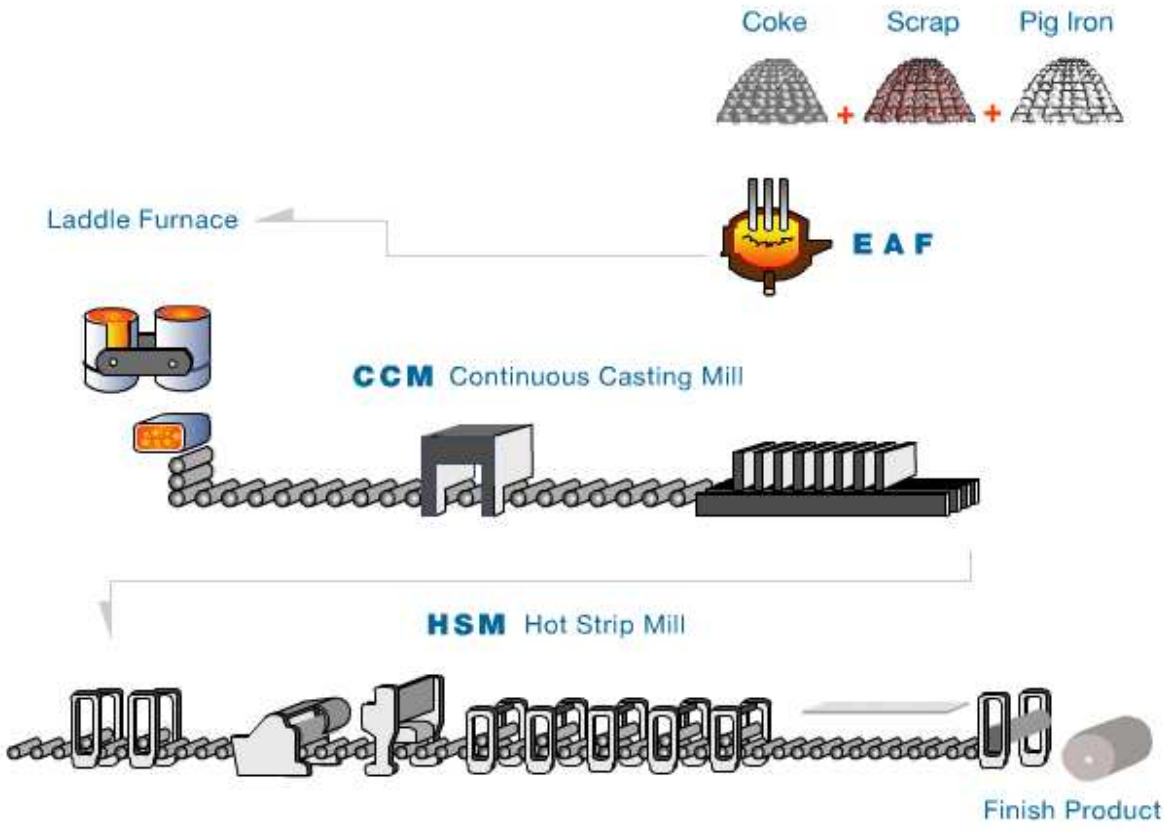

Figure 1.3: Main steps of production process of the hot-rolled steel strip [http://g-steel.com (2012)].

1.2 Evolution of oxide scale

1.2.1 Scale on the hot-rolled steel strips

In a hot rolling process, an oxide scale layer can be formed on the steel strips surface. At the reheating furnace temperature around 1250 to 1300°C, a primary scales thickness around 2 mm is formed on the slabs surface. The scale can be removed by hydraulic descaler by high pressure water jet, firstly before the entry of slab into the roughing mill and secondly before the entry of steel bar into the finishing stands. After the first descaling, secondary scale produces rapidly. Its thickness is usually less than 100 μm. This scale is secondly removed by water jet before entering the finishing mill. Afterwards, tertiary oxide scale layer develops in the finishing stands at temperature less than 1000°C. They are formed at the first stand, between stands and after the last stand. The oxide scale continuously grows during the steel strip coiling at the temperature less than 1000°C and also during storage until the temperature cool down to room temperature. The condition of scale formation in a conventional hot strip processing route are summarised in Table 1.2.

Table 1.2: Scale formation in a conventional hot strip processing route [Chen (2008)].

Type of scale	Thickness	Temperatures	Atmosphere	Duration
Primary scale	1 – 5 mm	1200 – 1300°C	Furnace gas	Hours
Secondary scale	100 – 300 μm	1100 – 1200°C	Air/steam	Minutes
Tertiary scale	10 – 30 μm	850 – 1100°C	Air/steam	Seconds
Scale retained on strip	5 – 15 μm	500 – 880°C	Air/steam	Days

After the hot rolling process, mechanical breaking of oxide scale followed by acid pickling is normally used to remove the hot-rolling scale. This is an important factor to surface quality of the steel strips for acceptance of the product.

1.2.2 Scale structure on the steel

The scale structure typically consists in three layers of iron oxide, a thin external layer of hematite (Fe_2O_3), an intermediate magnetite (Fe_3O_4) layer ($Fe^{2+}Fe_2^{3+}O_4^{2-} - spinel$), and a thick wüstite ($Fe_{1-x}O$) layer (non-stoichiometric) in contact with the metal as presented in Figure 1.4 [Kofstad (1988), Chen (2000), (2001), (2002), (2003), (2005), Sarrazin (2000), (2008), Gines (2002), Jiang (2006), Suárez (2007), Zhang (2007), Yang (2008), Segawa (2011)].

For the two-composition Fe-O system, the composition can vary via concentration gradients of oxygen, which in turn drive the diffusion process supporting scale growth. In binary two-phase regions in Fig. 1.4, wüstite cannot form as particles within the iron when pure metals are oxidised isothermally, an iron oxides formed always grow external scales rather than forming internal oxide precipitates.

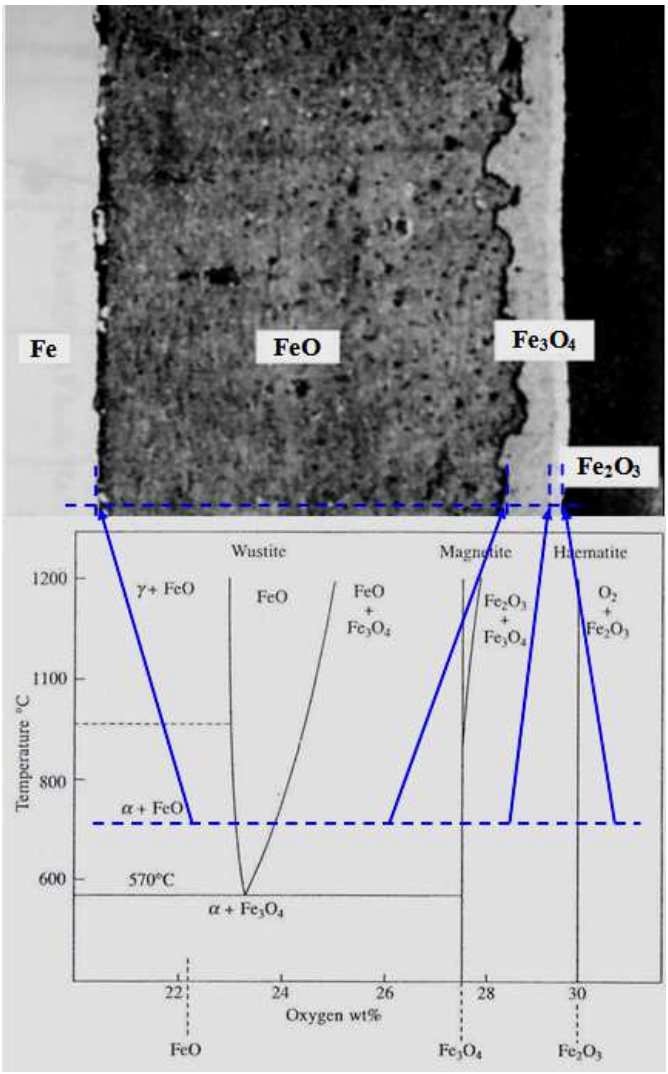

Figure 1.4: Cross-section of oxide scale grown on iron with diffusion path mapped on phase diagram [Young (2008)].

Sometimes magnetite is observed in the wüstite layer due to eutectoid decomposition at cooling. Sometimes also, the hematite layer may be absent (Fig. 1.5).

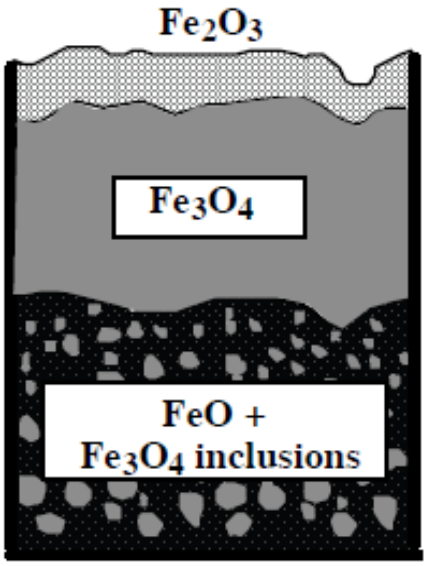

Figure 1.5: Schematic cross section of the scale obtained after oxidation of an iron sheet in air, at 1123 K (850°C) for 4 hours. The observed magnetite inclusions precipitated during cooling [Sarrazin (2008)].

The morphological development of oxide scale on the hot-rolled steel strip under various simulated coiling and cooling conditions was reported [Chen (2000)]. A classic three-layered oxide scale is produced when oxidised at 800°C, which comprises a thin hematite layer, an intermediate magnetite layer, and a thick wüstite layer. The different scale three types are shown in Fig. 1.6 to Fig. 1.8.

The Type-I scale is mostly retained wüstite with some magnetite precipitates formed inside the wüstite layer (Fig. 1.6). The outermost hematite sitting on magnetite layer is also observed.

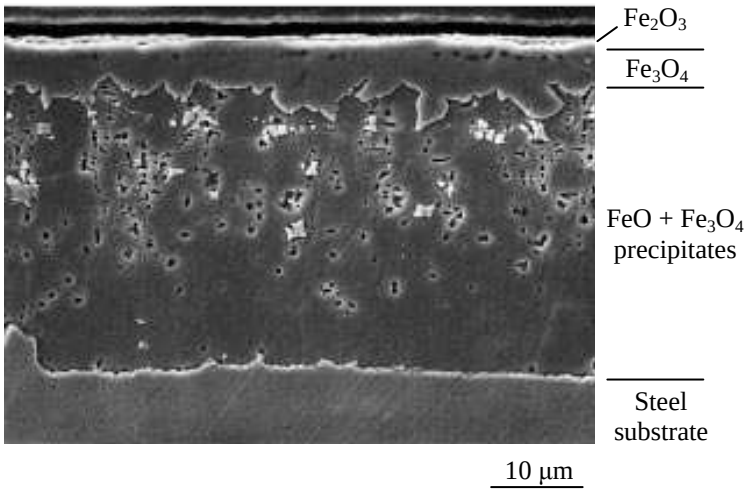

Figure 1.6: Typical structure of Type I scale (secondary-electron image, 2000 x). The scale structure was obtained under simulated coiling temperature of 650°C and simulated cooling rate of 15°C/min, showing that the entire wüstite layer was essentially retained [Chen (2000)].

The Type-II scale largely consists of retained wüstite with magnetite precipitate inside. The magnetite seam is also observed at the wüstite-steel interface, to accompany those formed inside the wüstite layer (Fig. 1.7). The outermost hematite sitting on magnetite layer is also observed as in the Type-I scale.

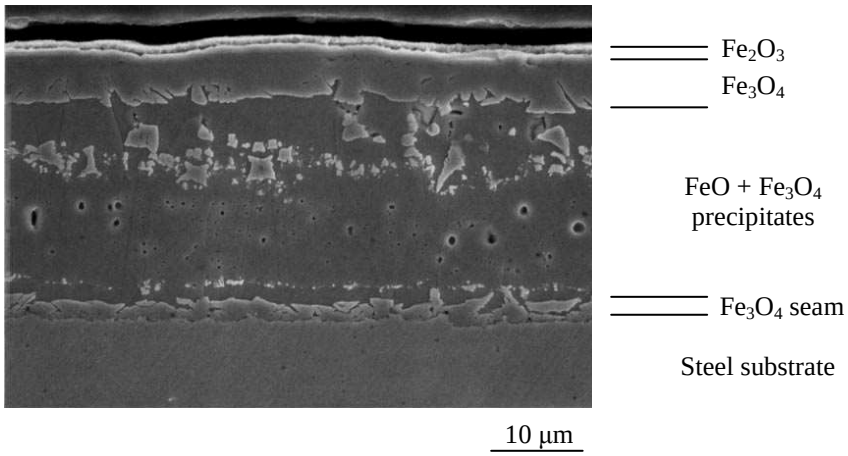

Figure 1.7: Typical structure of Type-II scale (secondary-electron image, 1500 x). The structure was obtained under simulated coiling temperature of 650°C and simulated cooling rate of 5°C/min, showing a magnetite layer at the scale-steel interface while the majority of the wüstite layer was retained [Chen (2000)].

The Type-III scale consists of the layer of former wüstite decomposed into a mixture of Fe_3O_4/Fe eutectoid and magnetite precipitates. A very small amount of retained wüstite may be present (Fig 1.8). Similar to the two former types of scale, the outermost hematite sitting on magnetite layer is also observed as in the Type-I scale.

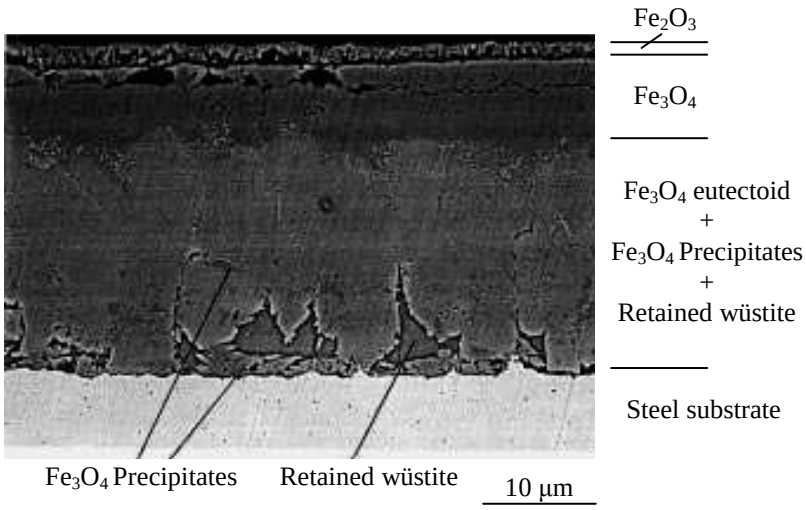

Figure 1.8: Typical structure of Type III scale (backscattered electron image, 2000 x). The structure was obtained under simulated coiling temperature of 650°C and simulated cooling rate of 1°C/min, showing that the majority of the wüstite layer was transformed to Fe/Fe_3O_4 eutectoid and a small amount of Fe_3O_4 precipitate [Chen (2000)].

Table 1.3: Summary of the features of the different scale types. The coiling and coil cooling conditions for forming the various types of oxide scales are mapped in Fig. 1.9.

Scale type	Fe_3O_4 precipitates inside wüstite	Fe_3O_4 layer at wüstite-steel interface	Fe_3O_4/Fe eutectoid	Retained wüstite
I	Yes	Nil	Nil	Continuous
I-II	Yes	Discontinuous	Nil	Continuous
II	Yes	Continuous	Nil or little	Continuous
II-III	Yes	Continuous	Yes < ~ 70%	Discontinuous
III	Yes	Continuous	Yes > ~ 70%	Little or nil

Formation of the different three types of scales can be predicted using the coiling temperature-cooling rate-transformation diagram shown in Fig. 1.9. At the same coiling temperature, comparing to the Type-I scale which is formed at relatively fastest cooling rate, it is observed that magnetite seam at the internal interface is formed when the cooling rate is slower. If the cooling rate is more and more slower, according to the Fe-O phase diagram in Fig. 1.4, the wüstite layer is transformed to be a eutectoid consisting of magnetite and lamellar iron as seen in the Type-III scale.

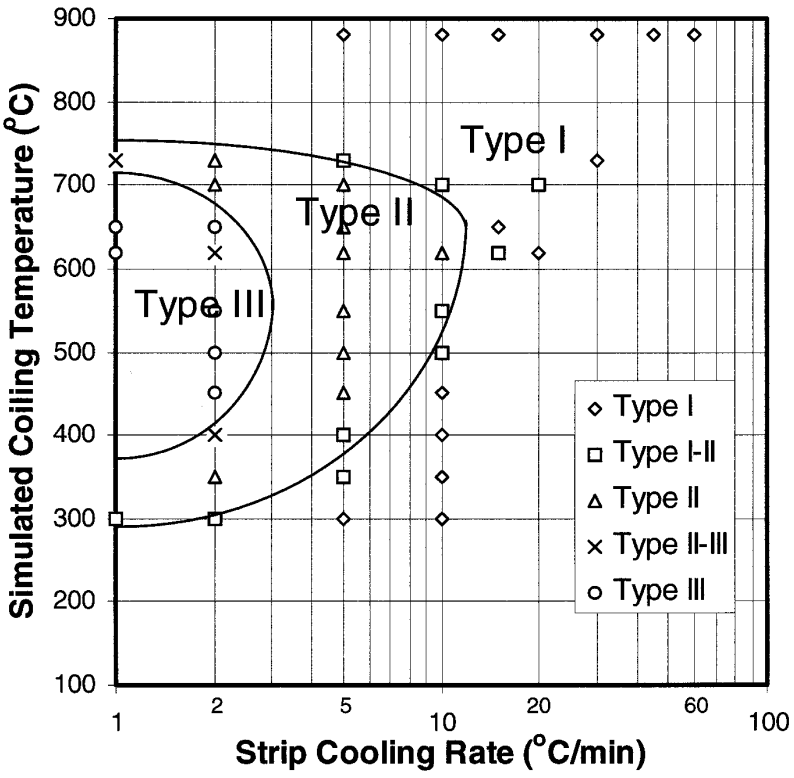

Figure 1.9: Scale type versus simulated coiling temperature and strip-cooling rate [Chen (2000)].

The three types of scales can be formed in laboratory by simulating the situation close to the hot-rolling process. However, the actual scale formed in the hot-rolling line, particularly at the inner part of the coil, is slightly different. The XRD pattern of oxide scale actually formed on steel in the hot-rolling line contains mainly iron and magnetite as will be shown in

Fig. 1.10 (a). Oxide scale was mostly a mixture of magnetite and layered-structure of eutectoid phase, where the white phase is iron and the gray phase Fe_3O_4 (Fig. 1.10 b). The iron oxide with higher ratio of oxygen, magnetite and hematite, was not observed. This might be because oxygen in the inner part of the coil is limited, resulting in oxidation of hose oxide to be the one with lower ratio of oxygen, wüstite. However, it is worthily noted that characterisation of scales actually formed on steel in the hot-rolled process has been mainly conducted for the conventional steel produced from the BF route. The extensive investigation of structure of scales actually formed on recycled steel in the hot-rolling conditions has not been yet reported.

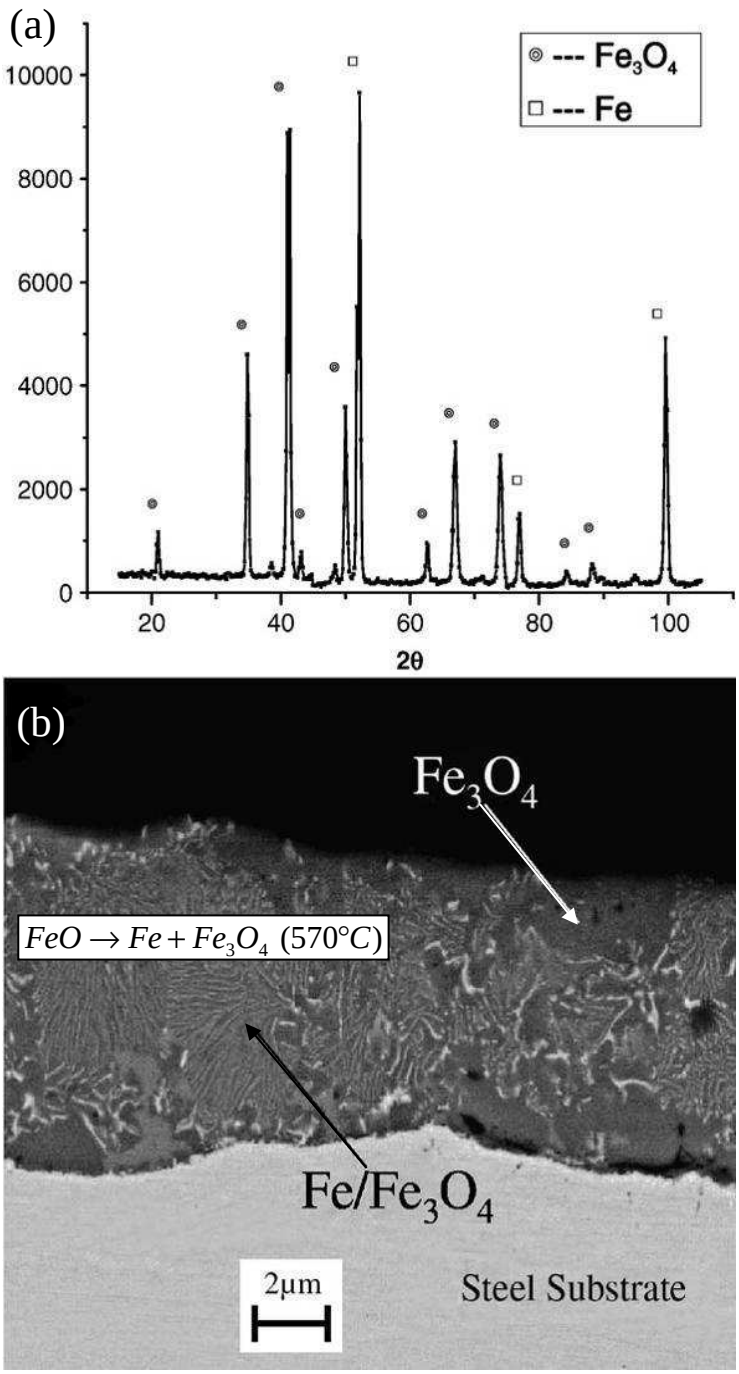

Figure 1.10: Oxide scale formed on the hot-rolled low carbon steel (a) XRD spectra, (b) SEM backscattered electron image of Fe/Fe_3O_4 eutectoid [Jie (2008)].

1.2.2.1 Oxidation of alloys

Oxidation processing of alloys is more complex than that of pure metals. Some small alloying elements can effect on the scale properties due to the following factors.

1. The alloy components may have different affinities for oxygen. Some of them oxidise more rapidly than other. In some alloys only one component (most reactive) oxidises, the process is called selective oxidation.
2. Different alloy components (metal ions) may have different diffusion coefficients in the oxide and alloy, which causes preferential oxidation of the component having higher diffusivity.
3. Complex oxide compounds (ternary and higher) may be formed in oxidation of alloys.
4. Some alloy components may oxidise out of the scale, within the alloy below the metal-scale interface (internal oxidation).

As previously mentioned, many elements can exist in the recycled steel and they can affect oxidation behaviour. Those which are interested in this work are silicon and copper. The roles of those elements on oxidation are reviewed as follows.

1.2.2.2 Effect of Si content on scale structure

In air oxidation, the scaling rate of steel can be decreased with increasing Si content as shown in Fig. 1.11 [Taniguchi (2001), Ishitsuka (2004), Takeda (2006), Yang (2008), Nishimoto (2011)]. Scale structure of Si-containing steel formed in H_2O/N_2 at 1060°C during 1 min and $20\%O_2/15\%H_2O/N_2$ at 1100°C during 15 min were studied [Ahtoy (2010), Issartel (2012)]. SiO_2 appears at the internal interface as shown in Figs. 1.12 (a). A layer of wüstite with fayalite precipitates was also observed as in Fig. 1.12 (b), and an internal oxidation zone at the steel-scale interface appeared.

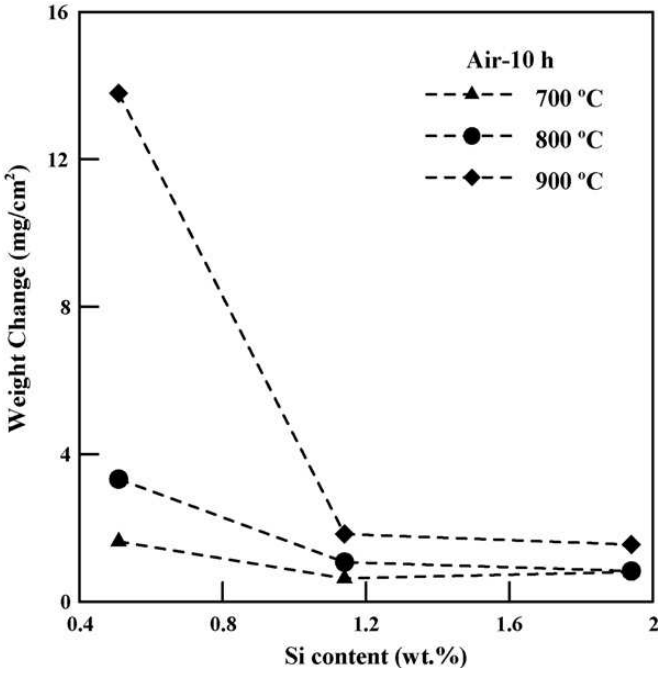

Figure 1.11: Relationship between silicon content and weight change of the steels oxidised in air for 10 h [Yang (2008)].

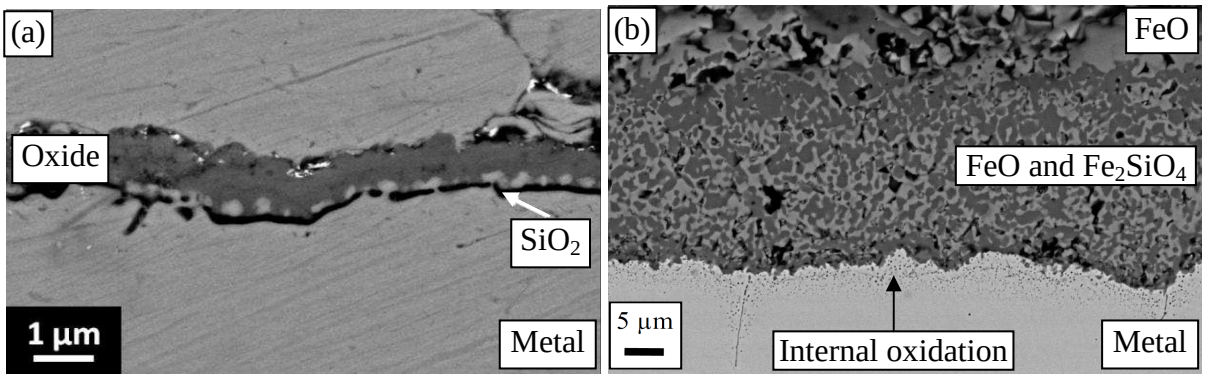

Figure 1.12: Cross section of the Si alloys steel (a) SiO_2 phase, (b) Fe_2SiO_4 phase between metal-oxide interface [Ahtoy (2010), Issartel (2012)].

The microstructure at the steel-scale interface of Fe-Si alloys after oxidation at 800°C in air was reported by [Nishimoto (2011)]. On the Fe-Si alloys with low Si content no inner scale was formed, while an internal oxidation zone was formed on Fe-0.5%Si and Fe-1%Si. The thickness and amount of internal oxidation zone increased with increasing Si content. The SEM images and phase maps of each iron oxide and α-Fe in the cross-sectional microstructure are shown in Fig. 1.13. The FeO layer was not observed in the scale on Fe-0.5%Si and Fe-1%Si. Furthermore, the Fe_3O_4 layer on Fe-1%Si became thinner than that of Fe-0.5%Si and the oxide scale consisted of mainly the Fe_2O_3 layer.

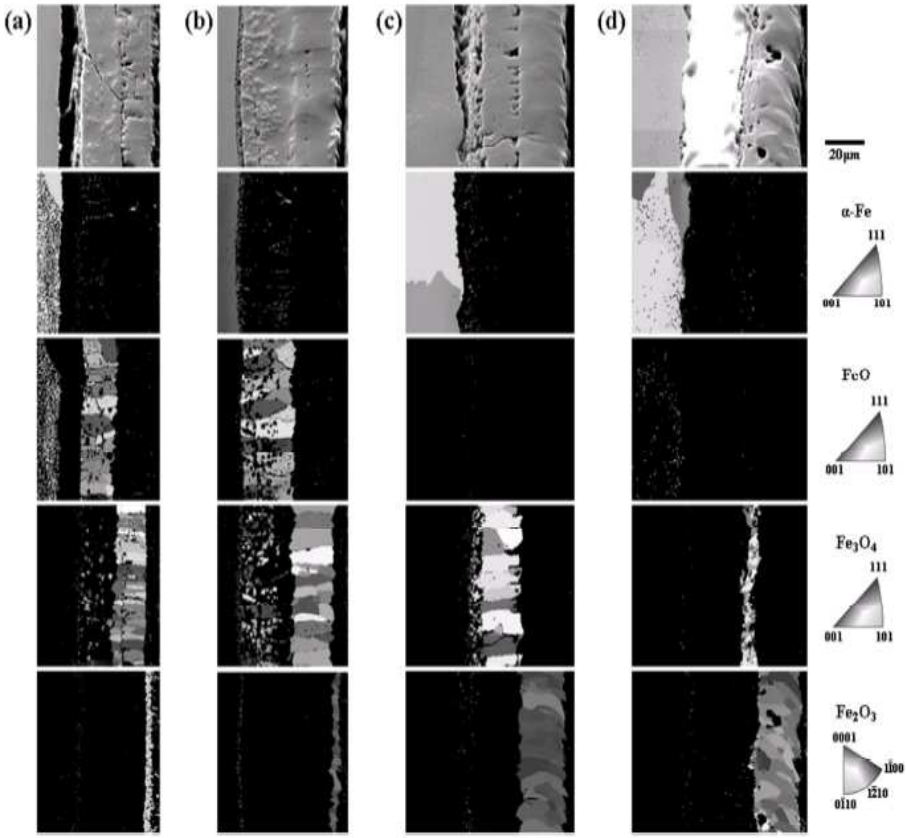

Figure 1.13: SEM images and EBSD of each iron oxide and α-Fe in the cross-sectional microstructures (a) Fe-0.004%Si, (b) Fe-0.1%Si, (c) Fe-0.5%Si and (d) Fe-1%Si.

In oxidation tests in water-vapour containing atmospheres with higher oxidation periods, a decarburisation zone was observed in the steel adjacent to the scale. The innermost scale is mixed with silica, fayalite and wüstite, while the major oxide layer was iron oxide (Fig. 1.14).

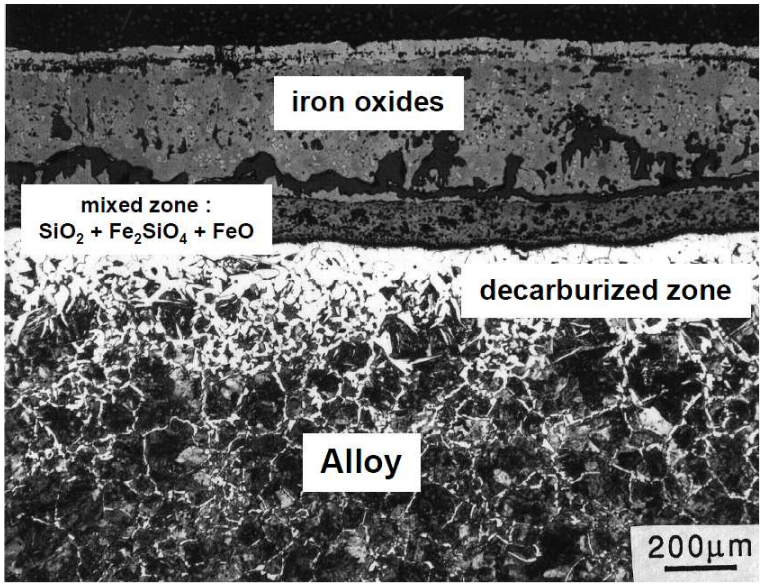

Figure 1.14: Non-isothermal test on a 2%Si industrial alloys, heating rate: 25 to 1100°C in 120 min, gas mixture N_2 + 7%O_2 + 15%H_2O [Ahtoy (2010)].

1.2.2.3 Effect of Cu content on scale structure

Copper is an element less oxidisable than iron, its diffusion is very slow in the iron matrix, particularly in ferrite, and is insoluble inside oxides. During oxidation, it is accumulated and forms a metallic layer at the metal-oxide interface [Chen (2005)]. Oxidation rate decreases when copper is more than 1 wt.%, resulting in loss of adhesion between iron and oxide [Hammar (1974)]. It might be from the low iron diffusion coefficient inside copper-containing steel [Métivier (1991)].

At temperature lower than 1000°C with oxygen atmosphere, copper has two possible stable oxides. Cuprite (Cu_2O) is in contact with the metal and tenorite (CuO) is in contact with the gas. The isothermal gravimetric rate law is parabolic with independence on oxygen pressure. The weight gain is only Cu_2O growth under the constant oxygen pressure fixed by the Cu_2O-CuO equilibrium. Observation of both layers shown in Fig. 1.15, the relative thickness of CuO reduces when the temperature increases. Activation energy for the self diffusion of copper ions in CuO is lower than that in Cu_2O [Sarrazin (2008)].

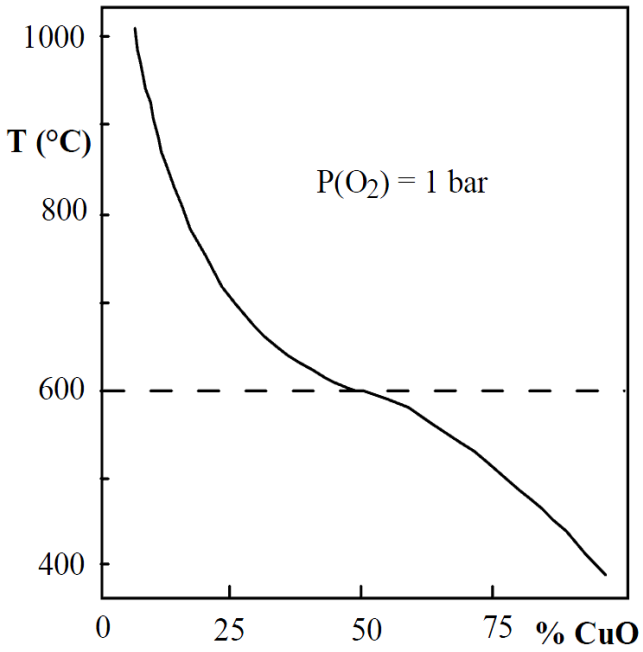

Figure 1.15: The change with temperature of the fraction of CuO in the Cu_2O-CuO duplex scale grown on copper in oxygen atmosphere [Sarrazin (2008)].

One of the roles of copper on high temperature condition is a “hot shortness” [Zou (1989), Uchino (2001), O’Neill (2002), Shibata (2002), Chihiro (2003), Chen (2005), Kunishige (2007)]. A root cause of this problem starts when the steel containing copper in solid solution is heated to high temperatures. In that condition, the nobler element, copper, will not oxidise and will concentrate at the steel oxide interface, forming a copper-rich liquid phase between the scaling layer and the base metal once its solubility in austenite is exceeded and the temperature is above the melting point of the copper-rich phase. This liquid metallic phase is able to penetrate into the base metal along austenite grain boundaries under tensile stresses, thus lead to hot shortness.

Some research works [Chen (2005), Kondo (2006)] were further reported that copper is not only enriched at the metal-scale interface but also exists within the scales. At the early stage of oxidation, the concentration of enriched copper at the steel-scale interface is low and the liquid copper has not yet precipitated at the interface (Fig. 1.16a) [Kondo (2006)]. After the scale becomes thicker, liquid copper precipitates at the interface (Fig. 1.16b). Considering the idea that copper is not precipitated at the early stage, it can be concluded that copper diffuses from the metal-scale interface to the magnetite layer through the wüstite layer. The proposed process of copper diffusion through the scale is schematically shown in Fig. 1.16. Liquid copper diffuses through wüstite layer because metal phase is stable in the wüstite layer (Fig. 1.16).

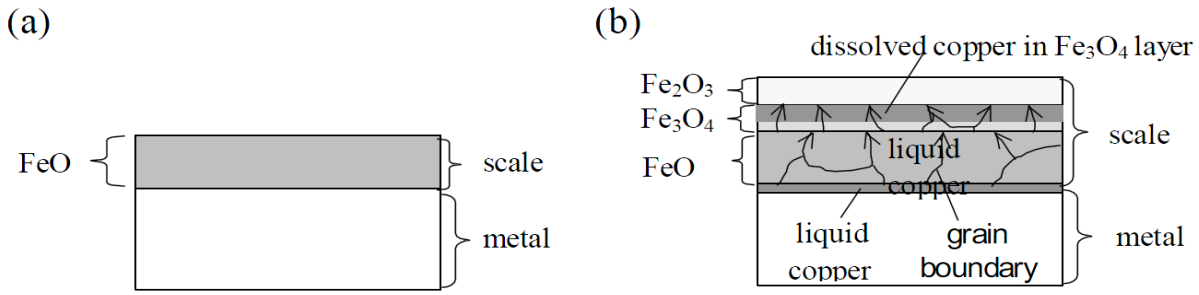

Figure 1.16: The schematic drawings of copper behaviour during the oxidation of steels containing copper, (a) Early stage of the oxidation, (b) Later stage of the oxidation [Kondo (2006)].

Fig. 1.17 shows the relationship between the temperature and oxygen pressure at which the metals of copper and iron equilibrate with their oxides. Magnetite is stable between the line of Fe_3O_4/Fe_2O_3 and that of FeO/Fe_3O_4. Interpretation of Fig. 1.17 explains how copper exists as oxide in the upper part of magnetite layer. Magnetite has spinel structure. The spinel oxide of Fe-Cu-O has a complete solid solution system between Fe_2CuO_4 and Fe_2FeO_4. This explains why copper exists as a state of solid solution in the upper part of the magnetite layer [Kondo (2006)].

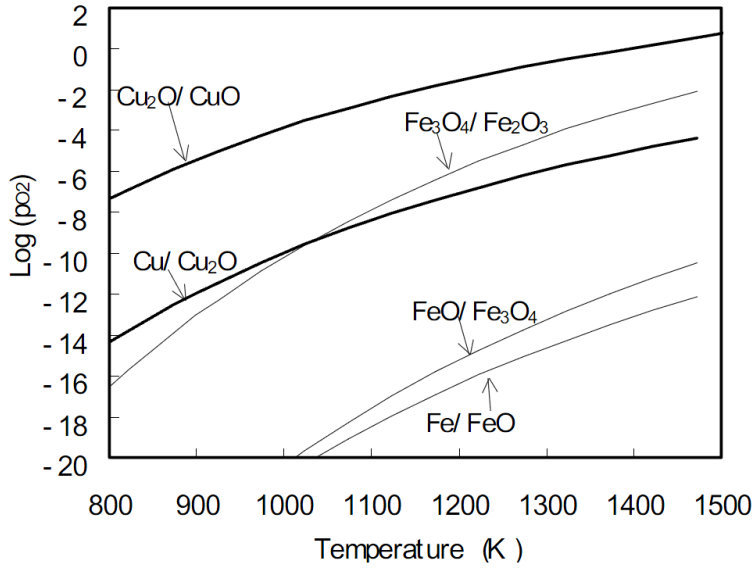

Figure 1.17: The equilibrium oxygen pressure of copper, iron, and their oxides [Kondo (2006)].

1.3 Oxidation of metals

1.3.1 Basic thermodynamics

Thermodynamics of materials will be described in the standard basic books [Ragone (1995), Khanna (2002), Birks (2006), Sarrazin (2008), Young (2008), Gaskell (2009)].

The second law of thermodynamics is most conveniently written in terms of the Gibbs free energy (G) of a system as a function of state that includes both energy and entropy terms given as

$$G = H - TS \qquad (1-1)$$

Where

G = Gibbs free energy (J.mol^{-1})
H = enthalpy, measures the energy change at constant pressure (J.mol^{-1})
T = absolute temperature (K)
S = entropy, measures the randomness of the system (J.mol^{-1}.K^{-1})

Thus for any change in state, equation 1 – 1 can write the extremely important relation as

$$\Delta G = \Delta H - T\Delta S \qquad (1-2)$$

Where

ΔG = Gibbs free energy change of reaction (J.mol^{-1})
ΔH = enthalpy change of reaction (J.mol^{-1})
ΔS = entropy change of reaction (J.mol^{-1}.K^{-1})

At high temperature such as the hot rolling process, steel is covered with oxide scale. The scale can be formed according to the general equation of the oxidation of metals as

$$aM + \frac{b}{2}O_2 = M_aO_b \qquad (1-3)$$

The Gibbs free energy change of reaction (1 – 3) as a function of the standard Gibbs free energy change of reaction with gas constant and absolute temperature is given by

$$\Delta G = \Delta G^\circ + RT \ln\left(\frac{a_{M_aO_b}}{a_M \cdot a_{O_2}^{b/2}}\right) \qquad (1-4)$$

Where

ΔG° = standard Gibbs free energy change of reaction (J.mol^{-1})
R = ideal gas constant (8.314 J.mol^{-1}.K^{-1})
a = thermodynamic activity of a component

Determine the standard Gibbs energy change of reaction according to

$$\Delta G^{\circ} = \Sigma \Delta G^{\circ}_{f\,(products)} - \Sigma \Delta G^{\circ}_{f\,(reac\tan ts)} \qquad (1-5)$$

Where

ΔG°_{f} = standard Gibbs free energy change of formation of products and reactants ($J.mol^{-1}$)

The standard Gibbs free energy change of formation (ΔG°_{f}) of products and reactants given by

$$\Delta G^{\circ}_{f} = \Delta H^{\circ}_{f} - T\Delta S^{\circ}_{f} \qquad (1-6)$$

Where

ΔH°_{f} = standard enthalpy change of formation ($J.mol^{-1}$)
ΔS°_{f} = standard entropy change of a substance ($J.mol^{-1}.K^{-1}$)

For the oxidation of iron, the useful values ΔG° of the formed oxides are provided as follows [Young (2008)].

The standard Gibbs free energy change of reaction of $Fe_{(s)} + \frac{1}{2}O_{2(g)} = FeO_{(s)}$ is given as

$$\Delta G^{\circ}_{FeO}\,(J.mol^{-1}) = -264\,890 + 65.4T \qquad (1-7)$$

The standard Gibbs free energy change of reaction of $3FeO_{(s)} + \frac{1}{2}O_{2(g)} = Fe_3O_{4(s)}$ is given as

$$\Delta G^{\circ}_{Fe_3O_4}\,(J.mol^{-1}) = -312\,210 + 125.1T \qquad (1-8)$$

The standard Gibbs free energy change of reaction of $2Fe_3O_{4(s)} + \frac{1}{2}O_{2(g)} = 3Fe_2O_{3(s)}$ is given as

$$\Delta G^{\circ}_{Fe_2O_3}\,(J.mol^{-1}) = -249\,450 + 140.7T \qquad (1-9)$$

Spontaneity of the reaction can be predicted by Gibbs free energy of reaction according to the following criteria.

$\Delta G < 0$ reaction is spontaneous
$\Delta G = 0$ reaction is equilibrium
$\Delta G > 0$ reaction is nonspontaneous

When $\Delta G = 0$, a reaction is at equilibrium, $a_{O_2} = P_{O_2}$ Equation 1.4 can be derived

$$\Delta G^{\circ} = -RT \ln\left(\frac{a_{M_aO_b}}{a_M \cdot P_{O_2,eq}^{b/2}}\right) \quad (1-10)$$

When activity (a) of a solid state = 1

$$\Delta G^{\circ} = -RT \ln\left(\frac{1}{P_{O_2,eq}^{b/2}}\right) \quad (1-11)$$

$$\Delta G^{\circ} = \frac{b}{2} RT \ln P_{O_2,eq} \quad (1-12)$$

Where

$P_{O_2,eq}$ = partial pressure of the di-oxygen molecule at equilibrium

Putting an Equation (1 – 12) in (1 – 4), the following equation can be derived.

$$\Delta G = \frac{b}{2} RT \ln\left(\frac{P_{O_2,eq}}{P_{O_2}}\right) \quad (1-13)$$

Where

P_{O_2} = partial pressure of the di-oxygen gas molecule in the studied atmosphere

The Reaction (1 – 3) is thermodynamically possible in the case of $\Delta G < 0$, corresponding to the condition of $P_{O_2,eq} < P_{O_2}$. On the contrary, the Reaction (1 – 3) is thermodynamically impossible in the case of $\Delta G > 0$, corresponding to the condition of $P_{O_2,eq} > P_{O_2}$.

Also, Equation (1 – 12) can be written

$$P_{O_2,eq} = \exp\left(\frac{\frac{2}{b}\Delta G^{\circ}}{RT}\right) \quad (1-14)$$

These $P_{O_2,eq}$ will be classically plotted as logarithmic scale as a function of temperature in the Ellingham diagram (Fig. 1.18). This diagram can be used for visualising the thermodynamic stability of the oxide formation.

The Ellingham diagram plots are from the second law of thermodynamics as the Gibbs free energy change (ΔG) for the oxidation reaction versus the temperature. The thick lines are on the diagram plots of Fig. 1.18 that for clearly observing the important chemical reactions of this work.

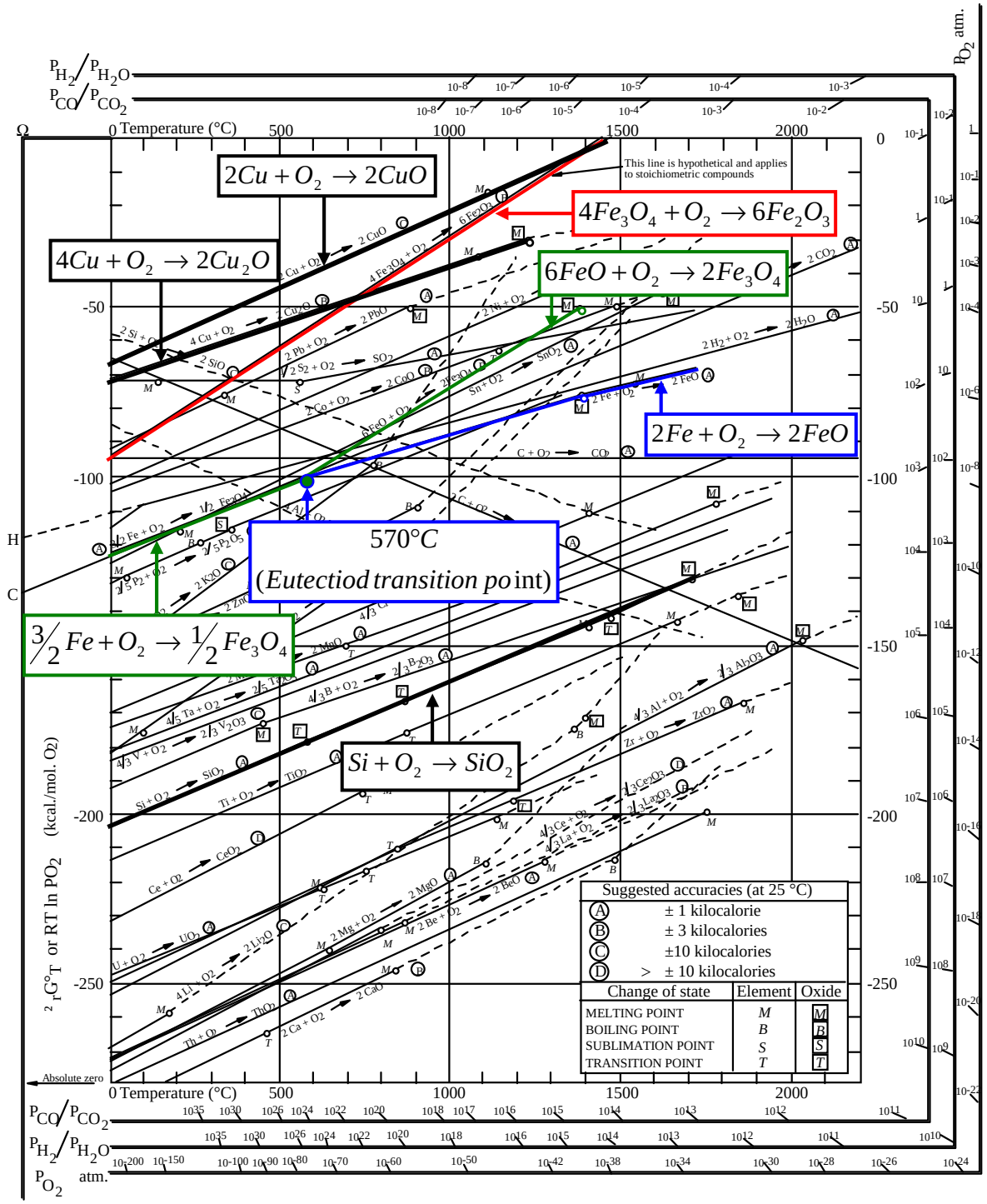

Figure 1.18: The Ellingham diagram for oxides of metals [Sarrazin (2000)].

Fig. 1.19 depicts equilibrium of various metal-oxide systems in logarithmic scale of pressure of oxygen in bar with reciprocal of temperature in Kelvin. From the diagram in Fig. 1.19, the partial pressures of oxygen of silicon and iron are less than that of water.

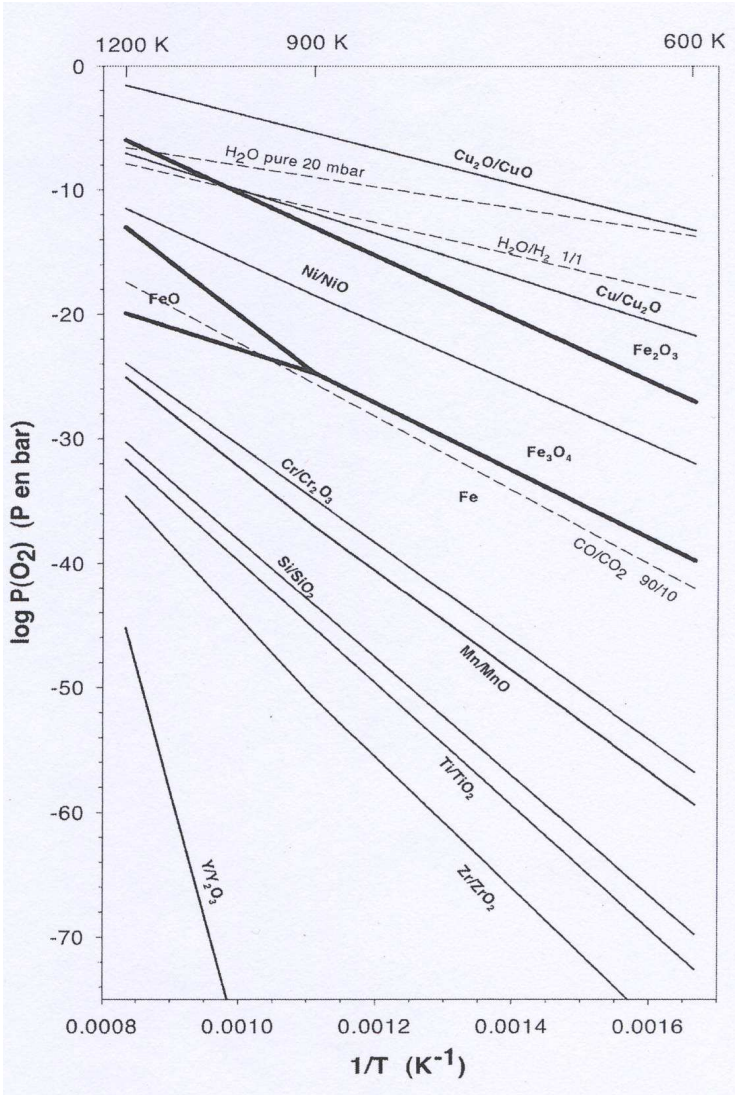

Figure 1.19: Straight equilibrium of various metal-oxide systems (activities of all solid phases are taken equal to unity). Lines in bold lines represent the equilibrium of the Fe-O [Thermodynamic data base from Barin (1989)].

1.3.2 Kinetics of high temperature oxidation

When steel oxidation takes place in oxygen, two possible mechanisms may be present to control the oxidation process. When the scale is relatively thin and iron diffusion flux through the oxide layer is sufficiently large, oxygen gas-phase diffusion through the gas-phase boundary layer on the sample surface may be too small to fully react with the arriving iron ions on the scale surface. In this case, the oxidation reaction rate is controlled by oxygen gas-phase diffusion and the oxidation kinetics follows the linear rate law. Once a relatively thick scale layer is developed and iron diffusion through the scale layer becomes the controlling step, the oxidation kinetics become parabolic.

1.3.2.1 Linear rate law

A non-protective (porous) scale can be formed in the process. The process rate is independent on the scale thickness, due to fast transfer of oxygen into the metal surface. The process rate is controlled by the reaction of oxidation. In this case the process rate is constant. The oxidation kinetics follows the linear law as

$$\frac{\Delta m}{A} = k_l \cdot t \qquad (1-15)$$

Where

Δm = mass gain of the scale (g)
A = unit area (cm^2)
k_l = linear rate constant dependent on the metal and the temperature ($g.cm^{-2}.s^{-1}$)
t = oxidation time (s)

1.3.2.2 Parabolic rate law

A protective (adherent and non-porous) scale normally forms on most metals. The process rate is controlled by solid state diffusion through the oxide scale. The process rate is obtained from the Wagner's law and follows the parabolic law as

$$\left(\frac{\Delta m}{A}\right)^2 = k_p \cdot t \qquad (1-16)$$

where

k_p = parabolic rate constant dependent on the metal and the temperature ($g^2.cm^{-4}.s^{-1}$)

During the formation of oxide layer, the reaction kinetics follows a parabolic rate law. Wagner has suggested two kinds of behaviours depending on the pressure of oxygen $P(O_2)$.

1. For n-type oxide, the parabolic rate constant k_p is independent of $P(O_2)$ [Sarrazin (2000)].
2. For p-type oxide, the parabolic rate constant k_p is proportional to $P(O_2)^{1/16}$ [Sarrazin (2000)] or to $P(O_2)$ [Dauzat (1991), Sarrazin (2000)].

During the oxidation process, an oxidation reaction maybe showing exaggerated. Possible features that would be revealed by continuous monitoring but missed by a discontinuous technique, lead to erroneous interpretation as describe in Fig. 1.20.

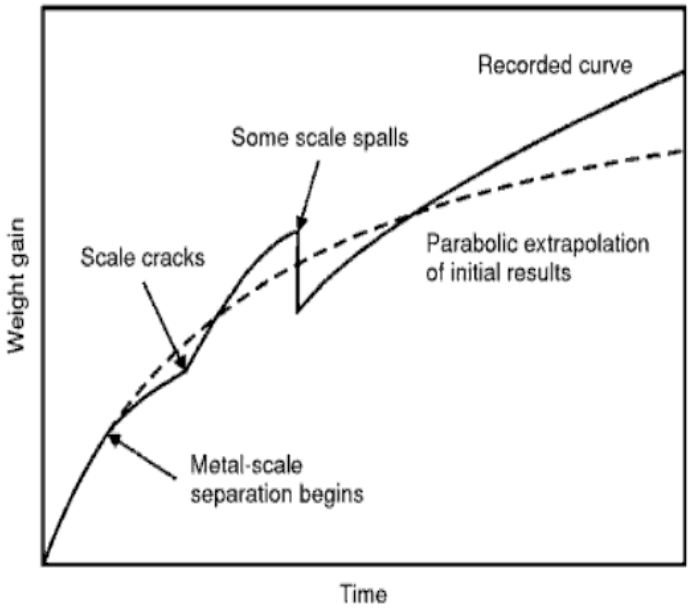

Figure 1.20: Hypothetical mass-gain versus time curve [Birks (2006)].

1.3.2.3 Determining the activation energy of a reaction

In the Arrhenius equation, the term activation energy (E_a) may define as the minimum energy required to starting a chemical reaction. As an empirically determined parameter that indicates the relationship between temperature and the rate constant for a reaction, it can be obtained from parabolic rate constant at various temperatures by plotting a line as in Fig. 1.21 as follows.

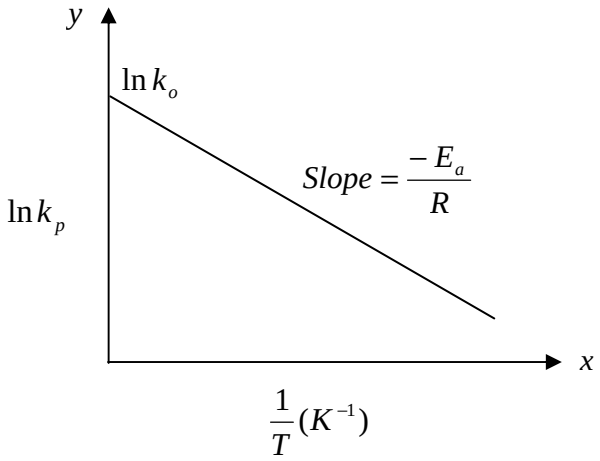

Figure 1.21: Illustration of the straight line graph.

Where

k_p = parabolic rate constant ($g^2.cm^{-4}.s^{-1}$)
k_o = proportionality constant ($g^2.cm^{-4}.s^{-1}$)
E_a = apparent activation energy of the oxidation ($J.mol^{-1}$)
R = ideal gas constant (8.314 $J.mol^{-1}.K^{-1}$)
T = absolute temperature (K)

A common form of a linear equation in the two variables x and y is

$$y = mx + b \qquad (1 - 17)$$

Where

m = slope
b = gives the y-intercept

Therefore

$$\ln k_p = m \cdot \left(\frac{1}{T}\right) + \ln k_o \qquad (1 - 18)$$

Take exponential function

$$k_p = k_o \cdot \exp\left(\frac{m}{T}\right) \qquad (1 - 19)$$

The Arrhenius equation given

$$K = A \cdot \exp\left(\frac{-E_a}{RT}\right) \qquad (1 - 20)$$

Where

K = reaction rate coefficient
A = pre-exponential factor
E_a = activation energy ($J.mol^{-1}$)
R = ideal gas constant (8.314 $J.mol^{-1}.K^{-1}$)
T = absolute temperature (K)

Considering equation (1 – 19) and (1 – 20), the relationship can be obtained as

$$m = \frac{-E_a}{R} \qquad (1 - 21)$$

The apparent activation energy (E_a) can be calculated from equation (1 – 21).

1.3.3 Mechanism of scale formation

A basic knowledge of scale growth is described by Kofstad in Fig. 1.22. Hence, there are two principal types of scale growth that are the growth of compact and porous scale. The reaction mechanism is complex and results from a series of elementary steps. The nature of these elementary steps depends on the structure of the scale formed.

1. The scale formed is compact and mass transport (protective scale) occurs by means of solid-state diffusion (Fig. 1.22 a).
2. The scale formed is porous and mass transport (non-protective scale) occurs by gas diffusion (Fig. 1.22 b).

Oxides with volume much greater (twice and more) than the volume of metal, from which the oxide was formed cause developing compressive stresses. The stresses may lead to cracking and scale spalled, which resulted in faster penetration of oxygen to the metal surface.

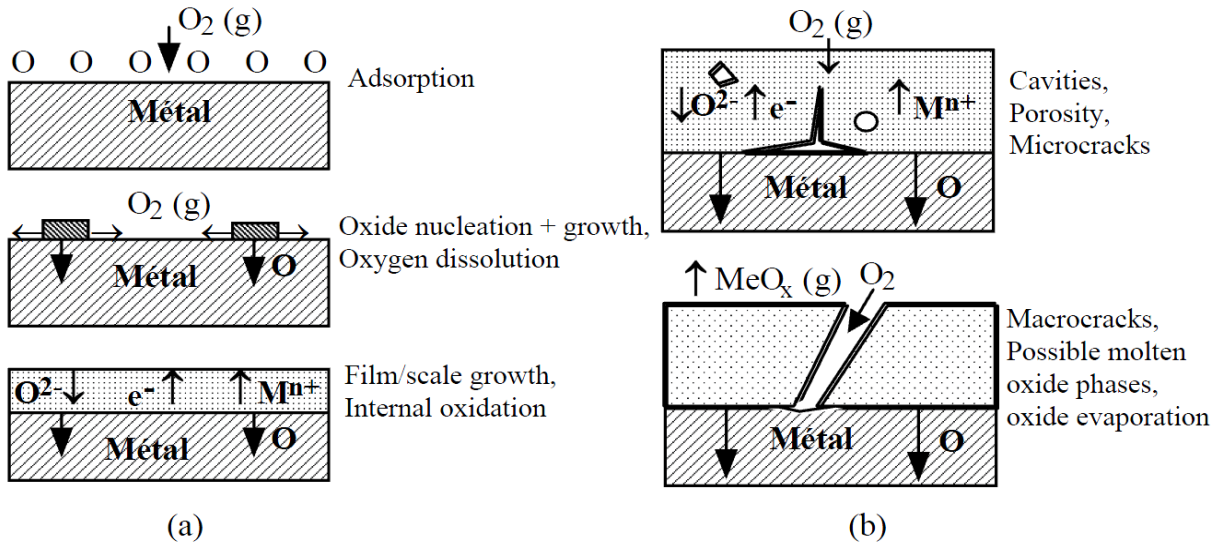

Figure 1.22: Schematic illustrations of some of the main aspects of metal-oxygen reaction [Sarrazin (2000); redrawn from Kofstad (1988)].

The direction of oxidation behaviour (internal or external) is also a very important indicator of the oxidation mechanism. Internal oxidation is associated with major transport of oxygen through the scale. Internal oxidation zone cannot be removed by conventional descaling methods. On the contrary, external oxidation is the result of major cation transport.

In case of a compact scale growth, in general, a schematic cross-sectional view of a growing oxide scale is shown in Fig. 1.23. The overall oxidation process can be subdivided into several steps.
1. Delivery of oxidant to the scale-gas interface via mass transfer in the gas phase.
2. Incorporation of oxygen into the oxide scale.
3. Delivery of reacting metal from the alloy to the alloy-scale interface.
4. Incorporation of metal into the oxide scale.
5. Transport of metal and/or oxygen through the scale.

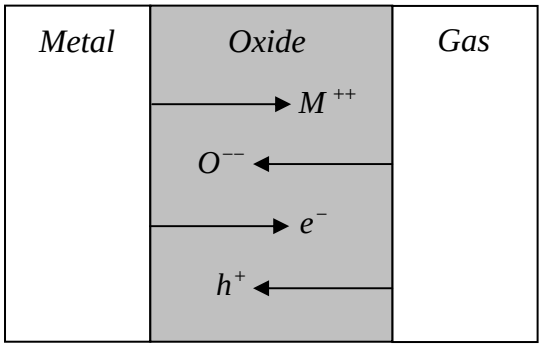

Figure 1.23: Transport of ions and electrons in gradients of oxygen activity and electric potential across a growing oxide scale [Atkinson (1985), Landolt (1997)].

Evolution of the rates at which these steps occur involves calculation of the gas phase mass transfer, calculated from the methods of fluid dynamics, and solid-state mass transfer or diffusion in the oxide and alloy, which can be described using diffusion theory.

The mechanism of iron oxidation is such that the different oxide layers grow mainly by the transport of iron cations from the metal surface toward the oxide-gas interface accompanied by the inward diffusion of electrons and outward diffusion of vacancies through the scale layers. A simplified mechanism for the oxidation of iron is given in Fig. 1.24. The kinetics of scale growth can be explained by a classical model of scale growth by the predominant vacancy diffusion at T < 1000°C of a three-layered oxide scale (wüstite, FeO: magnetite, Fe_3O_4 and hematite, Fe_2O_3) [Sarrazin (2008)].

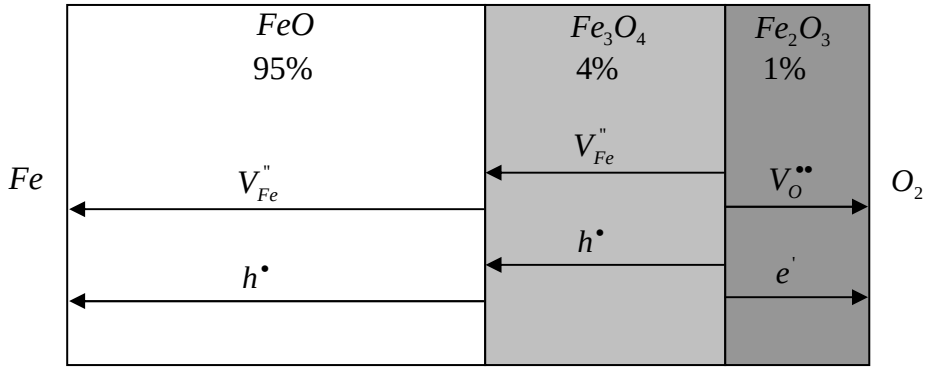

Figure 1.24: Vacancy diffusion for the growth of the three-layered oxide scale on iron [Sarrazin (2008)].

Using the Krogër-Vink notation, the reactions involved are as follows.

Oxide-gas interface

Dissociative sorption: $O_2 + 2s \leftrightarrow 2O - s$

External reaction: $O - s + \left(V_O^{\bullet\bullet}\right)_H + 2e^{'} \leftrightarrow \left(O_O\right)_H + s$

Hematite-magnetite interface

Hematite growth: $2\left(Fe_{Fe}\right)_M \leftrightarrow 2\left(V_{Fe}^{''}\right)_M + 2\left(Fe_{Fe}\right)_H + 3\left(V_O^{\bullet\bullet}\right)_H + 4h^{\bullet} + 6e^{'}$

Magnetite growth: $4\left(O_O\right)_H \leftrightarrow 3\left(V_{Fe}^{''}\right)_M + 4\left(O_O\right)_M + 4\left(V_O^{\bullet\bullet}\right)_H + 6h^{\bullet} + 8e^{'}$

Magnetite-wüstite interface

Transfer of iron vacancies: $\left(Fe_{Fe}\right)_W + \left(V_{Fe}^{''}\right)_M + 2h^{\bullet} \leftrightarrow \left(Fe_{Fe}\right)_M + \left(V_{Fe}^{''}\right)_W + 2h^{\bullet}$

Wüstite growth: $3\left(Fe_{Fe}\right)_M + 4\left(O_O\right)_M \leftrightarrow 3\left(Fe_{Fe}\right)_W + \left(V_{Fe}^{''}\right)_M + 4\left(O_O\right)_W + 2h^{\bullet}$

Metal-oxide interface

$$Fe + \left(V_{Fe}^{''}\right)_W + 2h^{\bullet} \leftrightarrow \left(Fe_{Fe}\right)_W$$

Where

V_{Fe}, V_O	= vacancies of iron and oxygen
Fe_{Fe}, O_O	= ions of iron and oxygen on normal lattice site
s	= site at the surface
$O - s$	= oxygen adsorbed onto a site at the surface
$h^{\bullet}$	= electron hole
$e^{'}$	= free electron
Subscripts H, M, W	= hematite, magnetite and wüstite respectively

From these equations, it can be appreciated that wüstite grows at its interface with the magnetite layer by the reduction of the latter. Magnetite grows at the magnetite-hematite interface where hematite also grows. This interface is therefore immobile due to the opposite directions of defect transport within these two oxides. The oxidation rate law is parabolic and assumed that all interfacial are equilibrium. The diffusion coefficients of the major diffusing species within each scale are shown in Fig. 1.25.

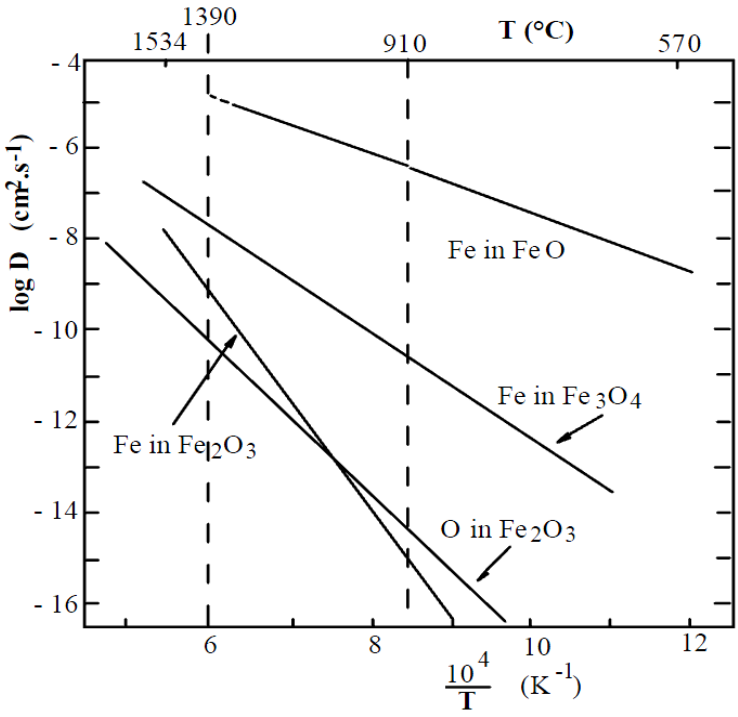

Figure 1.25: Self-diffusion coefficients of iron and oxygen in iron oxides [Sarrazin (2008)].

In case that other element is added in iron, mechanism of oxide scale growth can be changed. In case that silicon is added to iron, it is widely known that silicon oxide formed at the metal-scale interface plays as a diffusion barrier for Fe ions, resulting in an increase of the oxidation resistance. Fig. 1.26 proposed the mechanism of oxidation of Si-containing steel. The discussion is made that the fayalite phase formed at the internal interface inhibits the outward diffusion of iron ion. This then resulted in the thinner layer of the innermost wustite layer with larger outermost hematite scale as observed in that work [Nishimoto (2011)].

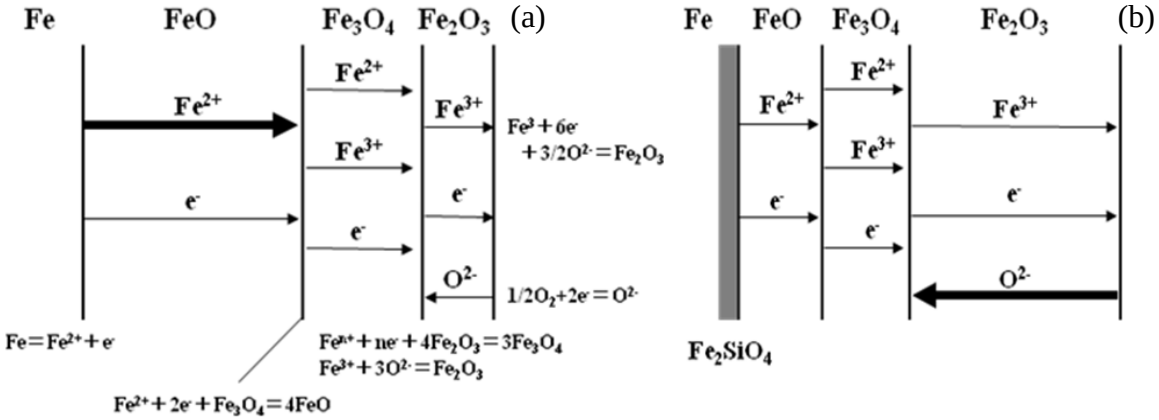

Figure 1.26: Schematic representation of the oxide scale formation on the Si alloys (a) on pure iron and low Si alloys, (b) on high Si alloys [Nishimoto (2011)].

1.4 Adhesion of thermal oxide scales

Adhesion of the scale described as oxide thickness increases, compressive stresses may also increase and result in localised spallation and/or cracking. An example of oxide spallation by a buckling process is shown schematically in Figure 1.27. Under tensile stresses, cracks appear as soon as the elastic fracture strain is reached. Under compressive stresses, the degradation leads to spallation and the mechanisms are more complex.

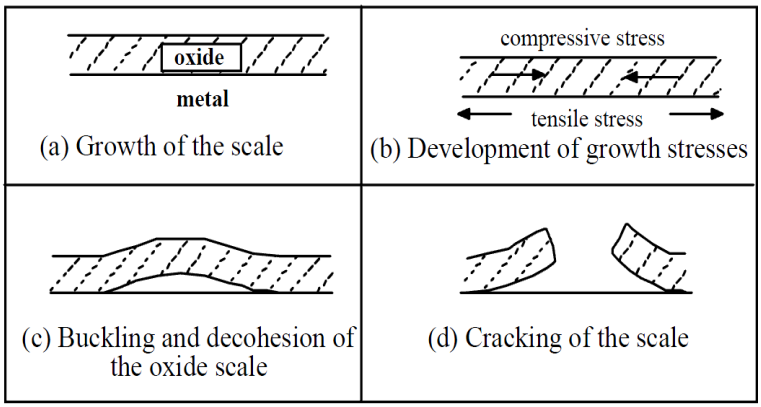

Figure 1.27: Schematic description of oxide scale buckling and cracking due to compressive stress [Sarrazin (2008)].

Fig. 1.28 illustrates two distinct mechanisms. Two routes to spallation have been identified, the case corresponding to a low cohesive strength of the oxide and a high adhesive strength of the scale on the substrate surface (route 1, cracking of the oxide before decohesion) and the case corresponding to a high cohesive strength of the oxide and poor adhesion of the oxide to the metal (route 2, decohesion before metal cracking).

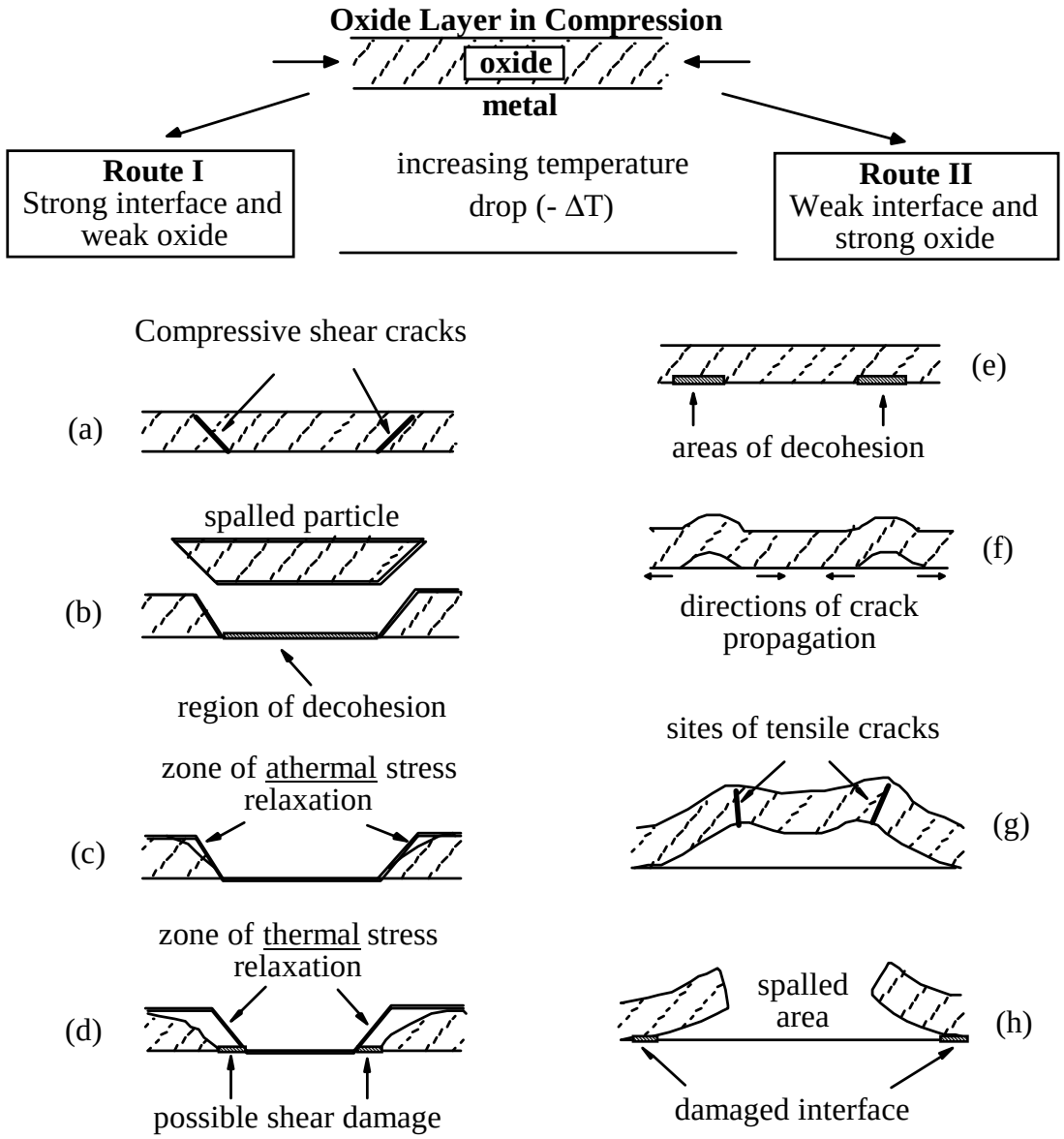

Figure 1.28: Cracking and spallation caused by compressive oxide stresses [Sarrazin (2000); redrawn from Evans (1995)].

In case of scale on iron, the mechanism of internal stress formation in iron oxide layers growing at temperatures above 570°C is proposed as in Fig 1.29. Owing to the weak texture in the entire iron oxide scale, epitaxial strains do not have a significant influence on the internal stress state of the individual sub-layers. More relevant sources of growth stresses are volumetric differences between the iron oxide phases at the early oxidation stages, and later new oxide formation within hematite and magnetite, wüstite consumption as well as pore formation in the magnetite layer. Magnetite initially grows under tensile stresses, whereas wüstite is subjected to increasing compression during the initial stages of oxidation of mild steel. A volumetric change in the iron lattice due to inward migration of oxygen ions, hematite has a greater atomic volume than magnetite. This rapidly leads to high compressive stresses in hematite during the early oxidation stages, but also supports the formation of tensile stresses in magnetite at its interface with hematite, as proposed by [Juricic (2010)].

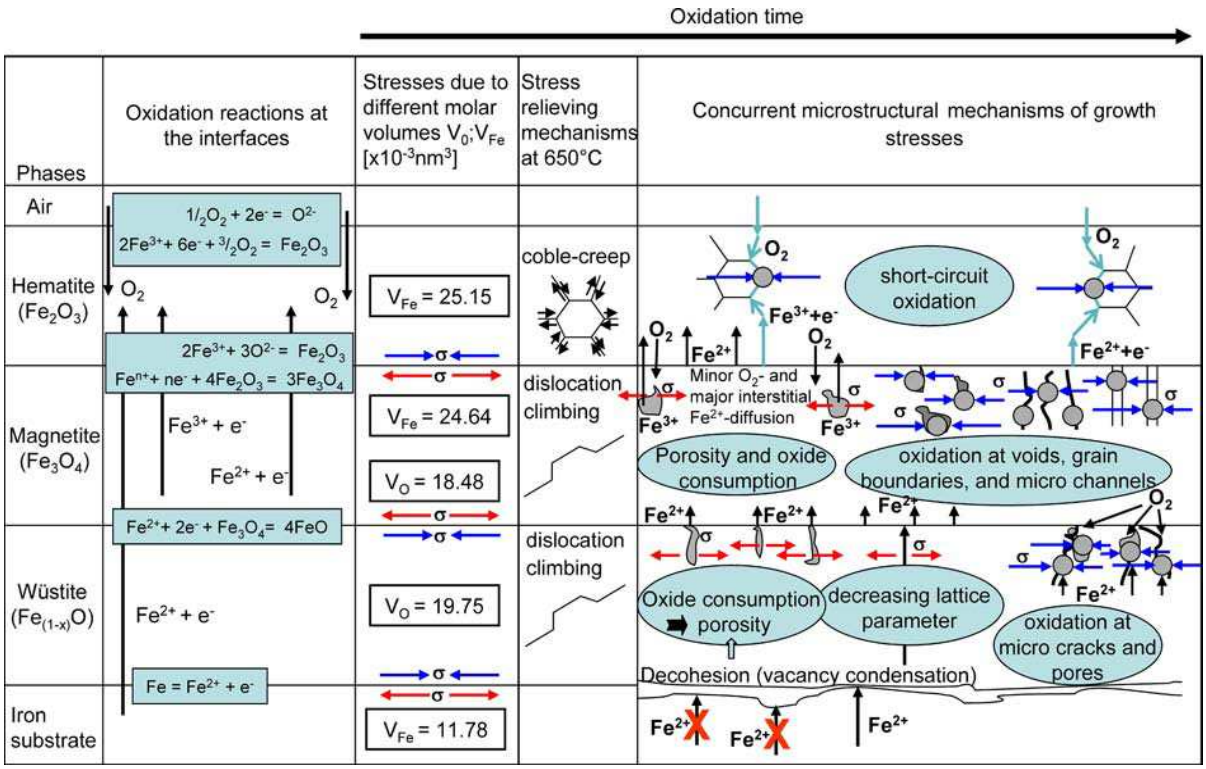

Figure 1.29: Mechanisms of internal stress formation in iron oxide layers growing at temperatures above 570°C [Juricic (2010)].

In order to understand adhesion behaviour of scale on metallic substrate, many testing methods have been developed to asses scale adhesion. The inverted blister test was used for measuring adhesion on thin materials, for example on ferritic stainless steel foils [Mougin (2002), (2003), Galerie (2004)]. The micro-tensile test operating in the scanning electron microscope chamber were operated for thicker strip particularly for stainless steel, comparing to that tested by the inverted-blister test [Galerie (2004), Toscan (2004), Chandra-ambhorm (2007), (2009)]. Other methods for evaluating the mechanical adhesion of scales on steel substrates are the macro tensile test [Krzyzanowski (1999), (1999), (2000), Genève (2010), Chiu (2011), Ngamkham (2011), Nilsonthi (2012), (2013)], the three point bending test [Galerie (2004)], the indentation test and the pull test [Monteiro (2011)]. Since the present work is applied tensile test to evaluate scale adhesion, the following paragraphs will review that issue.

[Nagl (1993)] proposed a failure mechanism for oxide scales under tensile stress, first through-scale cracks develop at regions of high stress concentration (Fig. 1.30). Elastic stress relaxation in the vicinity of these cracks can reduce the local stress concentration within the oxide segment. Plastic stress relaxation within the oxide is possible if sliding can occur at the metal-oxide interface. The shear translation may induce fracture damage at the interface which could result in delamination and subsequent spallation.

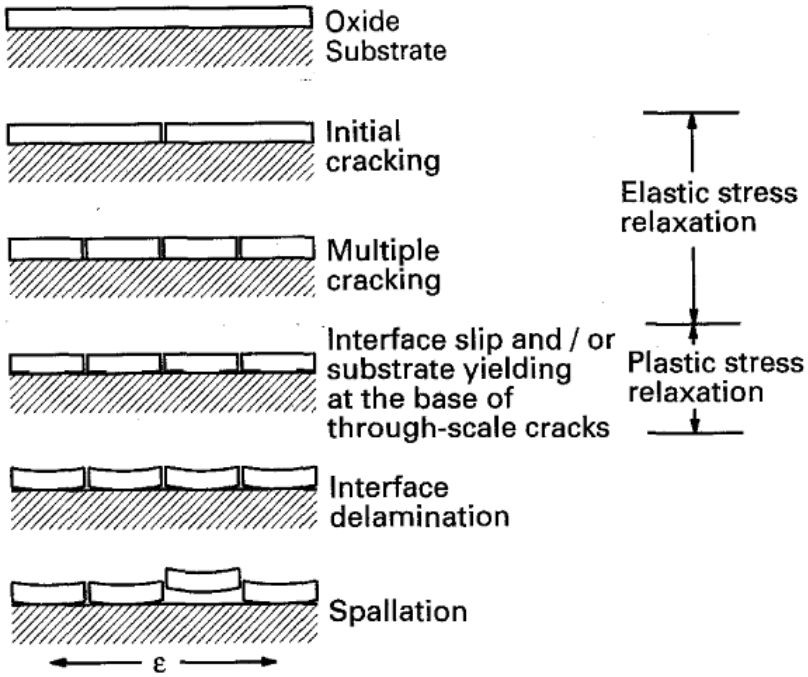

Figure 1.30: Schematic diagram of cracking and spallation caused by tensile oxide stress [Nagl (1993)].

After the transverse crack taking place during tensile loading, the oxide buckling can be generated by the transverse stress due to the Poisson's effect. The redistribution of the stress in metal-oxide system in the presence of crack is depicted in Fig. 1.31 [Evans (1995)]. As can be seen from this figure, it was found that the development of through-thickness tensile cracks, extended in Fig. 1.31 (a) depict the results in perturbation of distribution of average in-plane tensile stress. Fig. 1.31 (b) depicts the development of shear stresses at metal-oxide interface, and Fig. 1.31 (c) depicts the computations basing on the models of Grosskreutz, Nicholls and Tien and Davidson. It may be noted that the tensile stress in the vicinity of crack is relaxed as shown in this figure.

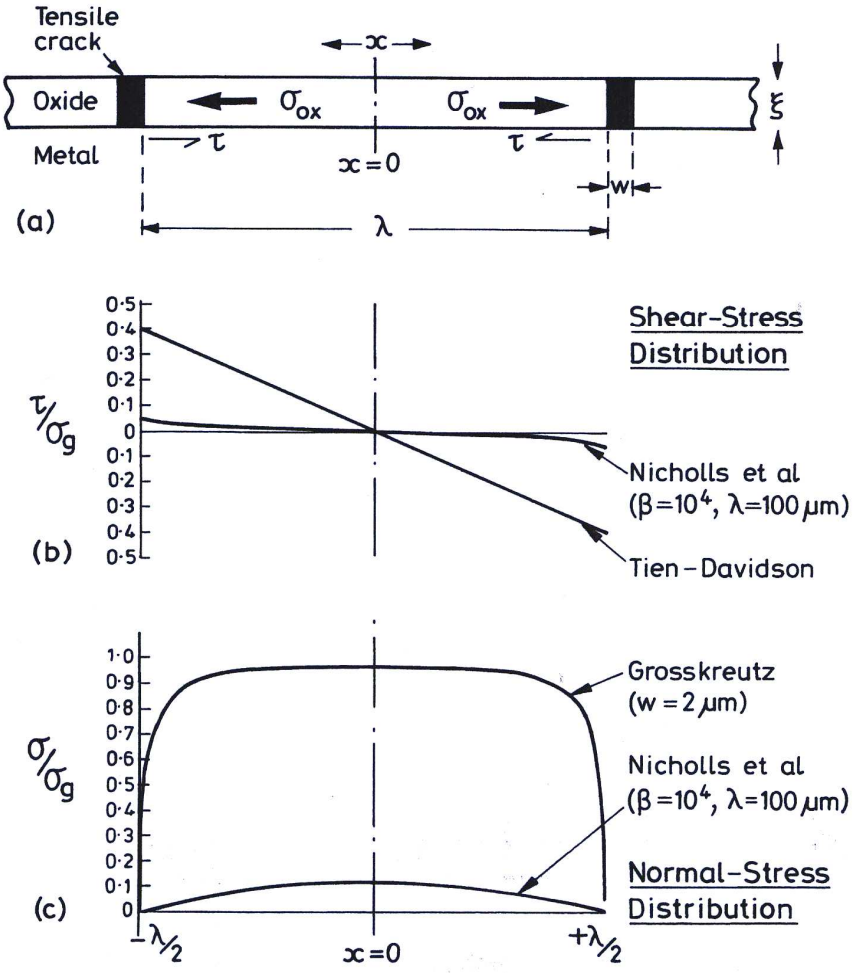

Figure 1.31: Redistribution of the shear and tensile stress in a cracked scale [Evans (1995)].

The tensile test has been developed to assess scale adhesion, as exemplified in Fig. 1.32. The figure shows the measured failure strains for iron oxide on mild steel as a function of oxide thickness. The failure strains decreased with increasing oxide thickness [Nagl (1993)]. It was reported that lower oxide thickness corresponded to higher crack density [Chandra-ambhorn (2006)].

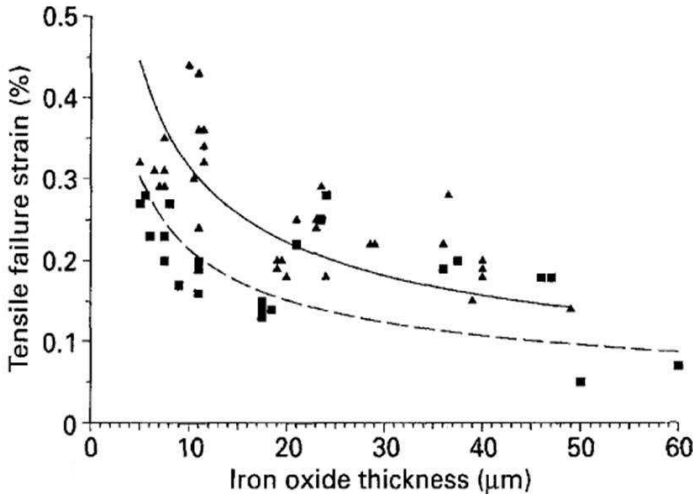

Figure 1.32: Measured failure strains as a function of thickness for iron oxides tested in tension at (▲) room temperature and at (■) 550°C using a strain rate of ~10^{-4} s^{-1} [Nagl (1993)].

1.5 Pickling test

Descaling by mechanical means generally employs high pressure water in a hydraulic descaler which follows the hot rolling part of the line. The main chemical means uses pickling by hydrochloric acid which is generally applied after mechanical descaling.

The picklability behaviour of scales on the steel substrate can be evaluated by an immersion test [Gines (2002), Chattopadhyay (2005), (2008), Bhattacharya (2006), Jatuphaksamphan (2006), (2010), Zhang (2007), Somphakdee (2010)]. Other methods for evaluating the picklability are the electrochemical test, e.g. the electrochemical impedance spectroscopy (EIS) method [Pérez (2006)] and potentiodynamic method [Onsanit (2006)].

Descaling or pickling time depends on hydrochloric acid and ferrous ion concentrations, and solution temperature. Temperature is the most important variable, followed by hydrochloric acid concentration. The ferrous ion concentration has little relevance on descaling time [Gines (2002), Jatuphaksamphan (2006)].

The magnetite (Fe_3O_4) and hematite (Fe_2O_3) are slightly soluble in acidic solution and therefore delay the pickling process in the scales [Chattopadhyay (2005)]. The scale full of wüstite (FeO) is easily pickled [Zhang (2007)].

As for the role of silicon on pickling ability of steel, it was reported [Chattopadhyay (2008)] that the pickling reaction kinetics of particular steel is mostly dependent on the oxide morphology of their steel. The Si content in the steel influences the oxide morphology. When the Si content in the steel is more than 0.35%, the fayalite phase formation dominates (Fig. 1.33) and influences the pickling kinetics (Fig. 1.34), suggesting more difficult descaling of scale on the steel (Fig. 1.35). In order to obtain better quality pickled steel strips, the Si content should be kept as low as possible.

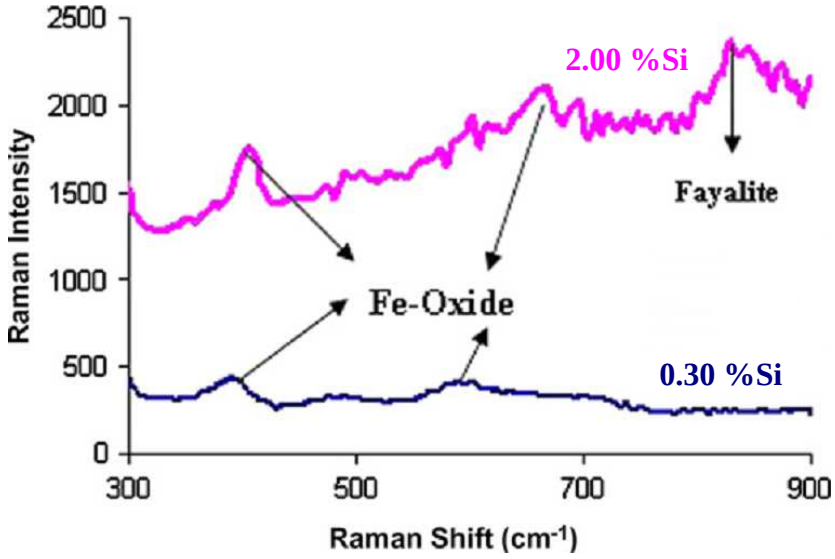

Figure 1.33: Raman spectroscopy results of steel 0.30 %Si and steel 2.00 %Si [Chattopadhyay (2008)].

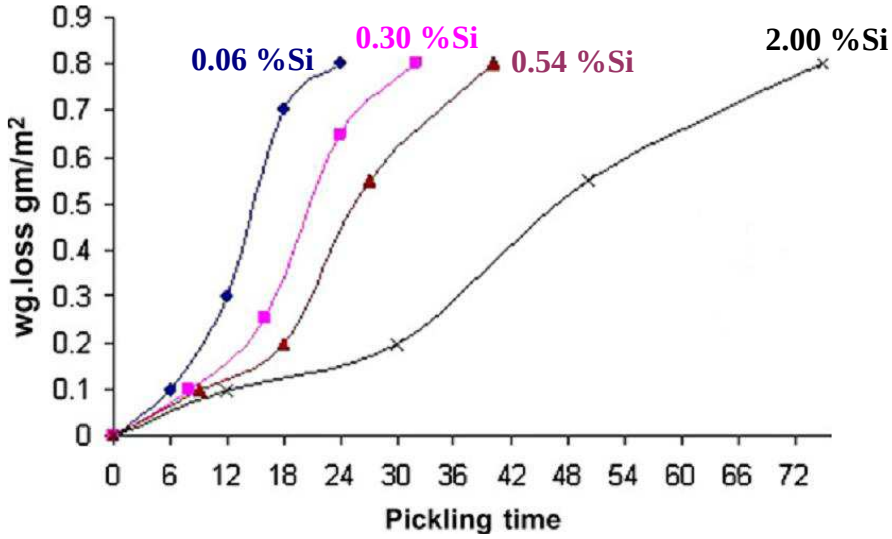

Figure 1.34: Picklability behaviour of different Si containing steels [Chattopadhyay (2008)].

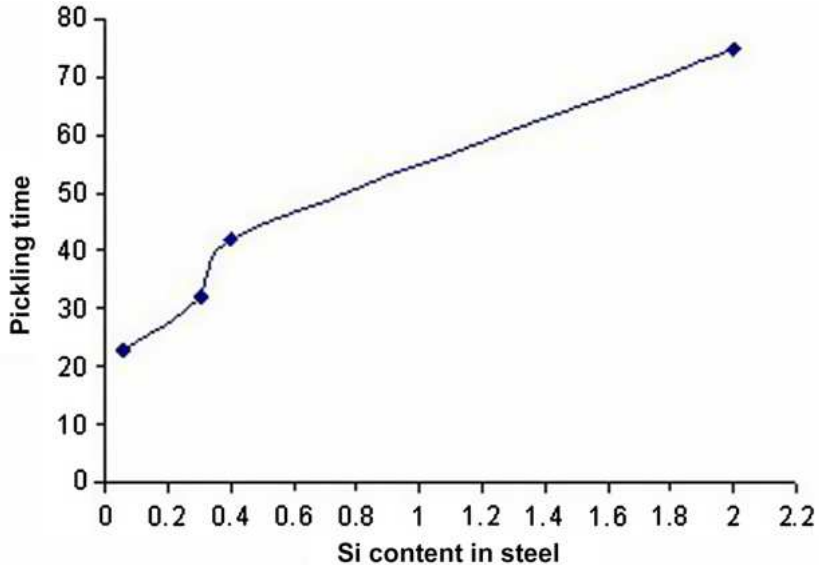

Figure 1.35: Relationship between the Si content in steel with the pickling kinetics [Chattopadhyay (2008)].

CHAPTER 2

EXPERIMENTAL METHODS

2.1 Materials

2.1.1 The hot-rolled steel strips as-received materials

The effect of slab elaboration process on mechanical adhesion was evaluated via two hot-rolled low carbon steels. The steels were cut from strips obtained from slabs produced by the blast-furnace route called in the present work conventional steel (provided by Sahaviriya Steel Industries (SSI) company in Thailand) and slabs produced by the electric-arc-furnace route called in the present work recycled steel (provided by G steel company in Thailand). The finishing and coiling temperatures of the conventional steel are 910°C and 610°C respectively, and for the recycled steel are 880°C and 580°C respectively. The thicknesses of the strips were 3.2 mm for the conventional steel and 6 mm for the recycled steel. Their chemical compositions are given in Table 2.1. It can be observed that the Si content of the recycled steel is 20 times larger than that of the conventional steel. Also Cu is 3 times higher in the recycled steel. This high level of those two elements is one of the characteristics of the recycled material, due to the use of various scraps.

Table 2.1: Chemical compositions of the studied hot-rolled steels (wt.%).

Steel	C	Si	Cu	Mn	Al	P	S	Fe
Conventional	0.033	**0.013**	**0.059**	0.232	0.043	0.006	0.009	bal.
Recycled	0.058	**0.267**	**0.168**	0.347	0.020	0.013	0.004	bal.

The particular effect of Si on mechanical adhesion was evaluated via two hot-rolled low carbon steel strips obtained from slabs produced by the blast-furnace route only (conventional steel, provided by SSI steel company), differing only by their Si content. They were produced using the same finishing and coiling temperatures of 860°C and 610°C respectively. The thicknesses of the strips were 3.2 mm. Chemical compositions of the studied steel are listed in Table 2.2. They contained lower Si content (0.026 wt%) called “0.026-wt% Si” steel, and higher Si content (0.193 wt%) called “0.193-wt% Si” steel.

Table 2.2: Chemical compositions of the studied hot-rolled steels (wt.%).

Steel	C	Si	Cu	Mn	Al	P	S	Fe
0.026-wt% Si	0.193	**0.026**	0.040	0.521	0.039	0.008	0.008	bal.
0.193-wt% Si	0.165	**0.193**	0.047	0.542	0.036	0.011	0.007	bal.

2.1.2 Model steel

Effects of Si and Cu alloying element on oxidation kinetics was evaluated via a model steel with various compositions of Si and Cu provided by ArcelorMittal company in France (courtesy of E. Ahtoy). This steel was prepared by adding adjusted amounts of alloying elements (Si, Cu) into an industrial iron base with very little residual elements, called reference steel. The special furnace for production of this steel is shown in Figure 2.1.

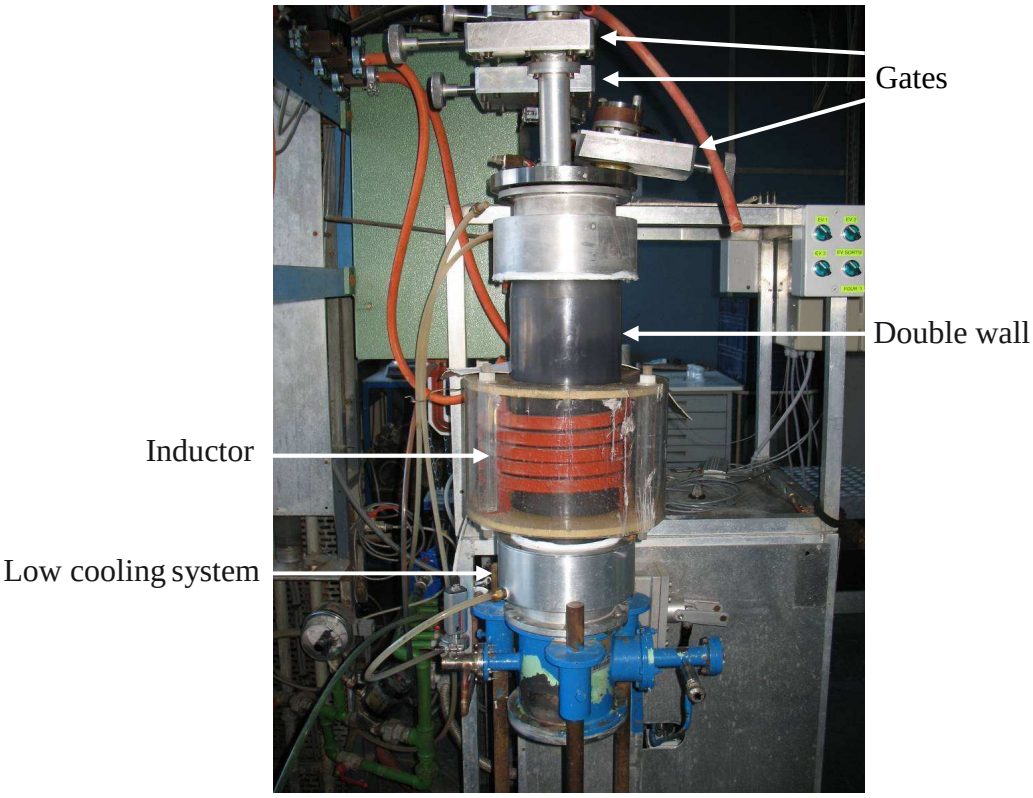

Figure 2.1: Furnace used for the model steel [Ahtoy (2010)].

The process was performed under vacuum with control of non-metallic (O, N, C and S) residuals. The steels were produced as cylinder shape with dimensions 10 cm of length and 5 mm of diameter. The chemical composition of the present steels was determined by optical emission laser spectroscopy. Their composition is listed in Table 2.3.

Table 2.3: Type of the studied industrial alloys steels.

Steel	Grade	
Fe	Reference (mainly Fe with a small amount of impurities)	
Si alloys (wt% Si)	0.25	0.84
Cu alloys (wt% Cu)	0.08	0.39

2.2 Physico-chemical characterisation

The oxide scale thickness was measured using scanning electron microscope (SEM, JEOL JSM-6400) observations of Calotest® imprints (Fig. 2.2) and also of polished cross-sections. The cross-sections of oxide scale were also observed by a scanning electron microscope (SEM, LEO S440). X-ray diffraction (XRD, Rigaku Miniflex II) was performed for phase identification. On the Calotest imprints, Raman spectroscopy (Raman, Renishaw RM 1000) was employed to observe the nature of oxides at different locations on the surface and within the scale, making possible to obtain the depth profile of the different phases.

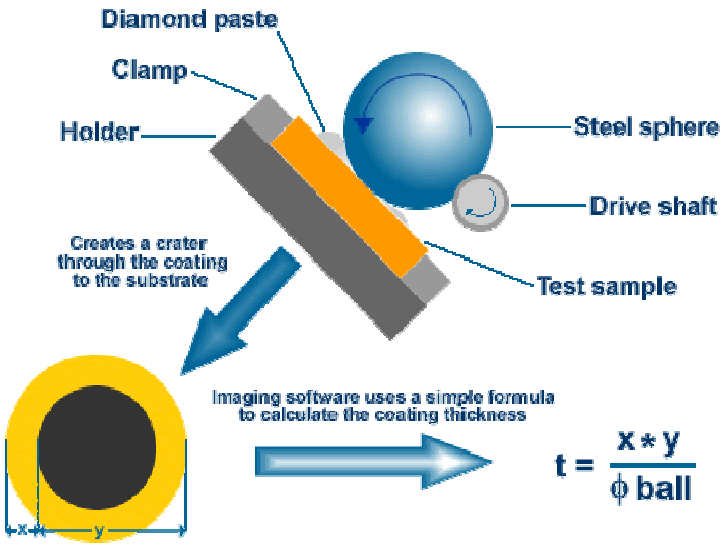

Figure 2.2: The Calotest is a simple method to determine the coating thickness [http://pvd-coatings.co.uk].

2.3 Oxidation kinetics

For studying oxidation kinetics, the model steel samples were prepared with dimensions of 5 mm in length and 5 mm in diameter. The steels were polished by SiC-papers up to 1200 grit, cleaned up by ethanol used in ultrasonic machine, dried in air and immediately placed in the furnace of the thermal gravimetric analyzer. Oxidation kinetics was investigated in 20%H_2O/Ar with the flow rate through 6 $L.h^{-1}$. Oxidation temperatures were studied in the range of 600 to 900°C during 16 hours. A sample oxidised was slowly cooled down in the furnace to ambient temperature. The slow cooling rate decreases the residual stresses which can be attributed to a relaxation phenomenon on the scales [Mougin (2001)].

The oxidation experiments were performed in the thermobalance as a model B 24 from SETARAM (Fig. 2.3). Experimental research conducted at Surface Interfaces Réactivité (SIR), Science et Ingénierie des Matériaux et Procédés (SIMaP), the laboratory of Science and Engineering of Materials and Process of Grenoble INP, Université de Grenoble, France.

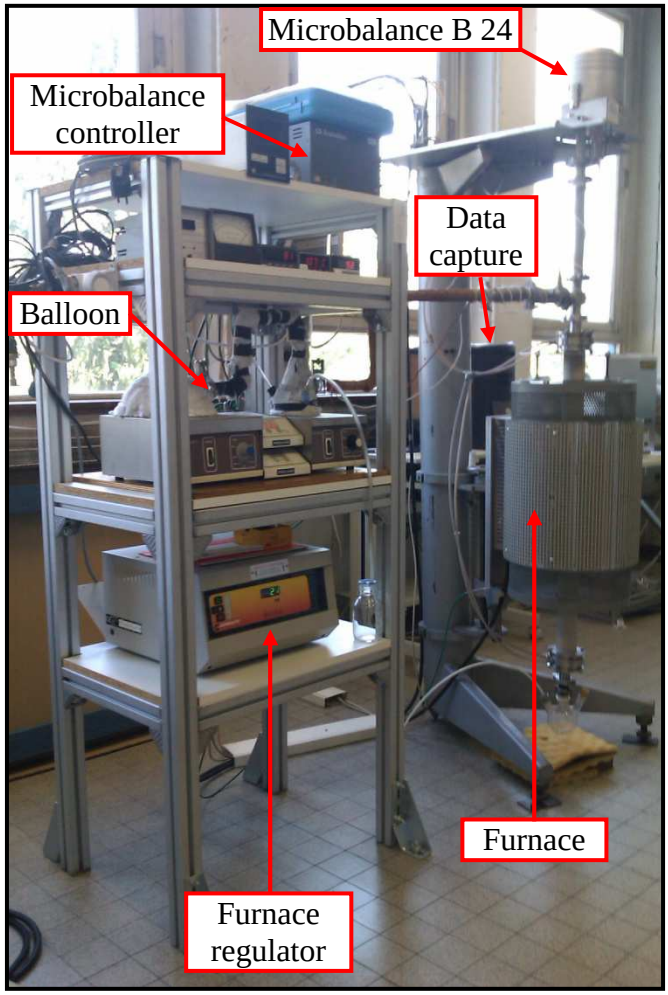

Figure 2.3: Thermobalance model B 24.

Fig. 2.4 gives a schematic view of a typical single-furnace thermobalance of this type used for studying the high temperature corrosion of metal in water vapour. A silica rod is the material used to hang the sample in the vertical alumina reaction tube. The electrically heated furnace is also placed vertically and a thermocouple is used to measure the temperature of the reaction vessel. The water-containing vessel is used to control the concentration of water vapour in the equipment.

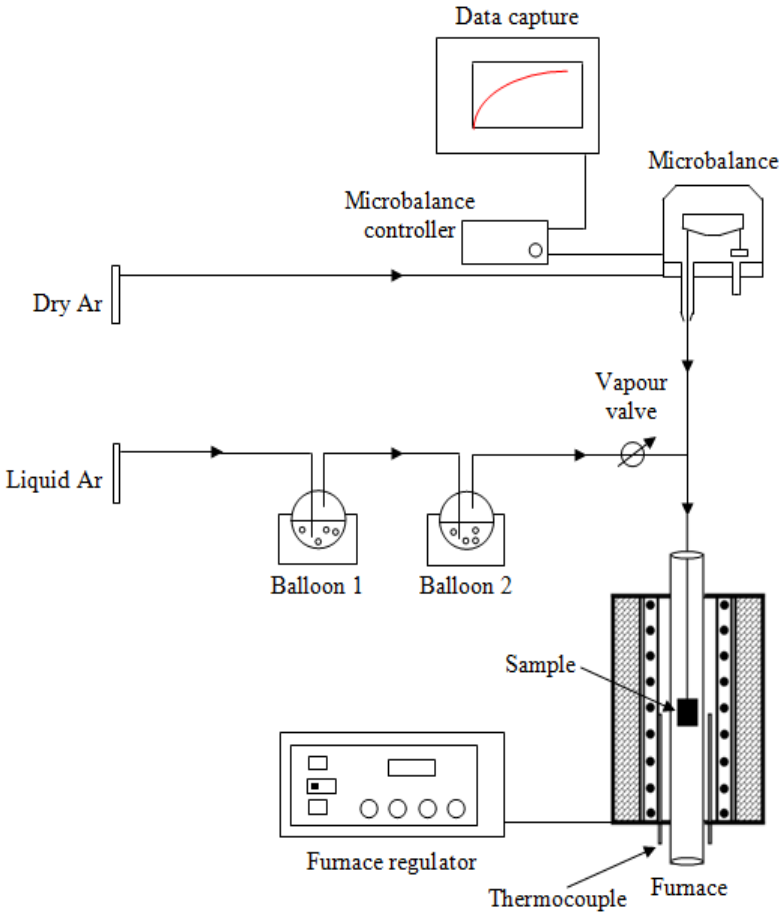

Figure 2.4: General view of a single-thermobalance setup.

Beam thermobalances are device as the pivoted-beam laboratory precision, used for analytical mass gain oxidised via a variation of the potential difference appeared. At one end of the beam the sample was hung using a silica rod (melting point temperature of silica ~ 1100°C), and at the other end is weight balance. Any mass variation perturbs the equilibrium of the beam, inducing a signal from the electro-optical system. This signal is amplified and drives the re-equilibration force applied to the system (Fig. 2.5). The mass variation and only the current are flowing in the solenoid changes proportionally to these variations. This current is measured and gives the mass changes after a simple calibration procedure [Sarrazin (2008)].

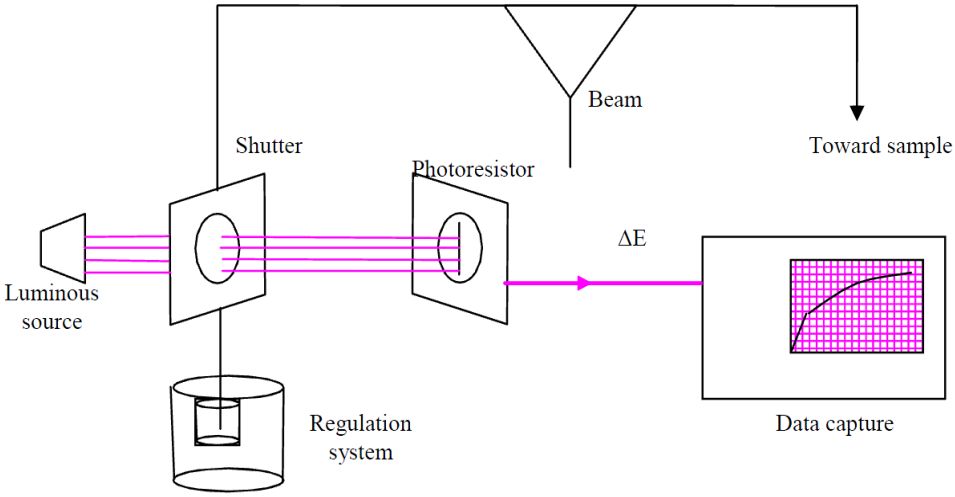

Figure 2.5: Principle of thermobalance operation [Sarrazin (2008)].

2.3.1 Determination of the equivalent gas flow

For the micro-tensile test, isothermal oxidation was conducted by a horizontal furnace (Fig. 2.6) in water vapour (20%H_2O/Ar) atmosphere for 1 to 3 minutes at 900°C with the flow rate 6 $L.h^{-1}$. Before oxidation runs, a sample is prepared by used SiC-papers up to 1200 grit for polishing scale the as-received hot-rolled low carbon steel strips (0.026-wt% Si and 0.193-wt% Si steels), the samples were cleaned up by ethanol used in ultrasonic machine, dried in air and immediately placed in the horizontal furnace.

Figure 2.6: General view of the horizontal furnace setup.

For the thermogravimetric runs, the oxidation was conducted in water vapour (20%H_2O/Ar) for 16 hours at 600 to 900°C with flow rate 6 $L.h^{-1}$ in the furnace contact with a single microbalance.

The various parameters used in the experiments can be calculated as follows.

Oxidation in water vapour **(**20%H_2O/Ar**),** gas flow rate used in each step as well as its pressure in balloon and vertical furnace can be determined as follows (Fig 2.7).

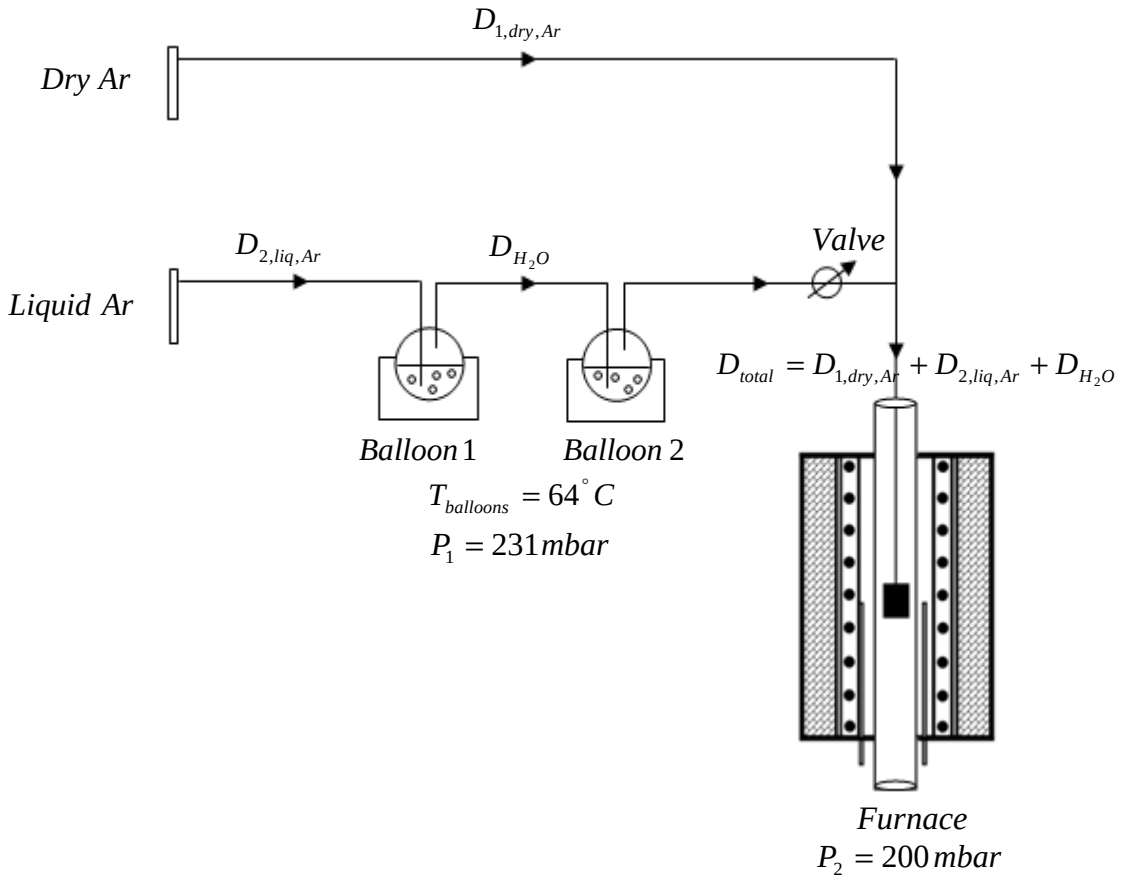

Figure 2.7: General view of the oxidation kinetics setup.

Flow chart calculation is shown below.

$$Total\ of\ \ flow\ rate\ (D_{total}) = 6\,L.h^{-1} = 100\,cm^3.\min^{-1}$$

$$20\,cm^3.\min^{-1}\ of\ H_2O_{(g)} \qquad 80\,cm^3.\min^{-1}\ of\ Ar\,(dry)$$

$$1bar \begin{cases} 600\,mbar\ of\ H_2O_{(g)} \\ 400\,mbar\ of\ Ar(liq) \end{cases}$$

$$Ar\,(dry) = (80\,cm^3.\min^{-1}) - (13.33\,cm^3.\min^{-1}) = 66.67\,cm^3.\min^{-1}$$

$$Ar\,(liq) = (20\,cm^3.\min^{-1}) \cdot (400\,mbar / 600\,mbar) = 13.33\,cm^3.\min^{-1}$$

Therefore

$$D_{1,dry,Ar} = 66.67\,cm^3.\min^{-1} = 4.00\,L.h^{-1}$$
$$D_{2,liq,Ar} = 13.33\,cm^3.\min^{-1} = 0.79\,L.h^{-1}$$
$$D_{H_2O} = 20.00\,cm^3.\min^{-1} = 1.20\,L.h^{-1}$$

$$D_{total} = 100\,cm^3.\min^{-1} = 6\,L.h^{-1}$$

Equations to find out the flow rate equivalent (D_{eq}) are as follows.

$$D_{1,eq,dry,Ar} = D_{1,dry,Ar} \cdot \sqrt{\frac{M_{Ar}}{M_{Air}}} \qquad (2-1)$$

And

$$D_{2,eq,liq,Ar} = D_{2,liq,Ar} \cdot \sqrt{\frac{M_{Ar}}{M_{Air}}} \qquad (2-2)$$

Where

$$M_{Ar} = Atomic\ weight\ of\ \ Ar = 39.95\,g.mol^{-1}$$
$$M_{Air} = Molecular\ \ weight\ of\ \ Air = 29\,g.mol^{-1}$$

As a result,

$$D_{1,eq,dry,Ar} = 4.00\,L.h^{-1} \cdot \sqrt{\frac{39.95\,g.mol^{-1}}{29\,g.mol^{-1}}} = 4.70\,L.h^{-1}$$

With (*Brooks tube size* $R-2-15-AA$, *Tantalum ball*, 47 *mm of high*)

And

$$D_{2,eq,liq,Ar} = 0.79\,L.h^{-1} \cdot \sqrt{\frac{39.95\,g.mol^{-1}}{29\,g.mol^{-1}}} = 0.93\,L.h^{-1}$$

With (*Brooks tube size* $R-2-15-AA$, *Stainless ball*, 19 *mm of high*)

Calculation of the saturated vapour pressure of water follows

$$Flow_{total} = D_{total} = D_{1,dry,Ar} + D_{2,liq,Ar} + D_{H_2O} = 6\,L.h^{-1}\,(100\,cm^3.\min^{-1})$$

With

$$D_{1,dry,Ar} = 4.00\,L.h^{-1}\,(66.67\,cm^3.\min^{-1})$$
$$D_{2,liq,Ar} = 0.79\,L.h^{-1}\,(13.33\,cm^3.\min^{-1})$$
$$D_{H_2O} = 1.20\,L.h^{-1}\,(20.00\,cm^3.\min^{-1})$$

Relationship of vapour pressure (P_1 *and* P_2) is as the following.

At balloons $$P_1 = \frac{D_{H_2O}}{(D_{1,dry,Ar} + D_{H_2O})} \qquad (2-3)$$

At furnace $$P_2 = \frac{D_{H_2O}}{D_{total}} \qquad (2-4)$$

As a result,

$$P_1 = \frac{1.20\,L.h^{-1}}{(4.00\,L.h^{-1} + 1.20\,L.h^{-1})} = 231 mbar$$

From Appendix III, Table A3.14 $P_1 = 231\,mbar$, $T_{balloons} = 64^{\circ}C$

A result from equation 2 – 4,

$$P_2 = \frac{1.20\,L.h^{-1}}{6.00\,L.h^{-1}} = 200\,mbar$$

2.3.2 Determination of the scale thickness

The steel oxidised at temperature of 600 to 900°C in the furnace with water vapour atmosphere. The scale thickness of iron oxide can be calculated as follows.

$$Oxide\ thickness\,(\mu m) = \frac{\Delta m\,(g)}{A(cm^2)} \cdot \frac{1}{M_O} \cdot M_{FeO} \cdot \frac{1}{\rho_{FeO\,(g/cm^3)}} \cdot 10^4 \qquad (2-5)$$

Where

$\Delta m = mass\ grain\ after\ oxidised\,(g) - mass\ grain\ before\ oxidise\,(g)$

$A = Area\,(cm^2)$

$M_O = Molecular\ weight\ of\ oxigen = 16\,g.mol^{-1}$

$M_{FeO} = Molecular\ weight\ of\ iron\ oxide = 72\,g.mol^{-1}$

$\rho_{FeO} = Density\ of\ iron\ oxide = 5.745\,g.cm^{-3}$

2.4 Tensile test

For studying the mechanical adhesion, the as-received hot-rolled oxidised steels were prepared. Two tensile test machines were used in this work for determining the strain at the first spallation and the evolution of the spalled fraction of scale. For the micro-tensile test, used in France, the samples were prepared with the specific shape fitting to the machine sitting in the chamber of the scanning electron microscope. During tensile loading, the evaluation of the failure of the scale was monitored by scanning electron microscopy (SEM). Image magnification was generally set at 200 x. The experimental set-up and quantification

method of the adhesion energy of this test were described elsewhere [Toscan (2004), Chandra-ambhorn (2006), Chandra-ambhorn (2007)]. The tensile strain rate of this test was fixed at 7×10^{-5} s^{-1}. For the new macro-tensile test, sitting in Thailand, the samples were prepared as required by the ASTM E8M standard. A macro-tensile testing machine of 600 kN force was used in this study. The tensile strain rate applied could be chosen at the following values 0.08, 0.33 and 0.83 s^{-1}. In this test, the evolution of scale failure was monitored by optical microscopy. Image magnification was generally set at 5 x. Notice that no extensive work has been applied to measure scale adhesion of low carbon steels at room temperature, even though this property is of importance for surface quality of the hot-rolled steel product. Samples prepared for the micro and macro-tensile testing machines are shown in Fig. 2.8.

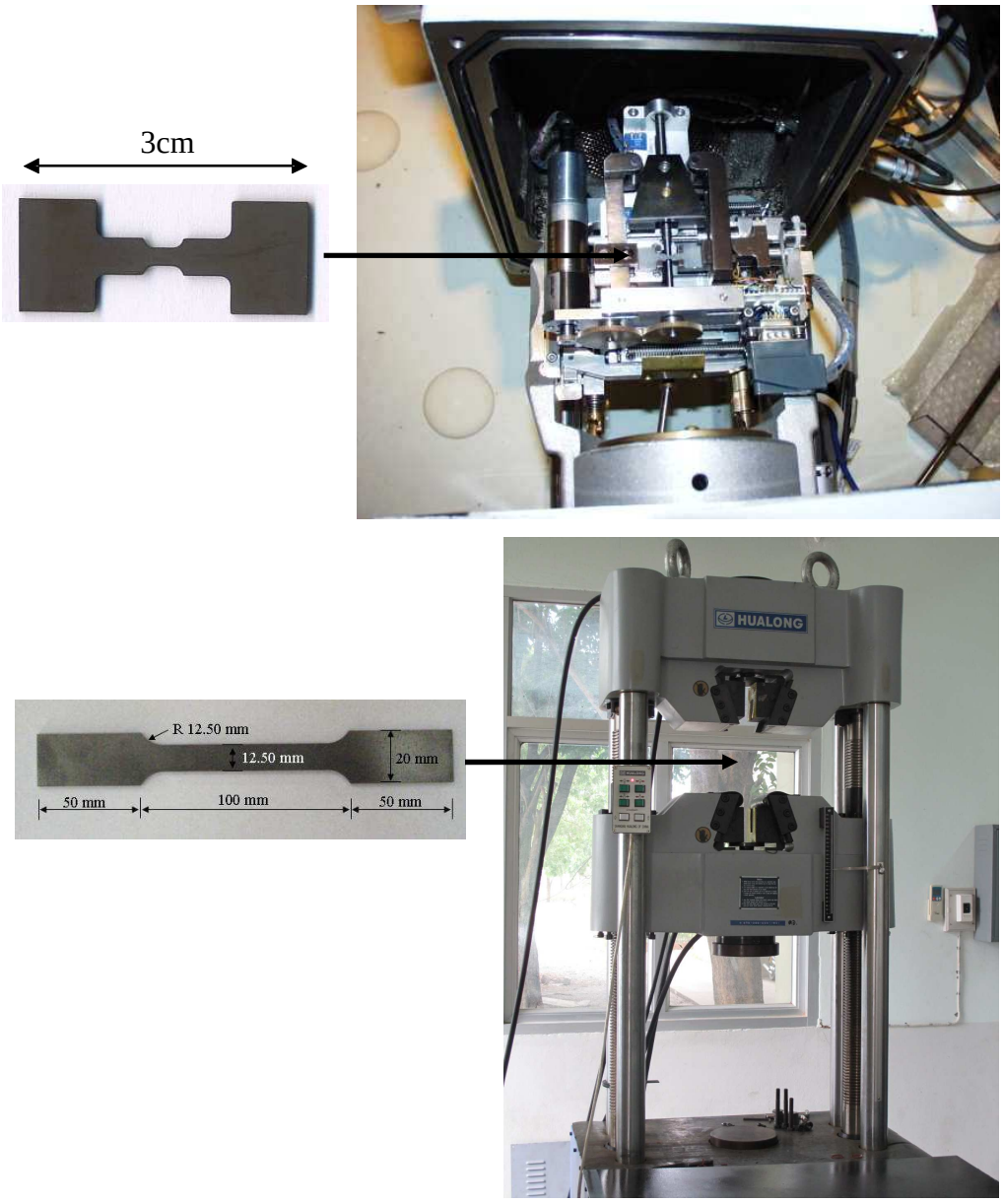

Figure 2.8: Typical shape of samples and general view of tensile machines for micro-tensile test (upper picture) [Toscan (2004)] and macro-tensile test (lower picture).

For the micro-tensile test, the small tensile machine which can be sat in the SEM chamber was used. In this case, the sample must be prepared with the special shape as shown in

Fig. 2.8. Elongation values recorded during the test was not the central of the sample since many other deformations, e.g. elongation of the sample holder or bending of the transmission arms, are occurred. The equation (2 – 6) was used to evaluate the actual metal strain, taking into account the actual Young's modulus of the metallic material and the actual measured elongation. The stress-strain relation in this case can be written as

$$\varepsilon_{act} = \varepsilon_{\exp} - \left[\sigma \cdot \left(\frac{1}{E_{\exp}} - \frac{1}{E_{met}} \right) \right] \qquad (2-6)$$

Where

ε_{act} = actual metal strain component along tensile axis
$\varepsilon_{\exp}$ = experimental strain of the metal
σ = metal stress component along tensile axis (GPa)
$E_{\exp}$ = experimental Young's modulus of the metal (GPa)
E_{met} = Young's modulus of the metal (GPa)

Fig. 2.9 indicated an example of both experimental and corrected curves for the hot-rolled low carbon steel for this study. The correction was applied to all experiments as described in the present work.

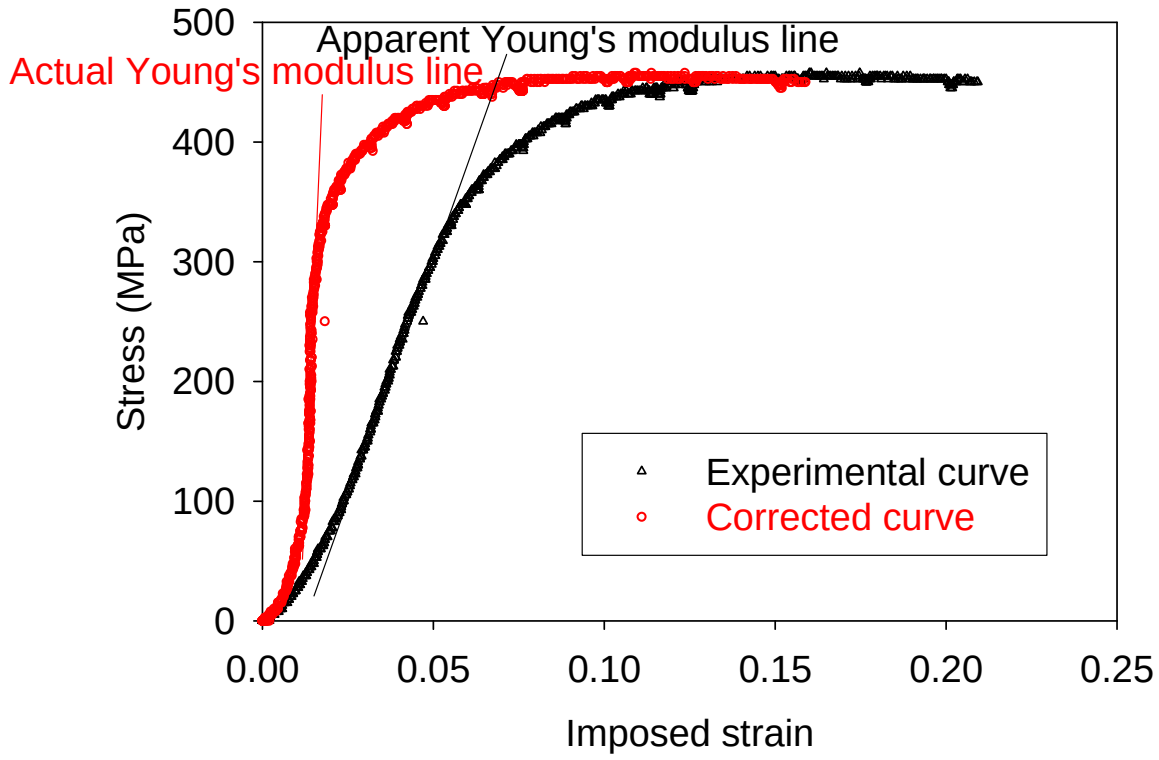

Figure 2.9: Example of correction stress-strain curves.

2.4.1 Determination of the mechanical adhesion energy

Determining the adhesion energy of oxide scale formed on the metallic surface is briefly reviewed from the references [Toscan (2004), (2004), Chandra-ambhorn (2006), Chandra-ambhorn (2007)]. As generally accepted [Evans (1995)], the perfect adhesion between metal-scale interface is assumed. The metal-scale interfacial fracture called as scale spallation. The mechanical adhesion energy at the first spallation can be given by

$$G_i = W_{total} \cdot e \qquad (2-7)$$

Where

G_i = mechanical adhesion energy ($J.m^{-2}$)
W_{total} = total elastic stored energy attaining the energy requires to form a new surface at the metal-scale interface ($J.m^{-3}$)
e = oxide scale thickness (m)

The total stored energy determination, the stress-strain evolution during the test is typically existed in both x and y directions parallel to the interface (x = tensile axis, y = transverse tensile axis), while that in z axis (perpendicular interface) is assumed to be zero (Fig. 2.10). The mechanical behaviour of the metal was initially elastically deformed and then subjected to a plastic deformation, while the oxide was still elastic until the first spallation takes place. The present work refers to metal by the subscript s (substrate) and to oxide by the subscript f (film). A second subscript indicates the main axis (x and y). The superscript indicates res for residual stress, el for elastic behaviour of the metal and pl for plastic behaviour of the metal.

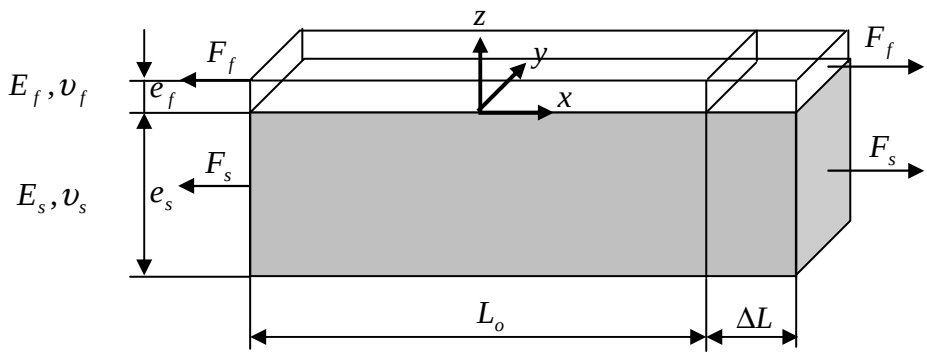

Figure 2.10: Tension of a coated substrate.

2.4.2 Quantification of the stored energy

The mechanical parameters for quantifying the stored energy are as the following.
The Young's modulus of the iron oxide (E_f) is $210\,GPa$,
the Poisson's ratio of metal and oxide are 0.3 ($\nu_s = \nu_f = 0.3$) by assuming perfectly adherent metal/oxide,
the Young's modulus of the metal (E_s) is $210\,GPa$,
the compressive residual stress of oxide (σ^{res}) is $-0.2\,GPa$,
the strain at limit of elasticity of iron oxide (ε_{fx}^{el}) is 0.00095 (0.095%).

The stored energy of film in both x and y directions can be calculated by the simple relation

$$W_{total} = \int \sigma \cdot d\varepsilon = \sum W_{fx} + \sum W_{fy} \qquad (2-8)$$

The generally different thermal expansion coefficients of the substrate and the iron oxides cause the development of phase-specific thermal stresses on cooling from the oxidation temperature to room temperature. These thermal stresses superpose the stress state existing at high temperatures prior to cooling to build-up the residual stresses experimentally determined at room temperature. The residual stresses after cooling exist also in the form of gradients due to abrupt changes in thermal expansion occurring at the inner scale interfaces.

During tensile loading, substrate is in tension elastically until to limit of elasticity ($\varepsilon_s^{el,\lim}$), and then is plastic deformation, whereas film is still elastically deformed until the first spallation takes place (strain at the first spallation marked as ε_{fs} which calculated from equation 2 – 8). Therefore, strain of film in parallel to x axis of the plastic deformation as presented in stage 3 of stored energy (ε_{fx}^{pl}) can be written as $\varepsilon_{fx}^{pl} = \varepsilon_{fs} - \varepsilon_{fx}^{el}$.

Stored energy development in film is considered in the three successive stages as follows [Chandra-ambhorn (2007)].

Stage 1: Film grows and cools down resulting in the accumulation of residual stress.

$$W_{fx}^{res} = W_{fy}^{res} = \frac{1}{2}\sigma^{res}\varepsilon^{res} = \frac{\left(\sigma^{res}\right)^2}{2M_f} \quad \text{with} \quad M_f = \frac{E_f}{1-\nu_f} \qquad (2-9)$$

Stage 2: Substrate and film are in tension elastically.

$$W_{fx}^{el} = \frac{1}{2}\sigma_{fx}^{el}\varepsilon_{fx}^{el} = \frac{M_f^{'}}{2}\left(1-\nu_f \cdot \nu_s\right)\left(\varepsilon_{fx}^{el}\right)^2 \qquad (2-10)$$

$$W_{fy}^{el} = \frac{1}{2}\sigma_{fy}^{el}\varepsilon_{fy}^{el} = \frac{M_f^{'}}{2}\left|\nu_f - \nu_s\right|\left(\varepsilon_{fx}^{el}\right)^2 \quad \text{with} \quad M_f^{'} = \frac{E_f}{1-\nu_f^2} \qquad (2-11)$$

Stage 3: Substrate and film are in tension. Substrate is deformed plastically but film is still elastic until the first spallation takes place.

$$W_{fx}^{pl} = \frac{1}{2}M_f^{'}\left(\varepsilon_{fx}^{pl}\right)^2 + 2M_f^{'}\nu_f\left(\sqrt{1+\varepsilon_{fx}^{pl}} - 1\right) - M_f^{'}\nu_f\varepsilon_{fx}^{pl} \qquad (2-12)$$

$$W_{fy}^{pl} = \frac{M_f^{'}\left(\varepsilon_{fy}^{pl}\right)^2}{2\left(1+\varepsilon_{fy}^{pl}\right)}\left(1+\varepsilon_{fy}^{pl} - 2\nu_f\right) \quad \text{whereas} \quad \varepsilon_{fy}^{pl} = \sqrt{\frac{1}{1+\varepsilon_{fx}^{pl}}} - 1 \qquad (2-13)$$

Before the micro-tensile test loading, the oxide film is considered to be a residual compressive stress due to oxide growth and/or cools down. Determination of stress and strain

in x axis (tensile direction) and y axis (transverse direction) during metal deformed elastically and then plastically. In-plane stress components can be calculated in function of strain, giving the curves presented in Figs. 2.11 and 2.12.

In Fig. 2.11, the residual compressive stress of the oxide along x axis is relaxed during the elastic deformation of metal (B to C), then the first part of plastic deformation of metal (C to D) before going to a tensile situation.
In Fig. 2.12, the residual compressive stress of the oxide along y axis is invariant during elastic contraction deformed of the metal (B to C), and also the compression increases when the metal deforms plastically (C to D).

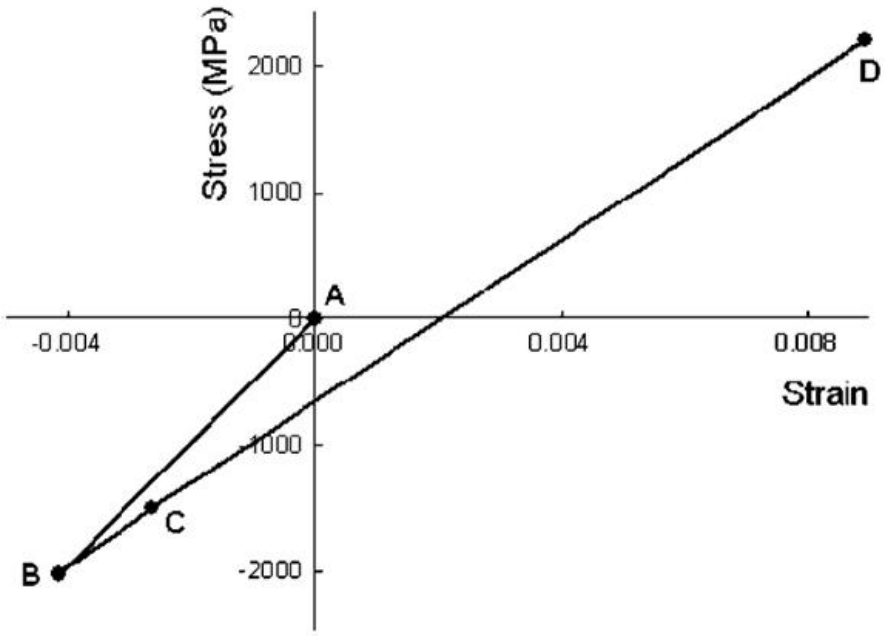

Figure 2.11: Evolution of oxide stress and strain along x axis (tensile direction): A to B at cooling down; B to C during test, metal still elastic; C to D during test, metal plastic [Chandra-ambhorn (2007)].

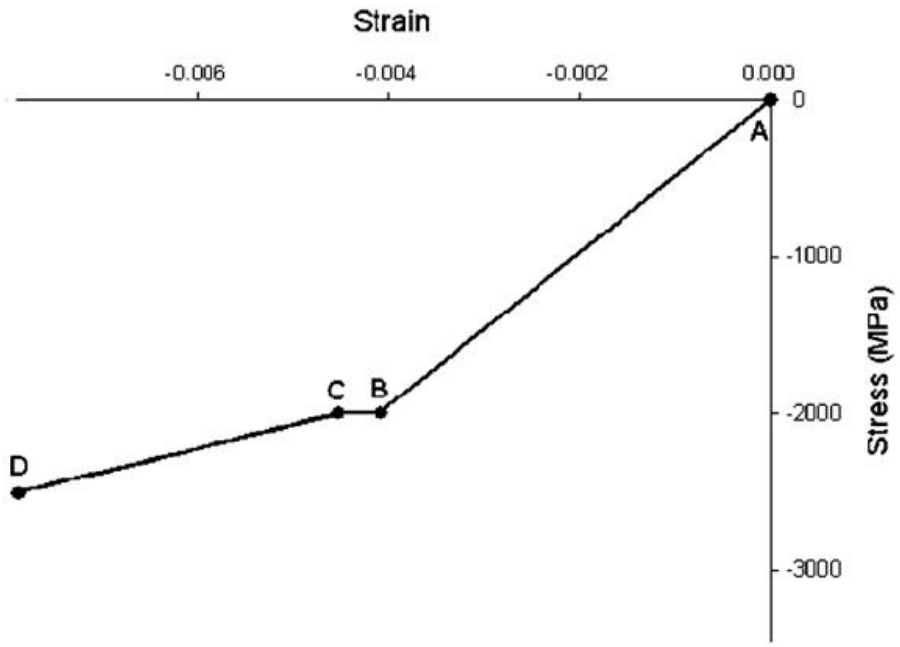

Figure 2.12: Evolution of oxide stress and strain along y axis (transverse direction): A to B at cooling down; B to C during test, metal still elastic; C to D during test, metal plastic [Chandra-ambhorn (2007)].

2.5 Pickling test

An immersion test was performed in this work to evaluate pickling ability (Fig. 2.13). For sample preparation for the test, the as-received hot-rolled steels were prepared with the width and length of 10 and 20 mm respectively, cleaned by alcohol and dried in air before immediately immersed in a 10%v/v HCl pickling solution at 80°C during 1 to 60 seconds. Weight loss per unit area was recorded as a function of pickling time.

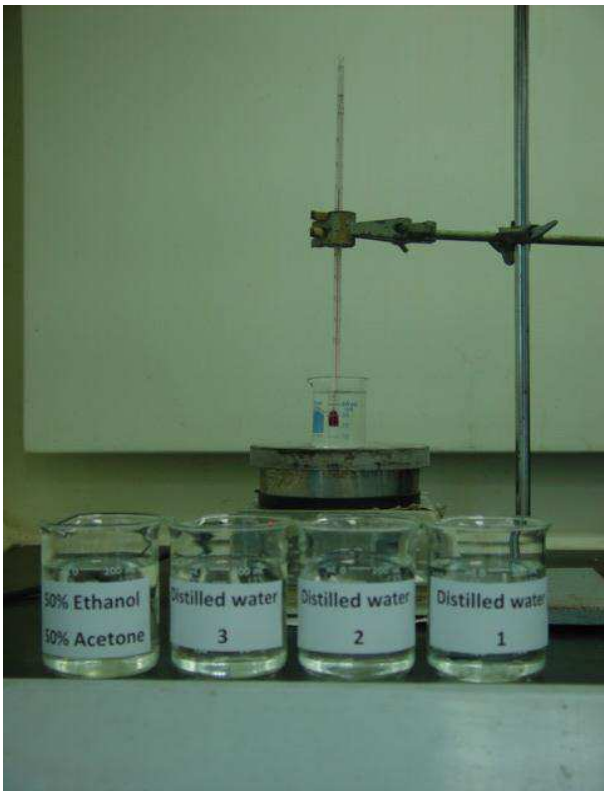

Figure 2.13: Immersion testing pattern [Tungtrongpairoj (2009)].

Equation to calculate dilution is given by

$$\text{Concentration}_{(\text{start})} \times \text{Volume}_{(\text{start})} = \text{Concentration}_{(\text{final})} \times \text{Volume}_{(\text{final})}$$

This equation is commonly abbreviated as,

$$C_1V_1 = C_2V_2 \qquad (2-14)$$

Where

C_1 = concentration of the stock solution
V_1 = volume of the stock solution
C_2 = concentration of the working solution
V_2 = volume of the working solution

After immersion test, weight loss is plotted as a function of the pickling time. By this graph, dissolution rate of scale and period of complete pickling can be determined as will see in the following chapters.

CHAPTER 3

ADHESION OF SCALES ON STEELS PRODUCED BY DIFFERENT PROCESS ROUTES

As mentioned in Chapter 1, there has been no extensive work investigating the scale actually formed on the recycled steel in the hot-rolling process, particularly in its adhesion to steel substrate. That topic is treated in the present chapter by the study of the as-received hot-rolled recycled steel. The as-received hot-rolled conventional steel is also studied for comparison.

3.1 Structure of scale on the as-received hot-rolled steel

A top view of scale subjected to the Calotest imprint and a side view of scale after cross section are shown in Figure 3.1. The averaged thicknesses of scales actually formed on the as-received hot-rolled conventional and recycled steels were 11.3 and 12.3 µm respectively. Using X-ray diffraction shown in Fig. 3.2, magnetite and iron peaks were observed on the hot-rolled conventional steel. Additional hematite appears on the hot-rolled recycled steel, probably due to lower cooling rate resulting from larger thickness, allowing time for oxidation of magnetite. Furthermore, from Raman spectroscopy results in Fig. 3.3, only magnetite was clearly observed on the as-received hot-rolled conventional steel. On the recycled steel, hematite and magnetite were identified near the scale-gas interface. In the inner part of the scale, only magnetite was detected. The results from XRD and Raman spectroscopy are therefore in agreement.

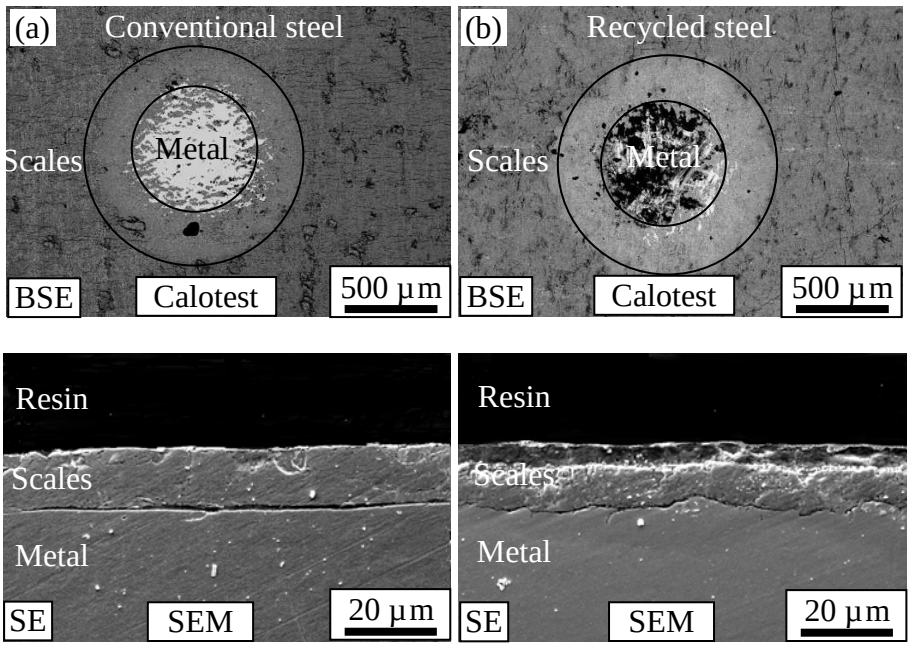

Figure 3.1: Calotest imprints and SEM cross-sections of scales on as-received hot-rolled conventional steel (a) and recycled steel (b).

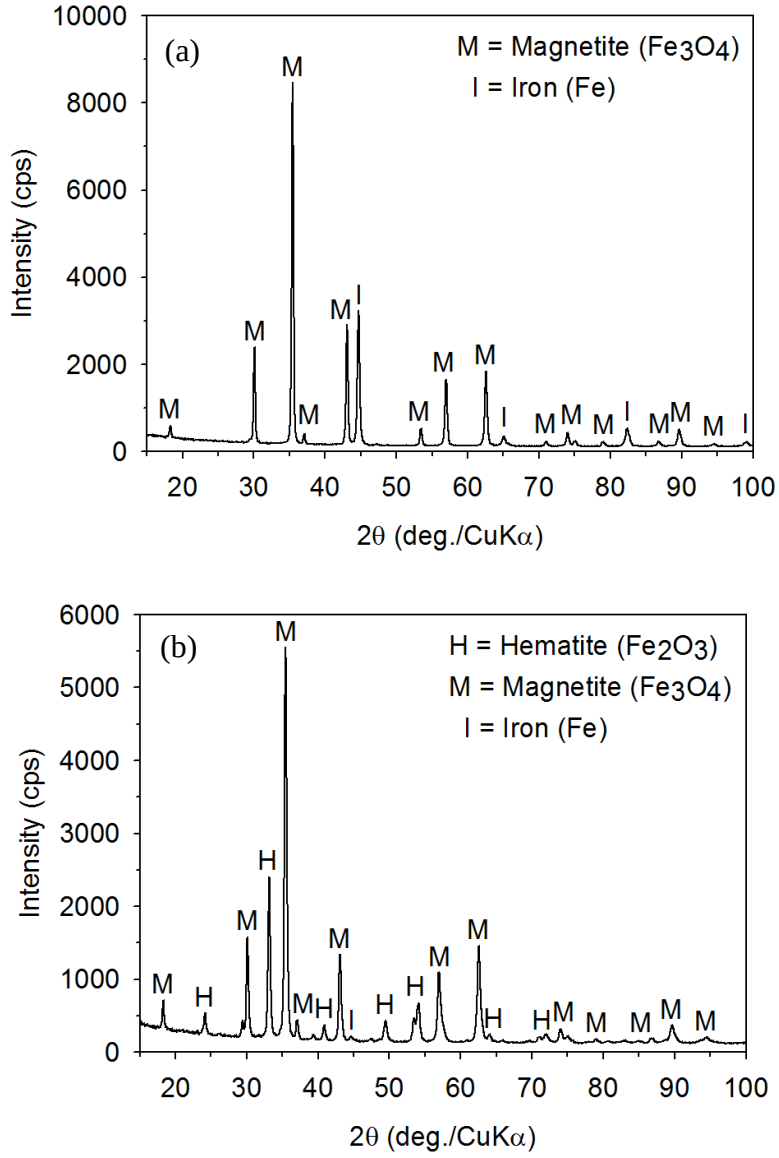

Figure 3.2: X-ray diffraction patterns of the as-received hot-rolled conventional steel (a) and recycled steel (b).

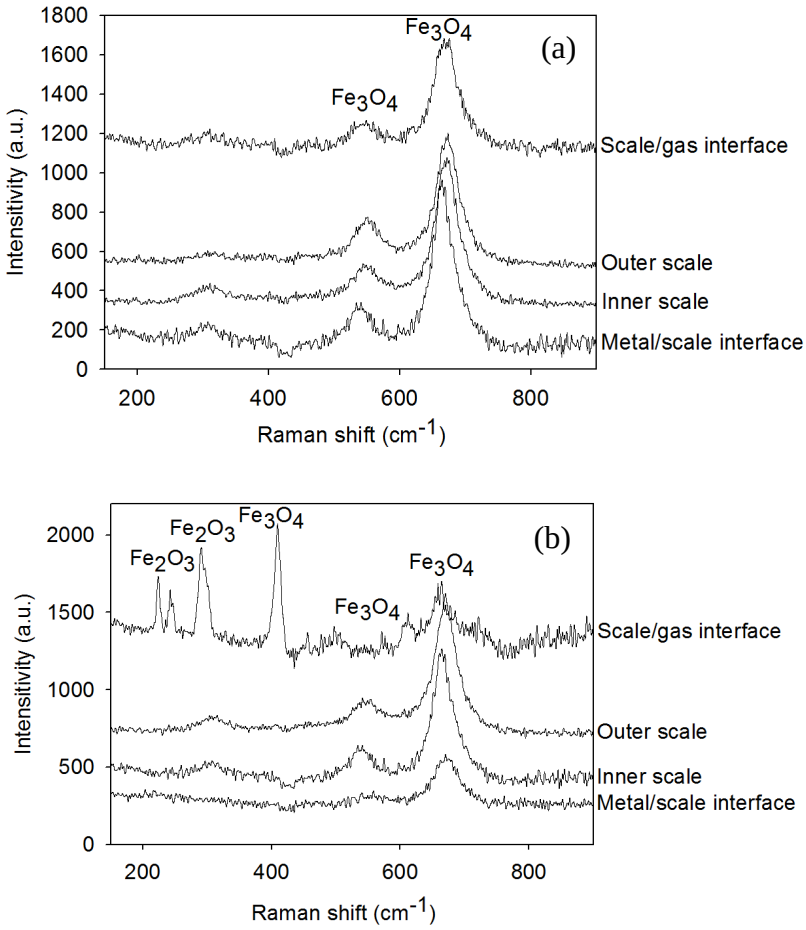

Figure 3.3: Raman spectroscopy patterns of oxides on the as-received hot-rolled conventional steel (a) and recycled steel (b).

3.2 Parameters affecting the assessment of scale adhesion by a tensile test

The micro- and macro-tensile tests were employed to investigate the mechanical adhesion of scale on the hot-rolled conventional and recycled steels. The micro-tensile test was employed for this test at the fixed strain rate of 7×10^{-5} s^{-1}, while the macro-tensile test can be performed at higher strain rates. Since the strain rate is one of the parameters that affect the testing results, the different strain rates of 0.08, 0.33 and 0.83 s^{-1} were then applied in the macro-tensile test to help discuss the results obtained from the two tensile testing machines.

Fig. 3.4 depicts the surface of scales on the as-received hot-rolled recycled steel subjected to the imposed strain during the tensile test as a function of strain rates. SEM and OM images in each row show the comparative scale surface of the steel after straining by the difference values. During tensile loading, transverse cracks perpendicular to the tensile loading were first observed, followed by local scale spallation. In each SEM and OM image taken during the both tensile test, the spallation ratio was quantified as the area where scale was spalled out normalised by the total area taken in the picture, in the following. Fig. 3.5 show the results for the recycled steel strained at different rates.

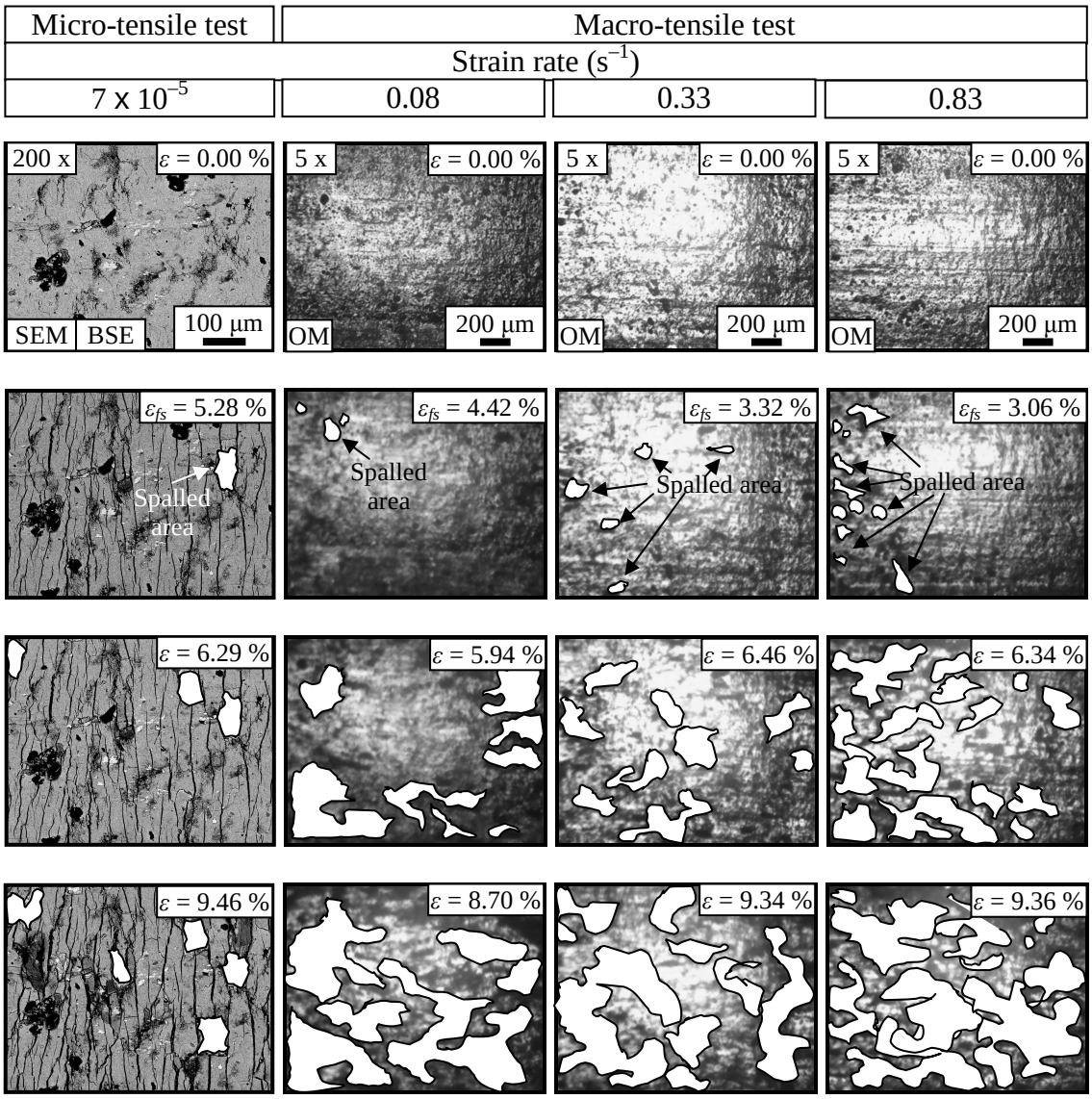

Figure 3.4: Evolution of scale failure on the as-received hot-rolled recycled steel (ε = strain values).

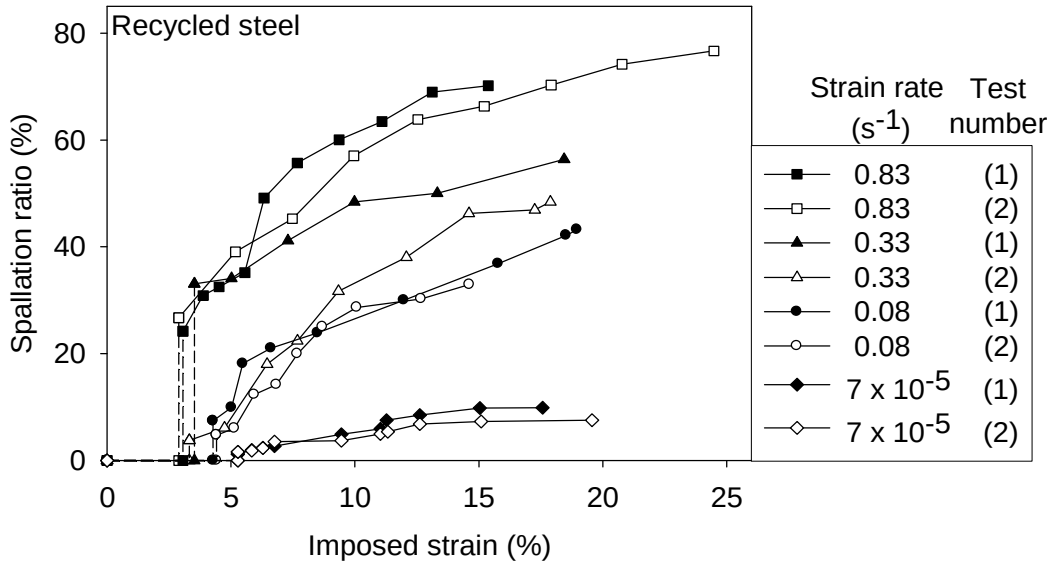

Figure 3.5: Spallation ratio of scale on the as-received hot-rolled recycled steel as a function of the imposed strain at difference strain rates.

Before advancing to the discussion, reproducibility of the test is firstly assessed. In the evaluation, the scatter of spallation ratio data points at imposed strains in the range 6 to 12% for each curve was used. The analysis of the data follow in equation (3 – 1) with illustrated in the following Fig. 3.6 as

$$Error(\%) = \frac{1}{7}\sum_{i=0}^{6}\left(\left|\Delta\%S\right|_{\%\varepsilon=6+i}\right) \qquad (3-1)$$

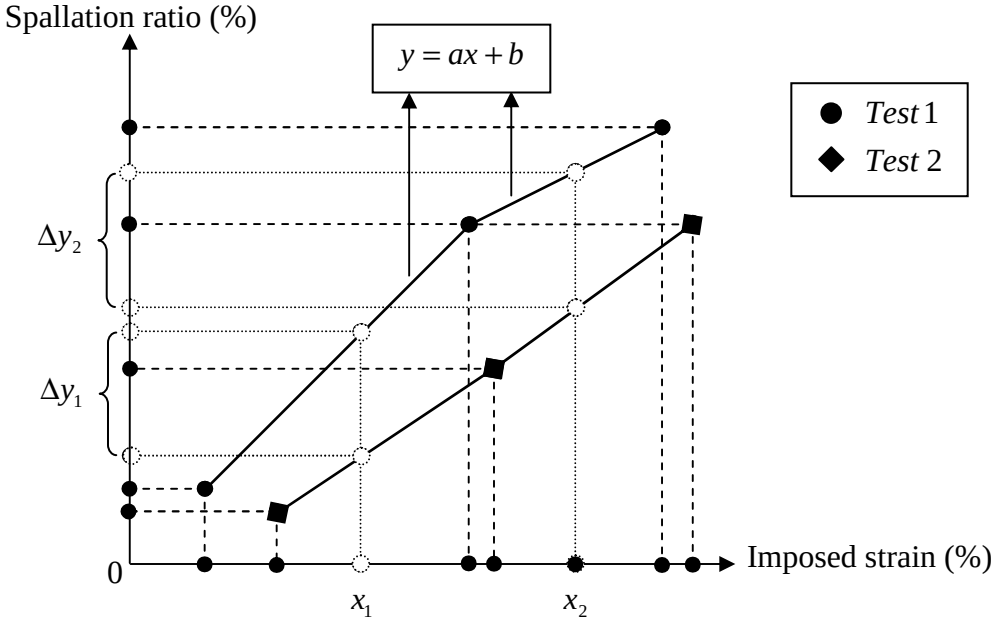

Figure 3.6: The reproducibility analysis of the experimental data.

$\%S$ is the percent of spallation ratio at a given strain, and $\%\varepsilon$ is the percent of strain. The reproducibility results obtained for each strain rate are given in Table 3.1 and compared with

the reproducibility of literature data (chromia scales on AISI 444) treated according to the same procedure (Table 3.2). It is observed that the reproducibility is in the range 3 – 9 %, probably better for the lower strain rates and for very uniform scales (AISI 444 in H_2O-containing atmosphere).

Table 3.1: Reproducibility of the experimental spallation ratio data.

The as-received hot-rolled recycled steel	Micro-tensile test	Macro-tensile test		
Strain rate (s^{-1})	7×10^{-5}	0.08	0.33	0.83
Error (%)	2.95	2.71	9.50	5.06

Table 3.2: Reproducibility of comparable data from the literature [Chandra-ambhorn (2007)].

Ferritic stainless steel	Micro-tensile test	
Strain rate (s^{-1})	7×10^{-5}	
Oxidation atmosphere	Synthetic air	$2\%H_2O/H_2$
Error (%)	4.95	1.46

From the results, the spallation ratio is observed to strongly depend on the strain rate, a higher tensile strain rate resulting in higher spallation ratio. At high strain rate, samples rapidly reach the tensile strength (Fig. 3.7), resulting in lower linear crack density (Fig. 3.8) and indicating lower relaxation of the scale. Such samples showed higher spallation ratio and lower strain at first spallation (Fig. 3.9). From the value of strain at the first spallation, the mechanical adhesion was derived and the results appear in Fig. 3.10. A higher strain rate resulted in lower adhesion energy (Fig. 3.10). All data were presented in Table 3.3.

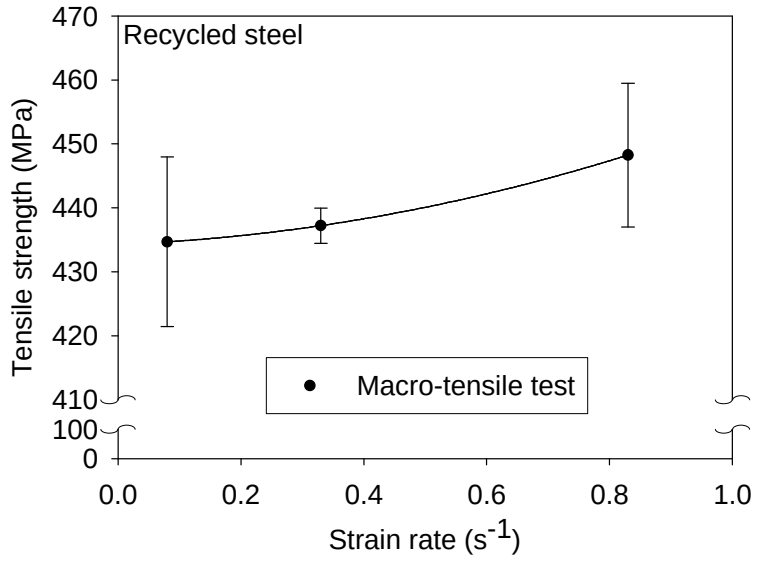

Figure 3.7: Tensile strength of steel on the as-received hot-rolled recycled steel as a function of strain rate.

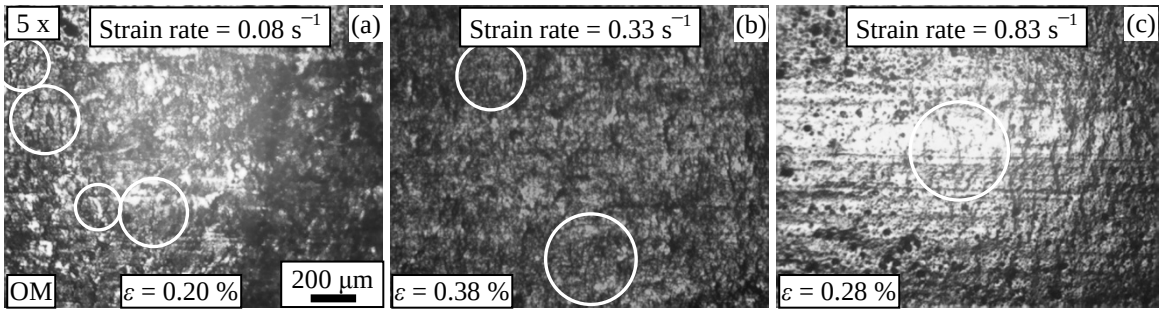

Figure 3.8: Crack before spallation as a function of strain rate of 0.08 s^{-1} (a), 0.33 s^{-1} (b) and 0.83 s^{-1} (c) of scale on the as-received hot-rolled recycled steel.

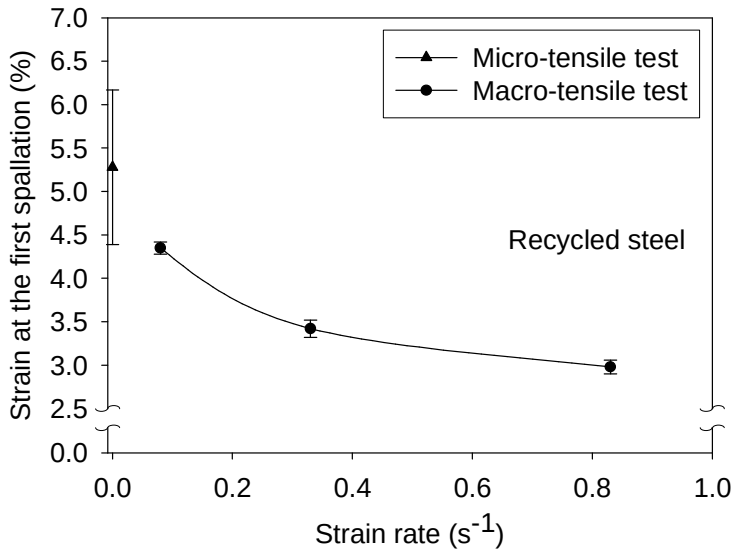

Figure 3.9: Strain at the first spallation of scale on the as-received hot-rolled recycled steel as a function of strain rate.

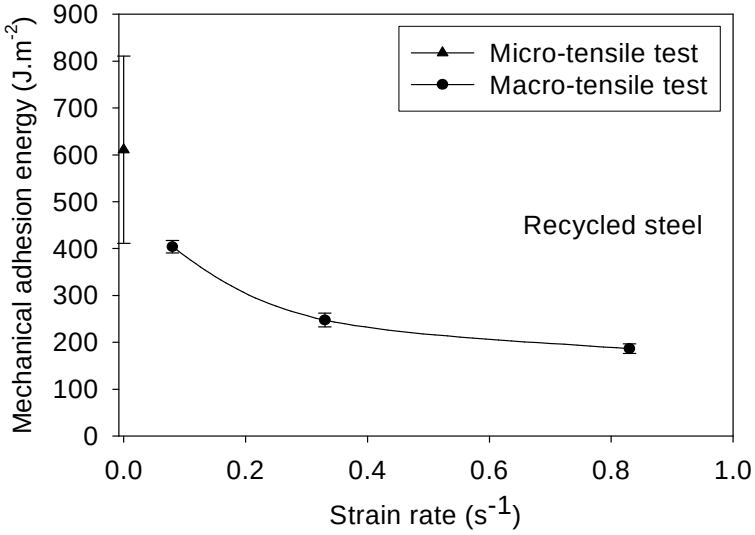

Figure 3.10: Mechanical adhesion energy of scale on the as-received hot-rolled recycled steel as a function of strain rate.

Table 3.3: Strain at the first spallation and mechanical adhesion energy of scale on the as-received hot-rolled recycled steel as a function of strain rate.

Parameters	The as-received hot-rolled recycled steel			
	Micro-tensile test	Macro-tensile test		
Strain rate (s^{-1})	7×10^{-5}	0.08	0.33	0.83
Strain at the first spallation (%)	5.28 ± 0.89	4.35 ± 0.07	3.42 ± 0.10	2.98 ± 0.08
Mechanical adhesion energy* ($J.m^{-2}$)	1833 ± 599	1212 ± 40	742 ± 44	559 ± 31
Mechanical adhesion energy ** ($J.m^{-2}$)	611 ± 200	404 ± 13	247 ± 15	186 ± 10

Remark: * calculated using the model described in [Chandra-ambhorn (2007)]
** calculated using the modified model described in [Chandra-ambhorn (2013)]

However, comparing to literature, it was found that the adhesion energy of scale on metallic substrate is reported in the range of decade up to hundreds $J.m^{-2}$. The values reported using the previous model described in [Chandra-ambhon (2007)] listed Table 3.3 are thus relatively large. In a more recent paper [Chandra-ambhorn (2013)], the discussion was made that for scale on the hot-rolled steel, cracks exist in scale due to coil handling during the process. These initial cracks could result in the distribution of stress as a function of distance from steel-scale interface towards the external interface. In the case that stress distribution in scale was uniform, the elastic strain energy stored per unit volume of scale is $\sigma^2/2E$ for uni-axial loading, where σ is the stress uniformly exerted on scale across its thickness and E is its elastic modulus. For linear distribution of stress in scale as depicted in Fig. 3.11, stress is a function of the distance from external scale-atmosphere interface (x) as follows.

$$\sigma = \frac{\sigma_m}{e} x \qquad (3-2)$$

σ_m stands for the maximum stress exerted on scale which equals to the one when it distributes uniformly across scale thickness, and e is scale thickness. The elastic strain energy stored per unit volume of oxide scale (W) can be calculated using the following equation.

$$W = \frac{1}{e}\int_{x=0}^{x=e} \frac{\sigma^2}{2E} dx = \frac{1}{3}\left(\frac{\sigma_m^2}{2E}\right) \qquad (3-3)$$

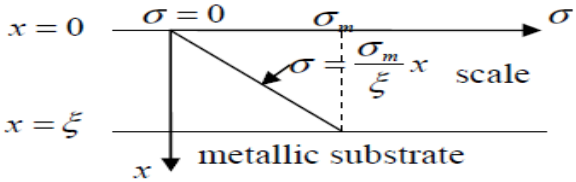

Figure 3.11: Schematic sketch of the linear distribution of stress in scale under tensile test [Chandra-ambhorn (2013)].

In case that the linear distribution of stress and the release of energy stored due to the residual stress are assumed, the adhesion energy quantified using the model [Chandra-ambhorn (2007)] adopted to this work is reduced by three times. By this discussion, the value of adhesion energy reported in Table 3.3 can be reduced to be in the range of 200 – 600 $J.m^{-2}$. In the following, the adhesion energy will be quantified using this modified model.

3.3 Adhesion of scales on the conventional and recycled steels

The as-received hot-rolled conventional and recycled steels were comparatively studied. Figs. 3.12 and 3.13 depict surfaces of scale subjected to different imposed strains during micro- and macro-tensile tests. From these tests, the first information obtained was strain provoking the first spallation as shown in Fig. 3.14. It was found that such critical strain on the recycled steel was much higher than that for scale on the hot-rolled conventional steel for both the micro- and macro-tensile tests.

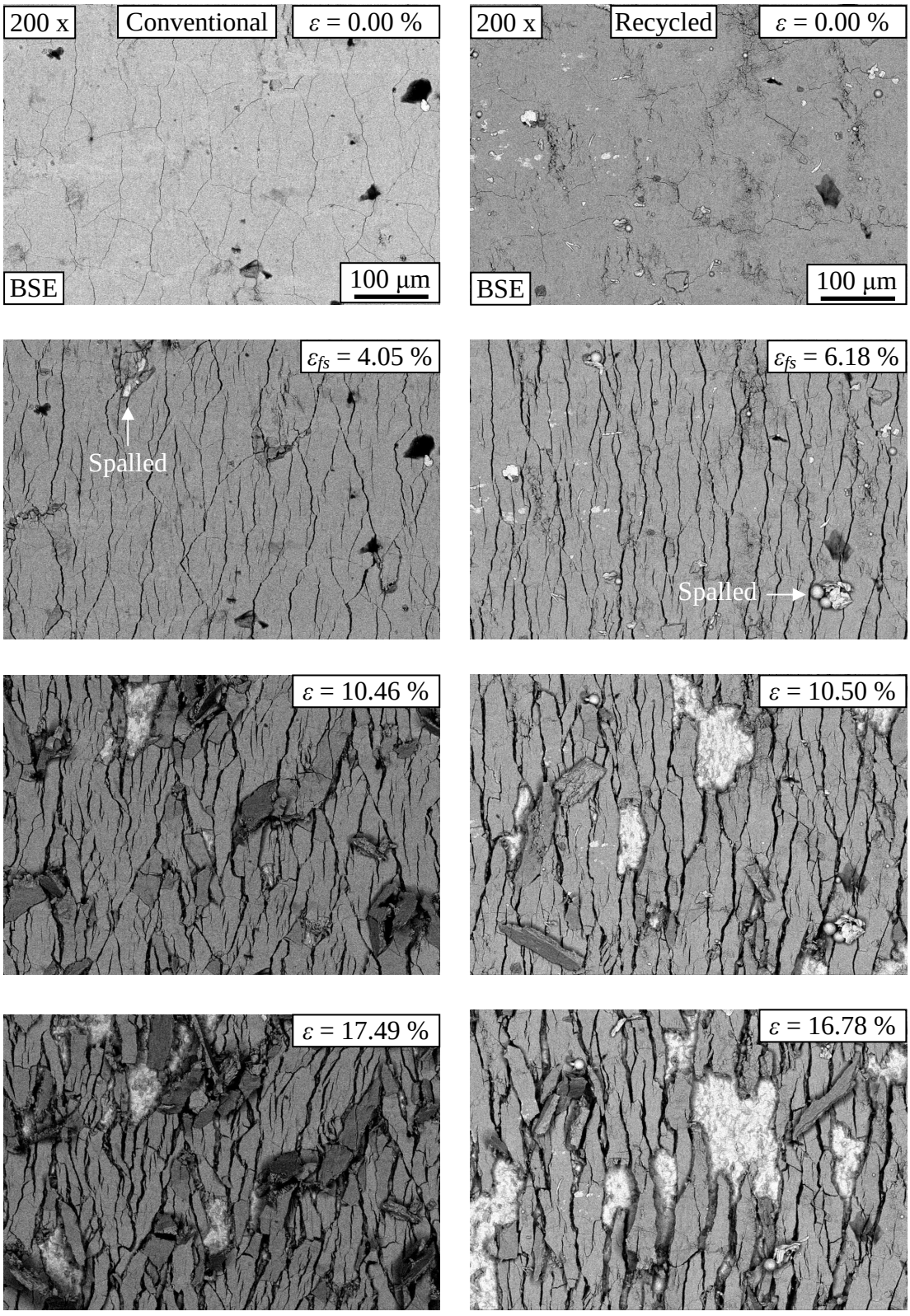

Figure 3.12: Evolution of scale failure on the as-received hot-rolled conventional steel (left) and the as-received hot-rolled recycled steel (right) as a function of imposed strain investigated by the micro-tensile test (strain rate = 7×10^{-5} s^{-1}).

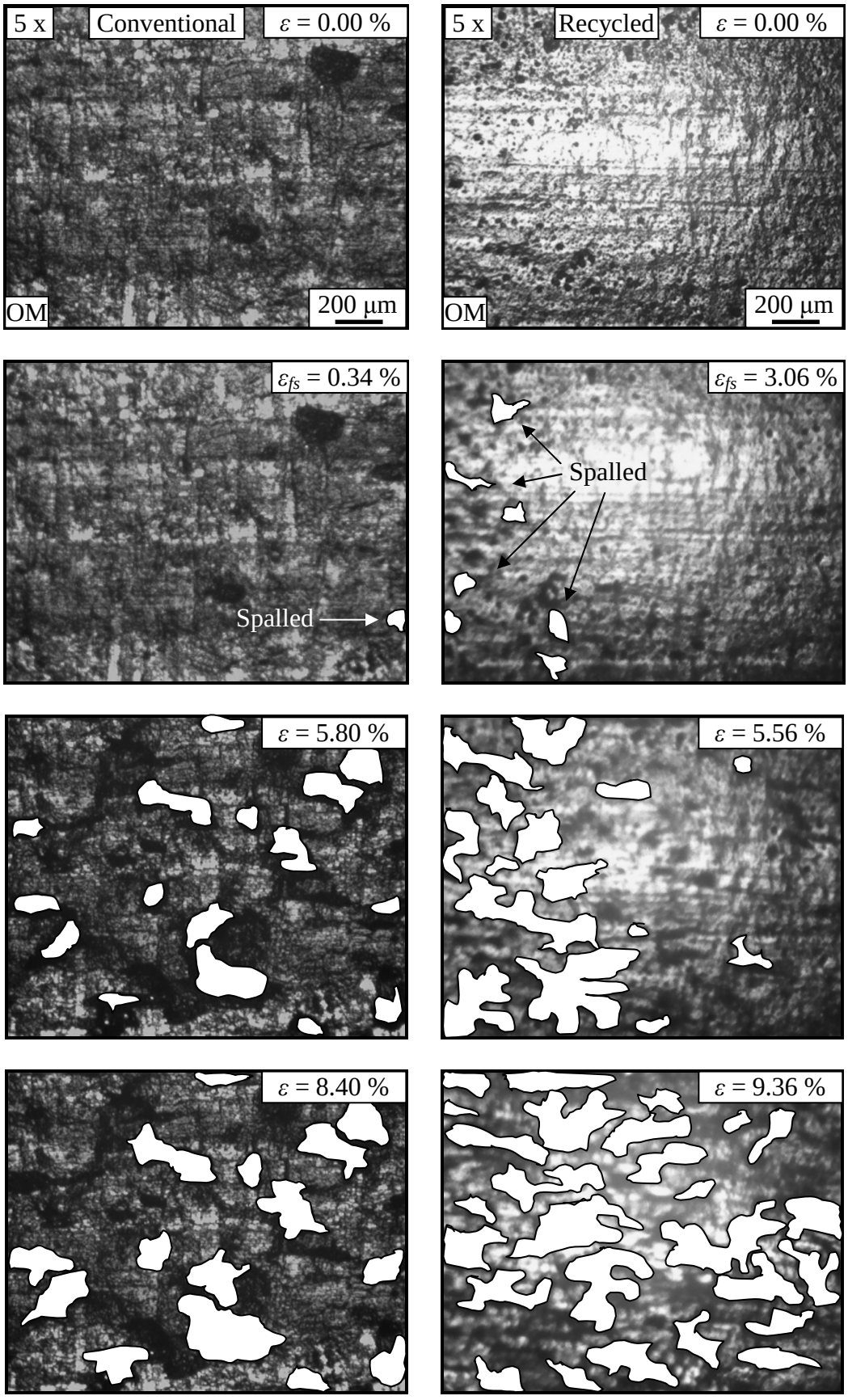

Figure 3.13: Evolution of scale failure on the as-received hot-rolled conventional steel (left) and the as-received hot-rolled recycled steel (right) as a function of imposed strain investigated by the macro-tensile test (strain rate = 0.83 s^{-1}).

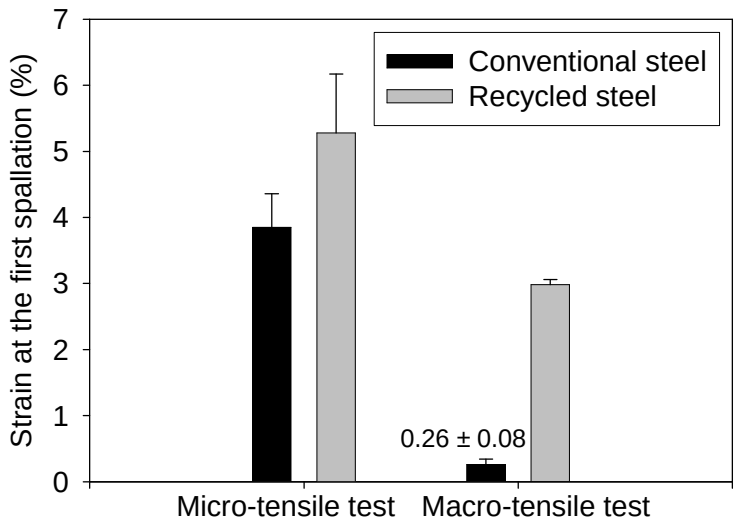

Figure 3.14: Strain at the first spallation of scale on the as-received hot-rolled conventional and recycled steels.

The second information obtained from the tests was spallation ratio (Figs. 3.15 and 3.16). It was found that the spallation ratio of scale on the conventional steel was lower than that of the recycled steel. The two types of tensile testing gave the same tendency. Discussing with the spallation ratio, it was found that scale on the recycled steel was more difficult to be spall out under the longitudinal tension. However, if once it was spalled, it is more sensitive to spall out with the increase of the imposed strain.

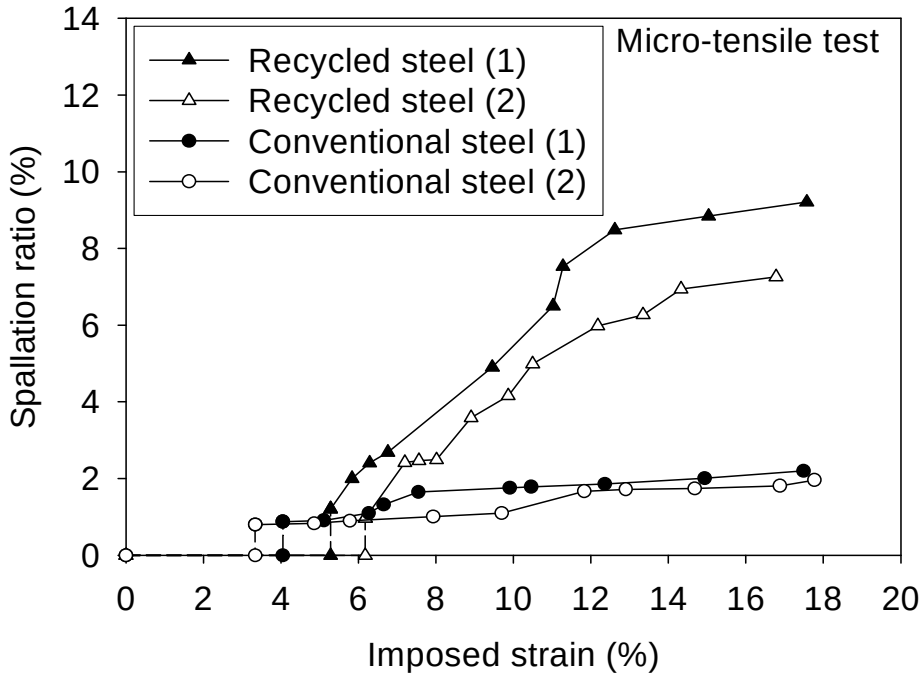

Figure 3.15: Spallation ratio of scales on the as-received hot-rolled conventional and recycled steels as a function of imposed strain investigated by the micro-tensile test (strain rate = 7×10^{-5} s^{-1}).

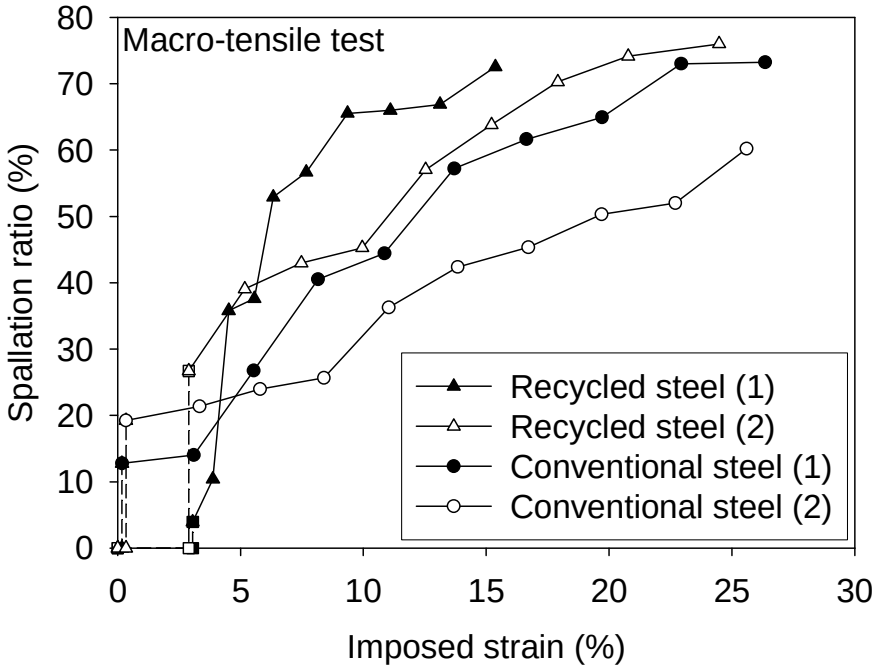

Figure 3.16: Spallation ratio of scales on the as-received hot-rolled conventional and recycled steels as a function of imposed strain investigated by the macro-tensile test (strain rate = 0.83 s^{-1}).

The third information obtained from the test was crack density and crack spacing. A crack density was defined as number of cracks counted per unit length on scale parallel to loading direction. Crack spacing was average length of between cracks measured in unit length of scale surface. These two parameters were plotted as a function of the imposed strain in Fig. 3.17. Parentheses (1) and (2) after description in the graph indicate that the test measured for the first and second times respectively. It was found that initial cracks existed in the scale. Initial crack density of scale on the conventional steel was higher than that of scale on the recycled steel. It might be from the process in the plant. During strain increased, a higher crack density observed on the conventional steel, corresponded to a lower crack spacing on the scale, was also observed.

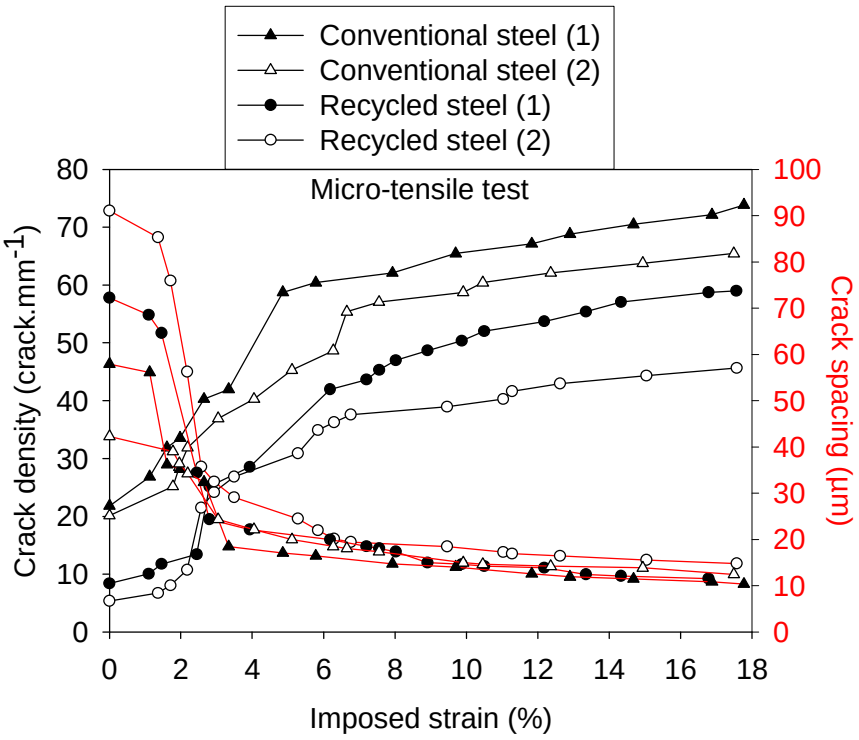

Figure 3.17: Crack density and crack spacing number of scale on the as-received hot-rolled conventional and recycled steels as a function of the imposed strain investigated by the micro-tensile test (strain rate = 7 x 10^{-5} s^{-1}).

Fig. 3.18 presents strain provoking the first spallation and mechanical adhesion energy respectively. The result shows that strain inducing the first spallation of scale on the recycled steel was higher than that of scale on the conventional steel. These result indicated the higher quantified adhesion energies of scale actually formed on the hot-rolled recycled steel than that of scale actually formed on the hot-rolled conventional steel. Table 3.4 lists information on the two steels concerning the thickness of scales actually formed on the hot-rolled steels, strain at the first spallation, and mechanical adhesion energy calculated using our model.

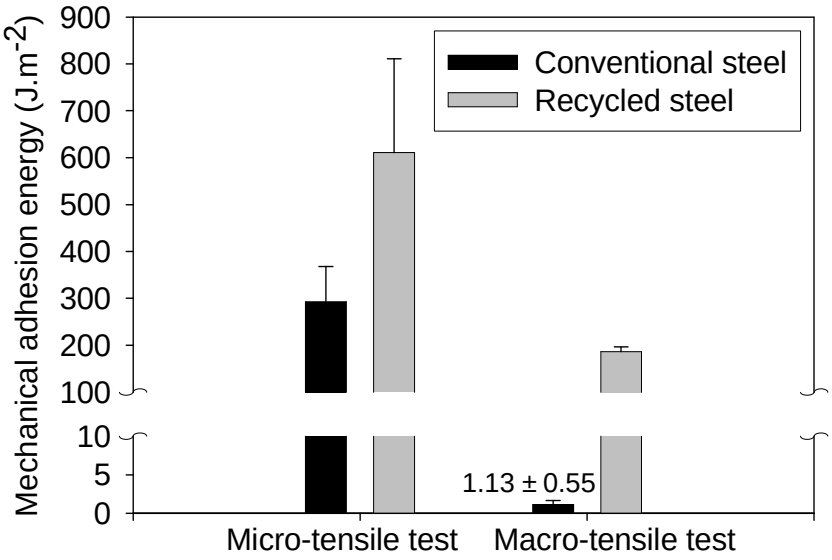

Figure 3.18: Mechanical adhesion energy of scale on the as-received hot-rolled conventional and recycled steels.

Table 3.4: Strain at the first spallation and mechanical adhesion energy of scale on the as-received hot-rolled conventional and recycled steels.

Parameters	Micro-tensile test ($\dot{\varepsilon}$ = 7 x 10^{-5} s^{-1})		Macro-tensile test ($\dot{\varepsilon}$ = 0.83 s^{-1})	
	conventional	recycled	conventional	recycled
Oxide thickness (µm)	11.32	12.27	11.32	12.27
Strain at the first spallation (%)	3.85 ± 0.51	5.28 ± 0.89	0.26 ± 0.08	2.98 ± 0.08
Mechanical adhesion energy ($J.m^{-2}$)	293 ± 75	611 ± 200	1.13 ± 0.55	186 ± 10

Fig. 3.19 depict the scale on the hot-rolled recycled steel after the tensile test. A spectrum from an energy dispersive spectroscopy (EDS) of the white zone in Figs. 3.19 (a) and (b) corresponding to the steel-scale interface is shown in Fig. 3.19 (c). On that area, the EDS spectrum includes the peaks of Fe, O, C as well as Si. It was found in our group [Tungtrongpairoj (2009), Chandra-ambhorn (2010)] that there existed oxide containing Si and Cu at the internal interface between scale and the hot-rolled recycled steel. It has been widely reported that the oxide containing Si, i.e. fayalite, existing at the steel-scale interface, promoted mechanical adhesion of scales on steel substrates [Chattopadhyay (2008), Taniguchi (2001), Yang (2008)] and worsened the picklability of scale [Chattopadhyay (2008)].

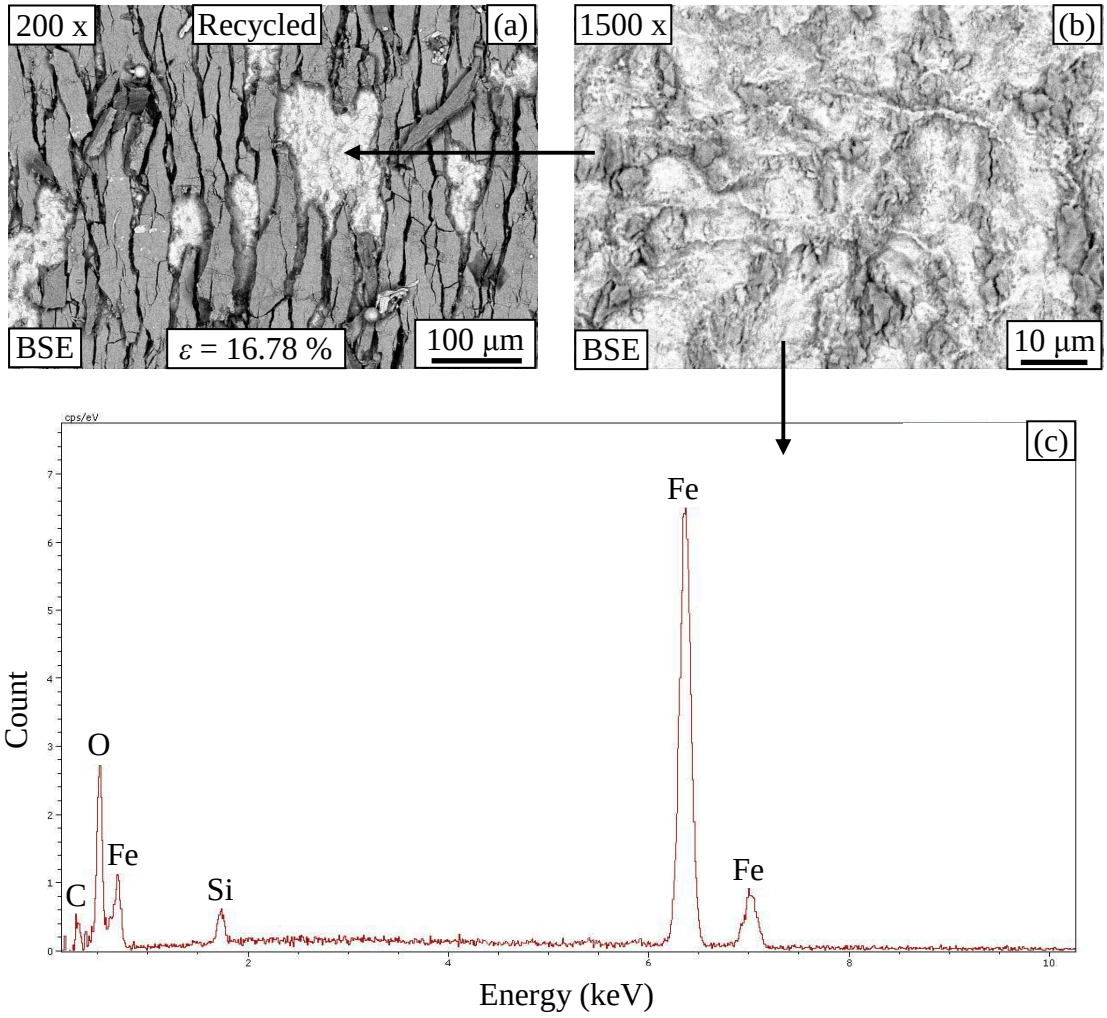

Figure 3.19: (a) Oxide scale and steel substrate of recycled steel, (b) internal interface between scale and substrate magnified from (a), and (c) EDS pattern on metal substrate observed as the white area in the upper micrograph.

Furthermore, the residual stress can affect the determination of mechanical adhesion energy. If the residual compressive stress in the oxide scale is high, when tensile loading is applied to the scale, higher strain must be applied to accumulate energy until achieving the threshold value provoking scale spallation. If scale contains higher residual stress, strain provoking the first spallation is higher. In the present case, the strip thickness of the hot-rolled recycled steel was 6 mm, much higher than that of the hot-rolled conventional steel which was 3.2 mm. This higher strips thickness of the recycled steel corresponds to higher residual stress in the oxide scale when the steel cooled down, resulting in higher strain provoking the first spallation.

A much higher measured strain at the first spallation of the hot-rolled recycled steel gave rise to the higher mechanical adhesion energy for the recycled steel compared to the conventional steel (Table 3.4). The particular chemical composition of the hot-rolled recycled steel which contains Si and Cu higher than the conventional steel could be one of the reasons of the observed difference. At the internal interface between scale and the hot-rolled recycled steel, oxide containing Si promoted mechanical adhesion of scales on the steel substrates. In the present case, interfacial silica precipitates increased adhesion between scale and substrate,

resulting in the mechanical adhesion on the hot-rolled recycled steel higher than the conventional steel.

The effect of Cu in steels has been also extensively studied using laboratory model alloys due to the well-known hot shortness industrial problem [Chen (2005), Kondo (2006)]. It was found that copper is not only enriched at the steel-scale interface but also exists within the scale. However, the papers did not report on the effect of copper on the mechanical adhesion of scales. In the present case, its effect is thought to be minor compared to that of Si.

3.4 Pickling ability

In the experiment, the as-received hot-rolled conventional and recycled steels were immersed in 10%HCl solution at 80 ºC. Fig. 3.20 plots weight loss per unit area as a function of the pickling time. The initial slope of the curve corresponds to the dissolution rate of the scale. This value is represented in Fig. 3.21. The slopes at long pickling times, graphically observed to be identical for the two lines in Fig. 3.20, correspond to the corrosion rate of the steel substrate.

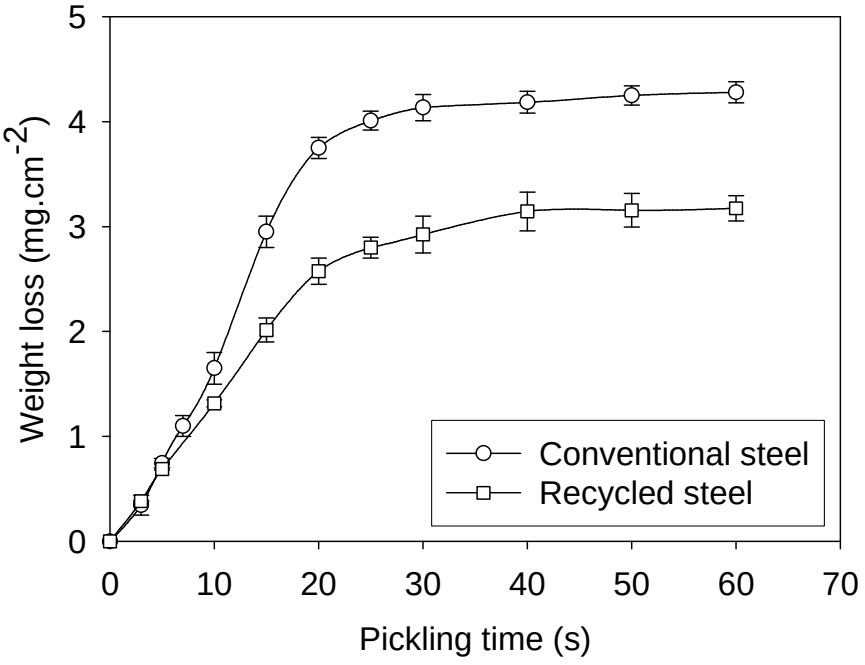

Figure 3.20: Weight loss for the as-received hot-rolled conventional and recycled steels in 10%v/v HCl solution at 80°C as a function of pickling time.

From Fig. 3.20, the dissolution rate of scale on the recycled steel was slower than that of scale on the conventional steel. It was also observed that the period of time for the complete pickling of scale on the recycled steel was ca. 23 seconds. It was a bit larger than that of the conventional steel which was ca. 21 seconds (Fig. 3.22). The slower rate (and longer period of time for the complete pickling of scale) on the hot-rolled recycled steel, might relate to the scale structure comprised hematite which is only slightly soluble in acid solution as proposed by [Chattopadhyay (2005)]. It might also relate to the superior mechanical adhesion of scale actually formed on the hot-rolled recycled steel due to oxide layer contained Si. Indeed, the pickling solution penetrates the cracks within the scales and acts mainly at the metal-scale interface, more efficiently when the interface is debonded.

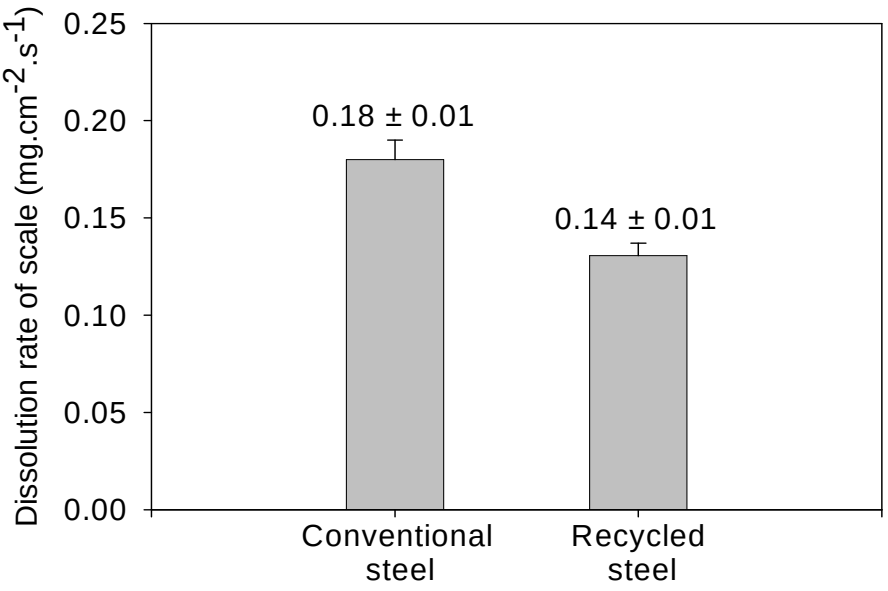

Figure 3.21: Dissolution rate of scale on the as-received hot-rolled conventional and recycled steels in 10%v/v HCl solution at 80°C.

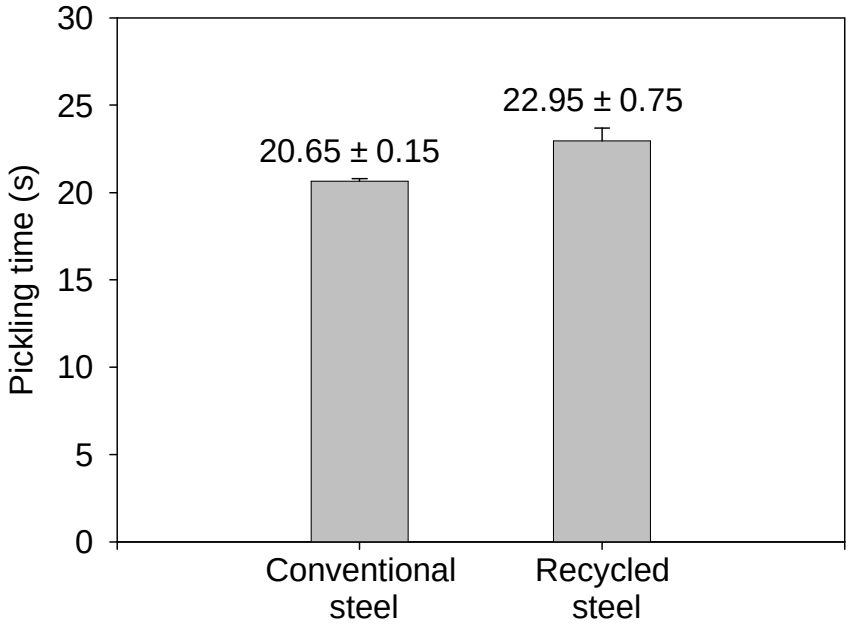

Figure 3.22: Pickling time of scale on the as-received hot-rolled conventional and recycled steels in 10%v/v HCl solution at 80°C.

CHAPTER 4

ADHESION OF SCALES ON HOT-ROLLED STEELS WITH DIFFERENT SILICON CONTENTS

In chapter 3, we have seen that adhesion of scale on the recycled steel is higher than that of the conventional steel, and the role of silicon on that behaviour is observed. However, discussion on the sole role of silicon on scale adhesion is limited in such case because the recycled steel contains not only silicon but many impurities. Thus the present chapter will focus on the role of silicon in steel by studying two hot-rolled steels containing different contents of silicon, 0.026 and 0.193-wt%. Scales actually formed on the steels in the hot-rolling process will be firstly investigated, followed by scales grown in laboratory.

4.1 Investigation of scale on the hot-rolled steels

4.1.1 Oxide scale structure

The studied materials in Section 4.1 are the as-received hot-rolled 0.026-wt% Si and 0.193-wt% Si steels. The left column in Figure 4.1 exhibits scale on the 0.026-wt% Si steel, and the right column shows scale on the 0.193-wt% Si steel. The upper row shows a top view of the scale with a Calostest imprint. It was found by this test that scale on the 0.193-wt% Si steel had the thickness of 8.5 µm, slightly lower than that on the 0.026-wt% Si steel which was 10.2 µm. The lower row of Fig. 4.1 depicts the side view of scale by cross-sectioning the samples. It was found by these pictures that thickness of scale on the 0.193-wt% Si steel was 6.6 µm, slightly lower than that of the 0.026-wt% Si steel which was 8.0 µm. The ratio between scale thicknesses is obviously the same with the two measuring procedures, but the values obtained using the Calotest seem to be slightly overestimated, possibly due to the difficult positioning of the external circle. X-ray diffraction was applied on both samples, and the peaks of magnetite were dominantly observed. The signal from iron was also detected, which might be from the oxide scale (wüstite decomposition at cooling) and/or steel substrate (Fig. 4.2). By Raman spectroscopy, magnetite was clearly observed on both steels (Fig. 4.3). According to literature, it was reported that scale structure at the inner part of low carbon steel strip was mainly eutectoid structure comprising magnetite and iron [Chen (2000), (2001)].

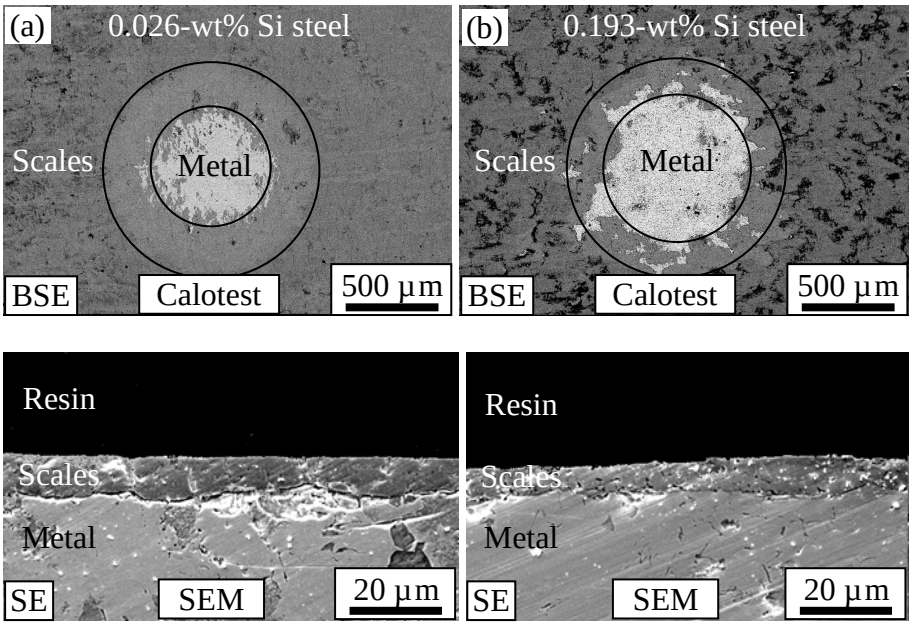

Figure 4.1: Calotest imprints and SEM cross-sections of the scales on the as-received hot-rolled 0.026-wt% Si steel (a) and 0.193-wt% Si steel (b).

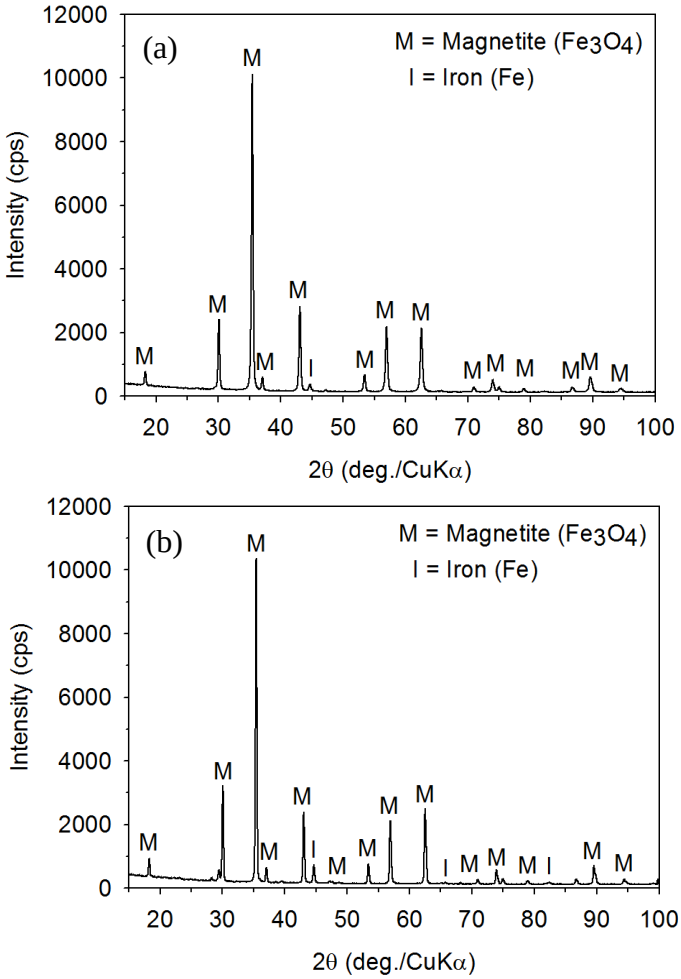

Figure 4.2: X-ray diffraction patterns of the as-received hot-rolled 0.026-wt% Si steel (a) and 0.193-wt% Si steel (b).

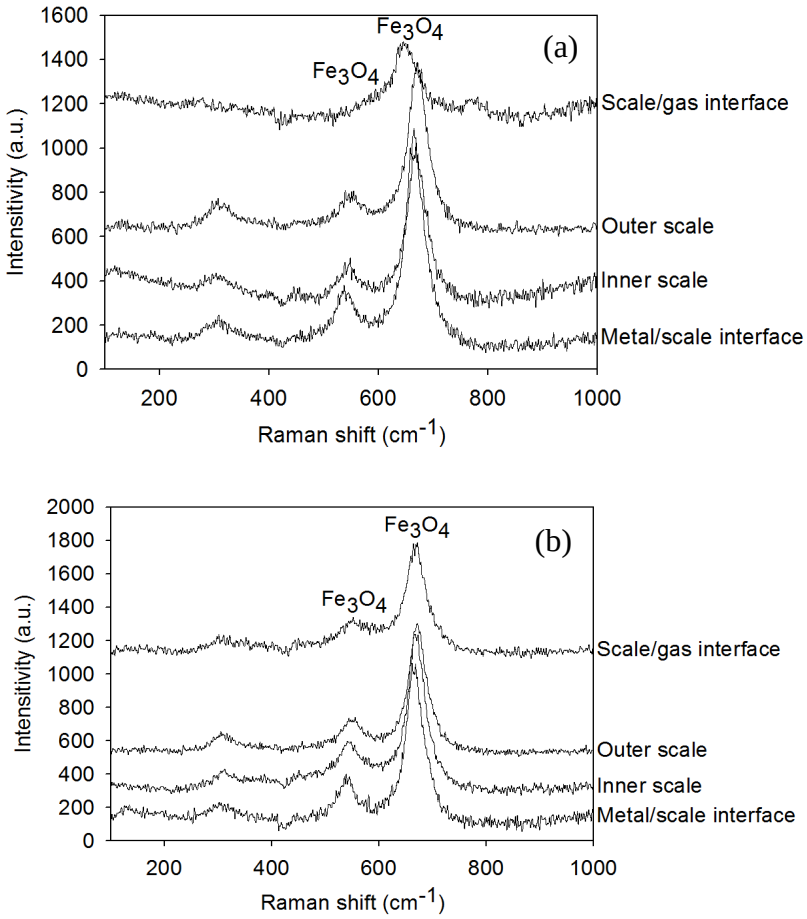

Figure 4.3: Raman spectroscopy patterns of oxides on the as-received hot-rolled 0.026-wt% Si steel (a) and 0.193-wt% Si steel (b).

4.1.2 Adhesion of scale on the hot-rolled 0.026-wt% Si steel

Adhesion of scale on the as-received hot-rolled steel was evaluated by the micro- and macro-tensile tests. Evaluation of scale failure during straining the samples is depicted in Fig. 4.4. The micro-tensile test was conducted at the strain rate of 7×10^{-5} s^{-1}, while the macro-tensile test was performed at the strain rates of 0.08, 0.33 and 0.83 s^{-1}. During tensile loading, scale exhibits cracking and spallation. For all samples, the tensile crack was normal to the direction of applied strain. Fig. 4.5 was show scale after the micro-tensile testing. From EDS, oxygen was not observed on the spalled area, indicating the adhesive delamination of scale from steel substrate.

From Fig. 4.4, spallation ratio as a function of strain rate was quantified and plotted in Fig. 4.6. Strain at the first spallation and mechanical adhesion energy are depicted in Fig. 4.7 and 4.8 respectively. Information on scale thickness with two parameters is listed in Table 4.1. From these results, it was found that spallation was incubated up to a certain value of the imposed strain. Once it occurred, the spallation ratio increased with the imposed strain. Increasing strain rate lowered strain initiating the first spallation, and therefore mechanical adhesion energy calculated at that strain. The effect of strain rate on adhesion behaviour in this part is in agreement with the results on adhesion behaviour of the recycled steel in Section 3.2 of the Chapter 3.

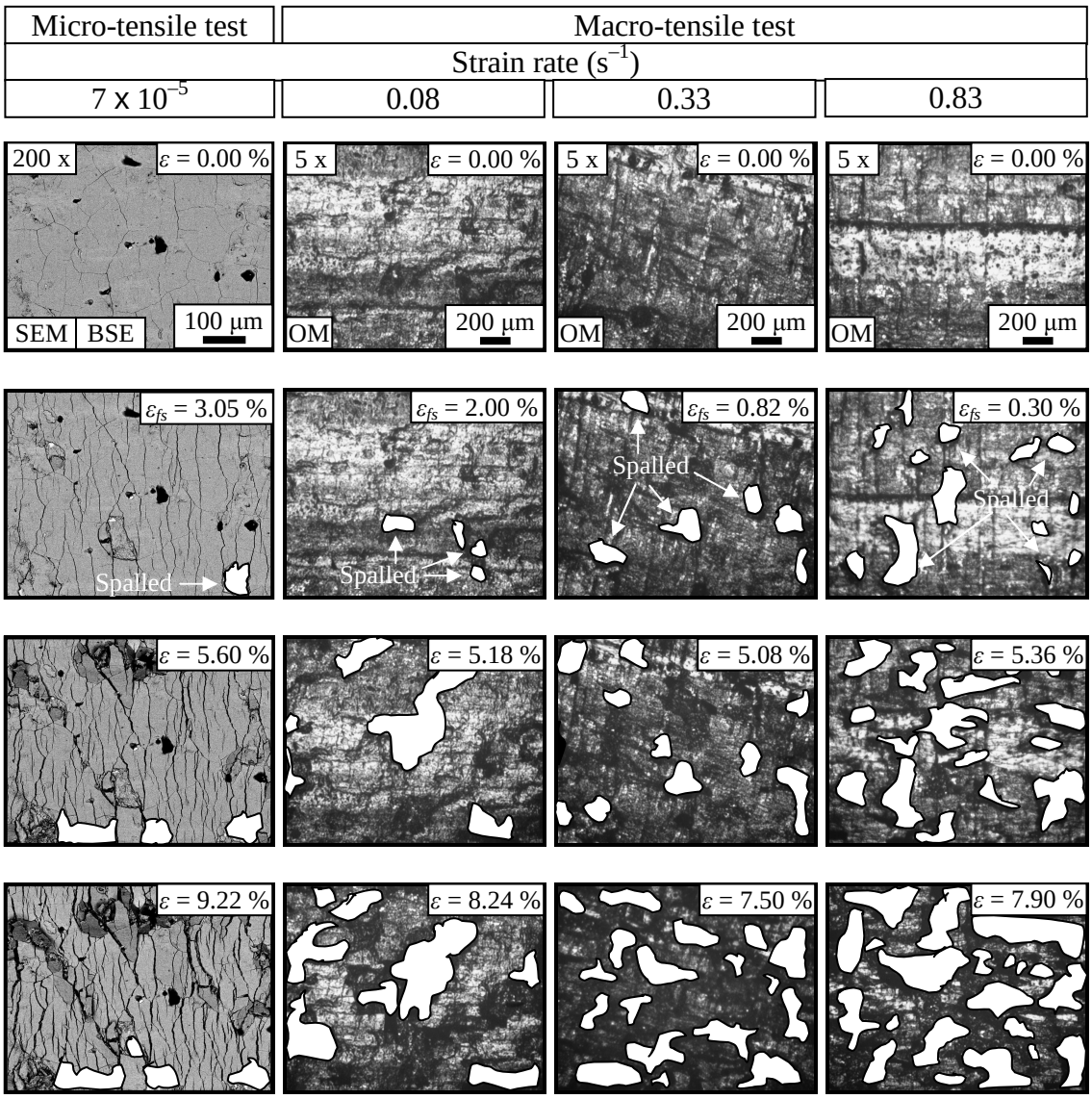

Figure 4.4: Evolution of scale failure on the as-received hot-rolled 0.026-wt% Si steel (ε = strain values).

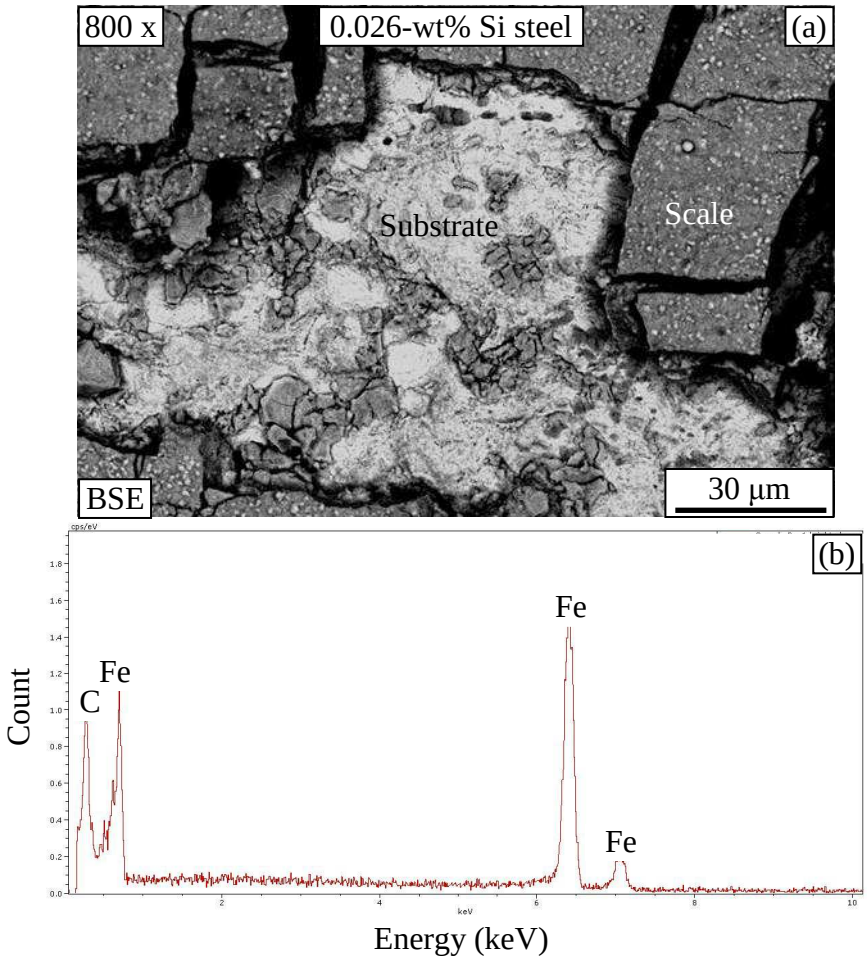

Figure 4.5: (a) Oxide scale and steel substrate of the as-received hot-rolled 0.026-wt% Si steel after the micro-tensile testing at straining by 7.20%, and (b) EDS pattern on metal substrate observed on the white area in the upper micrograph (a).

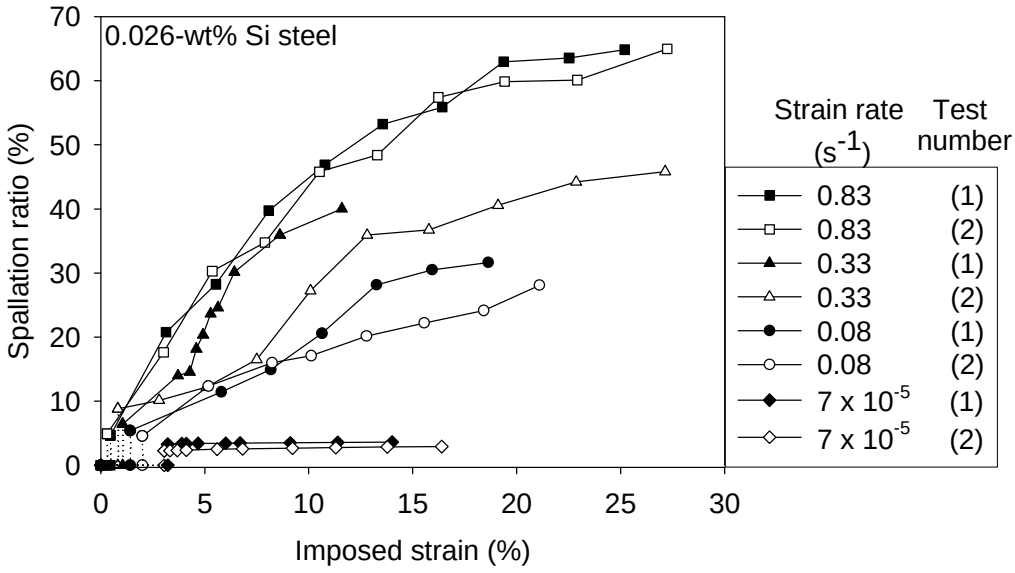

Figure 4.6: Spallation ratio of scale on the as-received hot-rolled 0.026-wt% Si steel as a function of imposed strain at strain rates.

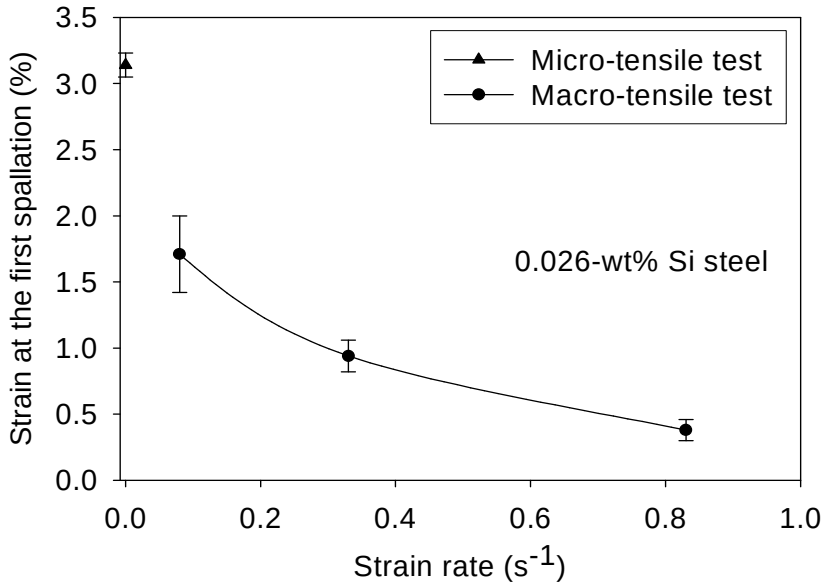

Figure 4.7: Strain at the first spallation of scale on the as-received hot-rolled 0.026-wt% Si steel as a function of strain rates.

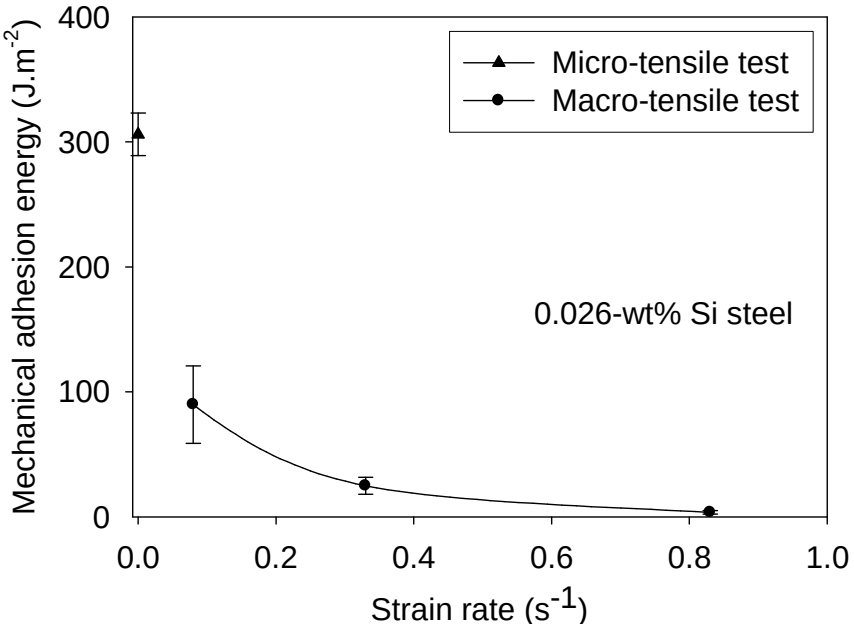

Figure 4.8: Mechanical adhesion energy of scale on the as-received hot-rolled 0.026-wt% Si steel as a function of strain rates.

Table 4.1: Strain at the first spallation and mechanical adhesion energy of scale on the as-received hot-rolled 0.026-wt% Si steel.

Parameters	The as-received hot-rolled 0.026-wt% Si steel			
	Micro-tensile test	Macro-tensile test		
Strain rate (s^{-1})	7×10^{-5}	0.08	0.33	0.83
Strain at the first spallation (%)	3.14 ± 0.09	1.71 ± 0.29	0.94 ± 0.12	0.38 ± 0.08
Mechanical adhesion energy ($J.m^{-2}$)	306 ± 17	90 ± 31	25 ± 7	3.6 ± 1.5

4.1.3 Adhesion of scale on the hot-rolled 0.193-wt% Si steel

The failure on scale of the 0.193-wt% Si steel at different strain rates is shown in Fig. 4.9. Fig. 4.10 shows scale after the micro-tensile testing. From EDS, C, Mn, O, Fe and Si were observed on the spalled area. This might indicate the existence of fayalite (Fe_2SiO_4) on this area.

From Fig. 4.9, spallation ratio is plotted as a function of the imposed strain in Fig. 4.11, while Figs. 4.12 and 4.13 exhibit strain at the first spallation and mechanical adhesion energy respectively. These two parameters are reported in Table 4.2. The effects of strain rate on the testing results are again confirmed to be in agreement with the results on adhesion of scale on the recycled steel (Section 3.2), and the 0.026-wt% Si steel (Section 4.1.2) in the following manners. Increasing strain rate lowered strain initiating the first spallation, increased spallation ratio at a given strain after the fisrt spallation occurs, and also increased the mechanical adhesion energy. However, it is interesting to note that the spallation ratio of scale on higher-silicon-containing steel (Fig. 4.11) was less sensitive to strain rate than the lower-silicon-containing steel (Fig. 4.6).

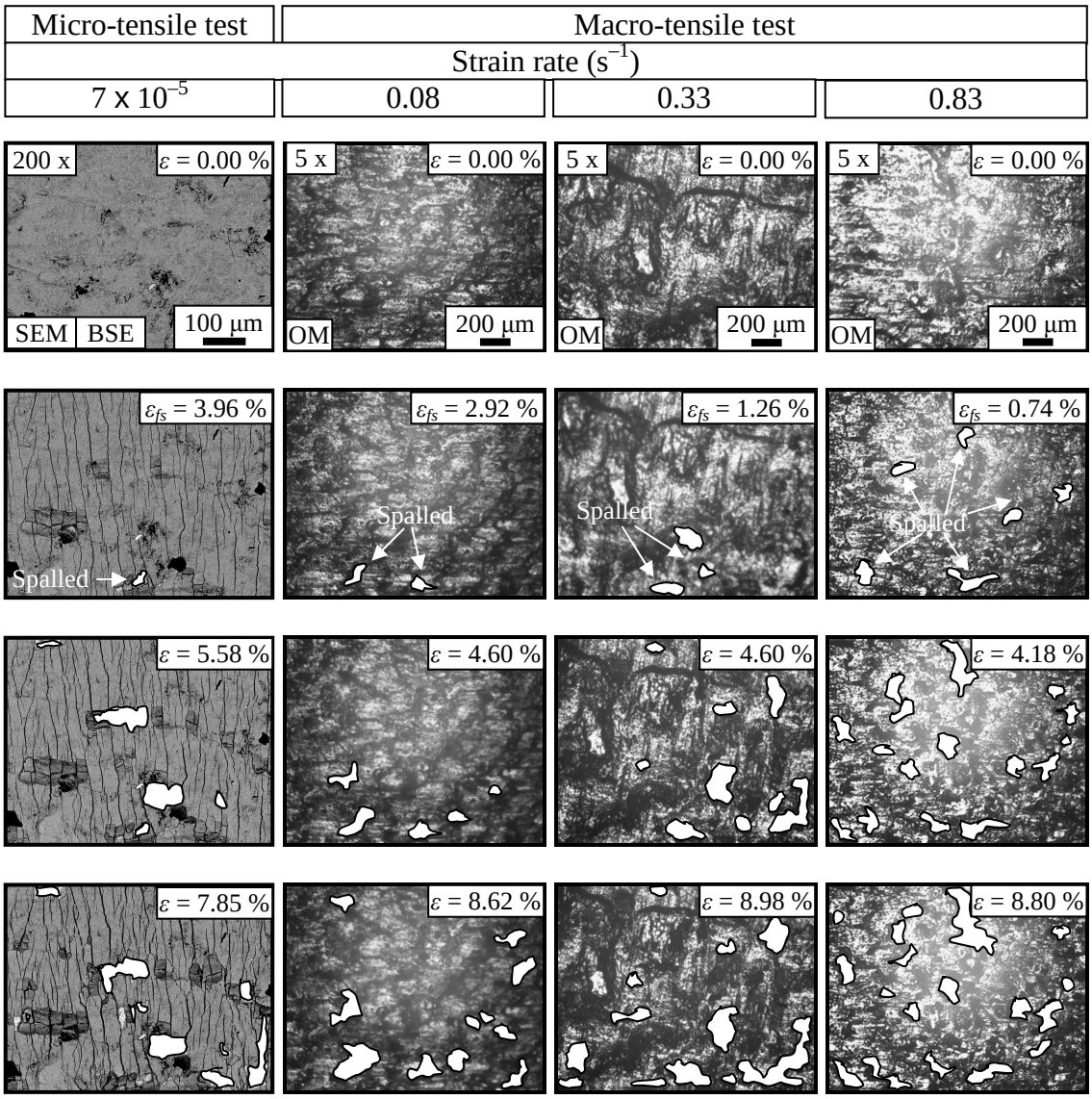

Figure 4.9: Evolution of scale failure on the as-received hot-rolled 0.193-wt% Si steel.

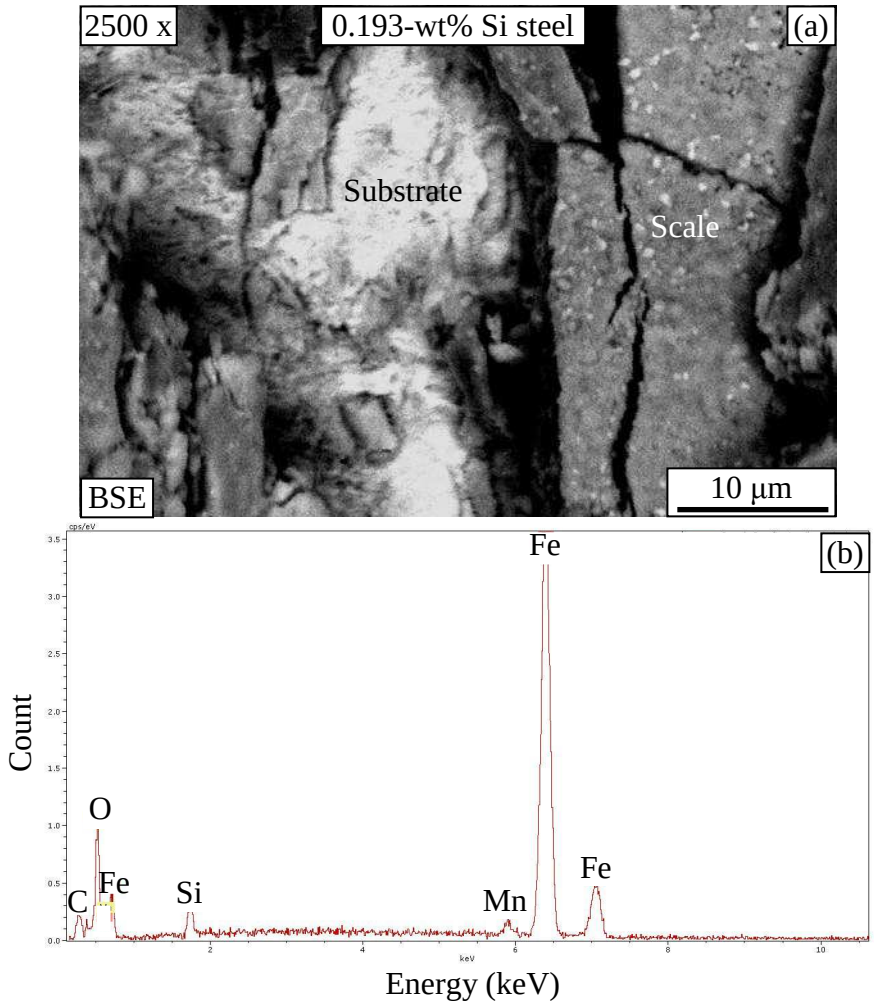

Figure 4.10: (a) Oxide scale and steel substrate of the as-received hot-rolled 0.193-wt% Si steel after the micro-tensile testing at straining by 16.63%, and (b) EDS pattern on metal substrate observed on the white area in the upper micrograph (a).

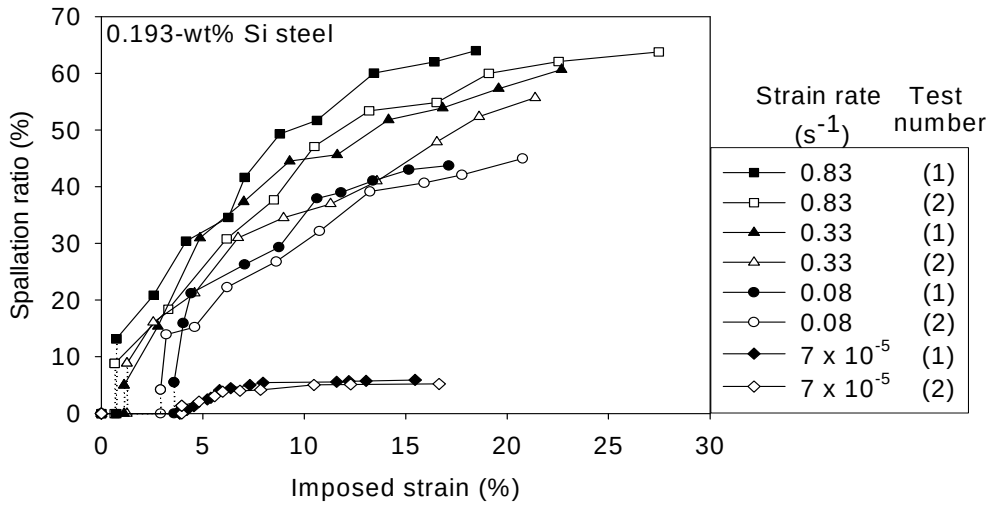

Figure 4.11: Spallation ratio of scale on the as-received hot-rolled 0.193-wt% Si steel as a function of imposed strain at strain rates.

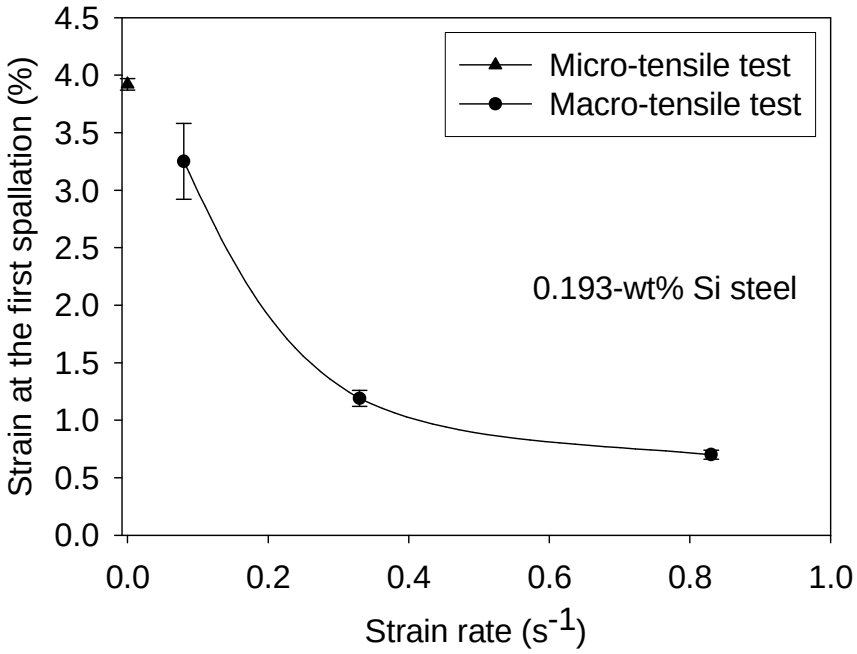

Figure 4.12: Strain at the first spallation of scale on the as-received hot-rolled 0.193-wt% Si steel as a function of strain rates.

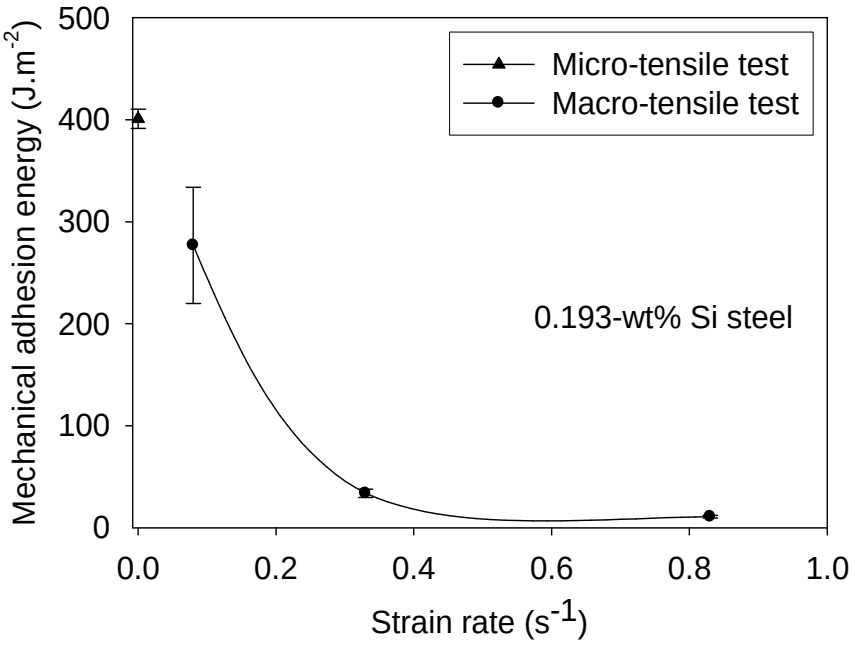

Figure 4.13: Mechanical adhesion energy of scale on the as-received hot-rolled 0.193-wt% Si steel as a function of strain rates.

Table 4.2: Strain at the first spallation and mechanical adhesion energy of scale on the as-received hot-rolled 0.193-wt% Si steel.

Parameters	The as-received hot-rolled 0.193-wt% Si steel			
	Micro-tensile test	Macro-tensile test		
Strain rate (s^{-1})	7×10^{-5}	0.08	0.33	0.83
Strain at the first spallation (%)	3.92 ± 0.05	3.25 ± 0.33	1.19 ± 0.07	0.70 ± 0.04
Mechanical adhesion energy ($J.m^{-2}$)	401 ± 9	277 ± 57	34 ± 4	10.7 ± 1.3

4.1.4 Comparison of adhesion of scales on the 0.026-wt% Si and 0.193-wt% Si hot-rolled steels

Figs. 4.14 and 4.15 depict surfaces of scale on the two steels subjected to different strains during micro- and macro-tensile tests. From the micro-tensile test, crack density was clearly observed. Its value and crack spacing are then quantified and plotted as shown in Fig. 4.16. Parentheses (1) and (2) after description is in the graph indicate the first and second trials respectively. From Figs. 4.14 and 4.15, it was seen that initial cracks existed in scale on the 0.026-wt% Si steel, while no considerable cracks were observed on the as-received scale on the 0.193-wt% Si steel. However, it was observed that after straining crack density of scale on the 0.193-wt% Si steel increased more rapidly with the imposed strain, resulting in the higher crack density than that of scale on the 0.026-wt% Si steel.

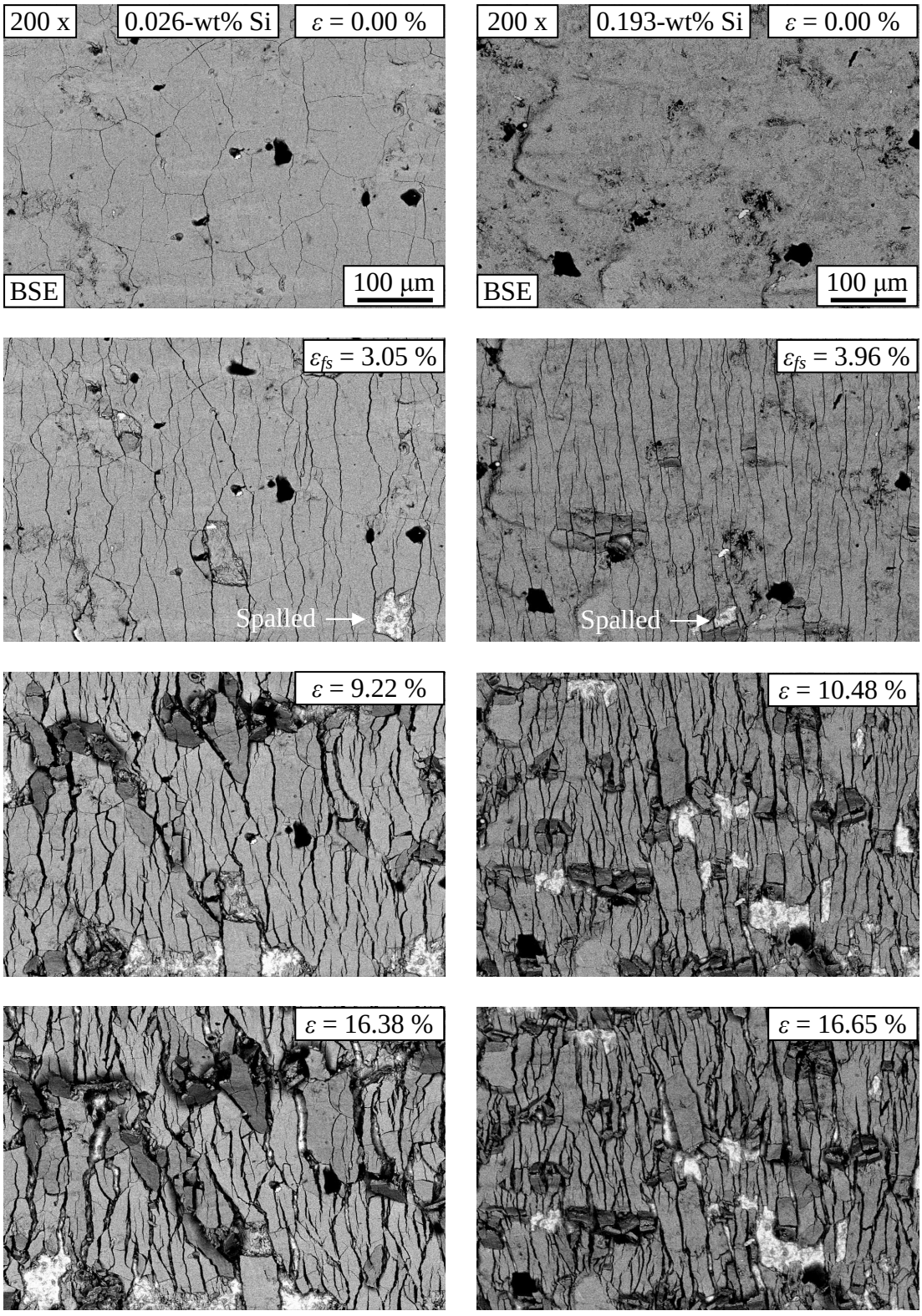

Figure 4.14: Evolution of scale failure on the as-received hot-rolled 0.026-wt% Si steel (left) and the as-received hot-rolled 0.193-wt% Si steel (right) as a function of imposed strain investigated by the micro-tensile test (strain rate = 7×10^{-5} s^{-1}).

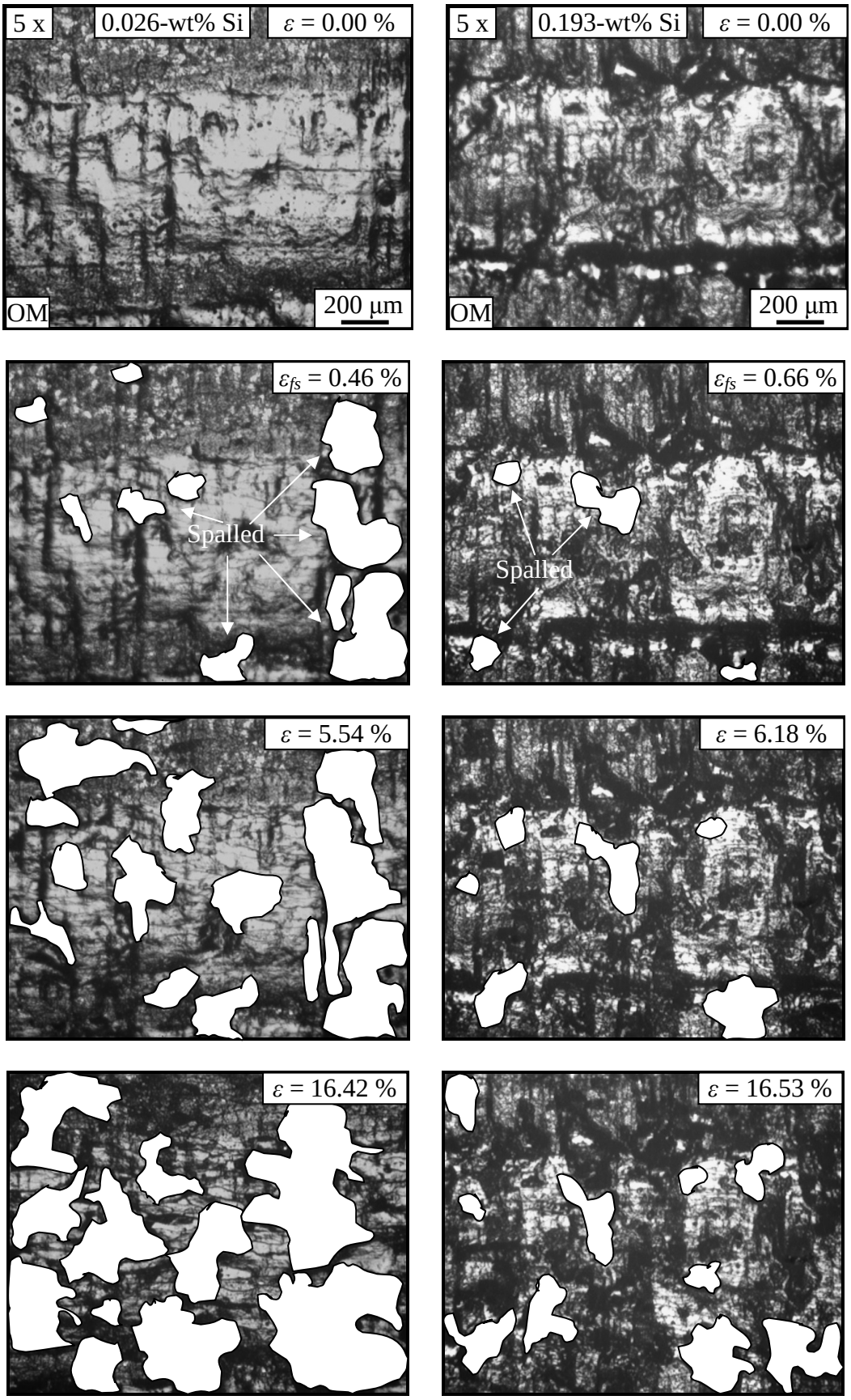

Figure 4.15: Evolution of scale failure on the as-received hot-rolled 0.026-wt% Si steel (left) and the as-received hot-rolled 0.193-wt% Si steel (right) as a function of imposed strain investigate by the macro-tensile test (strain rate = 0.83 s^{-1}).

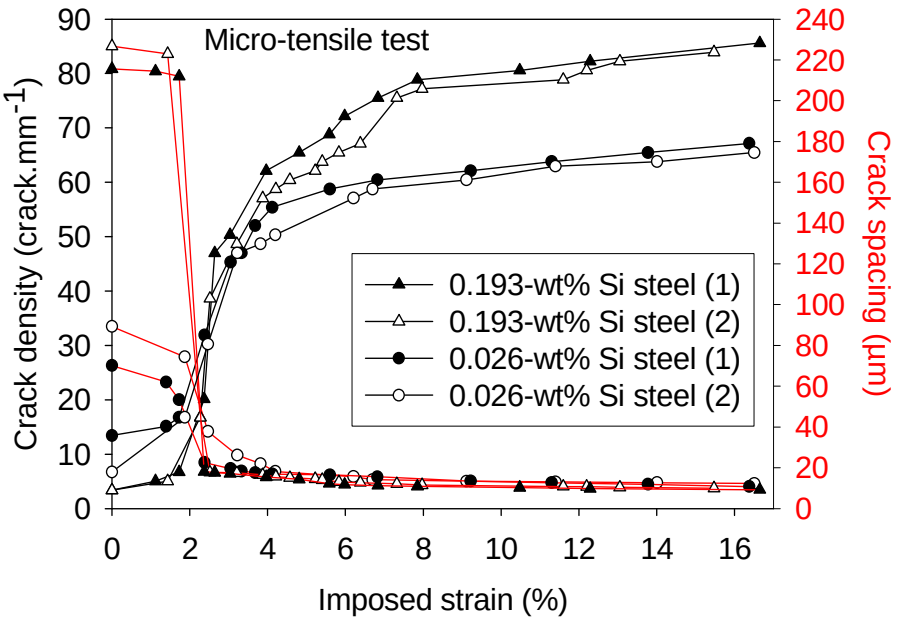

Figure 4.16: Crack density and crack spacing number of scale on the as-received hot-rolled 0.026-wt% Si and 0.193-wt% Si steels as a function of the imposed strain investigated by the micro-tensile test (strain rate = 7 x 10^{-5} s^{-1}).

From Figs. 4.14 and 4.15, spallation ratio at a given imposed strain can be quantified and plotted in Figs. 4.17 and 4.18. From these results, it was found that the spallation ratio of scale on steel with higher silicon content was lower than that of scale on steel with lower silicon content. However, it was observed that spallation ratio of the sample easier spalling (the 0.026-wt% Si steel) tended to saturate at 7% when using the micro-tensile test, but that value approached saturation at 70% when using the macro-tensile test. The latter saturation value was then much larger than the former one. This implies that evaluation of adhesion by the macro-tensile test using higher strain rate tended to give higher spallation ratio and higher gradient of spallation ratio in function of the imposed strain of the studied samples. This might help increase the difference in spallation ratio as a function of imposed strain, which is the benefit obtained in using the macro-tensile testing.

Furthermore, size of the spalled area can also measured as plotted in Fig. 4.19. It was found that the dimension of scale spalled on the 0.193-wt% Si steel smaller than that the 0.026-wt% Si steel for both the micro- and macro-tensile tests. This might be because the 0.193-wt% Si steel had wider crack spacing of scale, this then made the piece of the spalled oxide smaller.

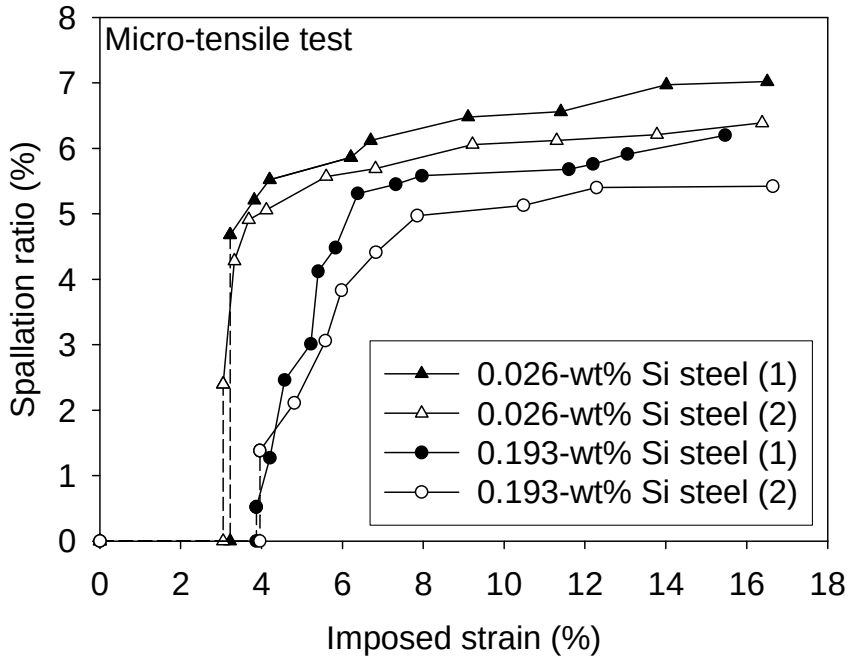

Figure 4.17: Spallation ratio of scales on the as-received hot-rolled 0.026-wt% Si and 0.193-wt% Si steels as a function of imposed strain investigated by the micro-tensile test (strain rate = 7 x 10^{-5} s^{-1}).

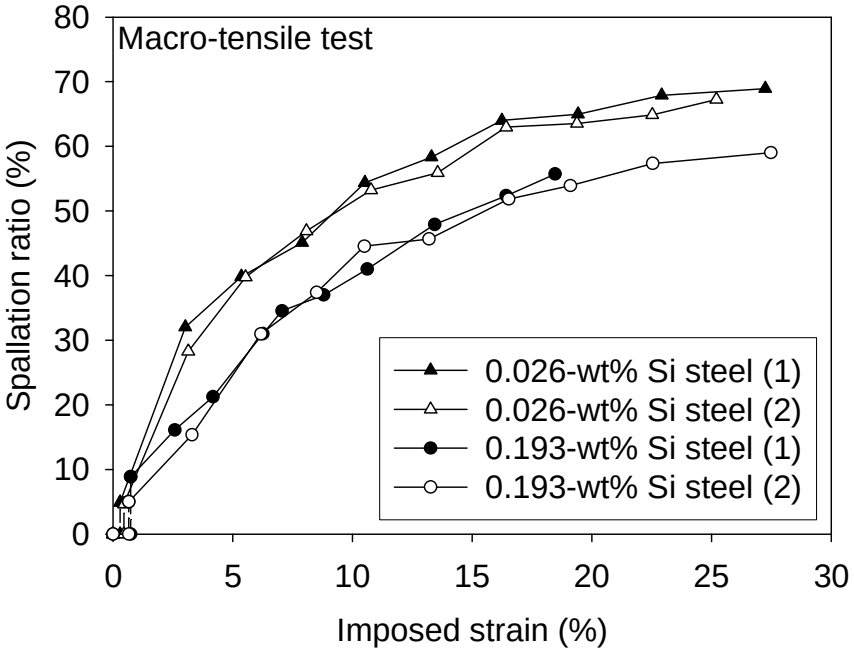

Figure 4.18: Spallation ratio of scales on the as-received hot-rolled 0.026-wt% Si and 0.193-wt% Si steels as a function of imposed strain investigated by the macro-tensile test (strain rate = 0.83 s^{-1}).

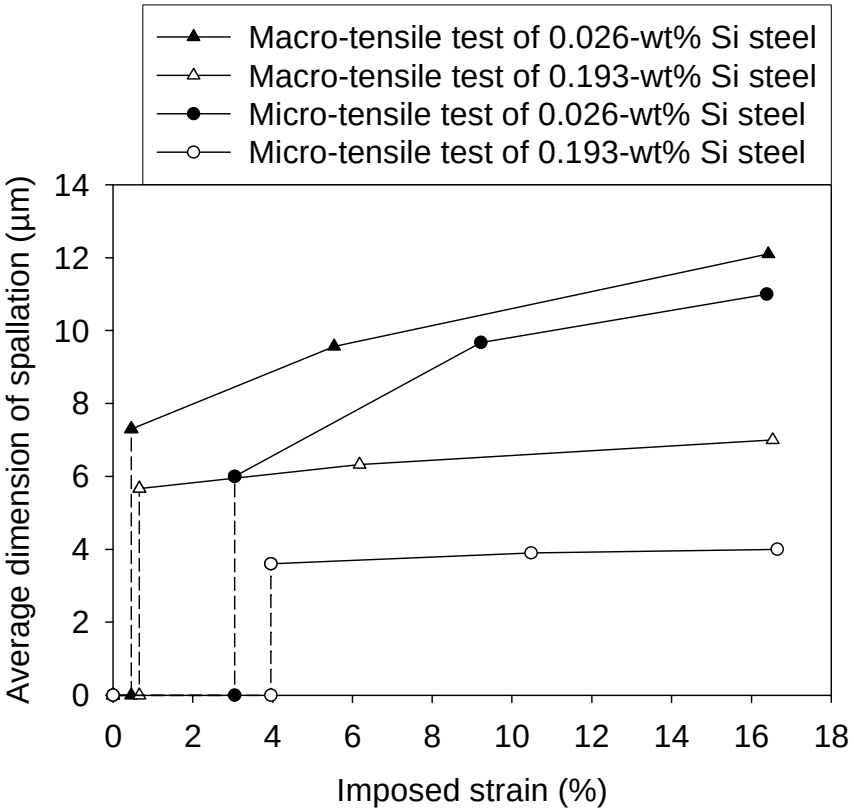

Figure 4.19: Average dimension of scale spallation on the as-received hot-rolled 0.026-wt% Si and 0.193-wt% Si steels as a function of imposed strain evaluated from Figs. 4.14 and 4.15.

From Figs. 4.17 and 4.18, strains provoking the first spallation are replotted as shown in Fig. 4.20. It was found that, when using micro-tensile test, strain provoking the first spallation of the hot-rolled sample with higher Si content was 3.92%. This value was higher than that of the hot-rolled sample with lower Si content which was 3.14%. When using the macro-tensile test, strain provoking the first spallation of the hot-rolled sample with higher Si content was 0.70%, evidently higher than the one of hot-rolled sample with lower Si content which was 0.38%. As for mechanical adhesion energy calculated at that critical strain, their values are shown Fig. 4.21. From Table 4.3, the mechanical adhesion energies for scale on the hot-rolled 0.026-wt% Si steel were 306 ± 17 $J.m^{-2}$ (micro-tensile test) and 3.6 ± 1.5 $J.m^{-2}$ (macro-tensile test). These are lower than that for scale on the hot-rolled 0193-wt% Si steel which was 400 ± 9 $J.m^{-2}$ (micro-tensile test) and 10.7 ± 1.3 $J.m^{-2}$ (macro-tensile test). Even with the large difference between the two tests, these results indicate higher mechanical adhesion of scale actually formed on the hot-rolled 0.193-wt% Si steel than that of scale actually formed on the hot-rolled 0.026-wt% Si steel.

The results by these two tests gave the same tendency that scale on the higher-silicon-containing steel had higher strain initiating the first spallation and also mechanical adhesion energy. This result was in agreement with the typically observed one [Bamba (2006), Chandra-ambhorn (2007] reporting that a thinner scale had higher strain initiating the first spallation and also adhesion energy. Furthermore, a significantly lower initial crack density of scale on the higher-silicon-containing steel indicated lower relaxation of the residual stress in scale during the tensile test, thus resulting in the higher strain initiating the first spallation and adhesion energy of the 0.193-wt% Si steel.

As for the assessment of the two testing methods, it should be noted that lowering strain rate gave higher strain initiating the first spallation, and therefore adhesion energy. By the higher value obtained, the differentiation between the two studied values might be easier. This is then the advantage of the micro-tensile test which runs at the lowest strain rate.

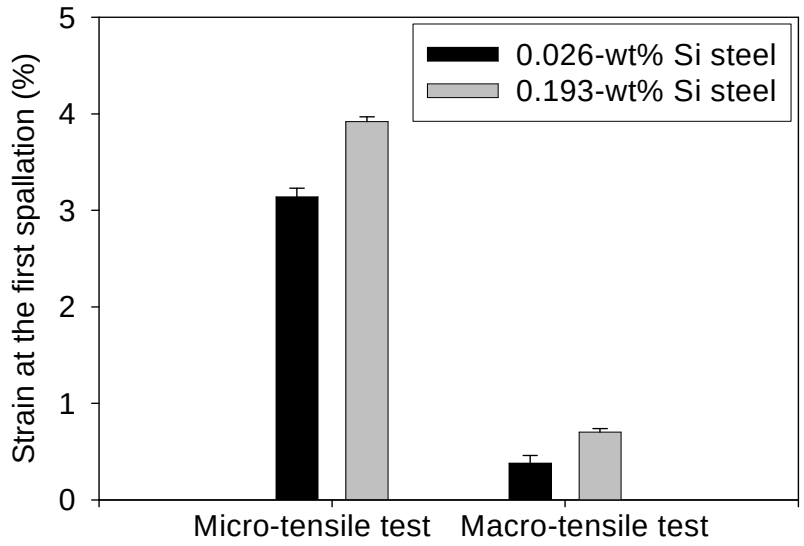

Figure 4.20: Strain at the first spallation of scale on the as-received hot-rolled 0.026-wt% Si and 0.193-wt% Si steels.

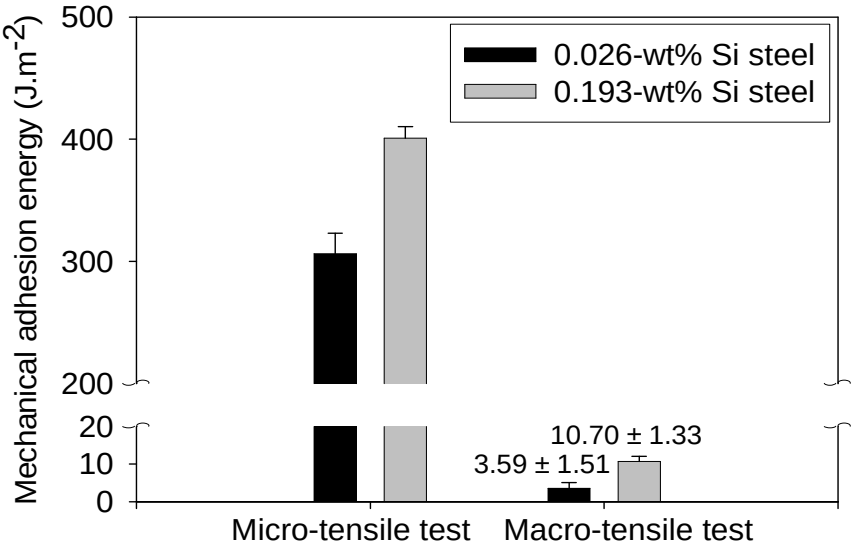

Figure 4.21: Mechanical adhesion energy of scale on the as-received hot-rolled 0.026-wt% Si and 0.193-wt% Si steels.

Table 4.3: Strain at the first spallation and mechanical adhesion energy of scale on the as-received hot-rolled 0.026-wt% Si and 0.193-wt% Si steels.

Parameters	Micro-tensile test ($\dot{\varepsilon} = 7 \times 10^{-5}\,s^{-1}$)		Macro-tensile test ($\dot{\varepsilon} = 0.83\,s^{-1}$)	
	0.026-wt% Si	0.193-wt% Si	0.026-wt% Si	0.193-wt% Si
Oxide thickness (μm)	9.08	7.55	9.08	7.55
Strain at the first spallation (%)	3.14 ± 0.09	3.92 ± 0.05	0.38 ± 0.08	0.70 ± 0.04
Mechanical adhesion energy ($J.m^{-2}$)	306 ± 17	401 ± 9	3.6 ± 1.5	10.7 ± 1.3

As a matter of discussion on the role of silicon on formation and adhesion of scale on steel substrate, Figs. 4.22 and 4.23 were illustrated the area that scale spalled out after the micro- and macro-tensile test respectively. An energy-dispersive spectroscopy (EDS) equipped with SEM was applied to characterise the area that metal surface was revealed. Peaks of Fe, Si, O and C were detected. This indicated the existence of oxide containing Si at the steel-scale interface. It was reported [Taniguchi (2001)] that fayalite (Fe_2SiO_4) was found near the steel-scale interface after oxidation of low carbon steel containing Si content up to 1.5 wt% in air. Existence of oxide containing silicon at that interface could increase bond strength there and then promotes scale adhesion. Also the presence of interfacial oxide particles can be thought to deviate the propagation of the interfacial crack, making the adhesion higher. Furthermore, increasing Si content in steel was also found to increase thermal stress for oxide spallation when the sample was cooled down from 1143°C [Taniguchi (2001)]. In quantification of mechanical adhesion energy from tensile test, it was proposed [Chandra-ambhorm (2007), (2008)] that residual stress played the role in determining mechanical adhesion energy. If scale contained higher residual stress, tensile loading in the early period must be used to relax the compressive stress due to the residual stress in the oxide scale. Therefore, higher strain must be applied to accumulate energy until achieving the threshold value provoking scale spallation. If scale on steel with higher Si had higher thermal stress and higher residual stress in scale, higher strain must be applied in order to initiate scale spallation. Thus, the higher measured strain provoking the first spallation of hot-rolled steel with higher Si content was observed as shown in Table 4.3.

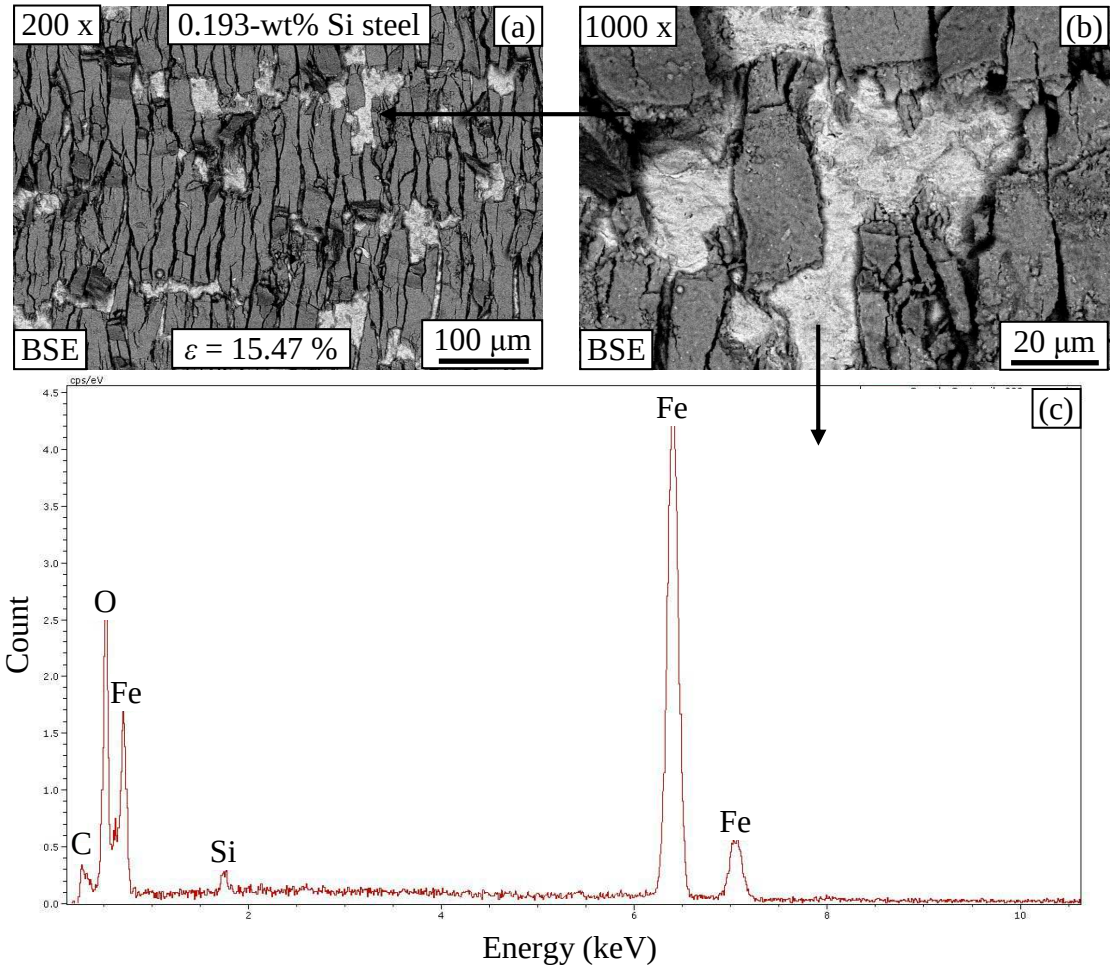

Figure 4.22: (a) Oxide scale and steel substrate of 0.193-wt% Si steel after the micro-tensile test, (b) internal interface between scale and substrate magnified from (a), and (c) EDS pattern on metal substrate observed on the white area in the upper micrograph.

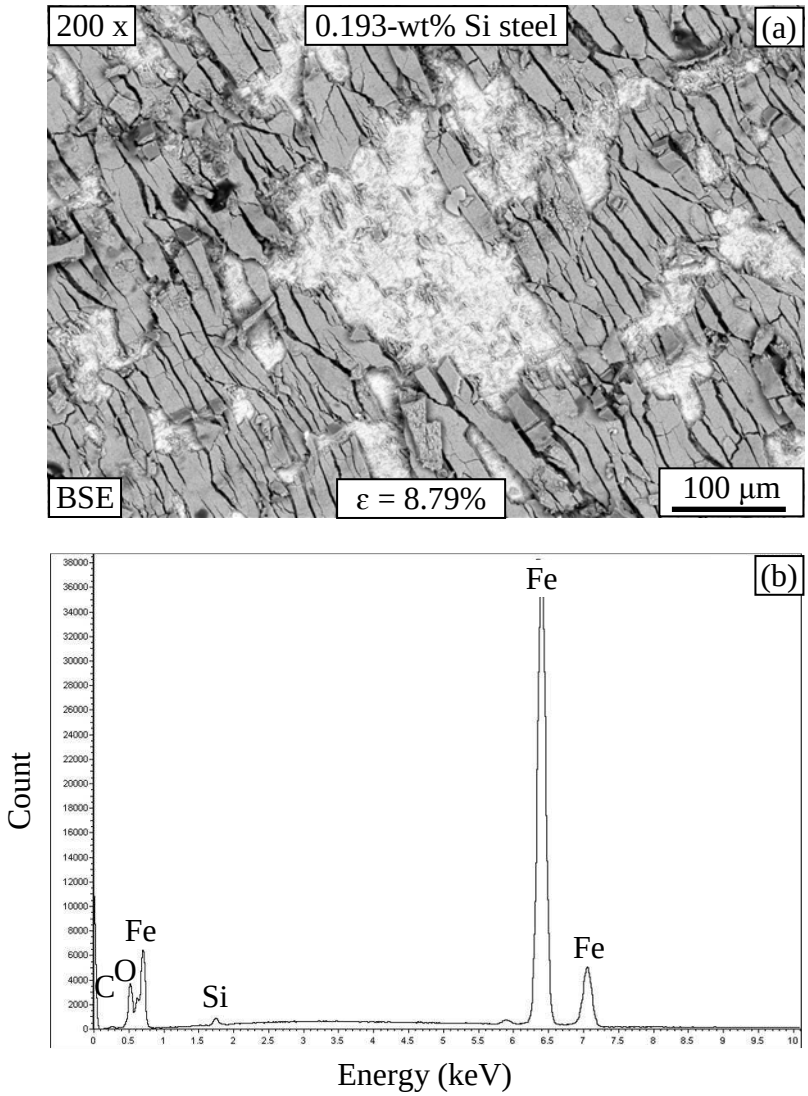

Figure 4.23: (a) Oxide scale and steel substrate of 0.193-wt% Si steel after the macro-tensile test, and (b) EDS pattern on metal substrate observed on the white area in the upper micrograph (a).

4.1.5 Pickling ability

Fig. 4.24 exhibits weight loss of the hot-rolled steels in function of the pickling time. Dissolution rate of scale corresponded to the slope of the graph in the early period, which is shown in Fig. 4.25. Period of time for the complete pickling is shown in Fig. 4.26. For the hot-rolled 0.193-wt% Si steel, the dissolution rate of scale was lower than that of the 0.026-wt% Si steel. This might be due to the existence of oxide rich in Fe, Si in the scale helping slow down the pickling rate and therefore retarding the time for the complete pickling. It was reported [Chattopadhyay (2008)] that a non-stoichiometric fayalite ($Fe_{2.44}Si_{0.55}O_4$) phase, which is found in the oxidised steel containing high levels of silicon, is not easily picklable. It was also noted that as the amount of Si increases, the pickling kinetics becomes slower.

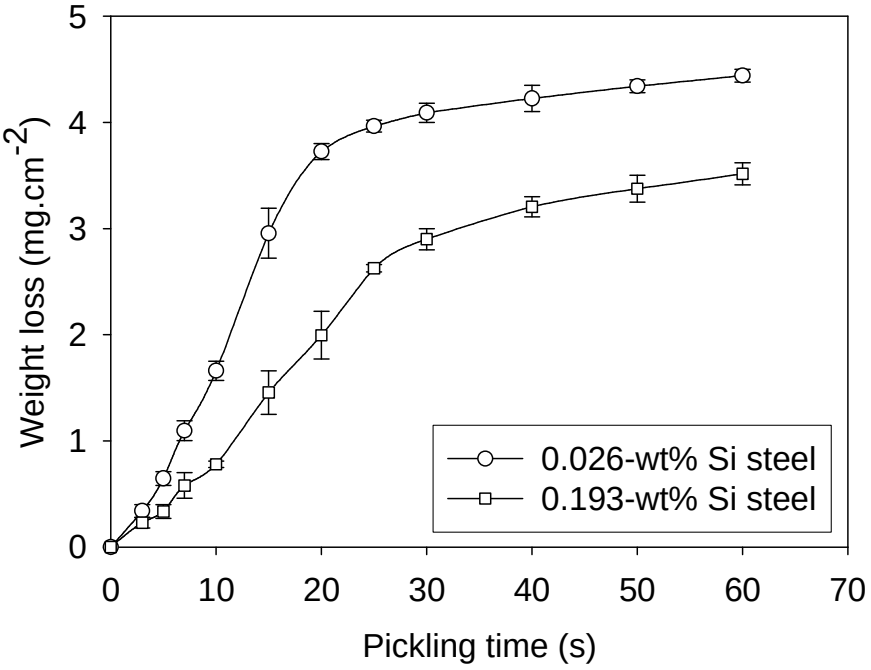

Figure 4.24: Weight loss for the as-received hot-rolled 0.026-wt% Si and 0.193-wt% Si steels in 10%v/v HCl solution at 80°C as a function of pickling time.

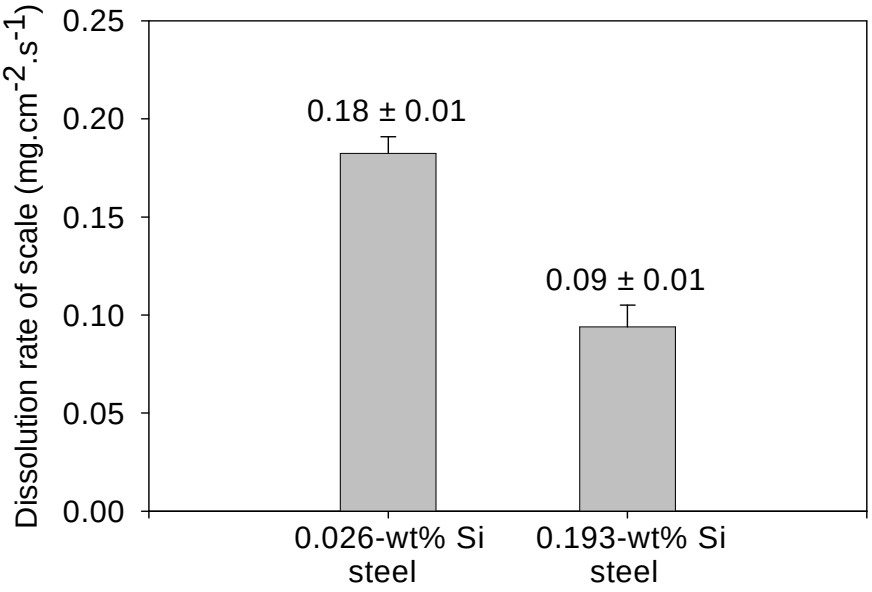

Figure 4.25: Dissolution rate of scale on the as-received hot-rolled 0.026-wt% Si and 0.193-wt% Si steels in 10%v/v HCl solution at 80°C.

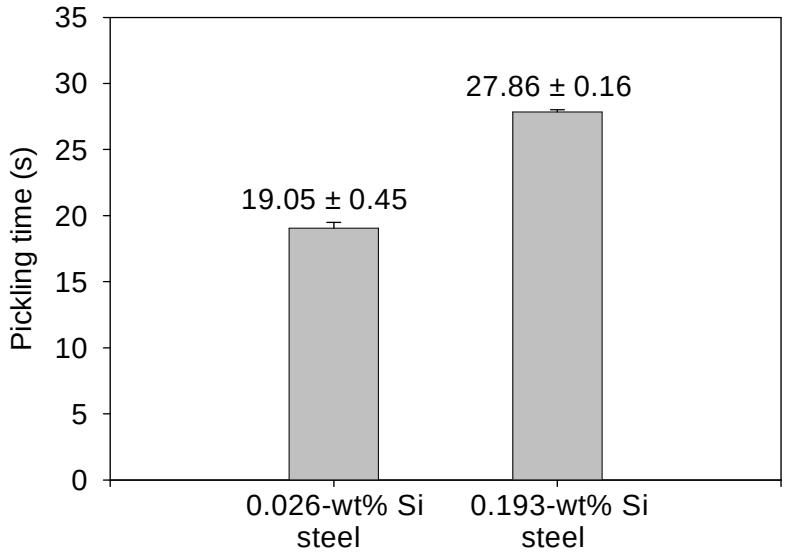

Figure 4.26: Pickling time of scale on the as-received hot-rolled 0.026-wt% Si and 0.193-wt% Si steels in 10%v/v HCl solution at 80°C.

4.2 Investigation of scale formed in laboratory

4.2.1 Oxide scale structure

In this part, the as-received hot-rolled 0.026-wt% Si and 0.193-wt% Si steels were polished down to the metal and then re-oxidised in 20%H_2O/Ar at 900°C for 1-3 minutes. Gravimetric measurements showed that the classical linear-parabolic rate law seems to be followed and that the steel with higher silicon content had lower oxidation rate (Fig. 4.27). These results are in agreement with literature reporting the oxidation of silicon-containing steel oxidised in air [Tanigushi (2001), Yang (2008)].

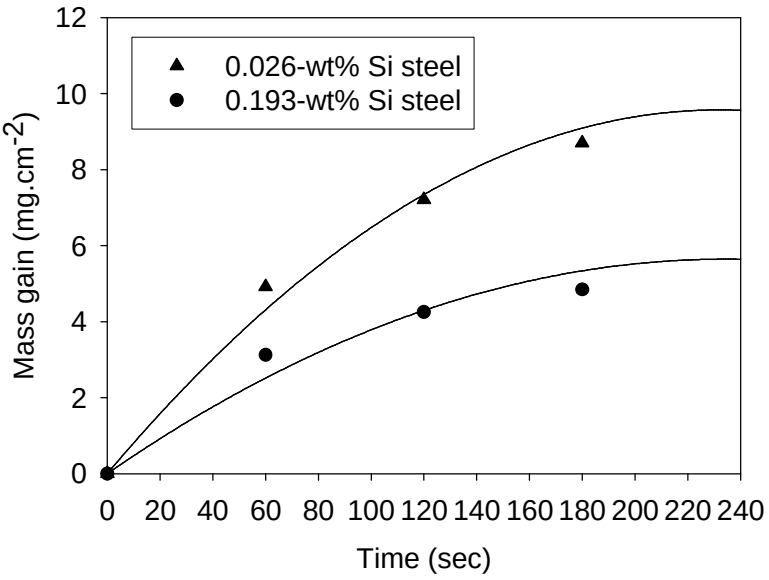

Figure 4.27: Mass gain as a function of the oxidising period of time of 0.026-wt% Si and 0.193-wt% Si steels in 20%H_2O/Ar.

To properly assess adhesion of scale on different steels, such evaluation has to be made among the oxidised steels having the same scale thickness. From Fig. 4.27, the tensile specimen made of steels with higher and lower silicon contents were chosen to be oxidised for 1 and 3 minutes respectively. This is to give scale on those steels with the same mass gained, which is assumed to have identical scale thickness. Using Equation 2 – 5, thicknesses of scales on the 0.026-wt% Si and 0.193-wt% Si steels were 1.10 and 1.19 µm respectively. Fig. 4.28 depicts scale surfaces on steels with lower and higher silicon contents oxidised in 20%H_2O/Ar before tensile loading. The nodule crystals were observed on those two surfaces. From XRD results, the peaks of hematite, magnetite and iron were observed from the oxidised steel with lower silicon content as shown in Fig. 4.29. The same peaks, but additionally fayalite, were detected from the oxidised steel with higher silicon content as depicted in Fig. 4.30.

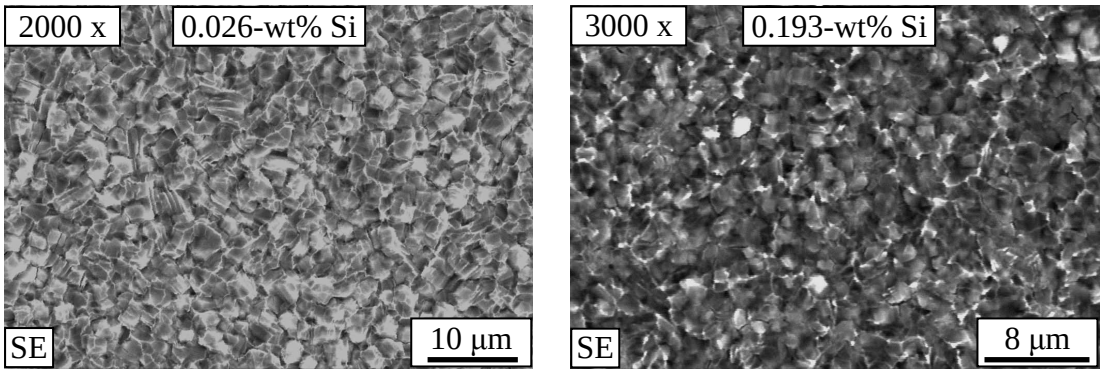

Figure 4.28: Scale surface morphology of the 0.026-wt% Si steel (left) and 0.193-wt% Si steel (right) oxidised at 900°C in 20%H_2O/Ar before the micro-tensile loading.

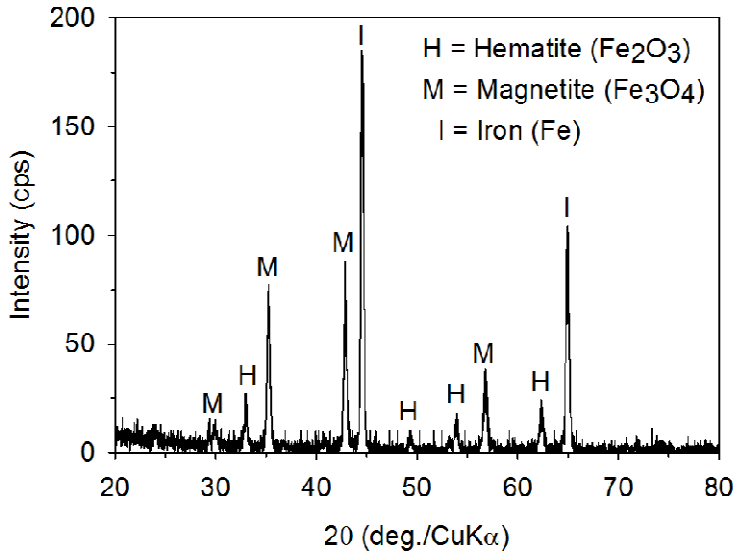

Figure 4.29: XRD pattern on oxide scale of the 0.026-wt% Si steel oxidised in 20%H_2O/Ar at 900°C for 1 min, observed after micro-tensile test.

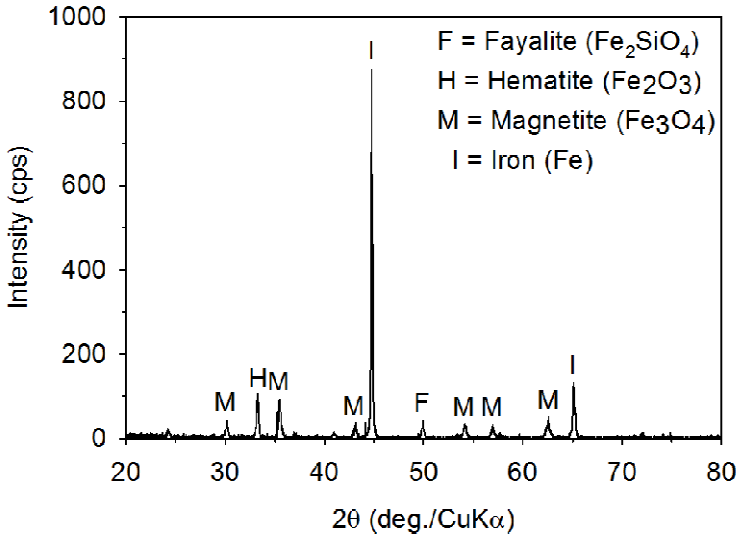

Figure 4.30: XRD pattern on oxide scale of the 0.193-wt% Si steel oxidised in 20%H_2O/Ar at 900°C for 3 min, observed after micro-tensile test.

4.2.2 Scale adhesion

Fig. 4.31 depicts comparative scale surface of both studied steels before and after the micro-tensile test. Even though the scale on steel with higher silicon content was strained up to ca. 14% while scale on steel with lower silicon content was stained up to ca. 11%, a priori, higher spallation of scale on the 0.193-wt% Si steel was observed.

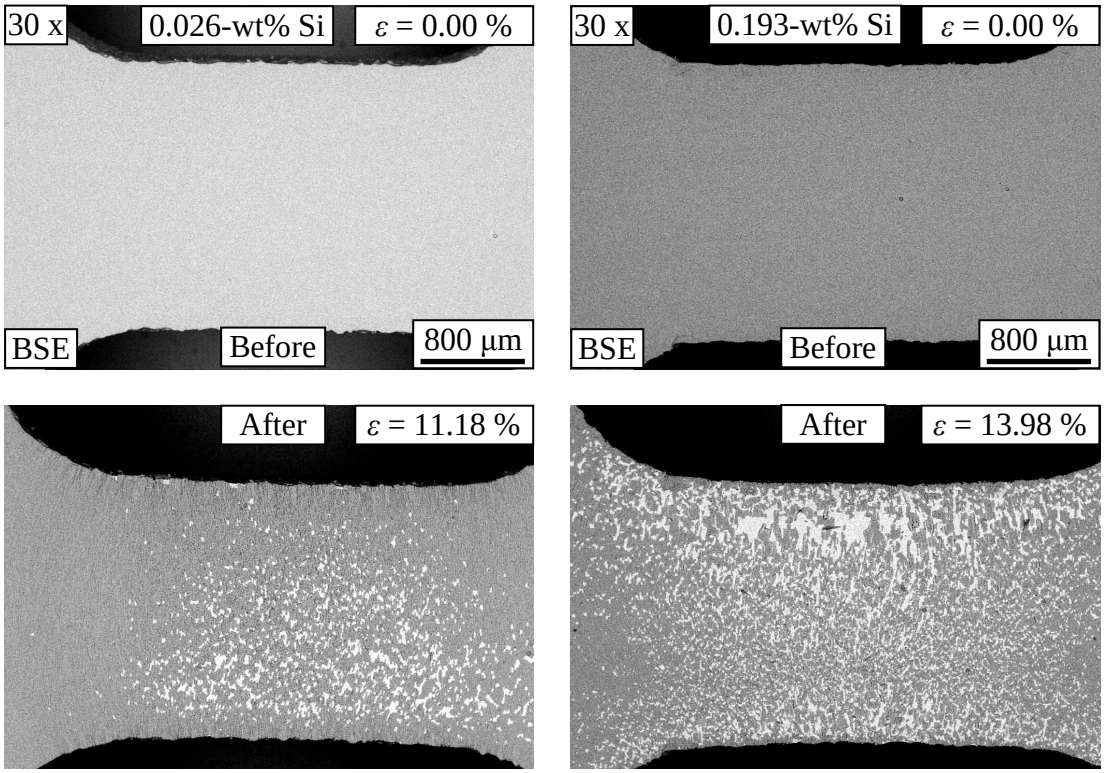

Figure 4.31: Scale surface morphology of the 0.026-wt% Si steel (left) and 0.193-wt% Si steel (right) formed at 900°C in 20%H_2O/Ar before and after the micro-tensile test.

Between before and after tensile test, failure of scales on the studied steels at different imposed strains is depicted in Fig. 4.32. From this figure, crack density and crack spacing was evaluated. A crack density and crack spacing as a function of the imposed strain measured using the micro-tensile test which is presented in Fig. 4.33 (a), and the crack spacing is magnified to Fig. 4.33 (b). It was found that scale on steel with higher silicon content had lower crack density, or higher crack spacing.

Furthermore, from Fig. 4.32, spallation ratio of the studied oxidised steels were assessed and plotted in function of the imposed strain as shown in Fig. 4.34. Strain initiating the first spallation is presented in Fig. 4.35 and Table 4.4. From these results, it can be seen that Increasing Si content from 0.026 to 0.193 wt% in steel much lowered strain initiating the first spallation from 5.88 to 2.73% . Moreover, after spallation took place, spallation ratio of the oxidised steel with higher silicon content was higher, as well as its sensitivity to spalling with the increment of the imposed stain. These results seem to indicate lower degree of adhesion of scale on steel with higher silicon content, but under the situation that delamination must occur between scale and steel substrate.

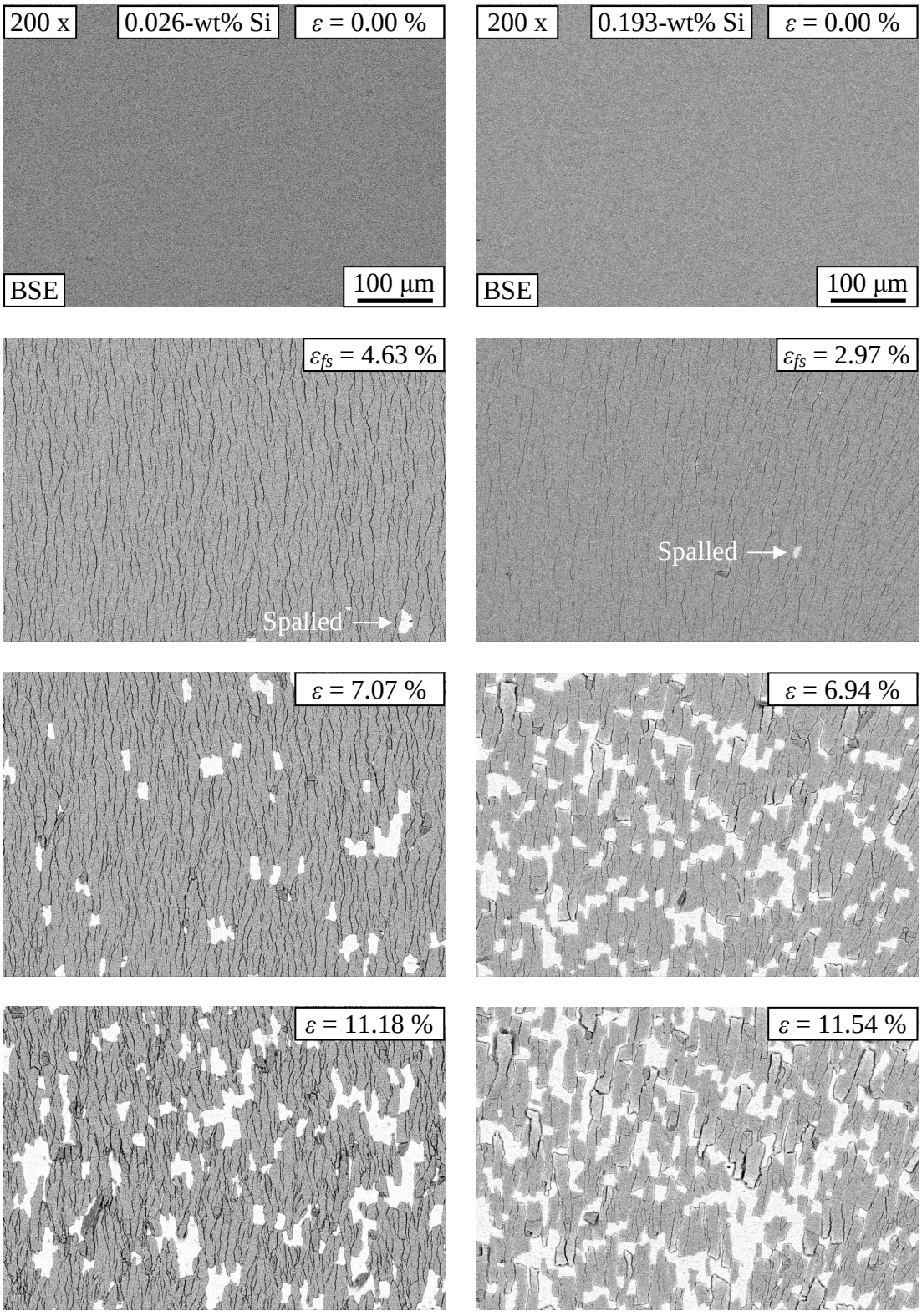

Figure 4.32: Evolution of scale failure on the 0.026-wt% Si steel (left) and 0.193-wt% Si steel (right) as a function of imposed strain.

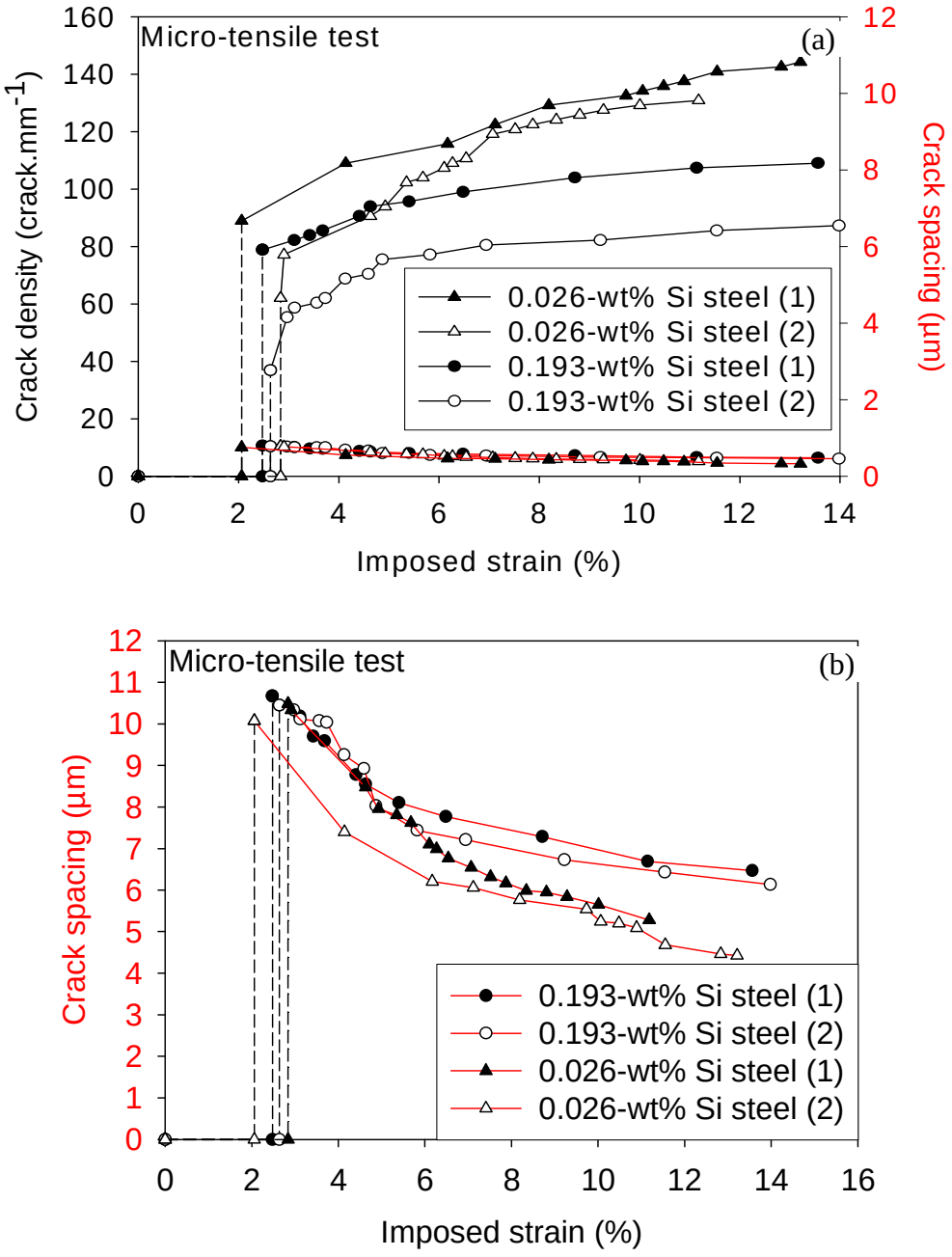

Figure 4.33: (a) Crack density and crack spacing number of scale on the 0.026-wt% Si and 0.193-wt% Si steels as a function of the imposed strain investigate by the micro-tensile test, and (b) crack spacing magnified from (a).

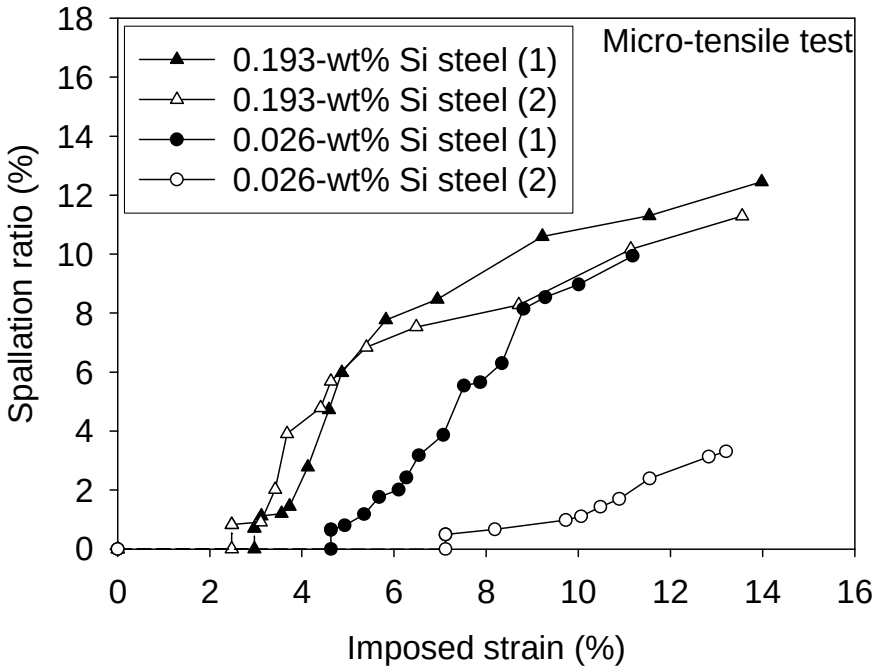

Figure 4.34: Spallation ratio of scales on the 0.026-wt% Si and 0.193-wt% Si steels as a function of imposed strain investigated by the micro-tensile test.

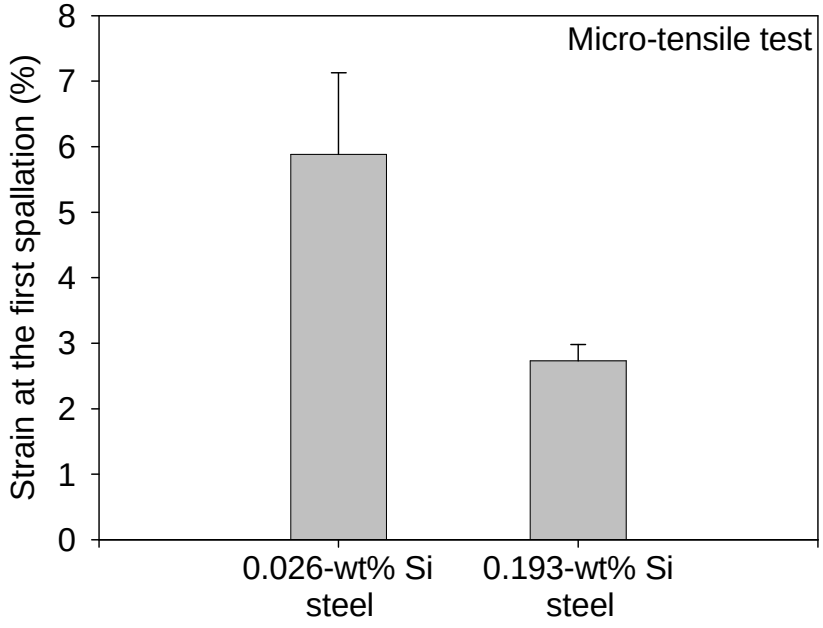

Figure 4.35: Strain at the first spallation of scale on the 0.026-wt% Si and 0.193-wt% Si steels investigated by the micro-tensile test.

Table 4.4: Strain at the first spallation and mechanical adhesion energy of scale on the 0.026-wt% Si and 0.193-wt% Si steels investigated by the micro-tensile test.

Parameters	Micro-tensile test ($\dot{\varepsilon} = 7 \times 10^{-5}\ s^{-1}$)	
	0.026-wt% Si steel	0.193-wt% Si steel
Oxide thickness (µm)	1.10	1.19
Strain at the first spallation (%)	5.88 ± 1.25	2.73 ± 0.25

After tensile test, SEM-EDS analysis was applied on the surface of the two studied samples as shown in Figs. 4.36 and 4.37. The main peaks of iron were detected on the spalled area on the sample containing lower silicon content, indicating the adhesive delamination between scale and steel substrate for this sample. On the contrary, peaks of iron and oxygen were observed on the spalled area of the sample with higher silicon content. This indicates partial spallation of scale, while some parts of oxide of iron still adhered to steel substrate. From Fig. 4.30 showing XRD analysis of scale on the 0.193-wt% Si steel, it was seen that the peaks of Fe, Fe_2O_3, Fe_3O_4 as well as Fe_2SiO_4 are present. This indicates fayalite existing at the steel-scale interface which promoted adhesion of the internal part of scales. However, the global adhesion of the rest of the scales was rather low.

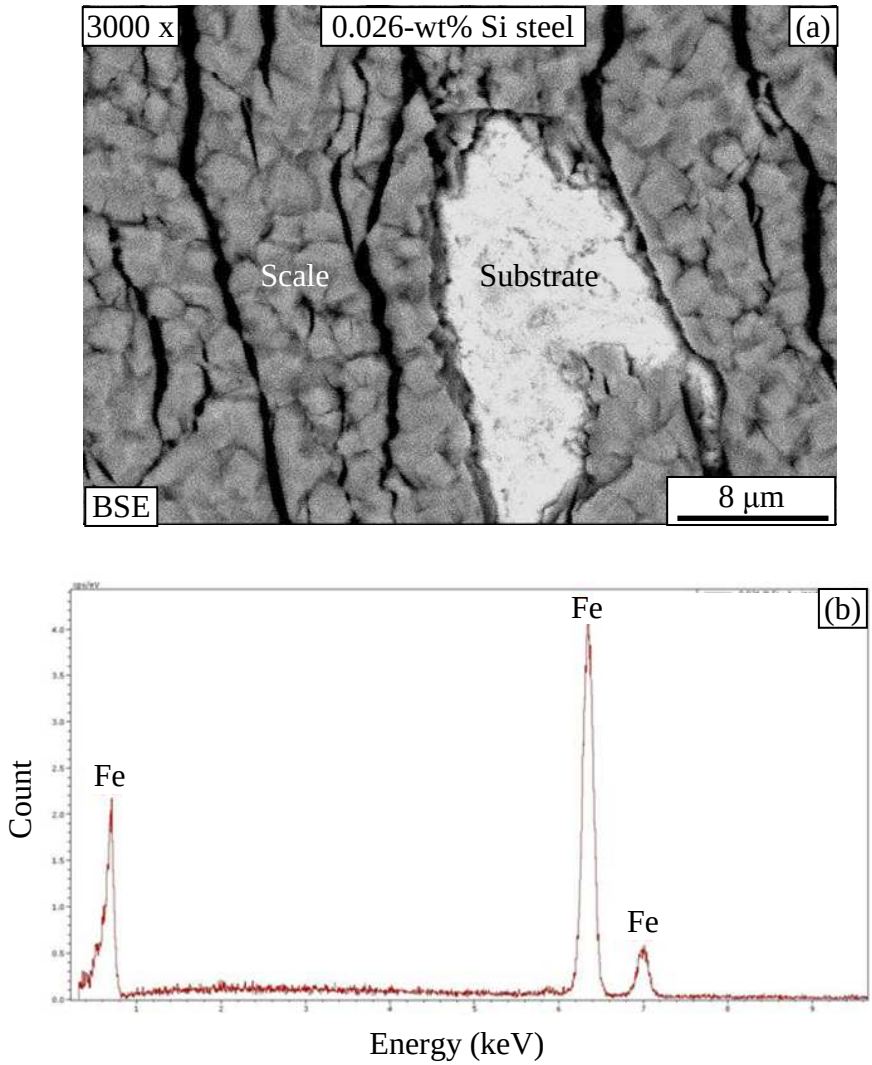

Figure 4.36: (a) Oxide scale and steel substrate of the 0.026-wt% Si steel after straining by 13.21%, and (b) EDS pattern on metal substrate observed on the white area in the upper micrograph (a).

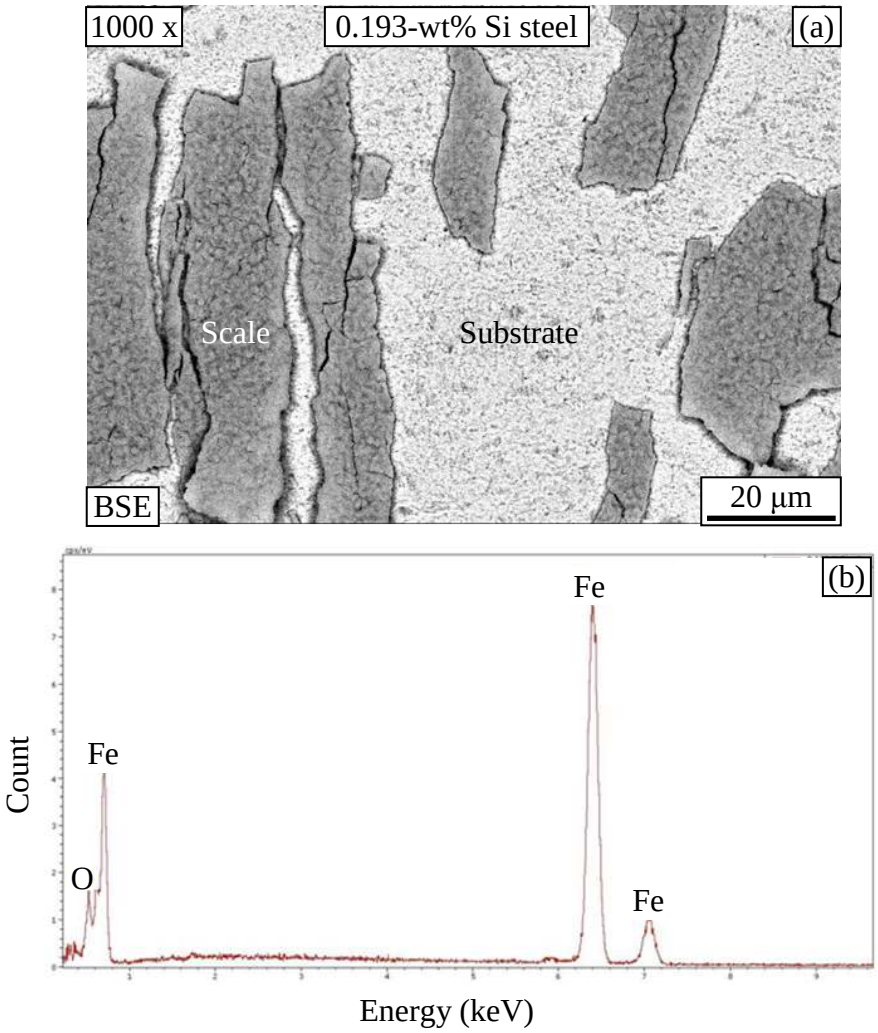

Figure 4.37: (a) Oxide scale and steel substrate of 0.193-wt% Si steel after straining by 13.98%, and (b) EDS pattern on metal substrate observed on the white area in the upper micrograph (a).

CHAPTER 5

OXIDATION OF SILICON-CONTAINING MODEL STEEL

In chapter 3, we have seen that the recycled steel contains many elements which can affect oxidation and adhesion of scale on the substrate particularly silicon and copper. In chapter 4, the study is conducted using steels with silicon content in the range of 0.026 to 0.193 wt% which are commercially available from the industry. In order to study the role of silicon on oxidation more profoundly, two model steels were prepared for the investigation in this chapter with a greater variety of silicon contents: 0.25-wt% Si and 0.84-wt% Si. The role of copper on oxidation will be focussed in the next chapter.

The oxidation tests were conducted by the thermobalance model B 24 from SETARAM. Silicon-containing model steels were prepared with cylindrical size with 5 mm of length and 5 mm of diameter. Oxidation study was carried out in 20%H_2O/Ar for 16 hours from 600 to 900°C.

5.1 Oxidation kinetics of model steels containing silicon

5.1.1 Oxidation rate as a function of time

It was found that the oxidation kinetics of the studied steels follow the linear-parabolic rate law as shown in Fig. 5.1 to Fig. 5.4. At 900°C after 5 hours, the kinetic of the 0.84-wt% Si steel was considerably higher than that of steel with lower Si. At 700°C and 800°C, the kinetic of the 0.84-wt% Si steel was lower than that of the reference and 0.25-wt% Si steels. However, the kinetic of the studied steels seemed to be similar at 600°C.

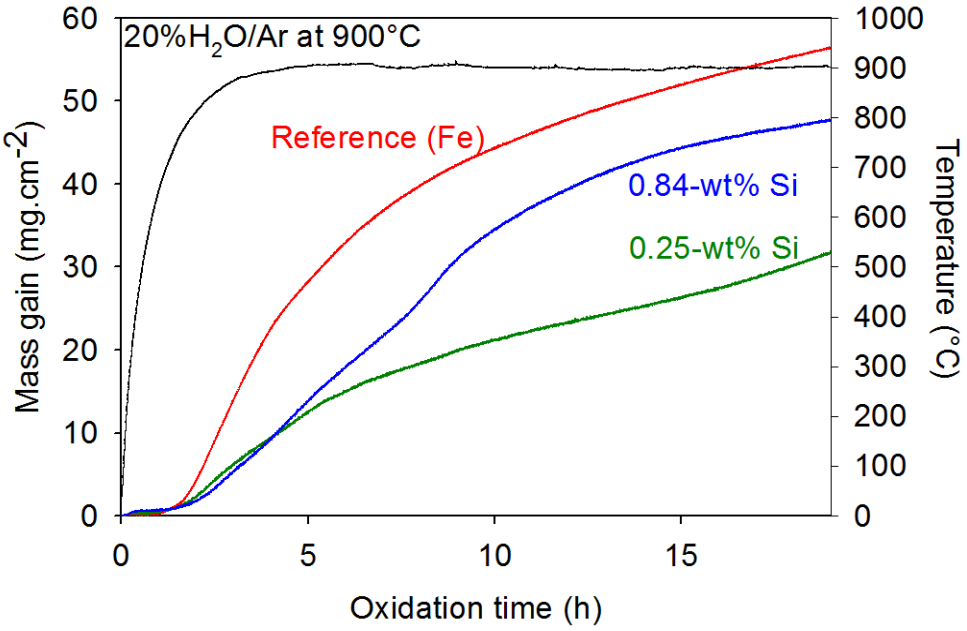

Figure 5.1: Mass gain of the reference (Fe), 0.25-wt% Si and 0.84-wt% Si steels oxidised in 20%H_2O/Ar at 900°C.

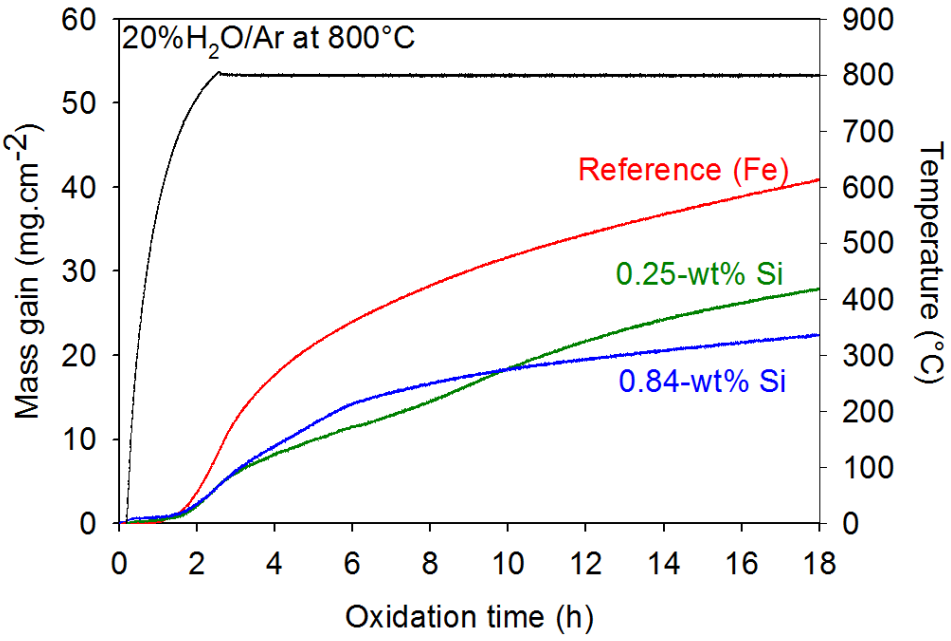

Figure 5.2: Mass gain of the reference (Fe), 0.25-wt% Si and 0.84-wt% Si steels oxidised in 20%H_2O/Ar at 800°C.

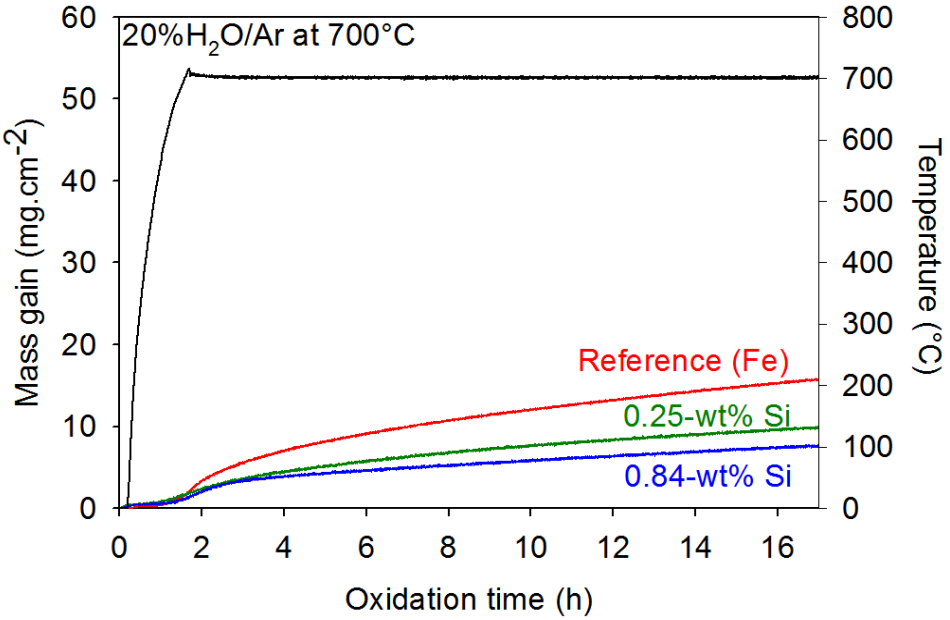

Figure 5.3: Mass gain of the reference (Fe), 0.25-wt% Si and 0.84-wt% Si steels oxidised in 20%H_2O/Ar at 700°C.

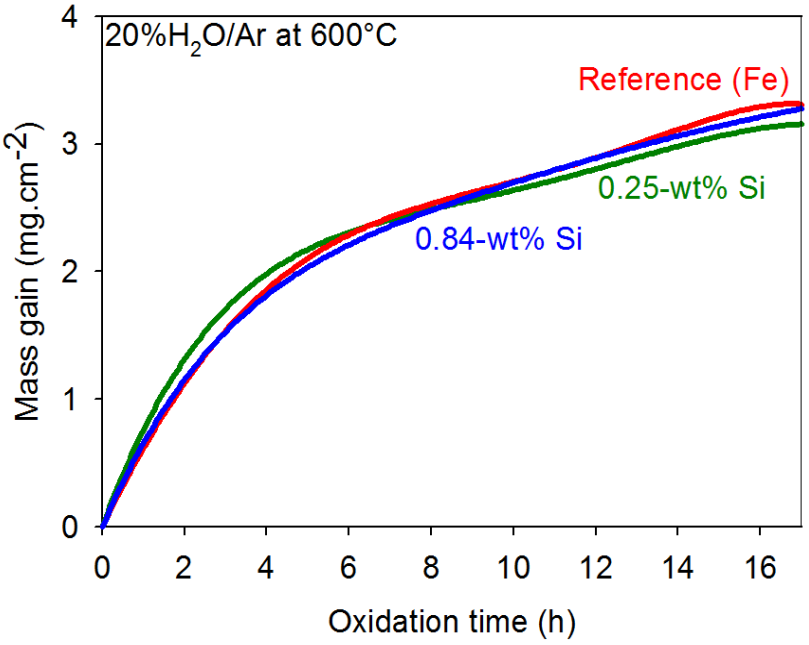

Figure 5.4: Mass gain of the reference (Fe), 0.25-wt% Si and 0.84-wt% Si steels oxidised in 20%H_2O/Ar at 600°C.

Fig. 5.5 to Fig. 5.7 compare the temperature effect of the reference, 0.025-wt% Si and 0.84-wt% Si steels at temperature range of 600 to 900°C. It was seen that the oxidation rate increased with increasing temperature. It can also be observed that the initial stage, which the oxidation rate was lower, seems to be identical for all steels.

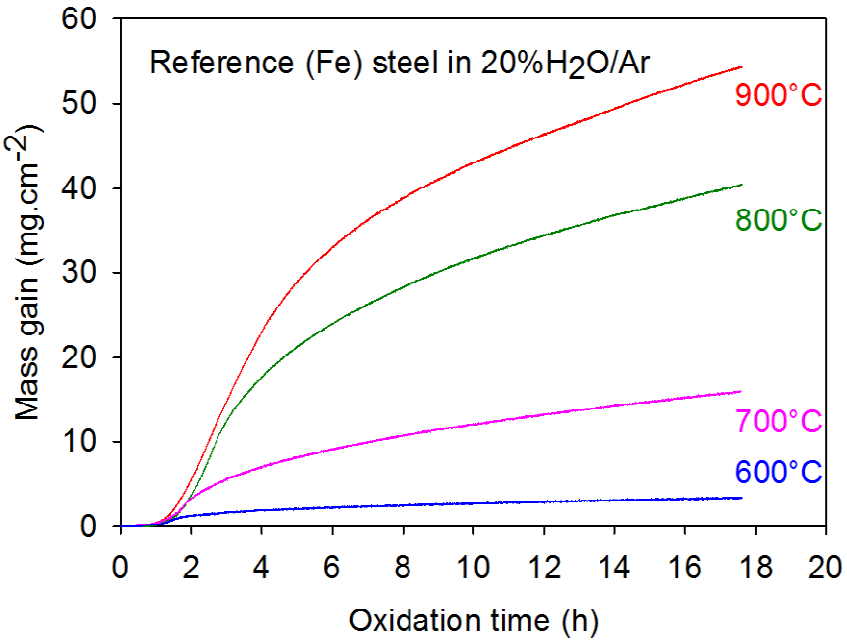

Figure 5.5: Mass gain of the reference (Fe) steel oxidised in 20%H_2O/Ar at different temperatures.

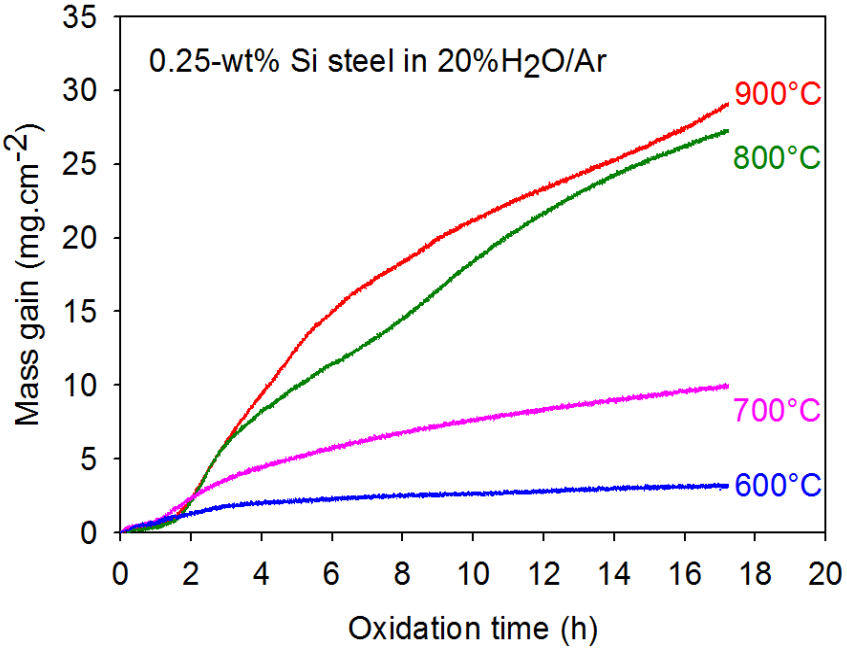

Figure 5.6: Mass gain of the 0.25-wt% Si steel oxidised in 20%H_2O/Ar at different temperatures.

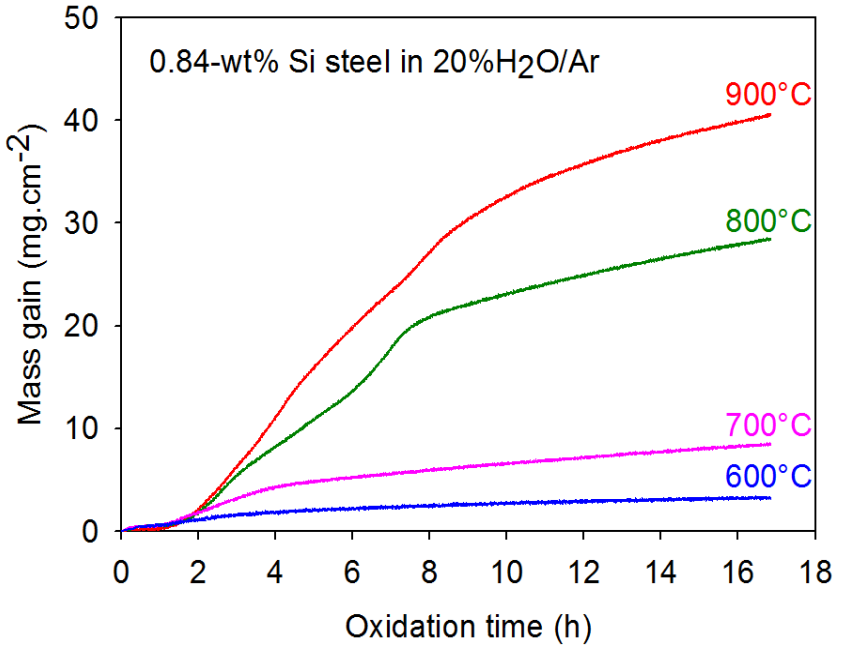

Figure 5.7: Mass gain of the 0.84-wt% Si steel oxidised in 20%H_2O/Ar at different temperatures.

For the oxidation of silicon containing steel, it can be observed that the behaviour of mass gain with the time elapsed are divided in three stages as shown in Fig. 5.8.
1. In the first stage, the oxidation kinetics follows a linear law, indicating the dominant surface reaction in the early period of oxidation.
2. In the second stage, the oxidation rates follows the parabolic rate law. This period might correspond to the one when the protective SiO_2 is formed [Ahtoy (2010)].
3. In the third stage, the oxidation rates also follows the parabolic rate law but with higher parabolic rate constant. It is possible that in this period the protective SiO_2 layer transform to the less protective layer containing wüstite and fayalite [Ahtoy (2010)].

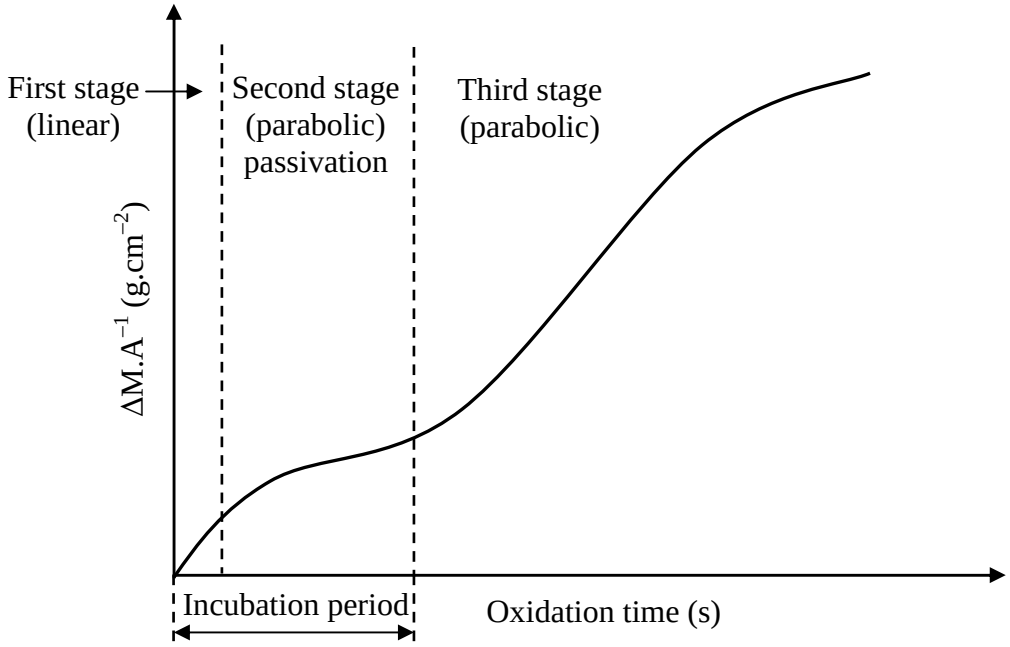

Figure 5.8: Typical curve of oxidation of silicon containing steel.

At the first stage, from a microscopic view of the weight gain-time plot as shown in Figs. 5.1 to 5.3, rate laws seem to be linear. However, when the region where the linear relationship between weight gain and time were zoomed. The large scatter of the raw data was observed as in Fig. 5.9. A linear relationship between weight gain and time can be statistically determined, but with a very low value of R^2 (0.32 for Fig. 5.9). This scatter was also observed for the oxidation results at the other oxidation temperatures. Thus, the linear rate constant (k_l) was not determined in this work.

However, the concept of incubation time which was used in some works, e.g. Fukumoto (2001), might be applied to qualitatively determine the period before the parabolic growth rate in stage 3 commences. It was observed evidently at 900°C as in Fig. 5.10 that when Si content in the steel increased, this incubation time was longer. This indicates the more effective passivity role of silica layer when Si content in the steel increases.

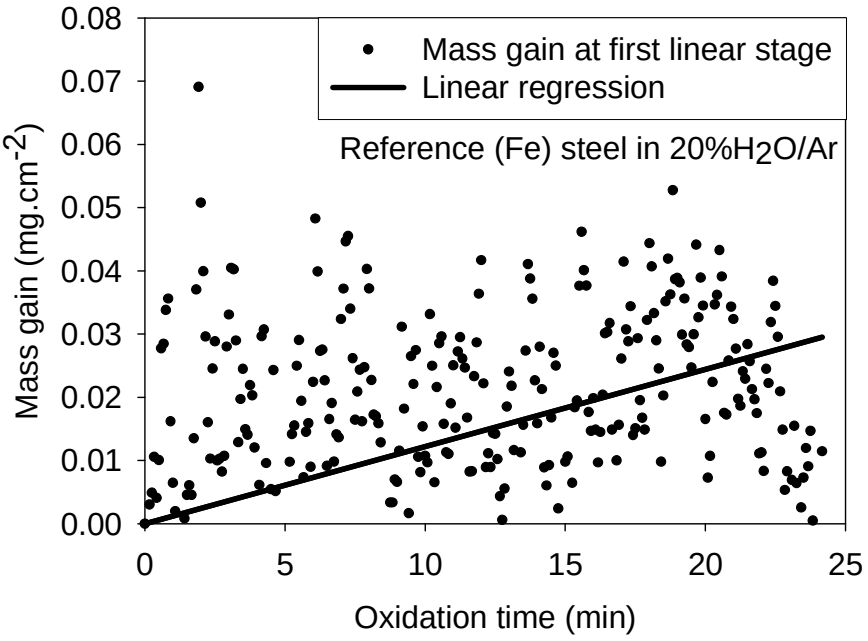

Figure 5.9: Mass gain of the reference (Fe) steel oxidised in 20%H_2O/Ar for 700°C at the first linear stage.

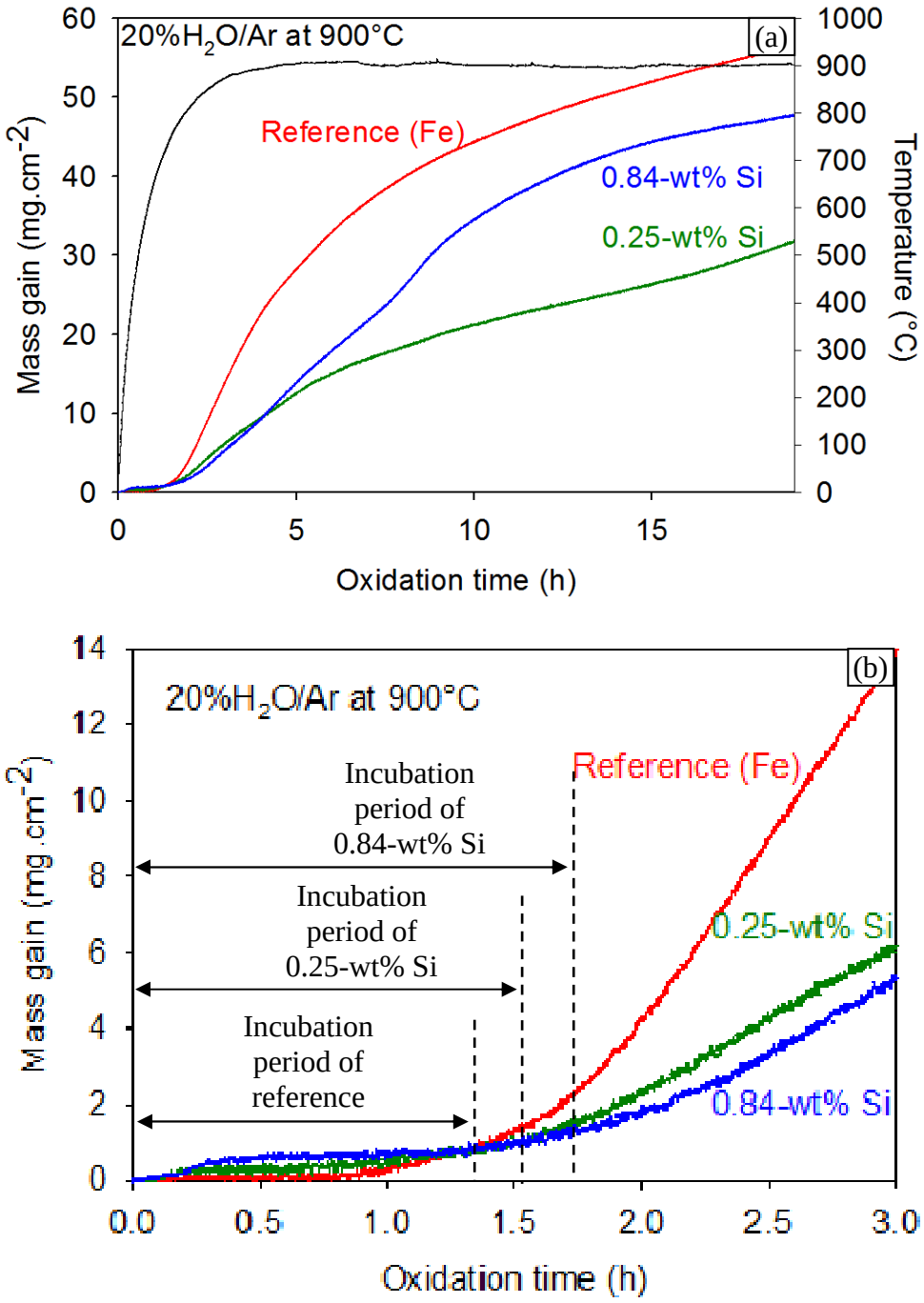

Figure 5.10: Mass gain with oxidation time of the reference (Fe), 0.25-wt% Si and 0.84-wt% Si steels oxidised in 20%H_2O/Ar at 900°C (a), and (b) incubation period magnified from (a).

The calculation of parabolic rate constants (k_p) are determined by following equation $\left(\frac{\Delta m}{A}\right)^2 = k_p \cdot t$. In the k_p determination, the first two stages of oxidation as classified in Fig. 5.8 was eliminated so that the k_p value was determined only from the data when the oxidation was in stage 3. A plot between $\left(\frac{\Delta m}{A}\right)^2$ as the y-axis and t as the x-axis was carried out. The slope of that graph, which corresponds to k_p, was then found out. The Arrhenius

form exhibiting relationship between parabolic rate constant and temperature is shown in Fig. 5.11 with data in Table 5.1.

Table 5.1: Parabolic rate constants (k_p) of different silicon-containing steels oxidised in 20%H_2O/Ar for 16 h at different temperatures.

Temp (°C)	Parabolic rate constants ($g^2.cm^{-4}.s^{-1}$)		
	Reference (Fe)	0.25-wt% Si	0.84-wt% Si
600	$2.00 \times 10^{-10} \pm 0.00$	$9.00 \times 10^{-11} \pm 1.00 \times 10^{-11}$	$1.50 \times 10^{-10} \pm 5.00 \times 10^{-11}$
700	$4.35 \times 10^{-9} \pm 2.50 \times 10^{-10}$	$1.50 \times 10^{-9} \pm 1.00 \times 10^{-10}$	$1.00 \times 10^{-9} \pm 1.00 \times 10^{-10}$
800	$2.35 \times 10^{-8} \pm 1.20 \times 10^{-9}$	$1.40 \times 10^{-8} \pm 4.15 \times 10^{-9}$	$9.30 \times 10^{-9} \pm 2.90 \times 10^{-9}$
900	$4.31 \times 10^{-8} \pm 5.50 \times 10^{-10}$	$1.18 \times 10^{-8} \pm 1.35 \times 10^{-9}$	$3.89 \times 10^{-8} \pm 1.03 \times 10^{-8}$

The activation energy can be calculated from Fig. 5.11. Information obtained from this figure is presented in Table 5.2. The parabolic rate constants of those steels are as follows.

For reference (Fe) steel $$k_p(g^2.cm^{-4}.s^{-1}) = 7.16\exp\left(\frac{-155064}{RT}\right) \quad (5-1)$$

For 0.25-wt% Si steel $$k_p(g^2.cm^{-4}.s^{-1}) = 7.61\exp\left(\frac{-147406}{RT}\right) \quad (5-2)$$

For 0.84-wt% Si steel $$k_p(g^2.cm^{-4}.s^{-1}) = 7.42\exp\left(\frac{-160807}{RT}\right) \quad (5-3)$$

where R is a gas constant (8.314 $J.mol^{-1}.K^{-1}$). Apparent activation energies of the reference (Fe), 0.25-wt% Si and 0.84-wt% Si steels were 155, 147, and 161 $kJ.mol^{-1}$ respectively.

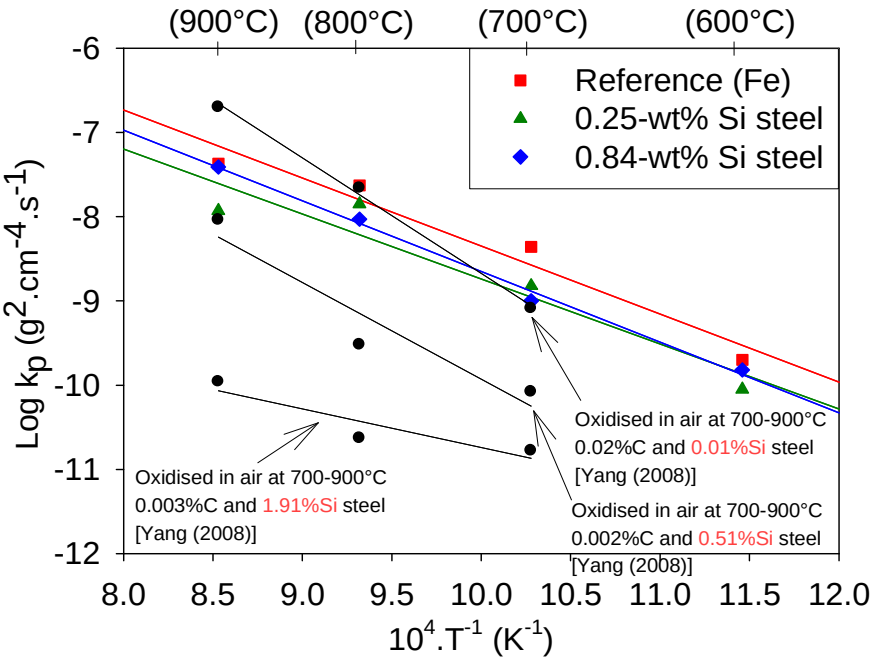

Figure 5.11: Parabolic rate constants (k_p) of different silicon-containing steels oxidised in 20%H_2O/Ar for 16 h at different temperatures.

Table 5.2: Various parameters data received from Fig. 5.11 of different silicon-containing steels oxidised in 20%H_2O/Ar for 16 h.

Parameters	Steel		
	Reference (Fe)	0.25-wt% Si	0.84-wt% Si
Slope, m	– 0.81	– 0.77	– 0.84
Proportionality constant, k_o ($g^2.cm^{-4}.s^{-1}$)	– 7.16	– 7.61	– 7.42
Apparent activation energy, E_a ($kJ.mol^{-1}$)	155	147	161

From the Arrhenius plot in Fig. 5.11, it was observed that the activation energies of all steels are identical. Comparing to literature on air oxidation of silicon-containing steel [Yang (2008)], it was reported increasing silicon content gave oxidation rate lower. Oxidation rate of steel with 0.51wt% Si oxidised in air [Yang (2008)] is higher than that of steel with 0.84wt% Si oxidised in water vapour observed in the present work. It might then be noted that oxidation rate seems to be higher when the silicon-containing steel is oxidised in water vapour comparing to dry air.

5.1.2 Derivative of mass gain as a function of time

Oxidation rate of steel can be plotted as the derivative of the oxidation rate in function of oxidation time. From the initial period up to the one corresponding to the first inflexion point, the rate of mass change is decreased when the oxidation time elapsed. This first stage indicates passivity behaviour of the oxide scale on the studied steel. After the first inflexion point, oxidation rate increased with the period of oxidation. This second stage might be due to passivity breakdown or transformation of the passive layer to the one which is less protective.

In the third stage after the second inflexion point, oxidation rate increased with time. This might be due to oxide scale growth obeying the parabolic rate law. Those sentences are presented in Fig. 5.12.

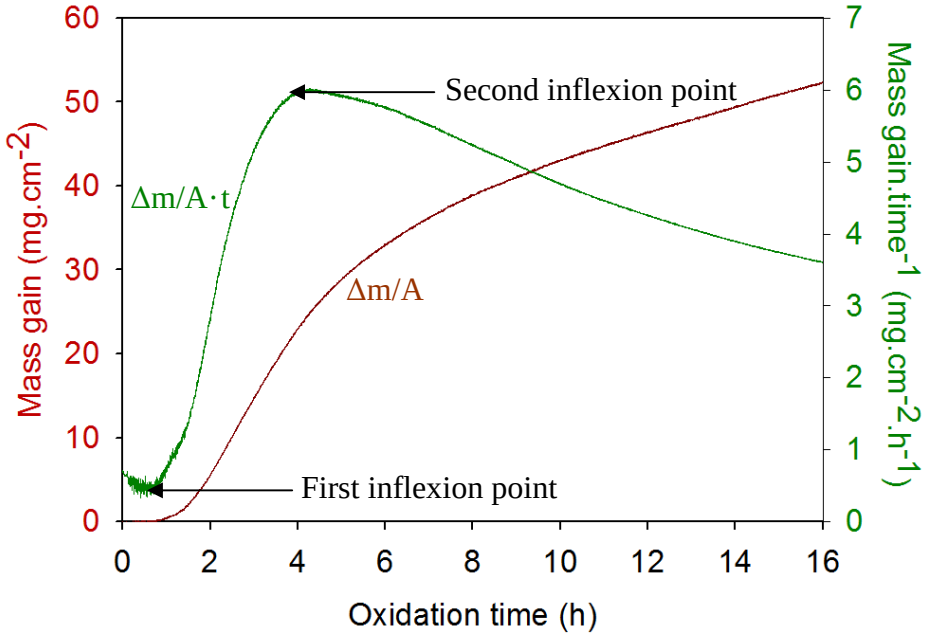

Figure 5.12: Derivative of mass gain in function of the oxidation time of the reference steel oxidised in 20%H_2O/Ar at 900°C.

At 900°C, passivity duration was calculated from Fig. 5.13 and plotted in Fig. 5.14 with data in Table 5.3. From these results, it is seen that the passivity and passivity breakdown durations are longer when silicon in steel increased.

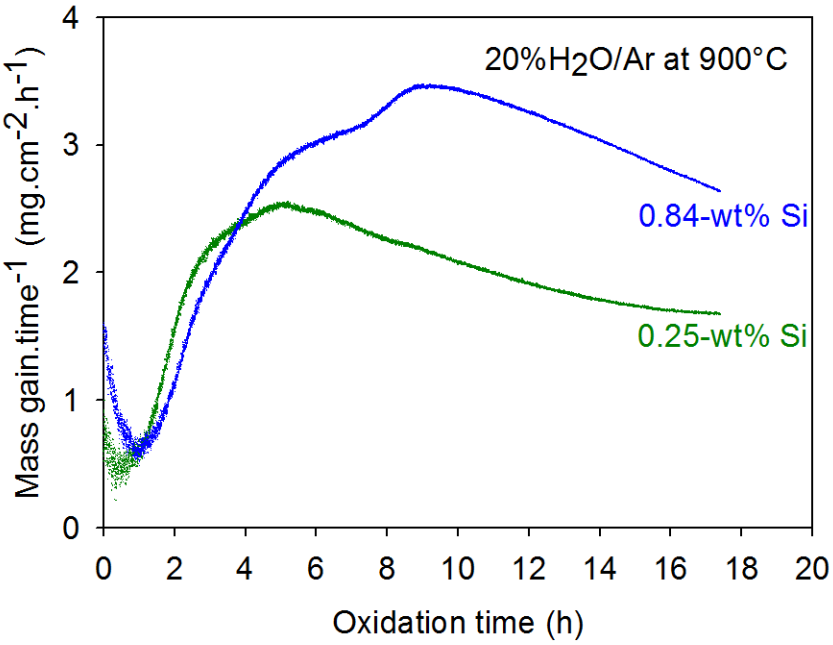

Figure 5.13: Derivative of mass gain in function of the oxidation time of silicon-containing steels oxidised in 20%H_2O/Ar at 900°C.

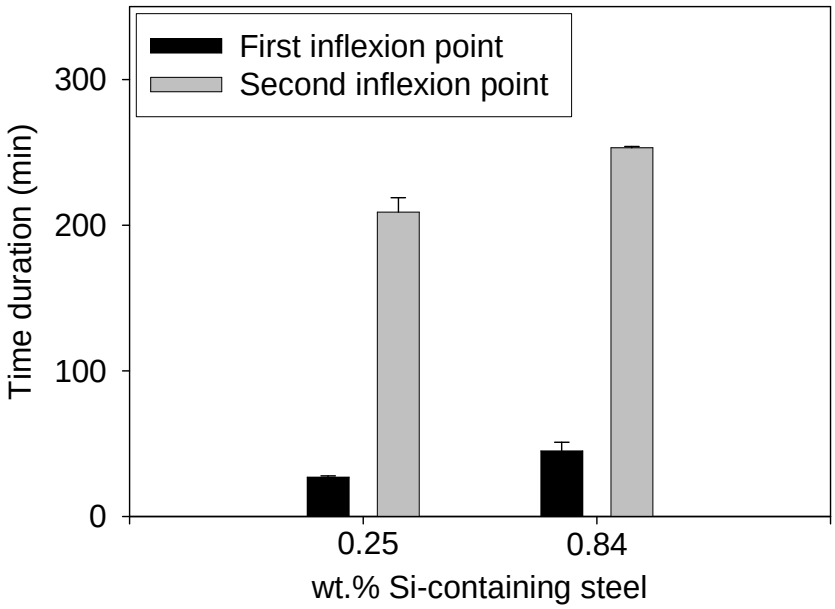

Figure 5.14: The first and second inflexion points of different silicon-containing steels oxidised in 20%H_2O/Ar at 900°C.

Table 5.3: Durations of the first and second inflexion points of different silicon-containing steels oxidised in 20%H_2O/Ar at 900°C.

Inflexion point	Steel	
	0.25-wt% Si	0.84-wt% Si
First	27 min ± 1 min	45 min ± 6 min
Second	3 h 29 min ± 10 min	4 h 13 min ± 1 min

To discuss the passivity and passivity breakdown behaviour of the studied steels, scale formation during those periods was investigated. From Raman spectroscopy, peaks of Fe_2O_3, Fe_3O_4 and SiO_2 were observed during passivity duration (Fig. 5.15). It is then possible that silicon oxide exists at the internal interface. Wüstite which is a metal-deficit oxide is not formed. This indicates that slow diffusion of iron through silica reduces iron activity, making the formation of FeO impossible under magnetite. This confirms the effective role of silica as a passive layer. Furthermore, from Raman spectroscopy in Fig. 5.16, peaks of Fe_2O_3, Fe_3O_4, SiO_2 and Fe_2SiO_4 were observed during passivity breakdown. It is then possible that silica which grows with time turns to be less passive, resulting in the formation of fayalite (Fe_2SiO_4 or ($2FeO + SiO_2$)) which could be from FeO and SiO_2.

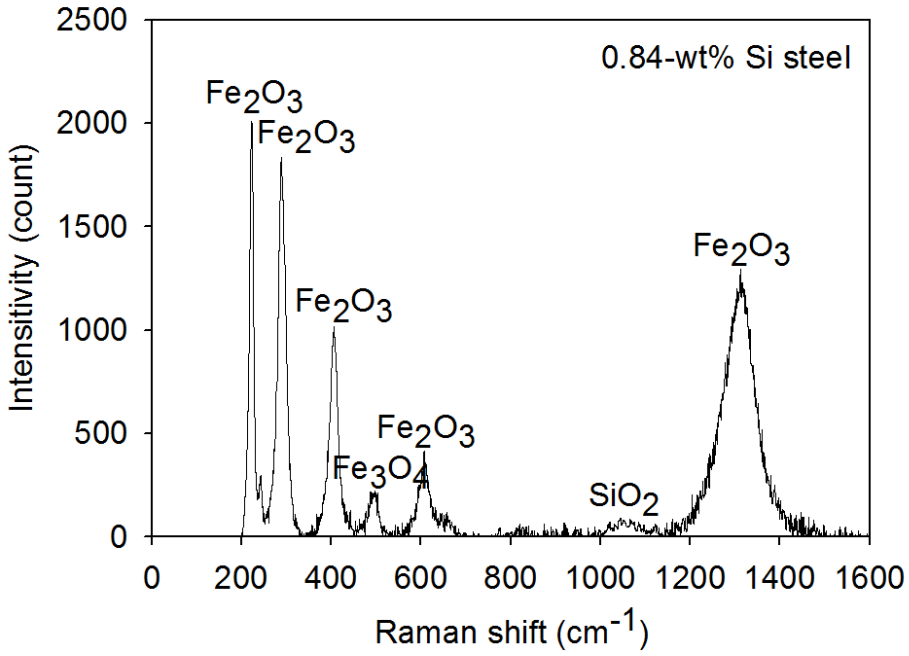

Figure 5.15: Raman spectrum at the first inflexion point of 0.84-wt% Si steel oxidised in 20%H_2O/Ar at 900°C for 29 min.

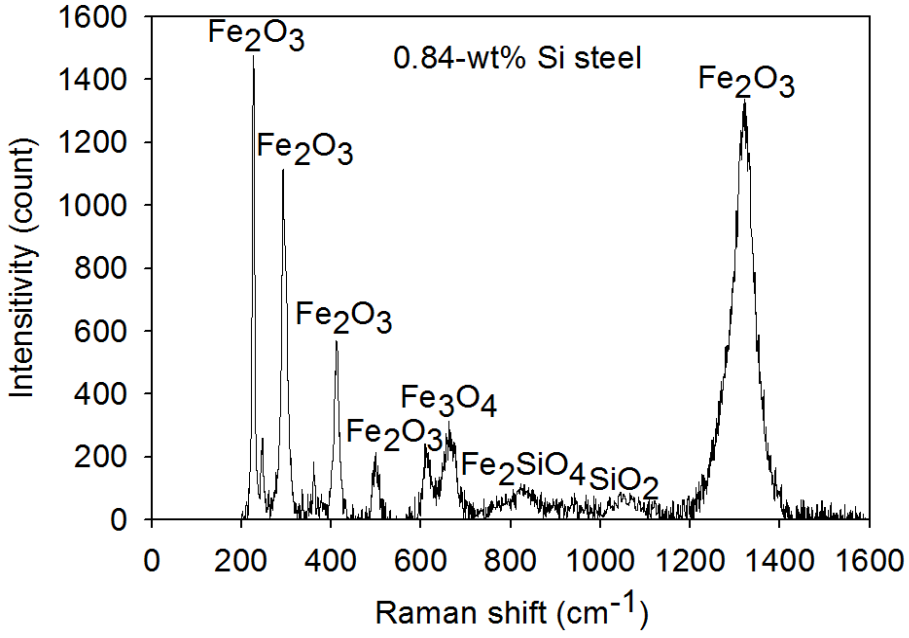

Figure 5.16: Raman spectrum at the second inflexion point of 0.84-wt% Si steel oxidised in 20%H_2O/Ar at 900°C for 5 h.

5.2 Characterisation of oxide scale

The steels with Si contents of 0.25 and 0.84-wt% were studied and Fe substantially without silicon as a reference steel was also studied for comparison. Cross-sections of oxide scales were examined using scanning electron microscopy (SEM). Compositions and phases of oxidation products were qualitatively determined by energy-dispersive X-ray (EDS), X-ray diffraction analysis (XRD) and Raman spectroscopy.

5.2.1 Reference steel

Fig. 5.17 depicts the SEM images of the oxide scale on the reference steel oxidised at 900°C for 16 h. The XRD pattern indicates the existence of iron, hematite and magnetite (Fig. 5.18). From these results and literature [Chen (2000)], it is possible that hematite exists as the thin outermost layer. The main layer is wüstite with magnetite precipitates. And magnetite might exist at the internal interface. In the FeO layer, a dark spot might be voids as compared with literature [Ahtoy (2010)].

Raman spectroscopy indicates the existence of hematite and magnetite at the outer most layer (layer A) (Fig. 5.19). Wüstite and magnetite were observed as an intermediate layer. This should be the layer of wüstite with magnetite precipitates (layer B) (Fig. 5.20). A higher peak of magnetite and lower peak of wüstite were observed on scale at steel-scale interface (layer C) (Fig. 5.21), indicating the existence of the magnetite seam at the internal interface. It should be noted that diameter of layer Raman is 80 µm. Thus, the peak of wüstite in Fig. 5.21 might be from layer B.

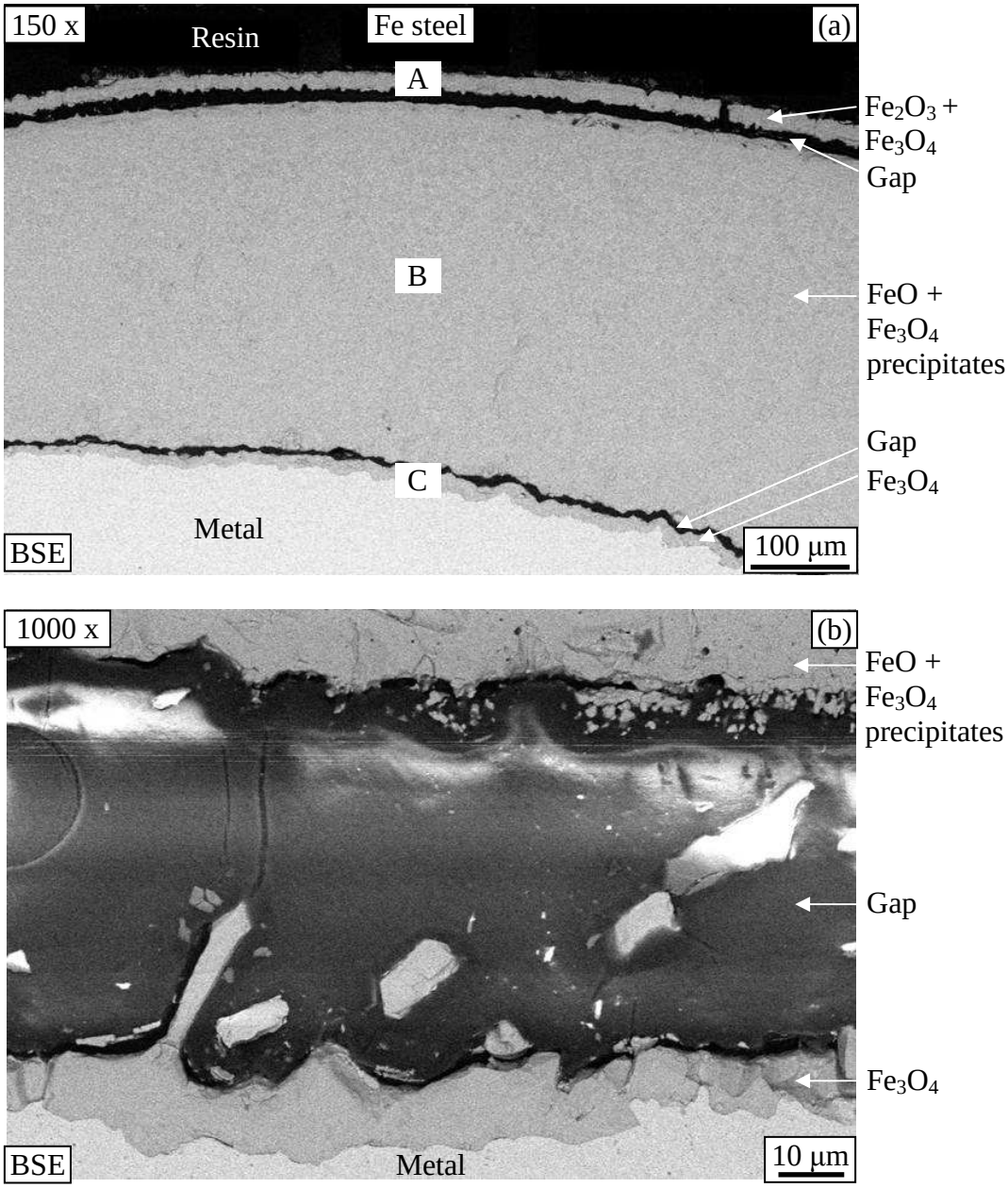

Figure 5.17: Cross-section of scale on the reference steel oxidised in 20%H_2O/Ar at 900°C for 16 h showing (a) oxide scale, and (b) the interface magnified from (a).

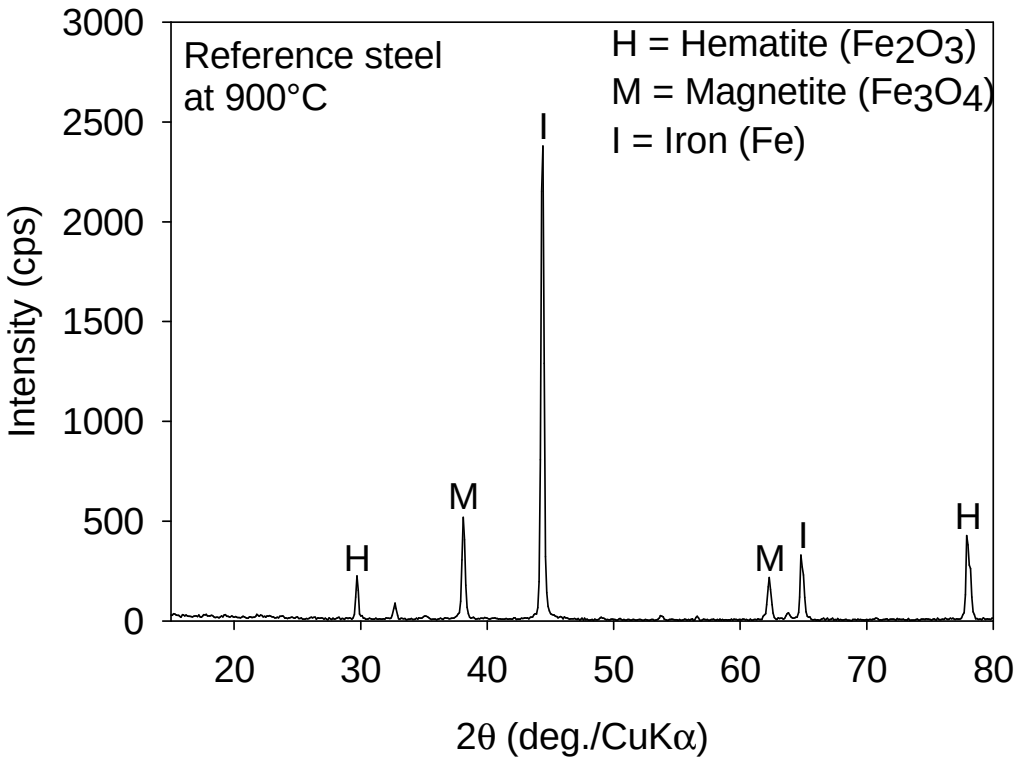

Figure 5.18: XRD pattern on oxide scale of the reference steel oxidised in 20%H_2O/Ar at 900°C for 16 h.

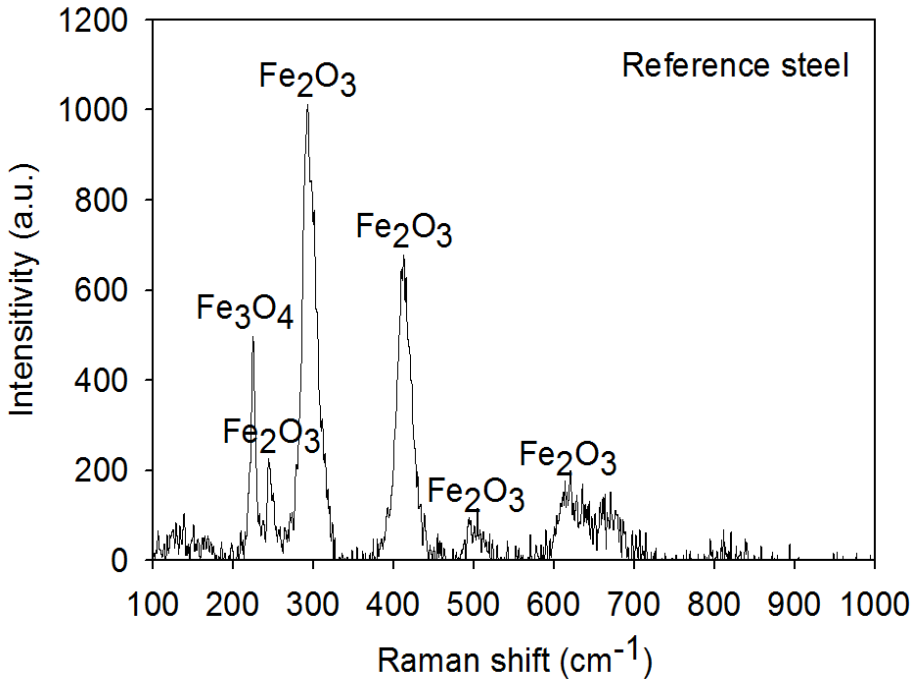

Figure 5.19: Raman peak on oxide scale observed on A in the Fig. 5.17 (a) of reference steel oxidised in 20%H_2O/Ar at 900°C for 16 h.

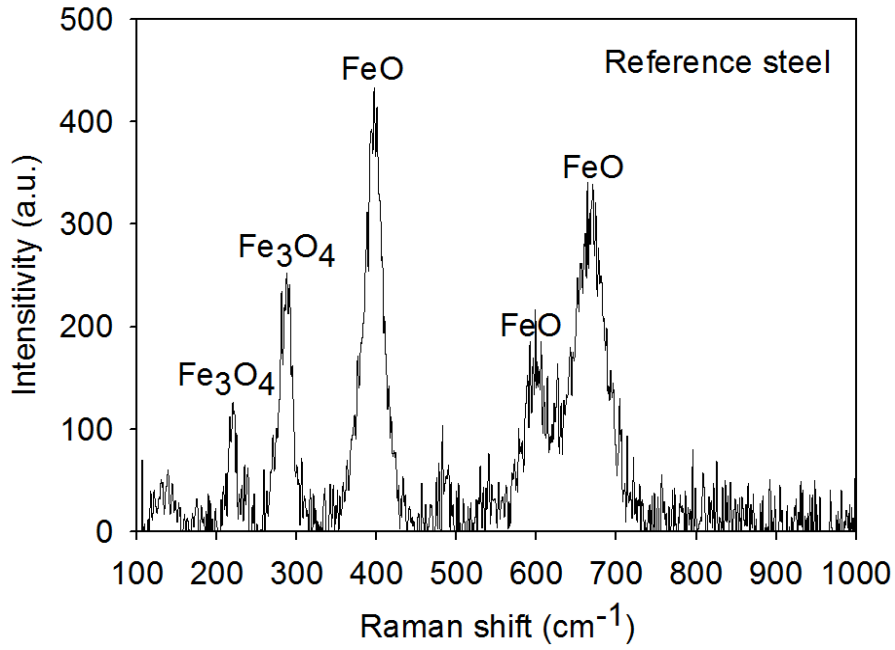

Figure 5.20: Raman peak on oxide scale observed on B in the Fig. 5.17 (a) of reference steel oxidised in 20%H_2O/Ar at 900°C for 16 h.

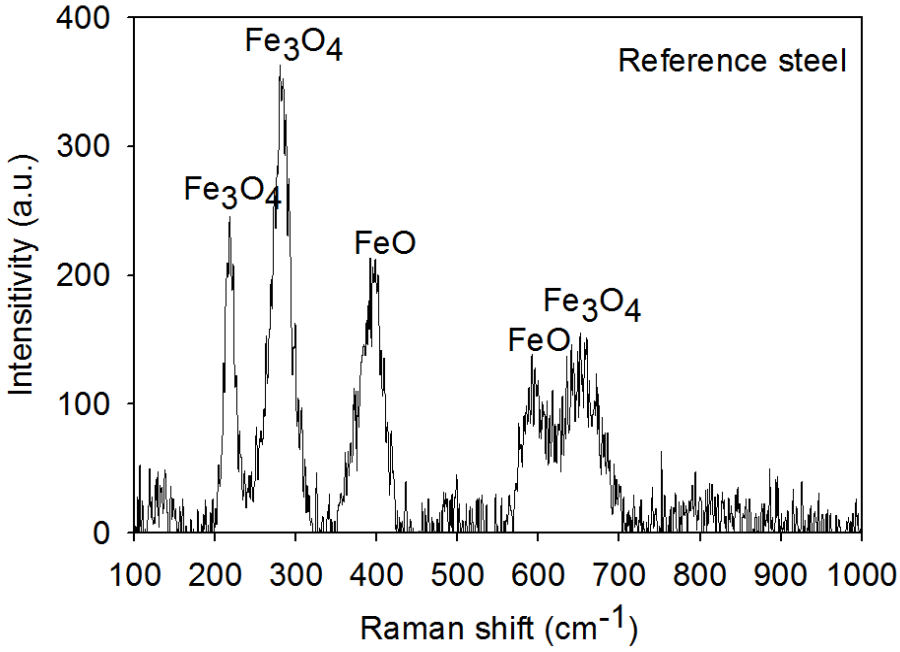

Figure 5.21: Raman peak on oxide scale observed on C in the Fig. 5.17 (a) of reference steel oxidised in 20%H_2O/Ar at 900°C for 16 h.

5.2.2 0.25-wt% Si steel

Fig. 5.22 depicts the SEM images of the oxide scale on the 0.25-wt% Si steel oxidised at 900°C for 16 h. From EDS in Figs. 5.23 and 5.24, the peaks of iron and oxygen were observed. A strong peak of carbon and slight peak of silicon were also found. XRD pattern indicates the existence of iron, hematite, and magnetite (Fig. 5.25). From these results and literature [Chen (2000)], it is possible that hematite and magnetite exists as the outermost layer.

From Raman spectroscopy, its pattern indicates the existence of wüstite and magnetite on layer B (Fig. 5.26). From this result and literature [Chen (2000)], it is possible that this layer is wüstite with magnetite precipitates. Wüstite, magnetite and fayalite were observed on scale near internal interface (layer C) (Fig. 5.27). It is possible that this layer is the mixture of wüstite and fayalite, which were reported in some works on oxidation of silicon-containing steel in water-vapour atmosphere [Fukumoto (2001) and Nakata (2011)].

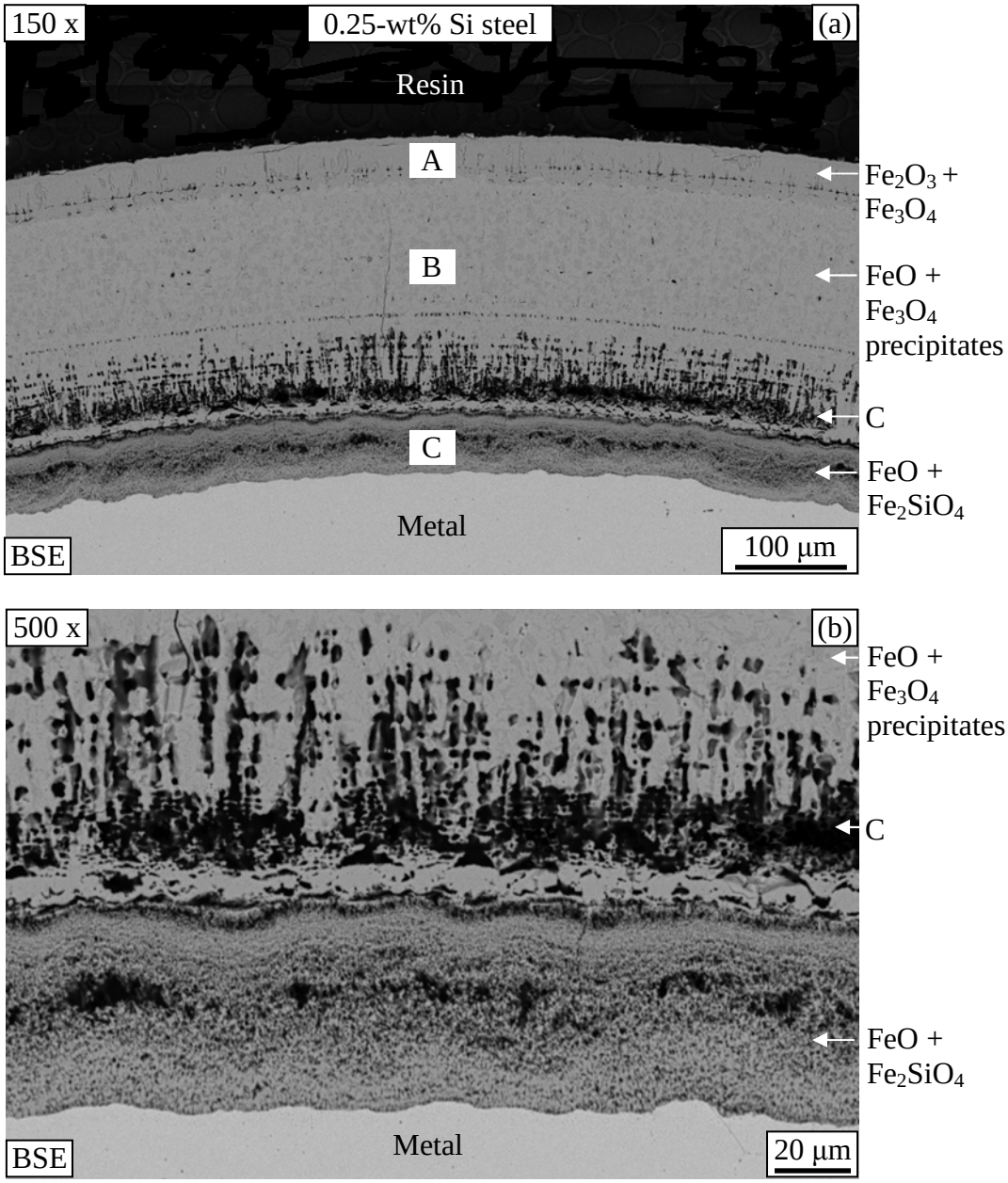

Figure 5.22: Cross-section of scale on the 0.25-wt% Si steel oxidised in 20%H_2O/Ar at 900°C for 16 h showing (a) oxide scale, and (b) the interface magnified from (a).

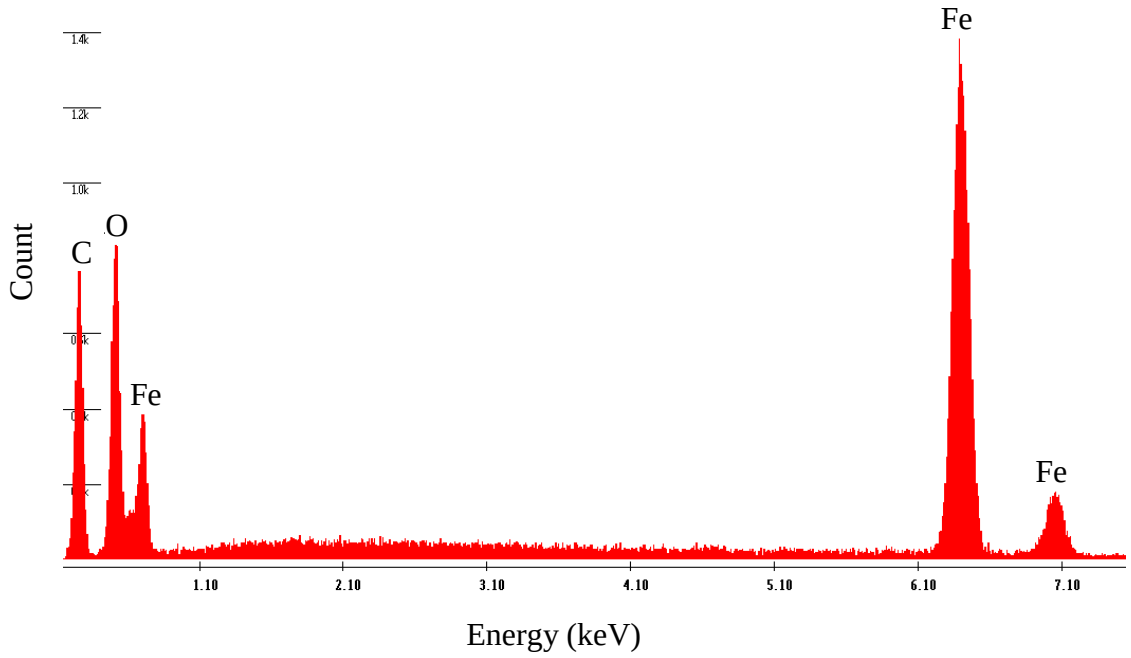

Figure 5.23: EDS pattern on oxide scale observed on B in the Fig. 5.22 (a).

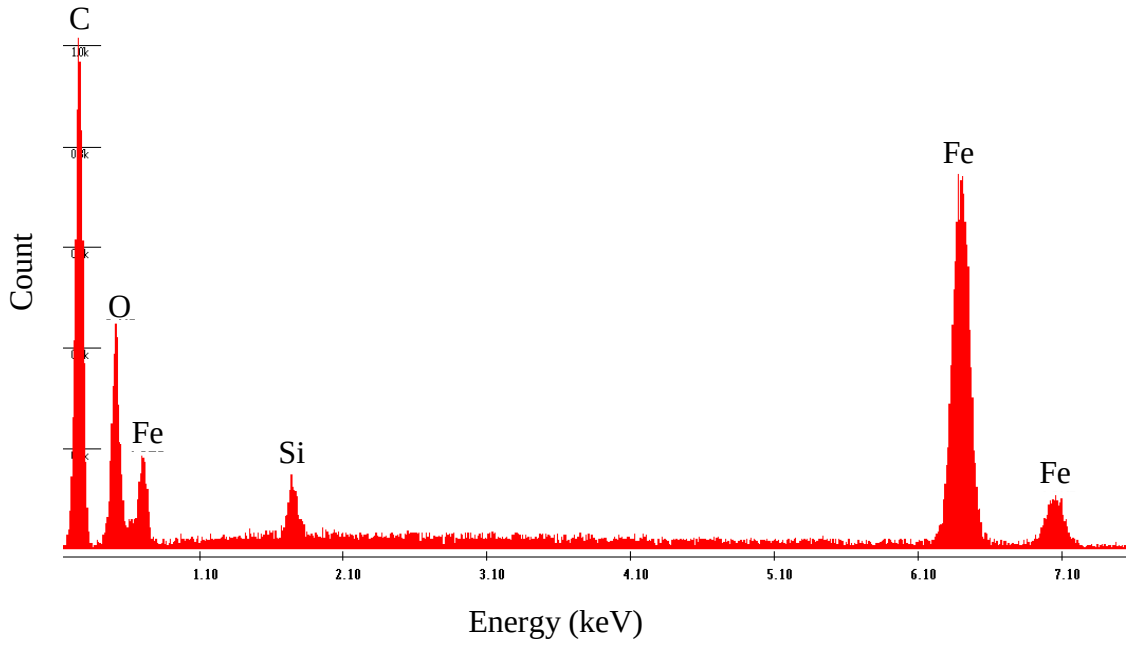

Figure 5.24: EDS pattern on oxide scale observed on C in the Fig. 5.22 (a).

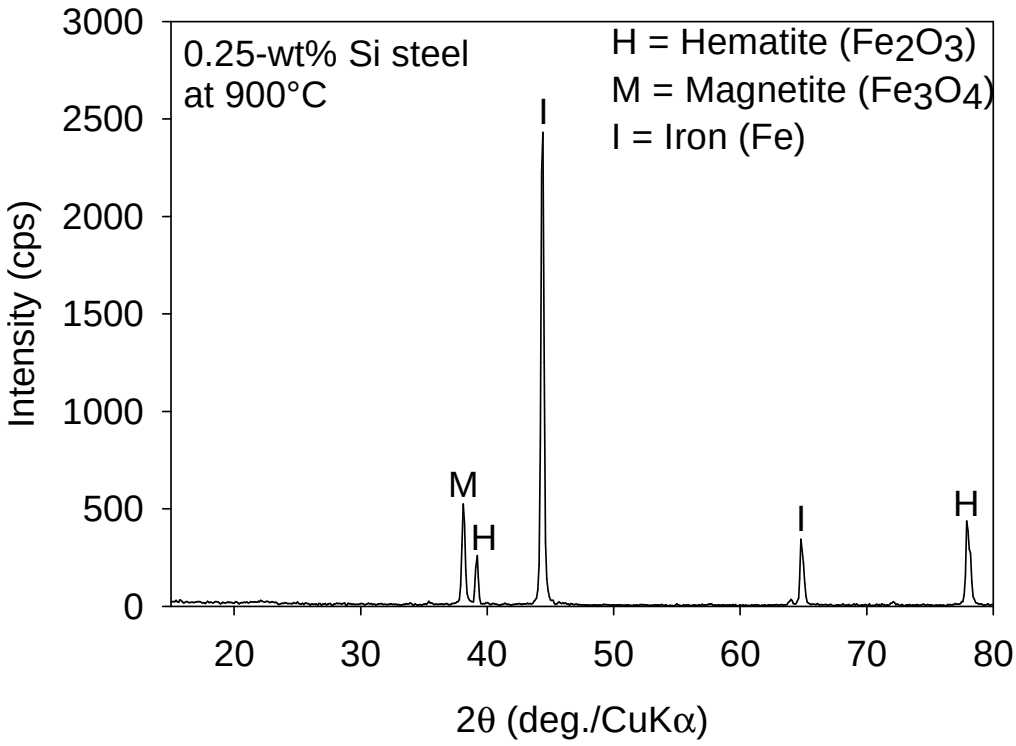

Figure 5.25: XRD pattern on oxide scale of the 0.25-wt% Si steel oxidised in 20%H_2O/Ar at 900°C for 16 h.

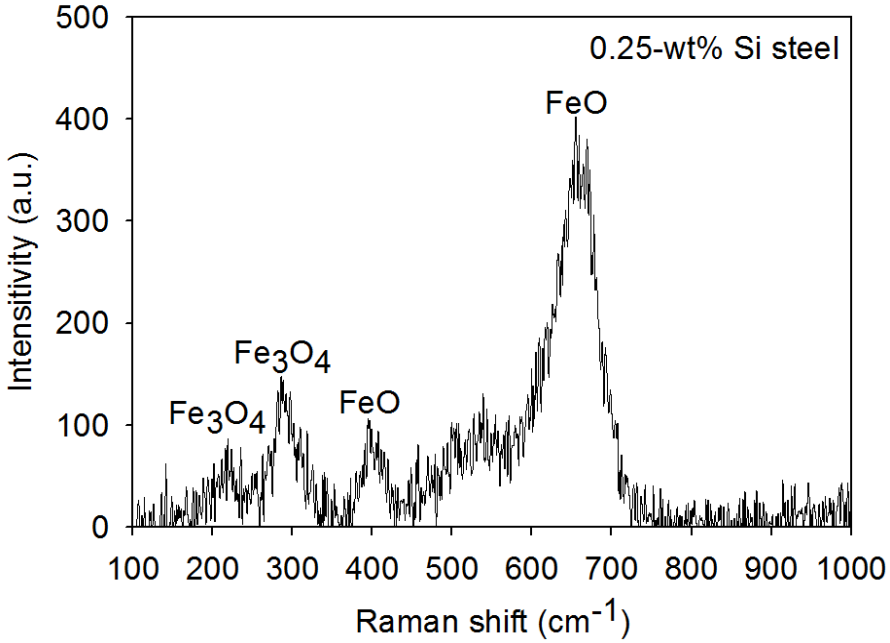

Figure 5.26: Raman peak on oxide scale observed on B in the Fig. 5.22 (a) of 0.25-wt% Si steel oxidised in 20%H_2O/Ar at 900°C for 16 h.

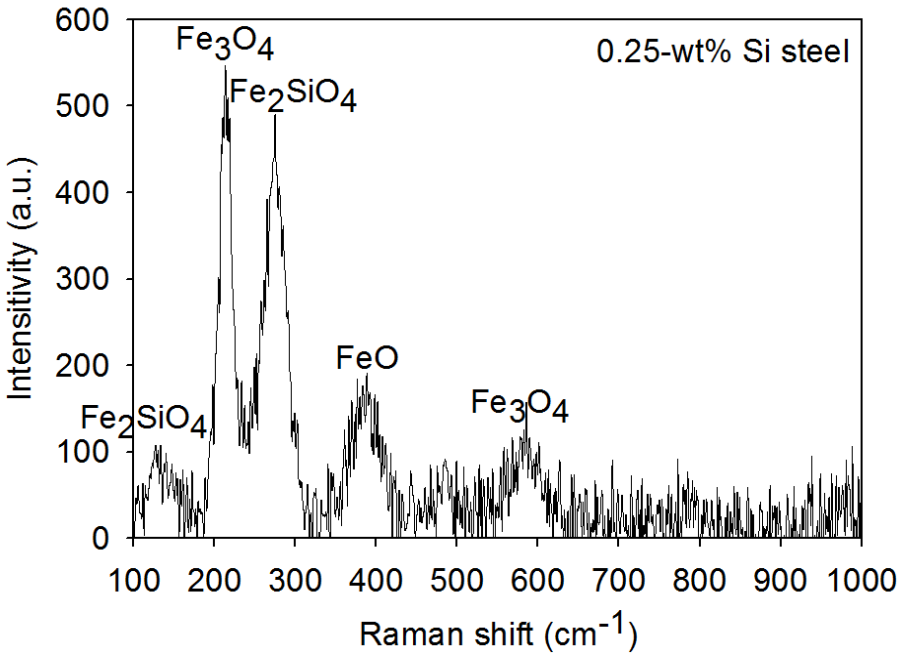

Figure 5.27: Raman peak on oxide scale observed on C in the Fig. 5.22 (a) of 0.25-wt% Si steel oxidised in 20%H_2O/Ar at 900°C for 16 h.

5.2.3 0.84-wt% Si steel

Fig. 5.28 depicts the SEM images of the oxide scale on the 0.84-wt% Si steel oxidised at 900°C for 16 h. From EDS in Figs. 5.29 and 5.30, the peaks of iron and oxygen were observed on layer A and layer B, indicating that the oxide in this area is a type of oxide of iron. EDS pattern observed on scale near steel-scale interface and internal interface is shown in Figs. 5.31 and 5.32 respectively. Peaks of O, Fe and Si were observed. Oxide containing silicon, possibly fayalite, might exist at its area. XRD pattern indicates the existence of iron, hematite, and magnetite (Fig. 5.33). It is possible that hematite and magnetite existed at the outermost layer.

From Raman spectroscopy, the pattern indicates the existence of hematite and magnetite on layer A (Fig. 5.34). At layer B, Raman peak exhibits wüstite and magnetite (Fig. 5.35). It is possible that this layer is a wüstite with magnetite precipitates. Wüstite, magnetite and fayalite were observed on layer C (Fig. 5.36). At the internal interface, fayalite was observed as in the part of the layer C and as internal precipitates in steel.

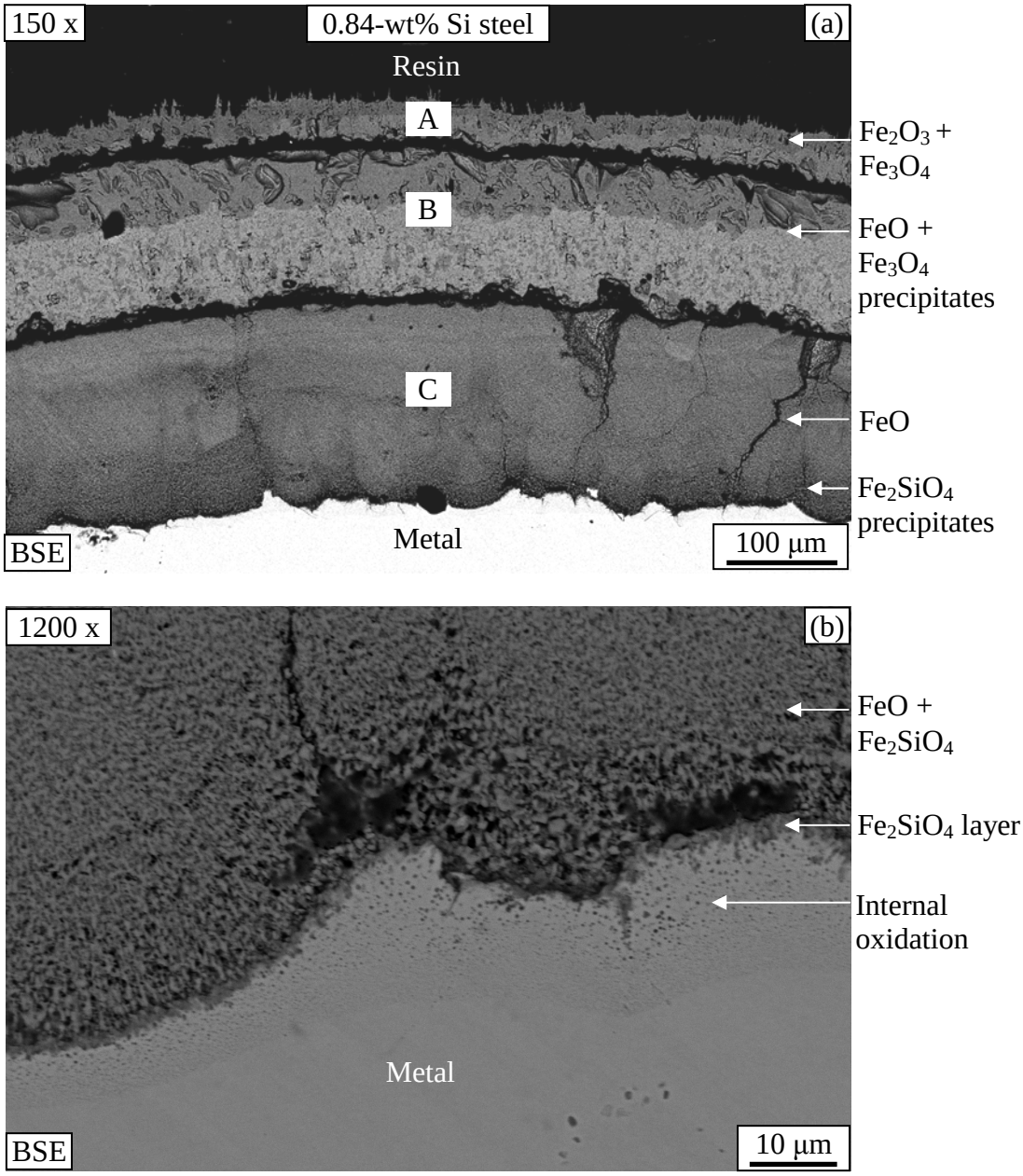

Figure 5.28: Cross-section of scale on the 0.84-wt% Si steel oxidised in 20%H_2O/Ar at 900°C for 16 h showing (a) oxide scale, and (b) the interface magnified from (a).

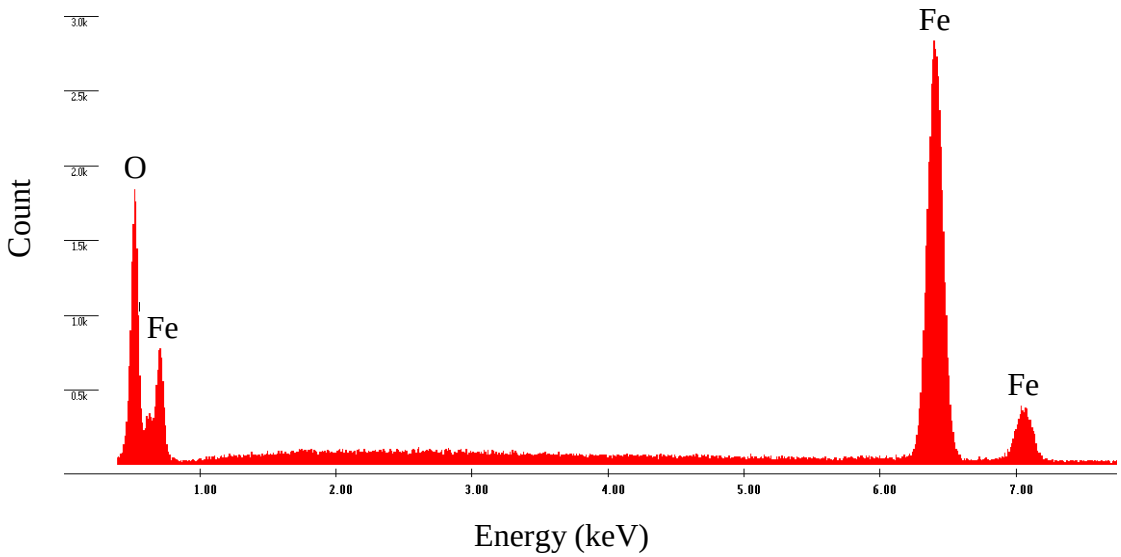

Figure 5.29: EDS pattern on oxide scale observed on A the Fig. 5.28 (a).

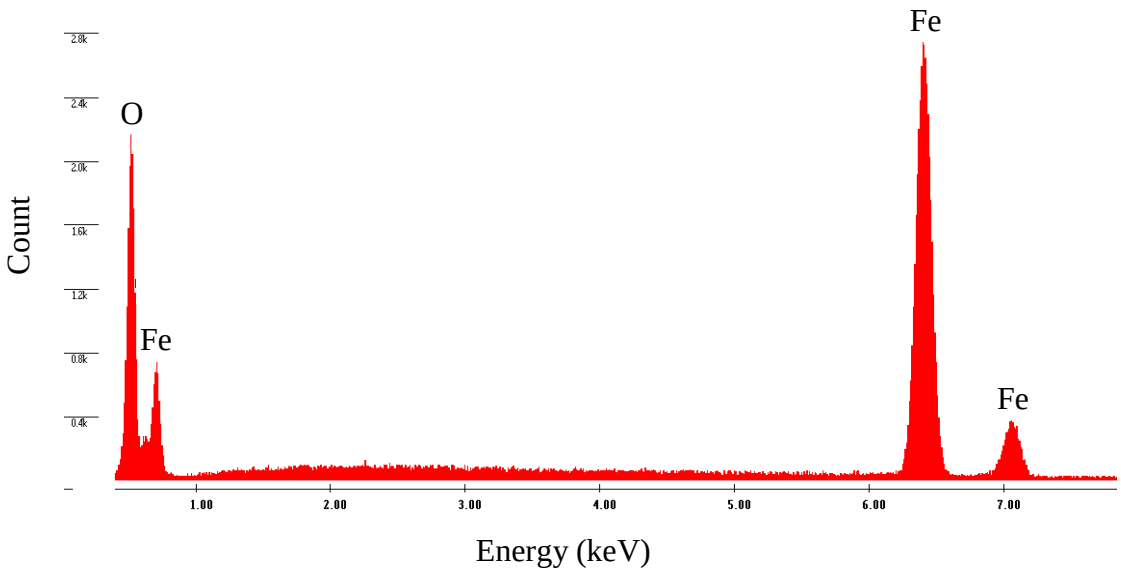

Figure 5.30: EDS pattern on oxide scale observed on B in the Fig. 5.28 (a).

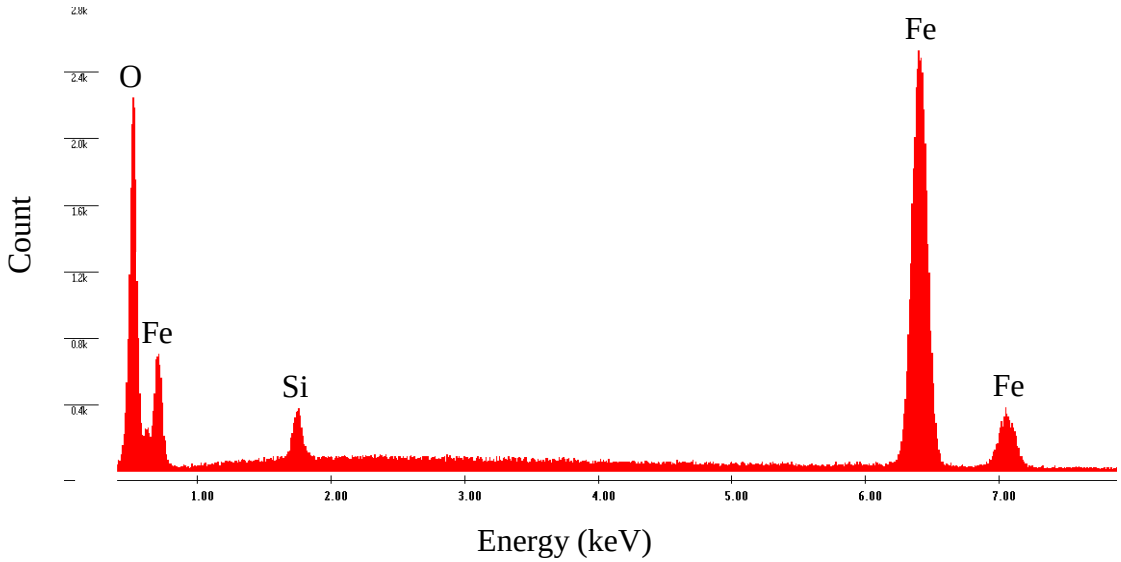

Figure 5.31: EDS pattern on oxide scale observed on scale near steel-scale interface in the Fig. 5.28 (b).

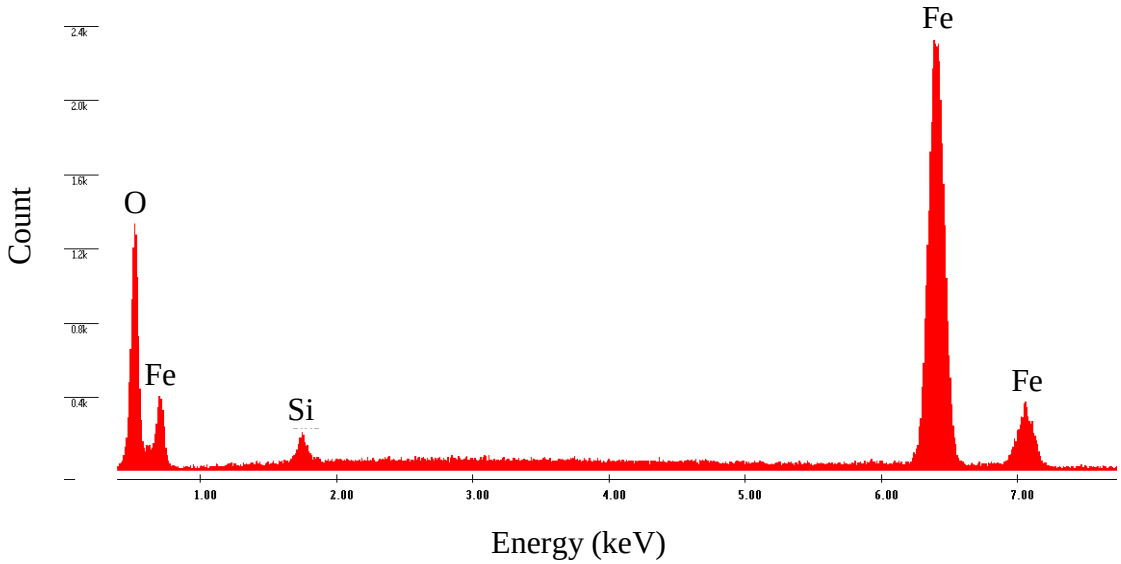

Figure 5.32: EDS pattern at the internal oxidation area in Fig. 5.28 (b).

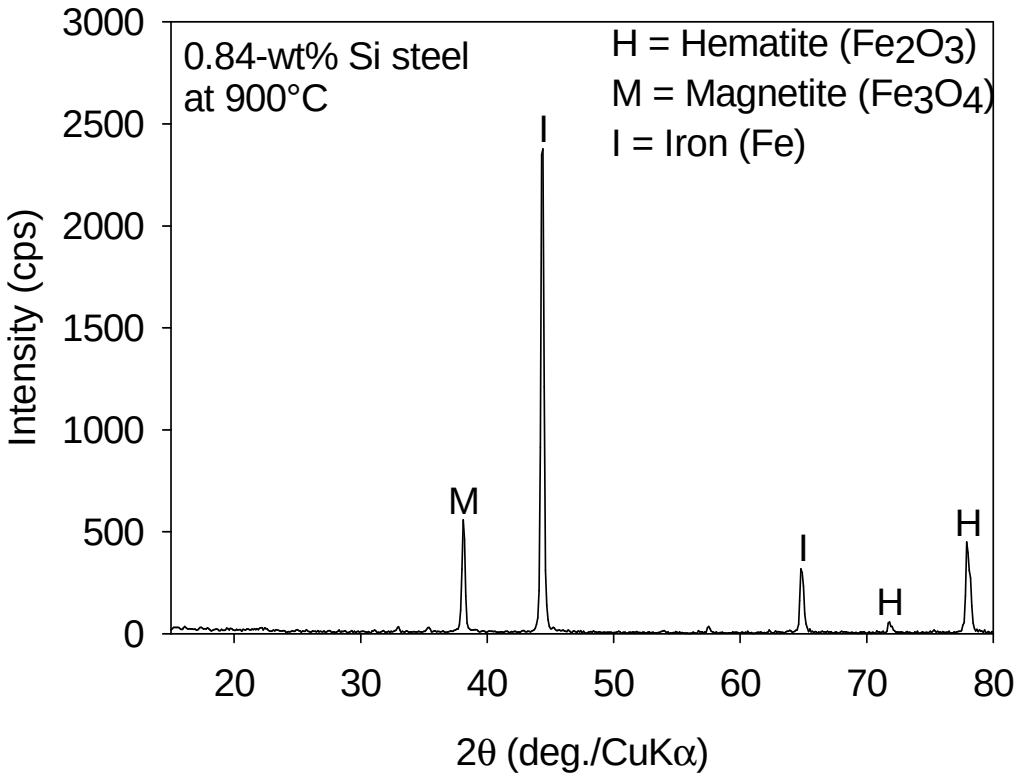

Figure 5.33: XRD pattern on oxide scale of the 0.84-wt% Si steel oxidised in 20%H_2O/Ar at 900°C for 16 h.

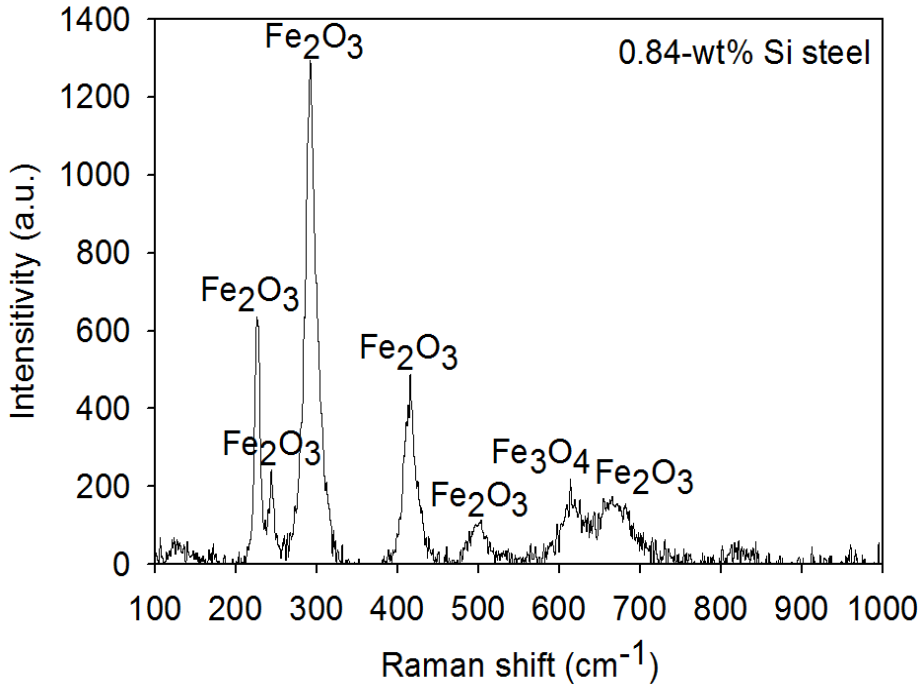

Figure 5.34: Raman peak on oxide scale observed on A in the Fig. 5.28 (a) of 0.84-wt% Si steel oxidised in 20%H_2O/Ar at 900°C for 16 h.

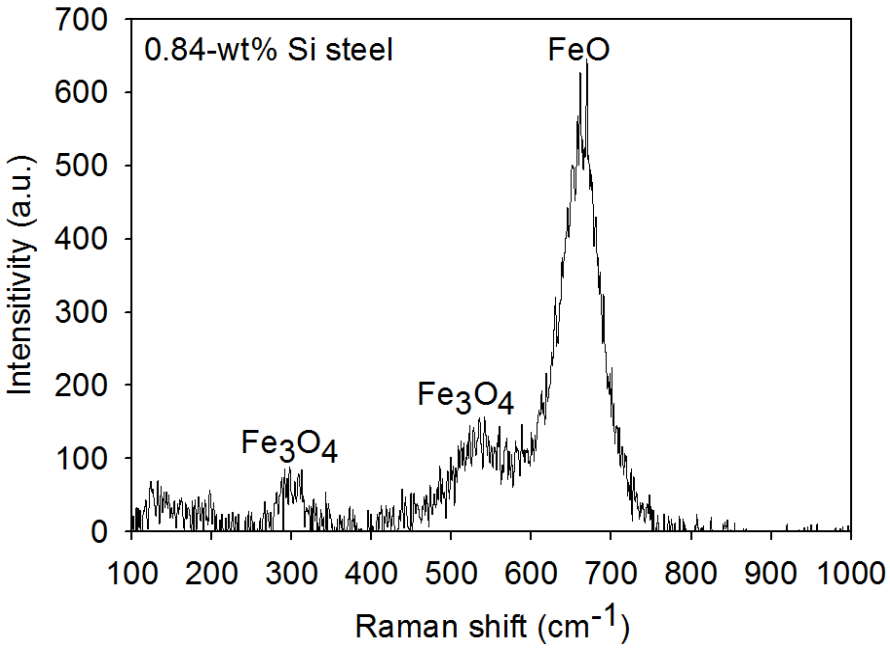

Figure 5.35: Raman peak on oxide scale observed on B in the Fig. 5.28 (a) of 0.84-wt% Si steel oxidised in 20%H_2O/Ar at 900°C for 16 h.

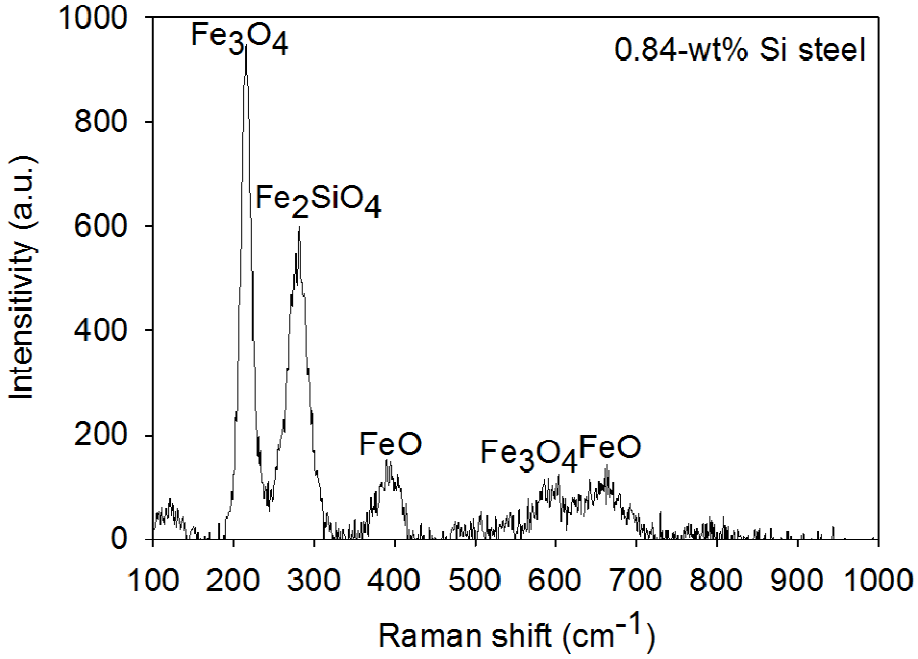

Figure 5.36: Raman peak on oxide scale observed on C in the Fig. 5.28 (a) of 0.84-wt% Si steel oxidised in 20%H_2O/Ar at 900°C for 16 h.

5.3 Comparison of oxide scales on steels with different contents of silicon

By comparing the steels containing different contents as silicon, it can be seen that increasing silicon content in steel tends to result in lower oxidation kinetics and scale thickness. These are in agreement with the widely known results on air oxidation of silicon-containing steel or iron [Taniguchi (2001), Suárez (2010), Nishimoto (2011)]. The more interesting results might then be evolution of sublayer of oxide scale on steel different in silicon contents as shown in Figs. 5.37 and 5.38.

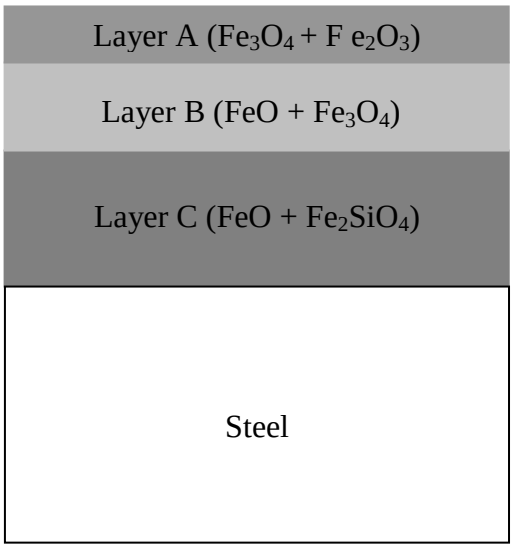

Figure 5.37: Illustration of the formation of the oxide layer.

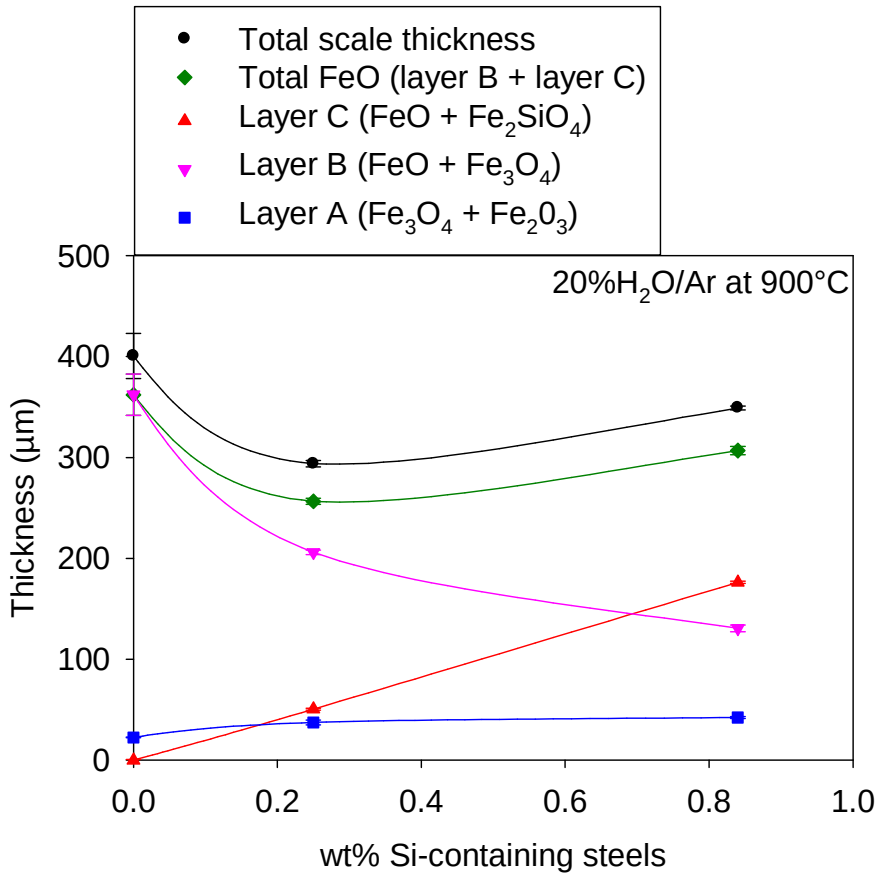

Figure 5.38: Thickness ratio of FeO and Fe_3O_4 as a function of silicon-containing steels oxidised in 20%H_2O/Ar at 900°C for 16 h.

From the figure, it can be seen that the layer A (hematite and magnetite) which is the outer part of scale is thicker when silicon content increased. The layer B which is wüstite containing magnetite precipitates is the major phase for the case of reference steel. This layer tends to be thinner when silicon in steel increases. In case of layer C which is the mixture of wüstite and fayalite, it tends to grow thicker with the increase of silicon content in steel.

As for layer C, the existence of this layer formed in oxidation in water-vapour-containing atmosphere has been reported in some literatures [Fukumoto (2001), Nakata (2011)], but the present work might be the first to show its evolution in function of silicon content in steel. It was reported [Fukumoto (2001)] that this layer on Fe-1.5Si is firstly formed in the form of Si-rich oxide. Based on our Raman result in Fig. 5.15, this layer in our work is SiO_2. After longer oxidation, it was reported [Fukumoto (2001)] that such Si-rich oxide transforms to be the mixture of wüstite and fayalite. Formation of this mixture was also found in scale on silicon-containing steel oxidised in air [Tanigushi (2001), Ahtoy (2010)]. It was reported that this biphasic layer is evolved from the silica which turns to be more porous after longer period of oxidation [Ahtoy (2010)]. From the marker experiment, it was found that the marker was placed between external oxide and the mixture of wüstite and fayalite after longer period of oxidation [Fukumoto (2001)]. This indicates the internal oxidation of that biphasic layer. From Fig. 5.28, it can be seen that when silicon content increases in steel, the oxidation rate of this sublayer is faster resulting in the thickening of this layer. Existence of this sublayer influence the growth of other sublayers as the following.

As for layer B, it was seen that this layer is wüstite with magnetite precipitates, which decreases with the increased silicon content. The present results on silicon-containing steel in water-vapour-containing atmosphere are similar to the recent one [Nishimoto (2011)] on oxidation of silicon-containing in air in many manners. In that work, the EBSD cross-sectional images of scales were conducted as shown in Fig. 5.39. Scales on steels with different silicon contents were made to have the same thickness for comparison. It is seen that increasing silicon content in steel made the wüstite thinner. The discussion was made that formation of fayalite at the internal interface inhibits diffusion of iron from steel to scale since diffusivity of iron through fayalite is much slower than through wüstite [Tanigichi (2001), Ahtoy (2010), Nishimoto (2011)]. As a consequence, the iron supply to form wüstite which is just next to fayalite is then reduced. The wüstite sublayer is then thinner when silicon is added in steel.

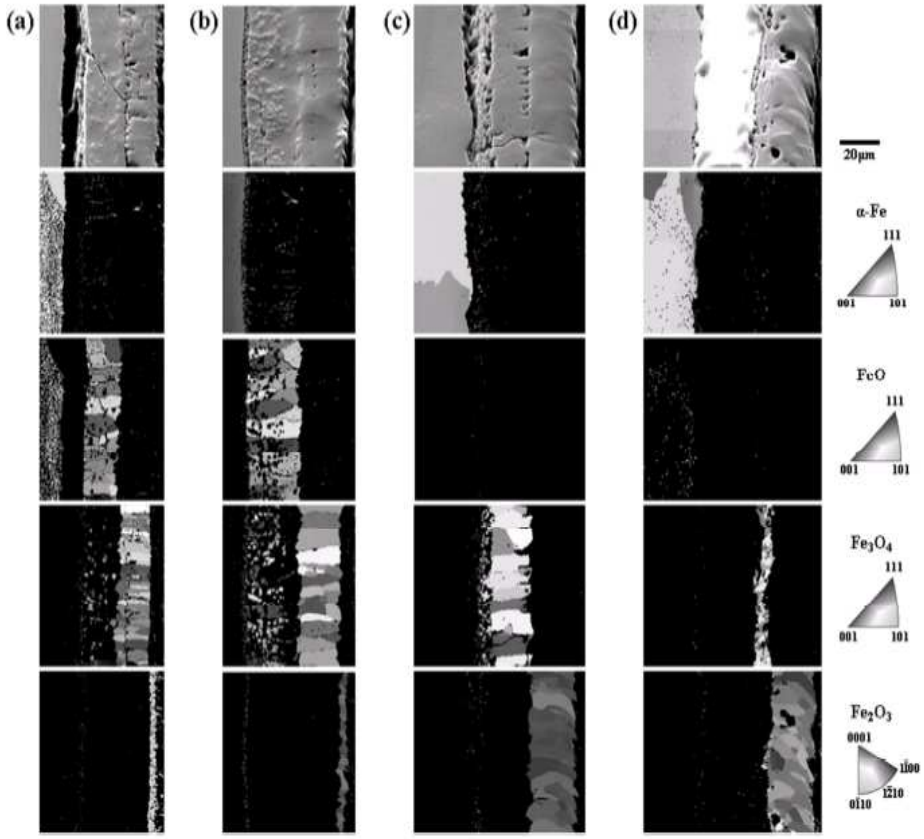

Figure 5.39: SEM images and EBSD of each iron oxide and α-Fe in the cross-sectional microstructures (a) Fe-0.004%Si, (b) Fe-0.1%Si, (c) Fe-0.5%Si and (d) Fe-1%Si [Nishimoto (2011)].

However, the discussion was not made in the previous work [Nishimoto (2011)] why wüstite is thinner or even disappeared when more than 0.5 wt% of silicon is added in iron. It was only assumed in that work that fayalite layer should form continuously when higher silicon is added in the metal. In the present work, formation of the mixture of wüstite with fayalite can be clearly observed, and it is seen that this sublayer grows thicker with the increased silicon content. The discussion can then be made that this continuous and thicker layer inhibit iron to diffuse outwards to form wüstite more efficiently.

Furthermore, it should be noted that in the present work, even though silicon is added in steel up to 0.84 wt%, when this steel is oxidised in water-vapour containing atmosphere at 900°C (Fig. 5.28) or 800°C (Fig. 5.40), sublayer of wüstite with magnetite precipitates can still be observed. This layer disappeared for Fe-0.5Si oxidized in air at 800°C (Fig. 5.39) [Nishimoto (2011)]. This result might indicate that iron can diffuse through the layer of wüstite mixed with fayalite which is formed in water-vapour-containing atmosphere easier than through fayalite layer which is formed in air.

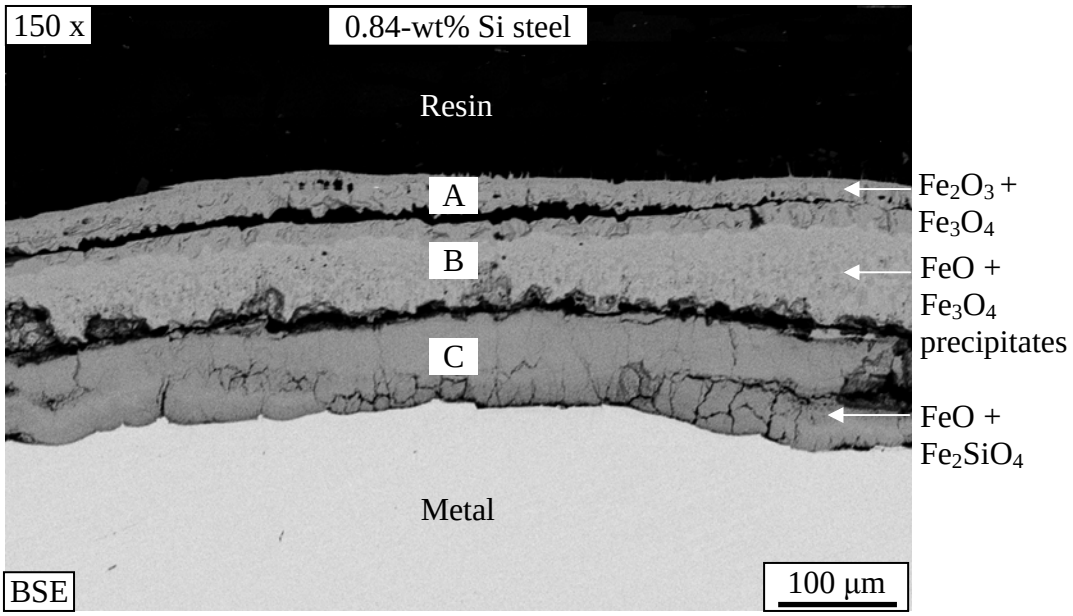

Figure 5.40: Cross-section of scale on the 0.84-wt% Si steel oxidised in 20%H_2O/Ar at 800°C for 16 h.

As for layer A, as previously mentioned for the case of silicon-containing steel, iron outwards diffusion from steel to scale is reduced due to the presence of fayalite-containing layer. Oxygen supply from atmosphere to scale is then more significant comparing to the outwards diffusion of iron [Nishimoto (2011)]. Thus, formation of iron oxide higher in oxygen ratio is promoted [Yang (2008)]. This results in the thickening of layer A consisting of hematite and magnetite with the increased content of silicon in steel.

CHAPTER 6

OXIDATION OF COPPER-CONTAINING MODEL STEEL

In chapter 5, in order to study the role of silicon on oxidation, the study is conducted using steels with 0.25-wt% Si and 0.84-wt% Si. The reference steel is also compared. In this chapter, to study the role of copper on oxidation, model steels are prepared for the investigation with the copper contents of 0.08 and 0.39 wt%. The results concerning reference steel reported in the previous chapter are used for comparison.

The oxidation tests were conducted by the thermobalance model B 24 from SETARAM. Copper-containing model steels were prepared with cylindrical size with 5 mm of length and 5 mm of diameter. Oxidation study was carried out in 20%H_2O/Ar for 16 hours at 600 to 900°C.

6.1 Oxidation kinetics of model steels containing copper

6.1.1 Oxidation rate as a function of time

It was found that the oxidation rates of the copper-containing steels follow the linear-parabolic law as shown in Fig. 6.1 to Fig. 6.4. From this study, at 900°C, the oxidation rate of the 0.39-wt% Cu steel was lower than that the 0.08-wt% Cu and the reference steels. At 700°C and 800°C, the oxidation rate of the copper-containing steels was lower than that the reference steel. However, the oxidation rate of the copper-containing steels seemed to be identical. At 600°C, the oxidation rates of the copper-containing steels were slightly higher than that of the reference steel.

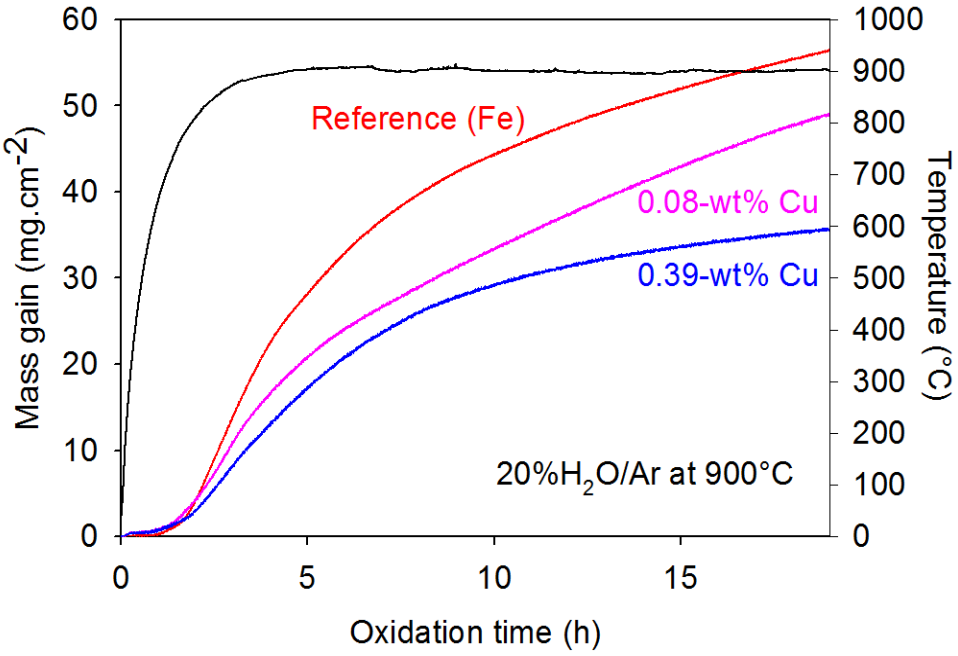

Figure 6.1: Mass gain of the reference steel (Fe), 0.08-wt% Cu and 0.39-wt% Cu steels oxidised in 20%H_2O/Ar at 900°C.

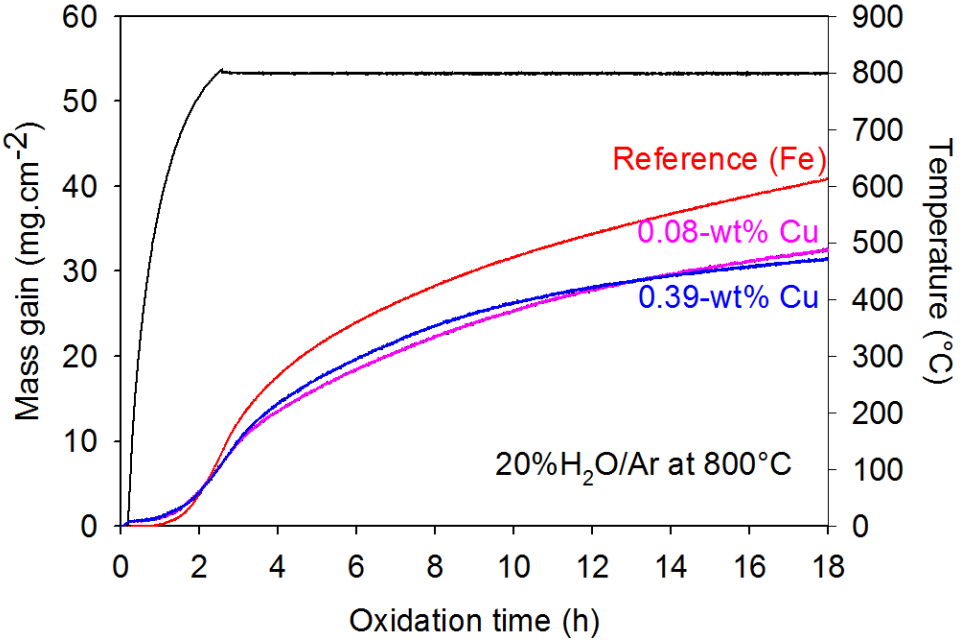

Figure 6.2: Mass gain of the reference steel (Fe), 0.08-wt% Cu and 0.39-wt% Cu steels oxidised in 20%H_2O/Ar at 800°C.

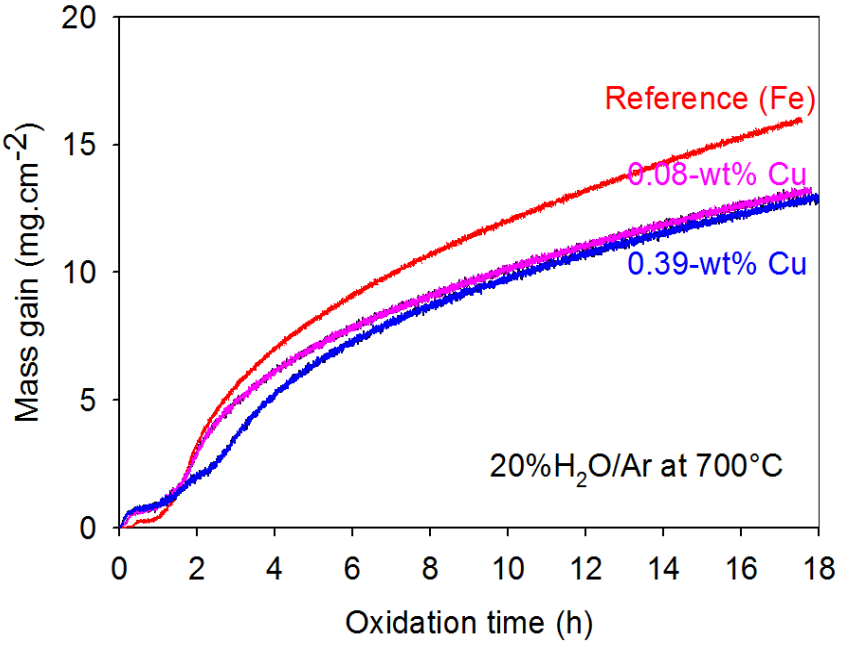

Figure 6.3: Mass gain of the reference steel (Fe), 0.08-wt% Cu and 0.39-wt% Cu steels oxidised in 20%H_2O/Ar at 700°C.

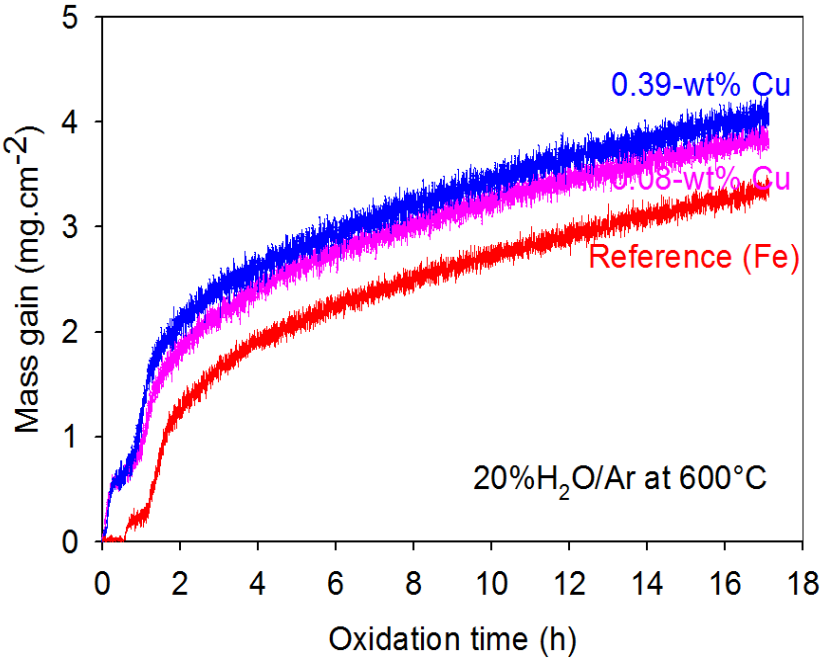

Figure 6.4: Mass gain of the reference steel (Fe), 0.08-wt% Cu and 0.39-wt% Cu steels oxidised in 20%H_2O/Ar at 600°C.

Fig. 6.5 to Fig. 6.6 compare the temperature effect for the 0.08-wt% Cu and 0.39-wt% Cu steels in the temperature range 600 to 900°C. It was seen that the oxidation rate increased with increasing temperature. It can also be observed that the initial stage, which the oxidation rate was lower, seems to be identical for all steels.

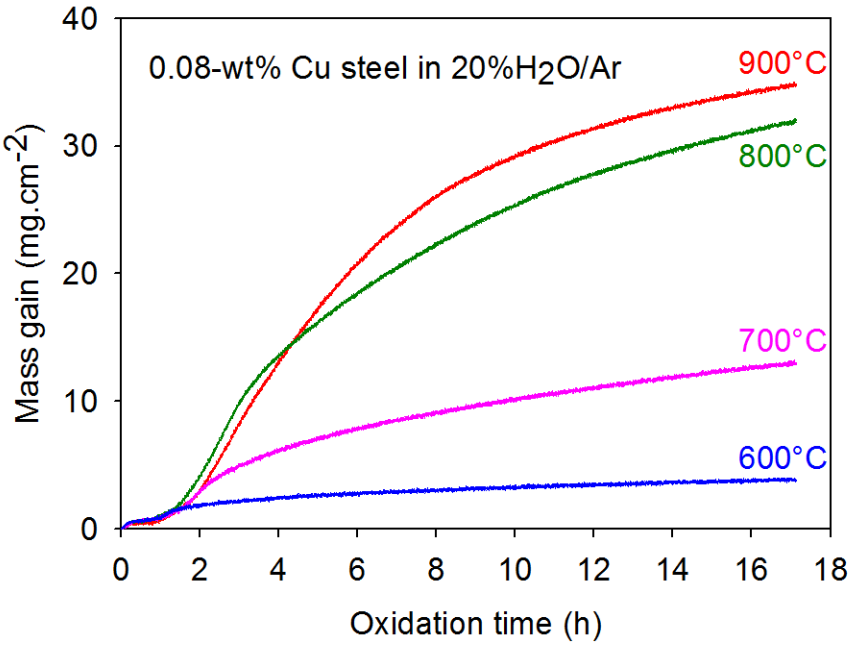

Figure 6.5: Mass gain of the 0.08-wt% Cu steel oxidised in 20%H_2O/Ar at different temperatures.

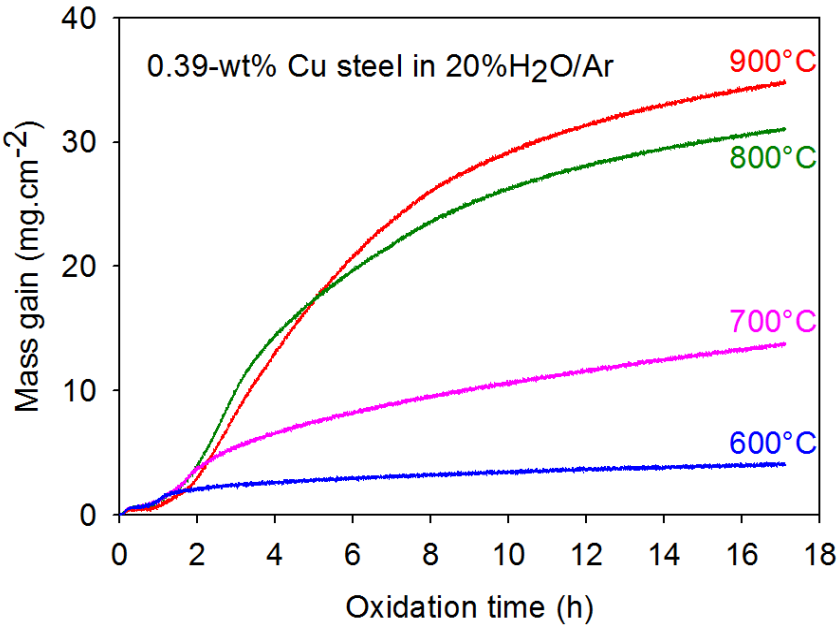

Figure 6.6: Mass gain of the 0.39-wt% Cu steel oxidised in 20%H_2O/Ar at different temperatures.

The Arrhenius form exhibiting relationship between parabolic rate constant and temperature is shown in Fig. 6.7 with data in Table 6.1.

Table 6.1: Parabolic rate constants (k_p) of copper-containing steels oxidised in 20%H_2O/Ar for 16 h at different temperatures.

Temp (°C)	Parabolic rate constants ($g^2.cm^{-4}.s^{-1}$)		
	Reference (Fe)	0.08-wt% Cu	0.39-wt% Cu
600	$2.00 \times 10^{-10} \pm 0.00$	$2.00 \times 10^{-10} \pm 0.00$	$2.00 \times 10^{-10} \pm 0.00$
700	$4.35 \times 10^{-9} \pm 2.50 \times 10^{-10}$	$2.75 \times 10^{-9} \pm 5.00 \times 10^{-11}$	$2.85 \times 10^{-9} \pm 1.50 \times 10^{-10}$
800	$2.35 \times 10^{-8} \pm 1.20 \times 10^{-9}$	$1.38 \times 10^{-8} \pm 4.10 \times 10^{-9}$	$1.27 \times 10^{-8} \pm 1.45 \times 10^{-9}$
900	$4.31 \times 10^{-8} \pm 5.50 \times 10^{-10}$	$2.53 \times 10^{-8} \pm 1.46 \times 10^{-8}$	$1.36 \times 10^{-8} \pm 4.15 \times 10^{-9}$

The activation energy can be calculated from Fig. 6.7. Information obtained from this figure is presented in Table 6.2. The parabolic rate constants of those steels are as follows.

For reference (Fe) steel $$k_p(g^2.cm^{-4}.s^{-1}) = 7.16\exp\left(\frac{-155064}{RT}\right) \quad (6-1)$$

For 0.08-wt% Cu steel $$k_p(g^2.cm^{-4}.s^{-1}) = 7.43\exp\left(\frac{-139749}{RT}\right) \quad (6-2)$$

For 0.39-wt% Cu steel $$k_p(g^2.cm^{-4}.s^{-1}) = 7.62\exp\left(\frac{-124434}{RT}\right) \quad (6-3)$$

where R is a gas constant (8.314 $J.mol^{-1}.K^{-1}$). Apparent activation energies of the reference (Fe), 0.08-wt% Cu and 0.39-wt% Cu steels were 155, 140 and 124 $kJ.mol^{-1}$ respectively.

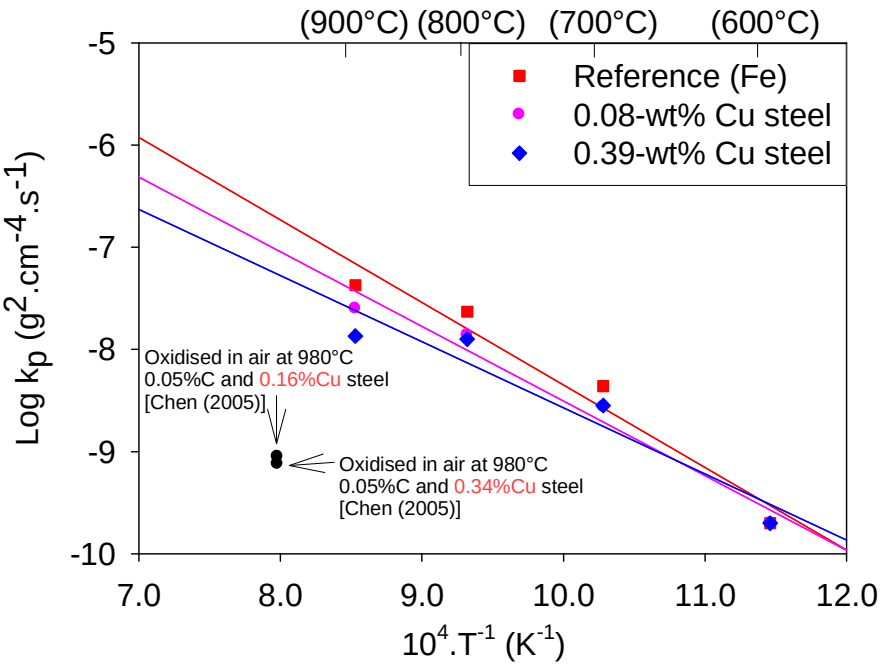

Figure 6.7: Arrhenius plot of copper-containing steels oxidised in 20%H_2O/Ar for 16 h at different temperatures.

Table 6.2: Data received from Fig. 6.7 for the copper-containing steels oxidised in 20%H_2O/Ar for 16 h.

Parameters	Steel		
	Reference (Fe)	0.08-wt% Cu	0.39-wt% Cu
Slope, m	– 0.81	– 0.73	– 0.65
Proportionality constant, k_o ($g^2.cm^{-4}.s^{-1}$)	– 7.16	– 7.43	– 7.62
Apparent activation energy, E_a ($kJ.mol^{-1}$)	155	140	124

From the Arrhenius plot in Fig. 6.7, it was observed that in the range of 700 to 900ºC, increasing copper content tends to reduce oxidation rate. This role is more pronounced with the increasing temperature. It was also observed that the activation energy is slightly lower for steel with higher copper content, indicating higher energy barrier for reaction to take place. Comparing to literature on air oxidation of copper-containing steel [Chen (2005)], it was reported that in air oxidation at 980ºC increasing copper content gave oxidation rate lower. Oxidation rate of steel with 0.34wt% Cu oxidised in air at 980ºC [Chen (2005)] is lower than that of steel with 0.39wt% Cu oxidised in water vapour at 980ºC in the present work. It might then be noted that oxidation rate seems to be higher when the copper-containing steel is oxidised in water vapour comparing to dry air. As for pure copper oxidised in oxygen with and without water vapour [Wang (2009)], it was reported that the rate of copper oxidation in oxygen containing water vapour was slightly higher than in dry gases.

6.1.2 Derivative of mass gain as a function of time

Oxidation rate of steel can be plotted as the derivative of the oxidation rate in function of oxidation time. At 900°C, passivity duration was calculated from Fig. 6.8 and plotted in Fig. 6.9 with data in Table 6.3. From these results, it is seen that the passivity and passivity breakdown durations are longer when copper in steel was increased.

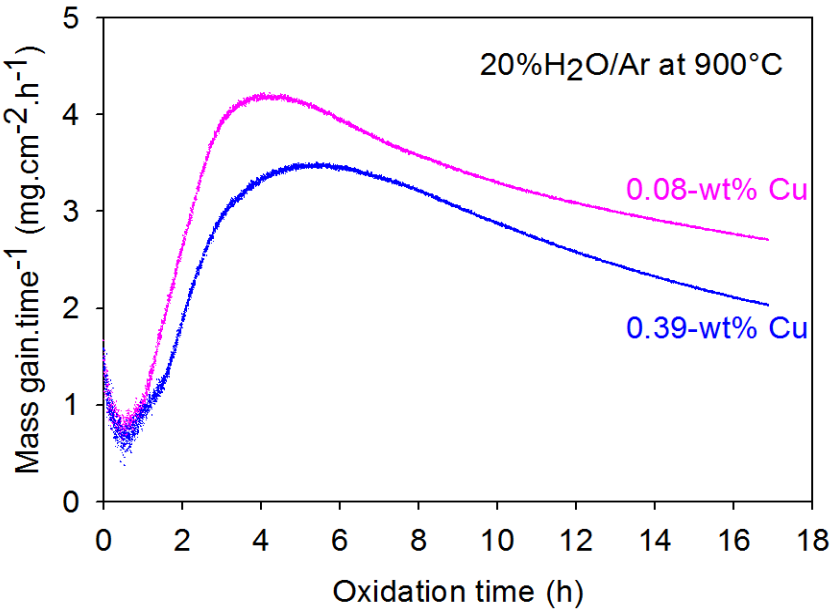

Figure 6.8: Derivative of mass gain in function of the oxidation time of copper-containing steels oxidised in 20%H_2O/Ar at 900°C.

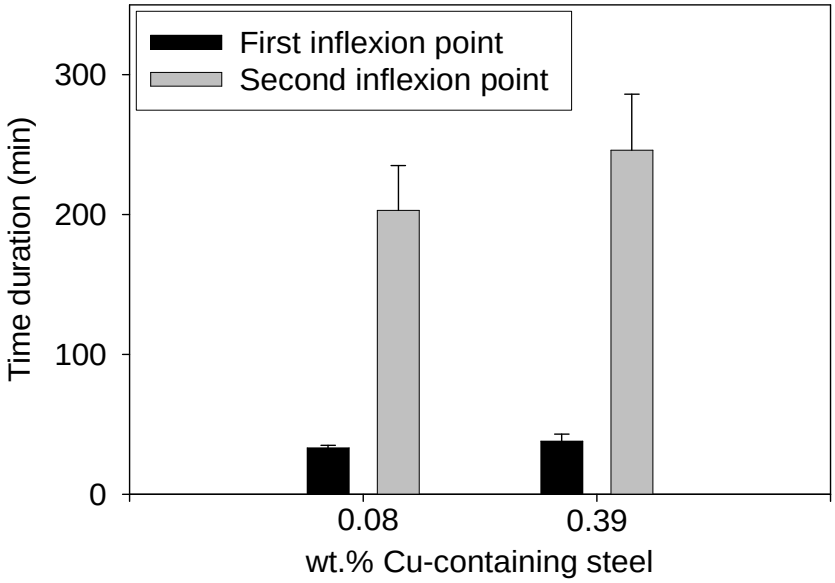

Figure 6.9: The first and second inflexion points of copper-containing steels oxidised in 20%H_2O/Ar at 900°C.

Table 6.3: Durations of first and second inflexion points of difference copper-containing steels oxidised in 20%H_2O/Ar at 900°C.

Inflexion point	Steel	
	0.08-wt% Cu	0.39-wt% Cu
First	33 min ± 2 min	38 min ± 5 min
Second	3 h 23 min ± 32 min	4 h 6 min ± 40 min

To discuss the passivity and passivity breakdown behaviour of the studied steels, scale formation during those periods were investigated. From Raman spectroscopy, peaks of Fe_2O_3, Fe_3O_4 and CuO were observed during passivity duration (Fig. 6.10).). It is then possible that copper oxide exists at initial stage. Wüstite which is a metal-deficit oxide is not formed. This indicates that diffusion of iron through copper oxide is slow, thus reducing iron activity and inhibiting the stability of lower iron oxides. This implies the effective role of copper oxide as a passive layer. In fact, the only iron oxide detected in this stage is hematite. This indicates the more significant role of oxygen on oxide formation with respect to the role of iron. At longer period of oxidation during passivity breakdown, Raman spectroscopy as in Fig. 6.11 exhibits the peaks of Fe_2O_3, Fe_3O_4, CuO and Cu_2O. It is then possible that CuO which is initially formed turns to be the more stable phase, Cu_2O, according to the stability diagram in Fig. 6.12.

Comparing to literature on air oxidation of pure copper [Prisedsky (2004)], it was reported that highly permeable fine-gained CuO layer is formed on the specimen's surface at initial stage. Then, after the outer dense layer of recrystallized CuO grains develops, the two-layered oxide zone with dominating Cu_2O layer arises. The dense outer layer of CuO closes the channels of easy oxygen transfer through the gas phase in porous scale. At this time, Cu_2O grains appear on the inner surface of scale and expands throughout the larger part of the diffusion zone. Under mechanical stress due to the difference in molar volume between metal and oxide, a complex pattern of cracks develops in oxide layer providing the channels of fast diffusion transfer. Also, comparing to literature on oxidation of pure copper in air [Zhu (2004)], it was reported that the products of initial oxidation consist of both CuO and Cu_2O. However, it was reported that CuO is firstly formed as a thin uniform film on the surface with the reaction $Cu + ½ O_2 = CuO$, and as then CuO film grows in thickness, the oxygen potential at the CuO/Cu interface was decreases. When it decreases to the pressure where Cu_2O is stable, the nucleation of Cu_2O will occur and the oxide will grow under the CuO film with reaction $Cu + CuO = Cu_2O$.

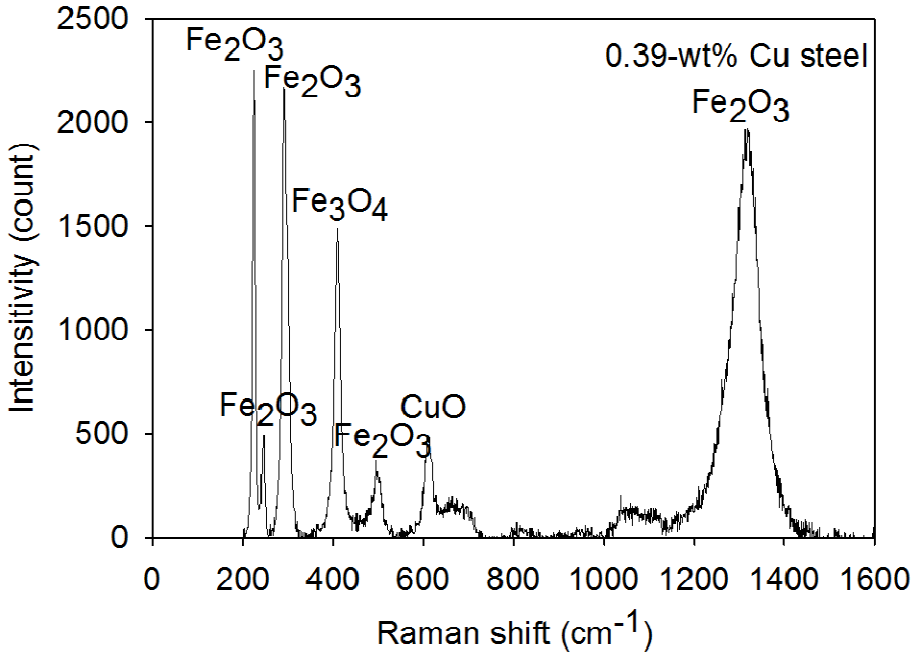

Figure 6.10: Raman spectrum at the first inflexion points of 0.39-wt% Cu steel oxidised in 20%H_2O/Ar at 900°C for 20 min.

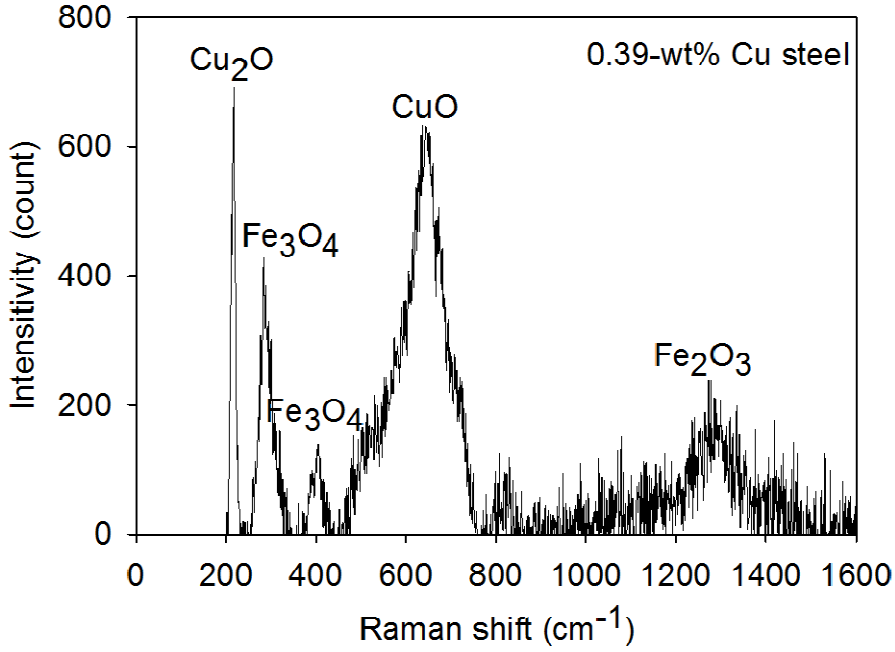

Figure 6.11: Raman spectrum at the second inflexion points of 0.39-wt% Cu steel oxidised in 20%H_2O/Ar at 900°C for 1 h 30 min.

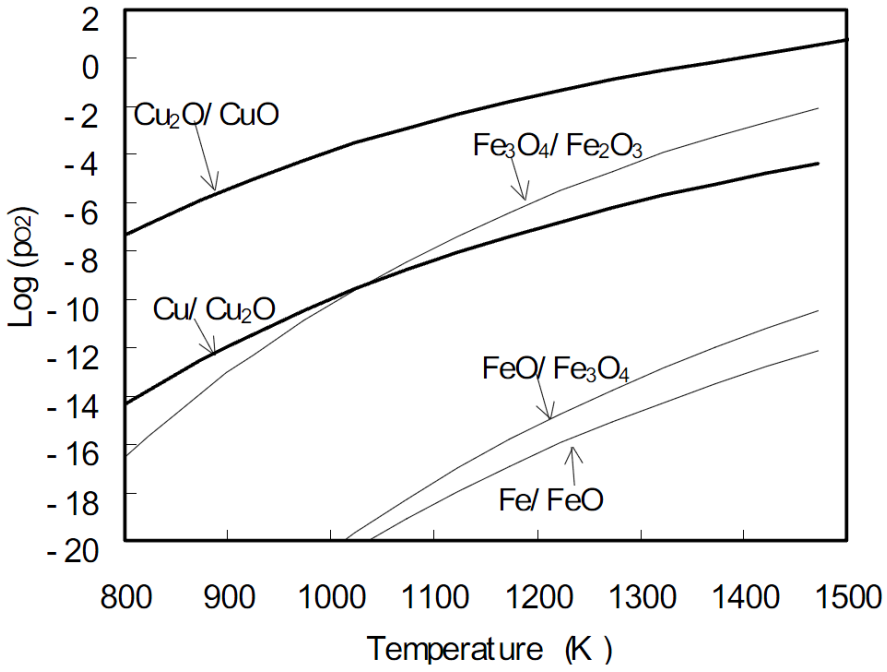

Figure 6.12: Stability diagram of copper, iron, and their oxides at various partial pressures of oxygen and temperature [Kondo (2006)].

6.2 Characterisation of oxide scale

The studied steels contain 0.08-wt% Cu and 0.39-wt% Cu. Cross-sections of oxide scales were examined using a SEM. Compositions and phases of oxidation products were qualitatively determined by EDS-SEM, XRD and Raman spectroscopy.

6.2.1 0.08-wt% Cu steel

Fig. 6.13 depicts the SEM images of the oxide scale on the 0.08-wt% Cu steel. EDS pattern observed on scale near internal interface is shown in Figs. 6.14 and 6.17 respectively. Peaks of O, Fe, C and Cu were observed.

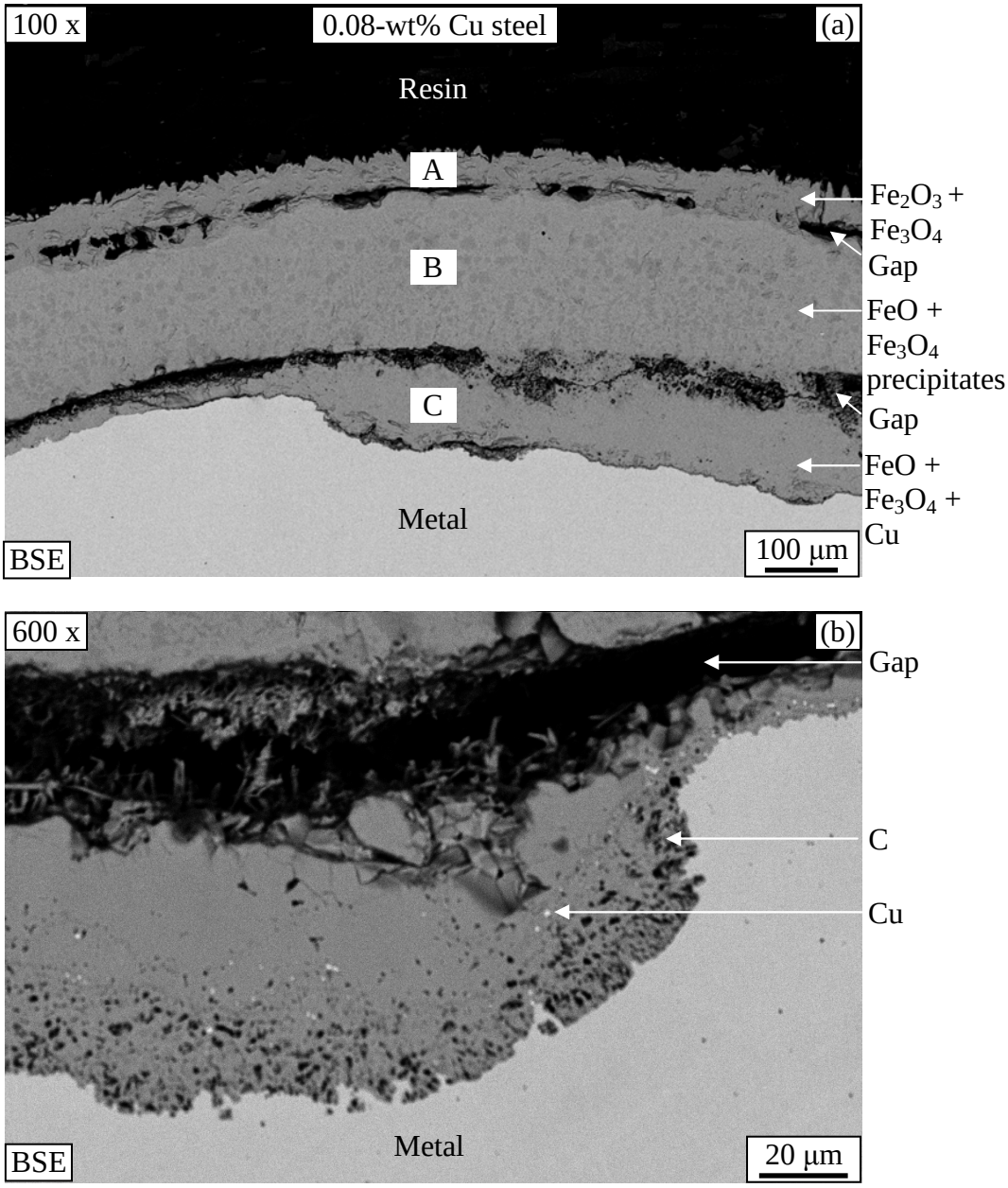

Figure 6.13: Cross-section of scale on the 0.08-wt% Cu steel oxidised in 20%H_2O/Ar at 900°C for 16 h observed on (a) oxide scale, and (b) interface magnified from (a).

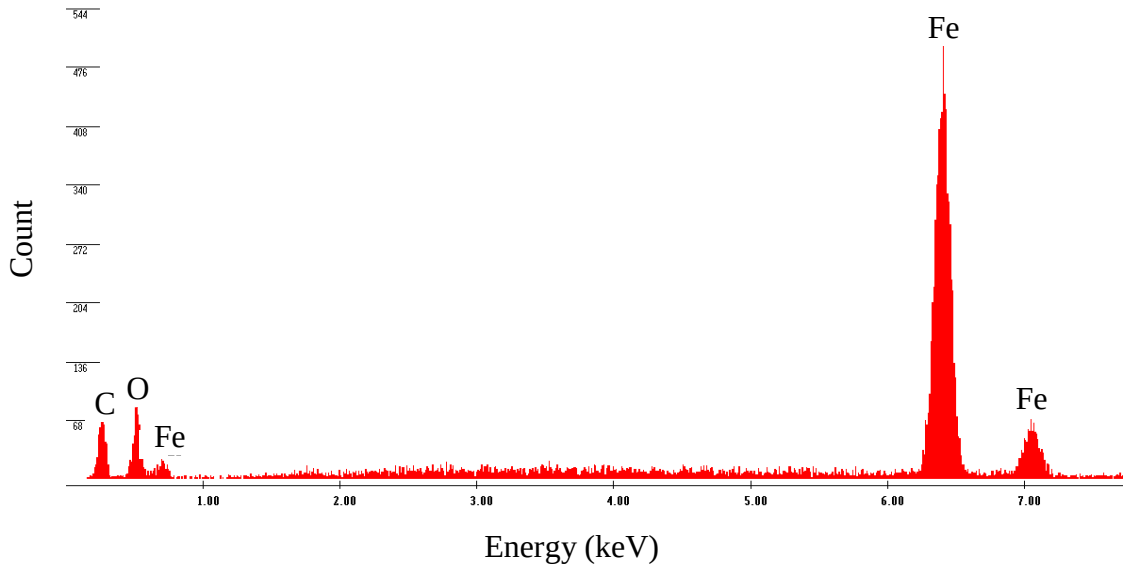

Figure 6.14: EDS pattern on oxide scale on scale near internal interface in the Fig. 6.13 (b) marked as C.

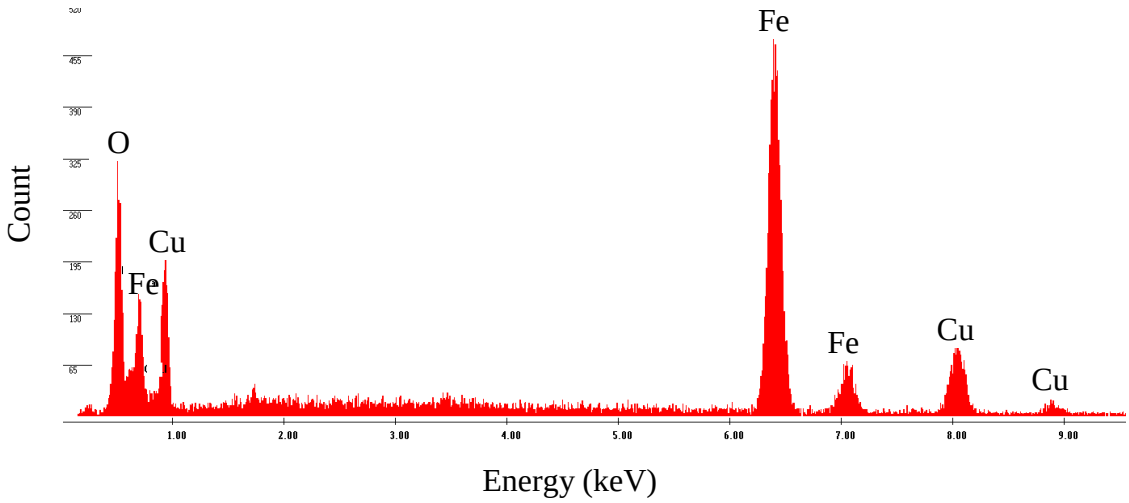

Figure 6.15: EDS pattern on oxide scale on scale near internal interface in the Fig. 6.13 (b) marked as Cu.

XRD pattern in Fig. 6.16 indicates the existence of iron, hematite, and magnetite (Fig. 6.16). Because of the relatively thick scale, the XRD can only identify the phases found on the outer part of scale. From Raman spectroscopy, its pattern indicates the existence of hematite and magnetite on layer A (Fig. 6.17). This indicates that hematite and magnetite exists as the outermost layer. For layer B, wüstite and magnetite were observed (Fig. 6.18). From this result and literature [Chen (2000), (2005)], this layer is wüstite with magnetite precipitates. The peaks of magnetite and wüstite were observed on scale near internal interface (layer C) (Fig. 6.19).

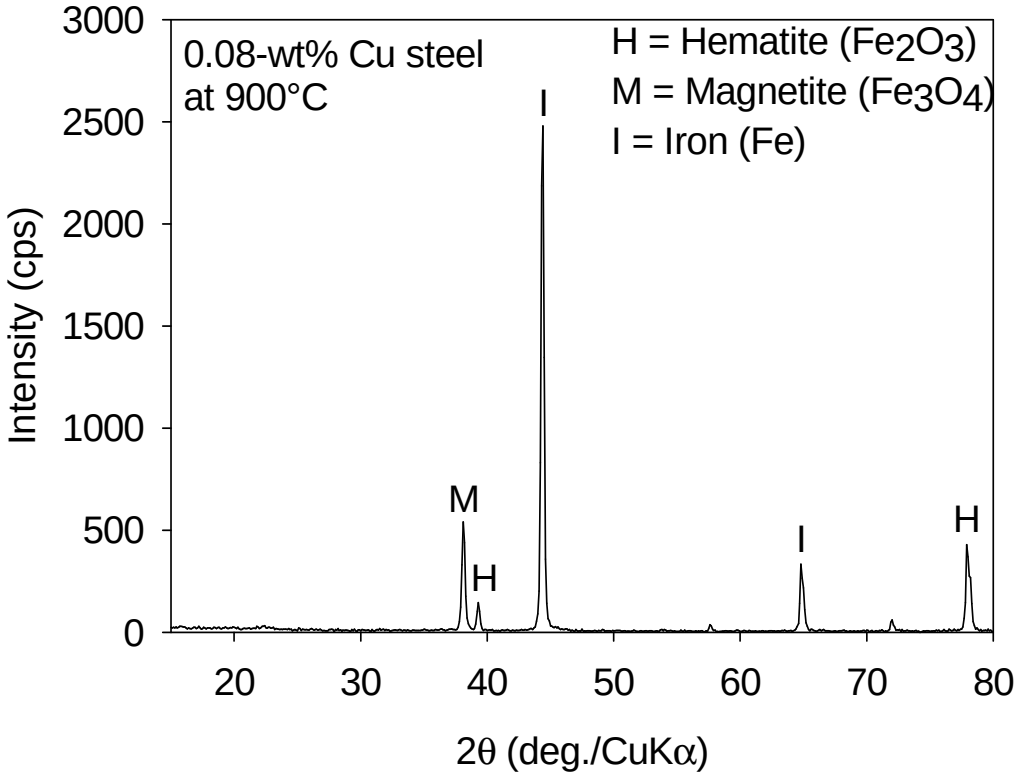

Figure 6.16: XRD pattern on oxide scale of the 0.08-wt% Cu steel oxidised in 20%H_2O/Ar at 900°C for 16 h.

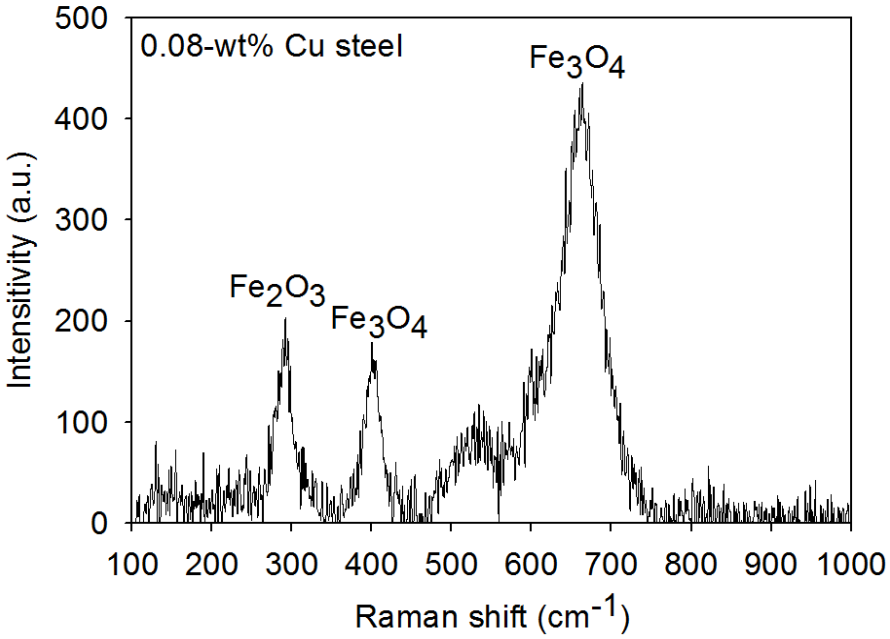

Figure 6.17: Raman peak on oxide scale observed on A in the Fig. 6.13 (a) of 0.08-wt% Cu steel oxidised in 20%H_2O/Ar at 900°C for 16 h.

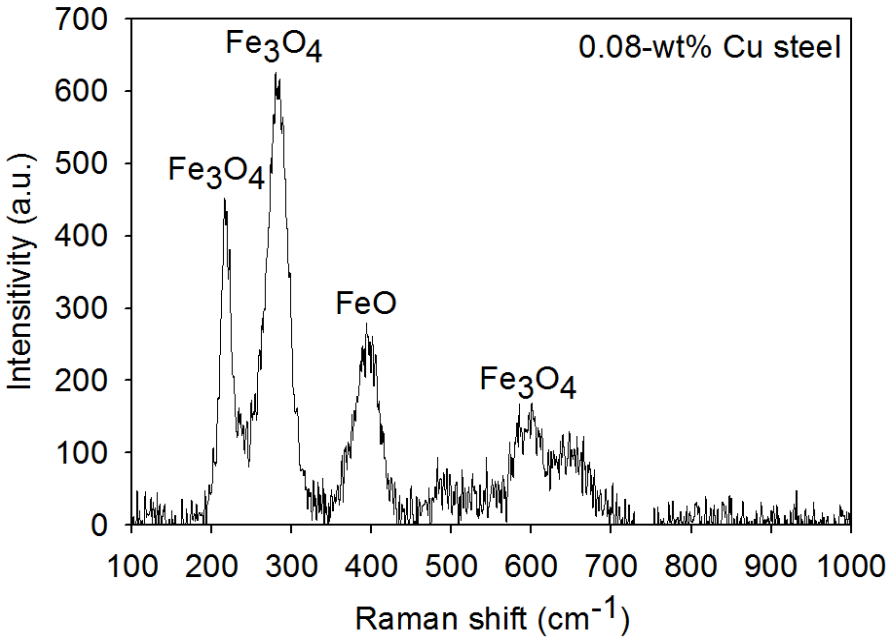

Figure 6.18: Raman peak on oxide scale observed on B in the Fig. 6.13 (a) of 0.08-wt% Cu steel oxidised in 20%H_2O/Ar at 900°C for 16 h.

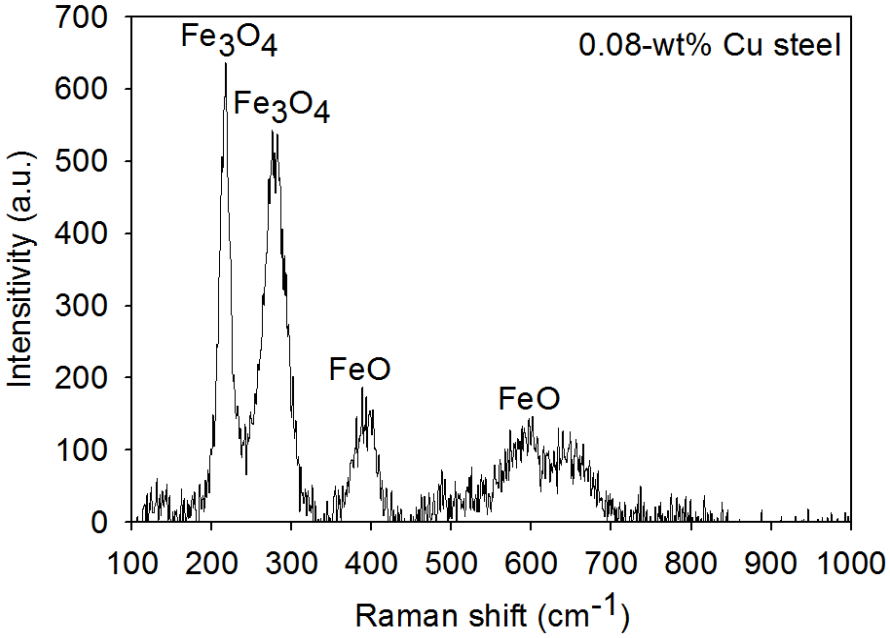

Figure 6.19: Raman peak on oxide scale observed on C in the Fig. 6.13 (a) of 0.08-wt% Cu steel oxidised in 20%H_2O/Ar at 900°C for 16 h.

6.2.2 0.39-wt% Cu steel

Figs. 6.20 and 6.21 depict the SEM images of the oxide scale on the 0.39-wt% Cu steel. From EDS in Figs. 6.22, 6.23 and 6.24, peaks of iron and oxygen were observed of all figures. A peak of carbon was also found near a gap and on scale near internal interface. A strong peak of copper was observed on scale near internal interface.

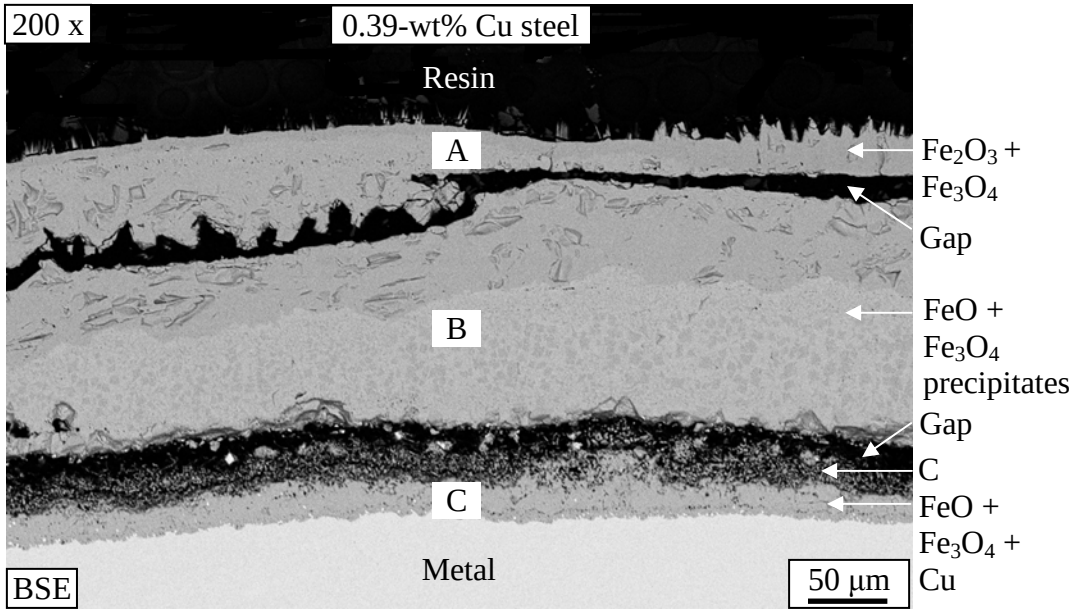

Figure 6.20: Cross-section of scale on the 0.39-wt% Cu steel oxidised in 20%H_2O/Ar at 900°C for 16 h.

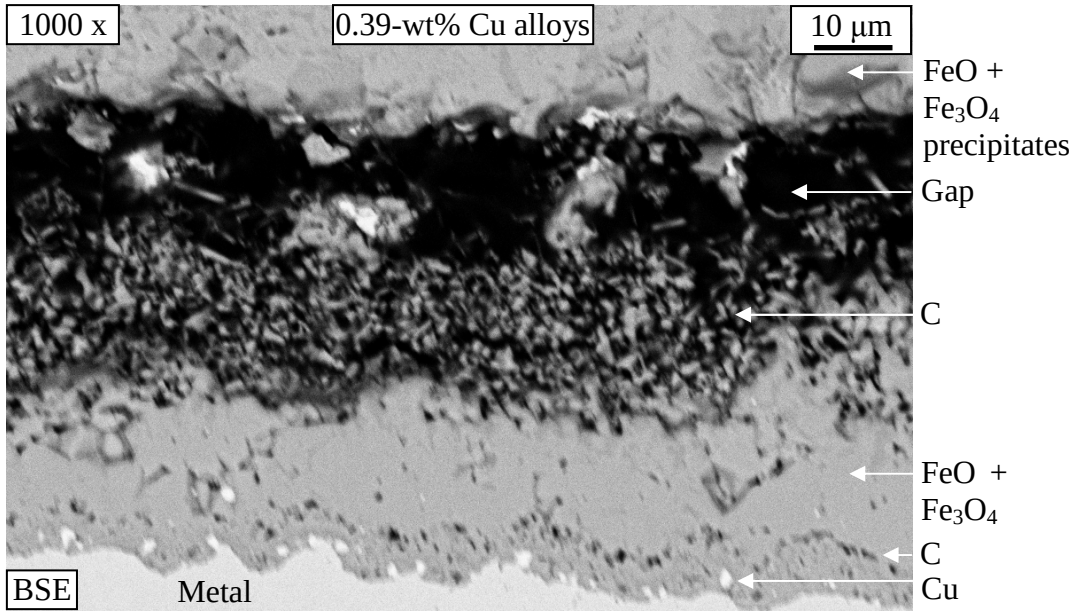

Figure 6.21: A metal-scale interface showing the carbon- and copper-rich phase in scale parallel to the metal-scale interface.

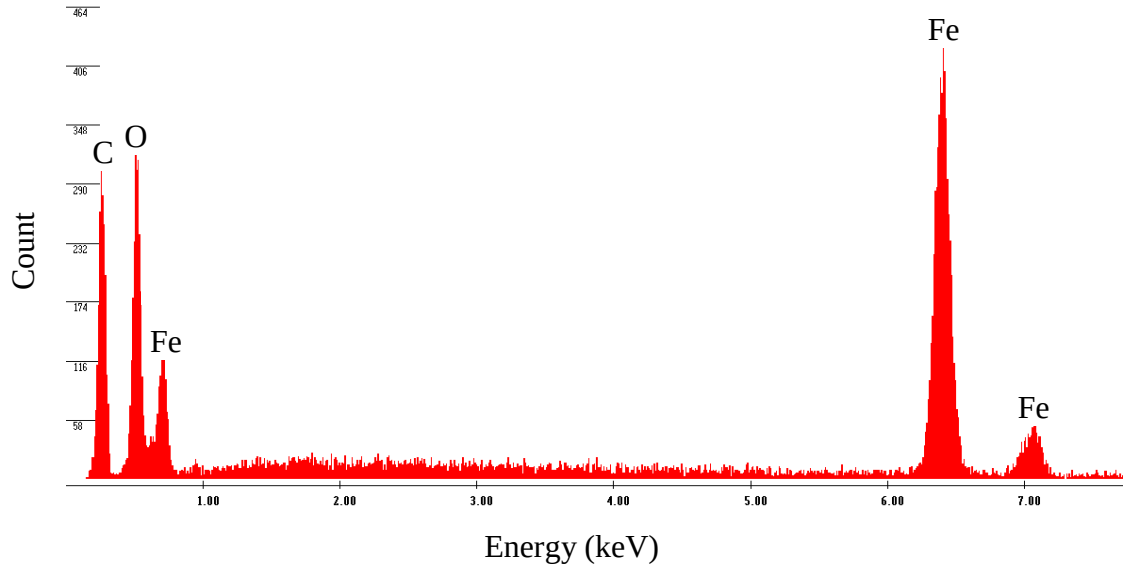

Figure 6.22: EDS pattern on oxide scale as C which is near a gap in the Fig. 6.21.

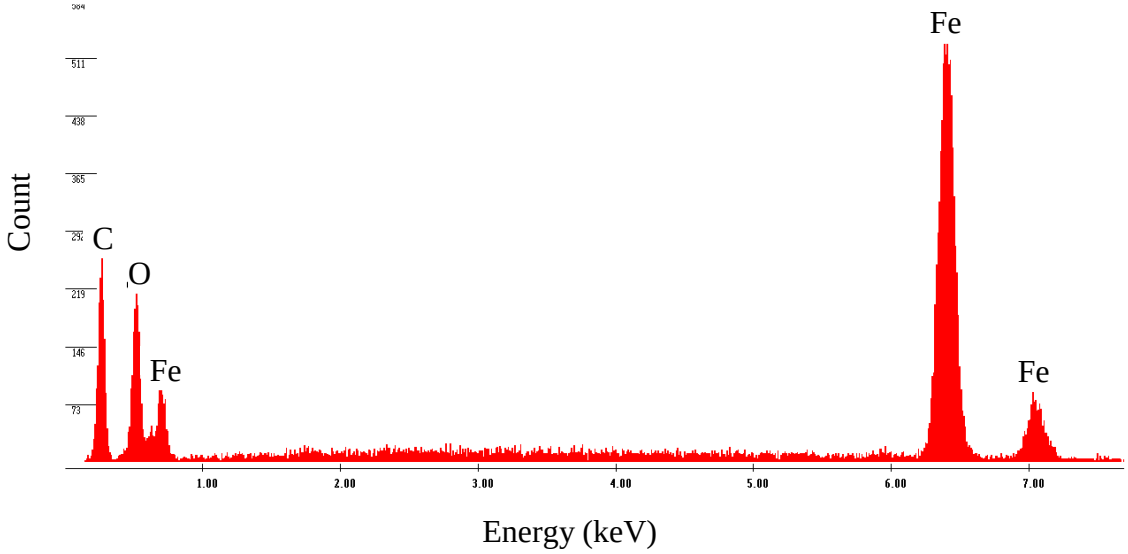

Figure 6.23: EDS pattern on oxide scale as C which is on scale near internal interface in the Fig. 6.21.

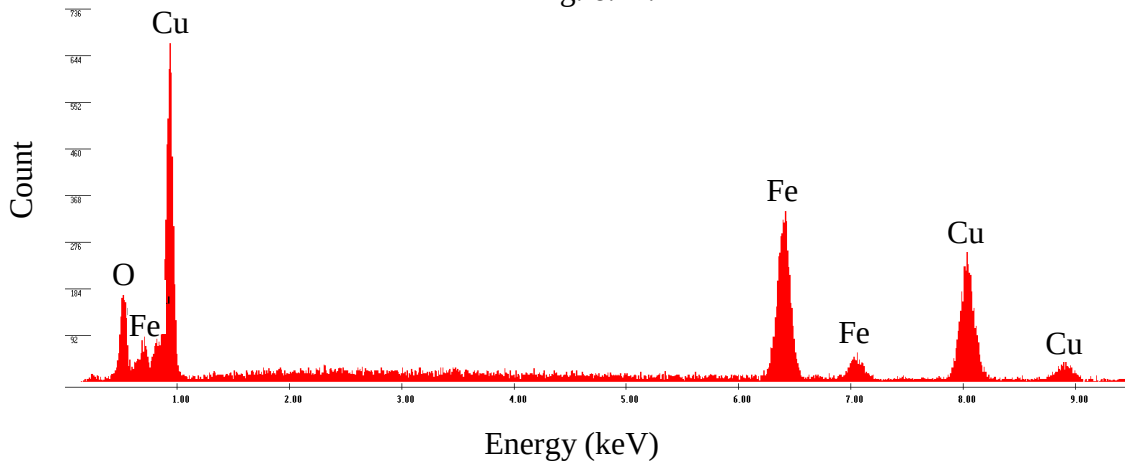

Figure 6.24: EDS pattern on oxide scale as Cu on scale near internal interface in the Fig. 6.21.

XRD pattern indicates the existence of iron, hematite, and magnetite (Fig. 6.25). From Raman spectroscopy, its pattern indicates the existence of hematite and magnetite on layer A (Fig. 6.26). From these results and literature [Chen (2000), (2005)], these two oxides exist as the outer layer. At layer B, wüstite and magnetite were observed on this layer (Fig. 6.27). From this result and literature [Chen (2000), (2005)], this layer is wüstite with magnetite precipitates. In Fig. 6.28, the peaks of magnetite and wüstite were observed on scale near internal interface (layer C).

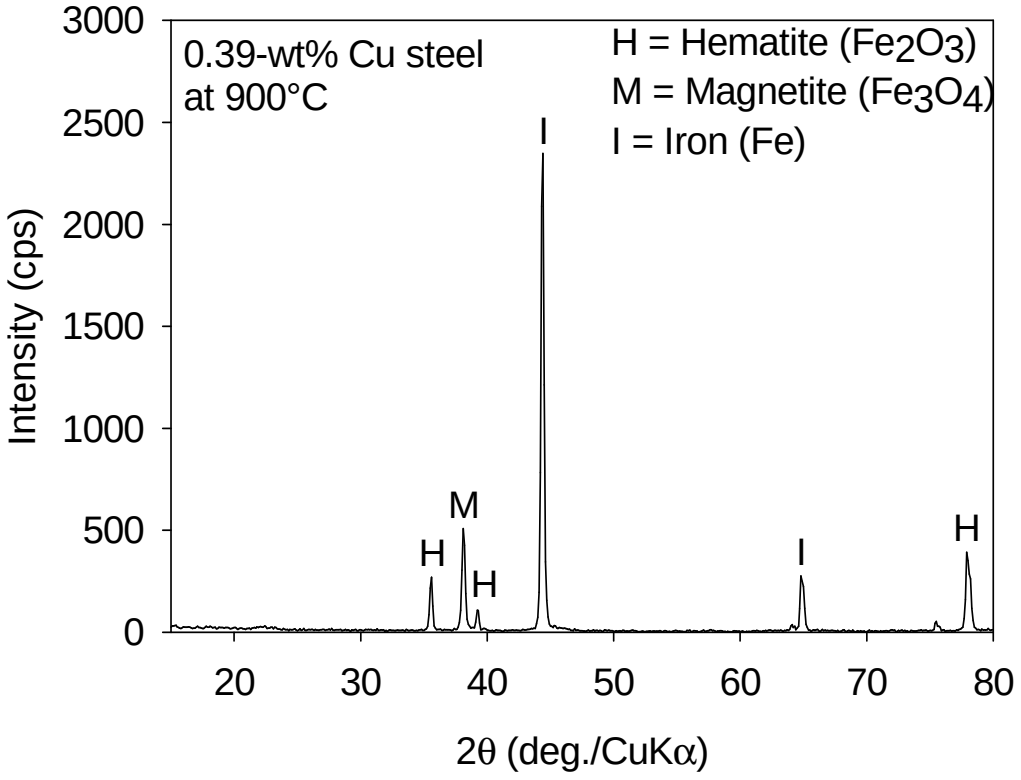

Figure 6.25: XRD pattern on oxide scale of the 0.39-wt% Cu steel oxidised in 20%H_2O/Ar at 900°C for 16 h.

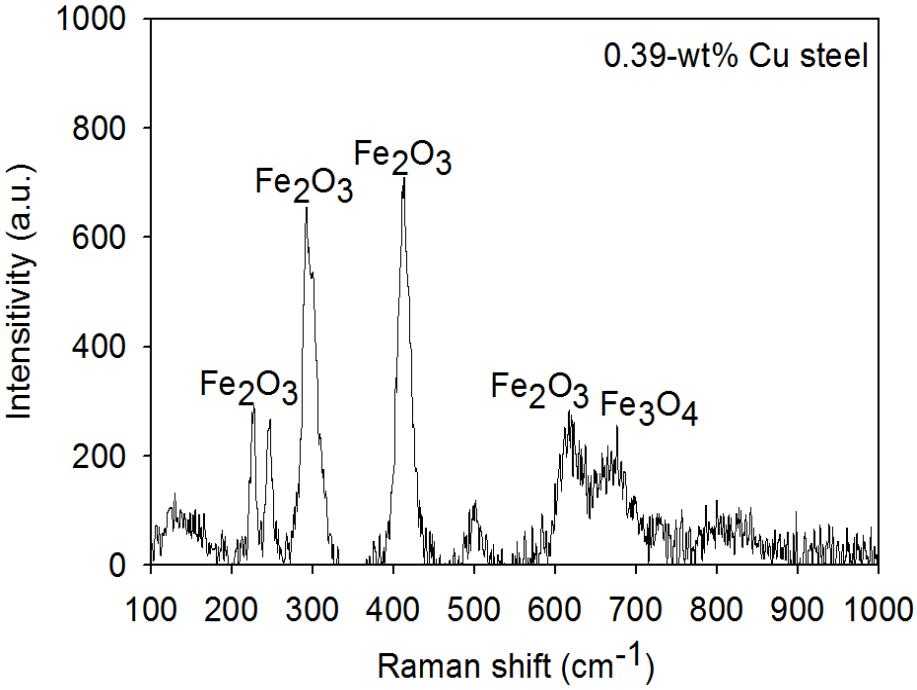

Figure 6.26: Raman peak on oxide scale observed on A in the Fig. 6.20 of 0.39-wt% Cu steel oxidised in 20%H_2O/Ar at 900°C for 16 h.

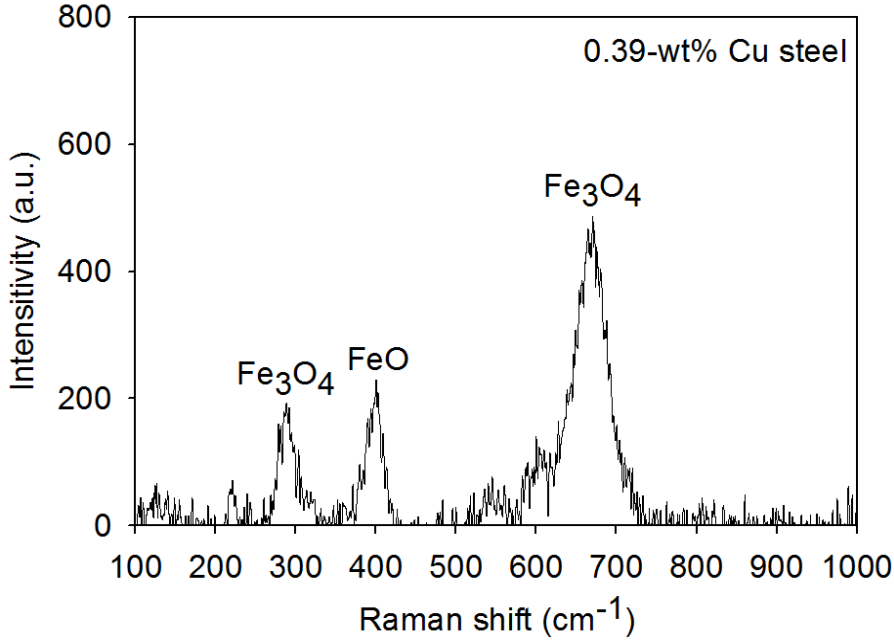

Figure 6.27: Raman peak on oxide scale observed on B in the Fig. 6.20 of 0.39-wt% Cu steel oxidised in 20%H_2O/Ar at 900°C for 16 h.

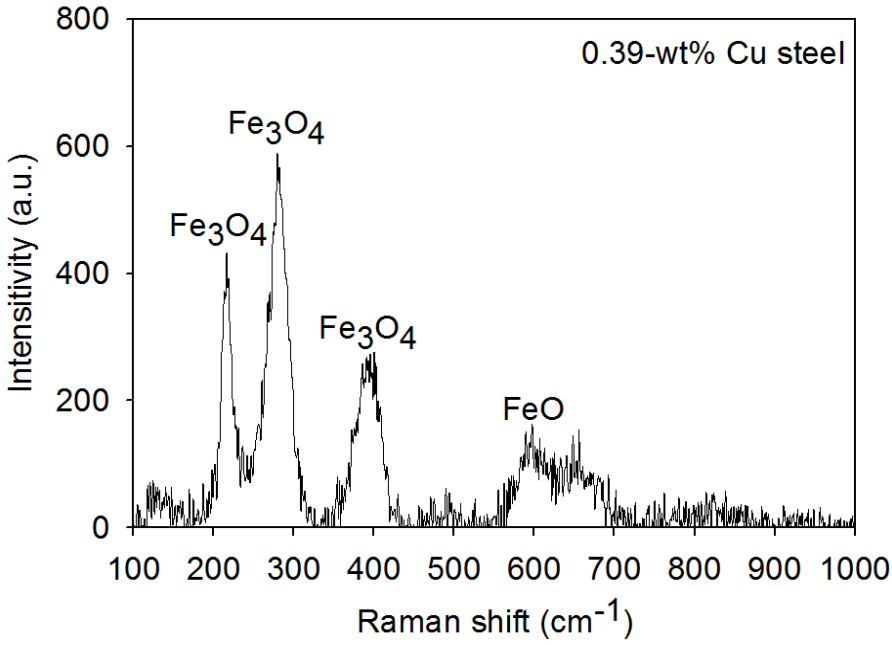

Figure 6.28: Raman peak on oxide scale observed on C in the Fig. 6.20 of 0.39-wt% Cu steel oxidised in 20%H_2O/Ar at 900°C for 16 h.

6.3 Comparison of oxide scales on steels with different contents of copper

From the previous sections, it can be synthetised as in Fig. 6.29 that scale consists of three layers according to its appearance and integrity observed. A layer A at the outermost consists of hematite and magnetite. A layer B is beneath the former layer and consists of wüstite with magnetite precipitates. Finally, a layer C at the innermost consists of wüstite, magnetite and copper rich phase. Evolution of each layer and the total scale thickness is depicted in Fig. 6.30. From this figure, it can be seen that the total scale thickness reduced with copper content in steel. For each layer, the layer A is thicker when copper in steel increased. This is opposite for the case of layer B where it is thinner with the increased copper content. The total layer mainly consisting of wüstite (layer B and C) is also thinner with the increased copper content in steel.

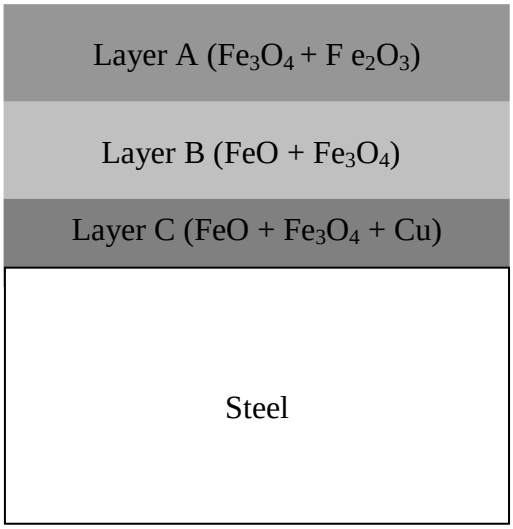

Figure 6.29: Illustration of the formation of the oxide layer.

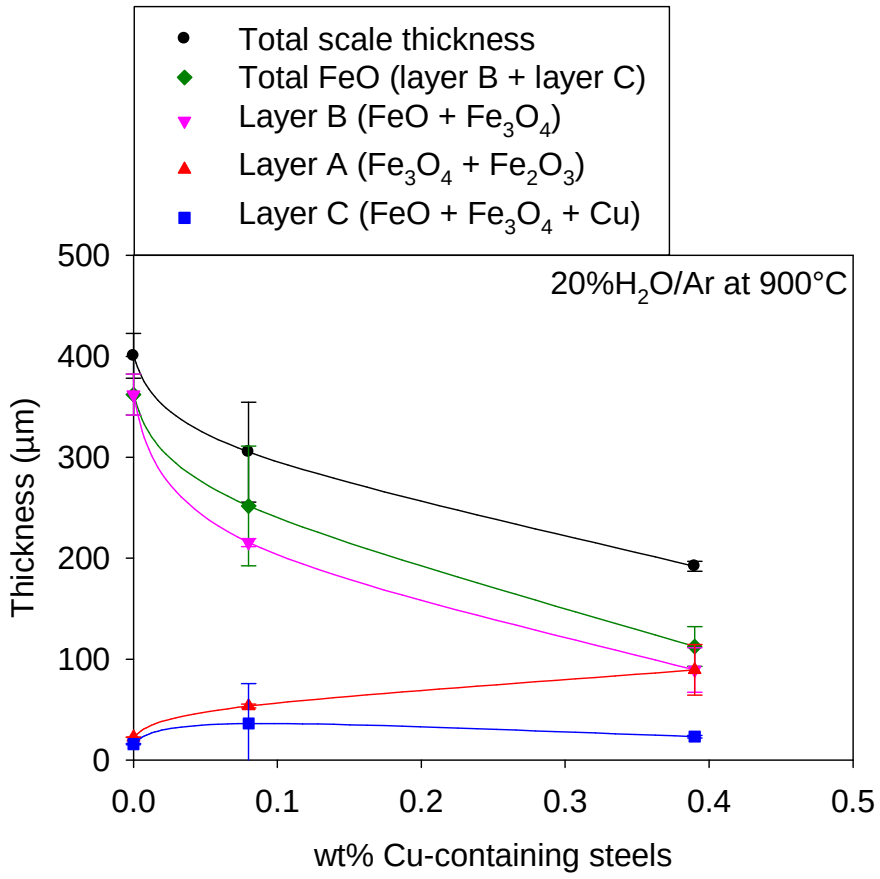

Figure 6.30: Thickness ratio of FeO, Fe_2O_3 and Fe_3O_4 as a function of copper-containing steels oxidised in 20%H_2O/Ar at 900°C for 16 h.

For layer C, three phases were detected: wüstite, magnetite, and copper-rich phase. From Fig. 6.10, CuO was primarily observed at the internal interface. It is possible that during oxidation copper is enrich at the surface and then reduce iron activity. This then results in the formation of CuO according to the reaction:

$$Cu + \frac{1}{2} O_2 = CuO$$

When CuO is formed, the partial pressure of oxygen at the CuO/steel substrate is reduced. According to stability diagram in Fig. 6.12, the more stable phase Cu_2O could then form according to the following reaction:

$$2\ CuO = Cu_2O + \frac{1}{2} O_2$$

However, according the stability diagram mentioned above, Cu_2O is less stable than FeO. At longer period of oxidation, it is possible that Cu_2O further reacts with the FeO resulting in Fe_3O_4 according to the following reaction.

$$Cu_2O + 3FeO = 2Cu + Fe_3O_4$$

This reaction results in the Cu dispersed in magnetite seam at the internal interface as observed in the present work particularly in steel with 0.39-wt% Cu. Furthermore, Cu was also found in wüstite in the layer C, and the magnetite peak was also detected in this layer. From TEM observation of copper-containing steel oxidised in water-vapour containing atmosphere [Kondo (2006), Kondo (2011)], oxide around copper existing in wüstite grain boundary was found to be magnetite. Thus, the existence of copper particle surrounding by magnetite in wüstite layer might also be possible in the present work.

For layer B, we can compare with the role of silicon in steel in the previous chapter. The existence of fayalite was discussed to be the cause for lower oxidation rate of steel. In this chapter, it seems that the existence of the copper-rich phase at the internal interface might also play a role on decreasing oxidation rate. Comparing to literature studying air oxidation of the copper-containing steel at 980°C [Chen (2005)], the copper-rich phase was reported to spread along the steel-scale interface of steel with 0.30 – 0.34 wt% Cu, and oxidation rates of those steels were reduced comparing to steel with lower copper content. The discussion in this work was in agreement with that one. However, it can bee seen more profoundly in the present work that reduction of the total scale thickness was due to the reduction of wüstite thickness (layers B and C). This could be because the existence of the copper-rich phase inhibits the transport of iron ion from steel to scale to form the wüstite layer. Furthermore, the discussion was further made in literature [Chen (2005)] that higher copper in steel reduced scale adhesion resulting in the blister between scale and steel substrate. Thus, the iron flux transported from substrate to scale is then reduced. This phenomenon was not found in the present work which might be due to the lower oxidising temperature.

For layer A, as formerly mentioned, the transport of iron ion from metal to scale is inhibited by the copper-rich phase at the internal interface. However, oxygen is relatively rich at the external interface. This two situations lead to formation of layer A consisting of oxides relatively rich in oxygen (hematite and magnetite) with the relative faster rate. Thicker scale of layer A is then observed for steel with higher copper content.

CHAPTER 7

CONCLUSIONS AND PERSPECTIVES

7.1 Conclusions

The present study investigated the characteristics, oxidation kinetics, mechanical adhesion and pickling behaviour of thermal oxide scale. The as-received conventional and recycled hot-rolled steels (Chapter 3), the conventional steel with 0.026-wt% Si and 0.193-wt% Si steels (Chapter 4), and the model steels with different silicon contents (Chapter 5) and copper contents (Chapter 6) were studied in this work. The following conclusions could be drawn.

7.1.1 Conclusions for chapter 3: Adhesion of scales on steels produced by different process routes

7.1.1.1 Scientific conclusions

1. The two types of tensile test, macro and micro ones, were comparatively applied in this work. Since one of the important parameters different in these two tests is the strain rate, its role on the testing results was first investigated. It was found that the forced spallation of scales increased with increasing the tensile strain rate. A higher strain rate resulted in a lower strain inducing the first spallation. It might be because, at higher strain rate, the system has no time to relax. Consequently, the apparent mechanical adhesion energy of scale actually formed on the hot-rolled recycled steel decreased with increasing the tensile strain rate.

2. Mechanical adhesion of scale on steel substrate was investigated by the micro- and macro-tensile test. Strains provoking the first spallation of scale actually formed on the hot-rolled conventional and recycled steel were 3.85% and 5.28% respectively when using the micro-tensile test. Those values were 0.26% and 2.98% for the macro-tensile test.

3. Mechanical adhesion energies operated by the micro-tensile test of scale actually formed on the hot-rolled conventional and recycled steels were 293 and 611 $J.m^{-2}$ respectively. The results from the macro-tensile test were as different as 1 and 186 $J.m^{-2}$. These results indicated the higher mechanical adhesion of scale on the hot-rolled recycled steel.

4. The pickling test of the as-received hot-rolled two studied steels was conducted. The dissolution rate of scale on the recycled steel was slower than that of scale on the conventional one. Period of time for the complete pickling scale on the recycled steel was longer than that on the conventional one. These results indicate the difficult de-scaling of scale actually formed on the hot-rolled recycled steel. It might be due to the recycled steel had hematite layer which is hard to be pickled.

5. The thicknesses of scales actually formed on the hot-rolled conventional and recycled steels were 11 and 12 µm respectively. The scales consisted mainly in magnetite on the hot-rolled conventional steel. The hot-rolled recycled steel showed the presence of external hematite.

7.1.1.2 Technical conclusions

1. The micro-tensile test, using very low tensile strain rates, allows relatively high relaxation phenomena. The obtained adhesion energies are therefore probably over-estimated.

2. For the micro-tensile test, samples have to be thin and actual strips cannot be tested directly. For the macro-tensile test, using higher tensile strain rates with thick samples and was very convenient for testing hot rolled strips.

3. Using the macro-tensile test with higher strain rate gave the more spallation ratio during straining. This facilitates the discussion in case that the spallation ratio obtained from the micro-tensile test was slight.

7.1.2 Conclusions for chapter 4: Adhesion of scales on hot-rolled steels with different silicon contents

1. Spallation of scale actually formed on the 0.026-wt% and 0.193-wt% Si steel during straining increased with increasing the tensile strain rate. The increased tensile strain rate resulted in decreased strain inducing the first spallation. These results confirmed the other ones found in the study in chapter 3.

2. The micro-tensile test used to investigate the mechanical adhesion of scale actually formed on the steel substrate. Lower strain provoking the first spallation was observed when Si content in steel was lower. Steel with higher Si content exhibited a lower susceptibility of scale spallation under the imposed strain. The macro-tensile test gave the results with the same tendency as the ones obtained by the micro-tensile test.

3. The results from the tensile test indicated the higher adhesion energies of scale actually formed on the steel with higher Si content which was 401 and 11 $J.m^{-2}$ for the micro- and macro-tensile tests respectively. As a result, steel with lower Si content present as 306 $J.m^{-2}$ for the micro-tensile test and 4 $J.m^{-2}$ for the macro-tensile test. This result was indicating scale adherence of the 0.193-wt% Si steel. This might be due to the existence of oxide containing Si at steel-scale interface, which can be promoted adhesion of scale on steel substrate.

4. The as-received steel with actual scale on the hot-rolled 0.026-wt% Si and 0.193-wt% Si steels were used in pickling test. The results indicated that a lower dissolution rate of scale and longer time for complete de-scaling for the 0.193-wt% Si steel. For the best surface quality of hot-rolled steel strips after pickling, the Si content should be kept as low as possible.

5. Scale actually formed on the 0.026-wt% Si and 0.193-wt% Si steel was polished. The two studied steels were oxidised in 20%H_2O/Ar at 900°C for 1 to 3 min. Using the micro-tensile test, strain provoking the first spallation on the 0.193-wt% Si steel was 2.73%, much lower than that for scale on the 0.026-wt% Si steel which was 5.88%. However, the partial spallation, a decohesion of a part of oxide from another part, was observed in this case.

6. Thickness of scale actually formed on the steel with higher Si content was 8 µm, which was less than the one on steel with lower Si content (9 µm). XRD and Raman pattern indicated that the scale consist of magnetite and iron.

7.1.3 Conclusions for chapter 5: Oxidation of silicon-containing model steels

1. Since the range of silicon content in steel available from the industry is only up to 0.193-wt% in the previous chapter. The model steel with silicon content up to 0.84-wt% was further prepared. Oxidation study was focussed in this chapter. It was found that the oxidation rate of various silicon-containing steels obeyed the parabolic law. Oxidation rate tends to decrease with increasing Si content. The oxidation rate increased with increasing temperature of all steel.

2. The passivity and passivity breakdown durations are longer when silicon in steel increased. This might be from the formation of SiO_2 in the first stage, and a more porous SiO_2 in the second stage. After silica turns to be fayalite in the last stage, the protective stage commenced.

3. Oxide scale formed on different silicon-containing steels after isothermal oxidation had a three-layer structure, an outer hematite and magnetite layer, an intermediate is wüstite with magnetite precipitates, and an inner wüstite with fayalite layer. Furthermore, internal oxidation of Si can be observed on scale with 0.84-wt% Si steel at 900°C.

4. Increasing silicon content tends to promote the protective layer of fayalite at the internal interface. As a result, wüstite which is formed by the outward diffusion of iron ion from steel to scale was reduced with increased silicon content. In the contrary, the role of oxygen for oxide formation is more significant than the role of iron which is limited by the fayalite barrier previously mentioned. The oxide of iron which is relatively rich in oxygen, hematite and magnetite, increased with the increased of silicon content.

7.1.4 Conclusions for chapter 6: Oxidation of copper-containing model steels

1. The oxidation rates of the copper-containing steels followed the parabolic law. Oxidation rate tends to be lowered with increasing Cu content. The oxidation rate increased with increasing temperature of all steel.

2. The passivity and passivity breakdown durations were also observed in this case. In the first stage, the formation of CuO was found at the internal interface. In the second one, the existence of CuO and Cu_2O was observed.

3. The scale structure consists in external layer of hematite and magnetite, an intermediate layer of wüstite with magnetite precipitates. Scale at the internal interface consists of wüstite, magnetite and copper. It is possible that copper precipitated at that area inhibits the outward diffusion of iron from steel to scale. This results in the reduction of wüstite thickness when copper content in steel increases. Similar to the case of silicon-containing steel, when iron diffusion previously mentioned in inhibited, the role of oxygen for oxide formation is more significant than the role of iron. The oxide of iron which is relatively rich in oxygen, hematite and magnetite, increased with the increased of silicon content.

7.2 Perspectives

The alloying elements in steel play an important role in the oxidation behaviour, mechanical adhesion and surface quality of the product. The understanding in the transformation of scale structures provides a substantial foundation for controlling the final surface of the hot-rolled steel. The following suggestions are recommended for the future research.

1. The further experiment should address on the role of alloying elements particularly Sn, Pb, As, Ni, Cr, Mo, and W which contaminates in scraps on scale structure, oxidation kinetics and mechanical adhesion of scale on steel strips.

2. The present work studied oxidation of steels with silicon and copper in water vapour. The additional study in synthetic air should be carried out for comparison.

3. The present work studied only oxidation of copper-containing steel. The role of Cu on mechanical adhesion of scale on steel substrate should further be investigated by the tensile test or other methods e.g. the indentation test.

REFERENCES

[A]

Effect of alloying elements (Si, P, Al, B) on low carbon steel oxidation in process at high temperatures: mechanisms and modelling
Ahtoy E.
Ph.D. Thesis, Institut polytechnique de Grenoble (Grenoble INP), France, 2010 (in English).

American Museum of Natural History, Bushveld Intrusive, Limpopo Province, South Africa
Web site http://rruff.info/. Accessed 12 Mar 2010.

American Museum of Natural History, Franklin, Sussex County, New Jersey, USA
Web site http://rruff.info/. Accessed 12 Mar 2010.

American Museum of Natural History, Dannemora, Uppsala Province, Sweden
Web site http://rruff.info/. Accessed 12 Mar 2010.

Characterization of corrosion products formed on steels in the first months of atmospheric exposure
Antunesa R.A., Costaa I., de Fariab D.L.A.
Materials Research, Vol.6, 2003, p.403 – 408.

Transport processes during the growth of oxide films at elevated temperature
Atkinson A.
Reviews of Modern Physics, Vol.57, No.2, 1985, p.437 – 470.

[B]

Thermal oxidation kinetics and oxide scale adhesion of Fe-15Cr alloys as a function of their silicon content
Bamba G., Wouters Y., Galerie A., Charlot F., Dellali.
Acta Materialia, Vol.54, 2006, p.3917 – 3922.

Thermochemical data of pure substances
Barin I.
VCH, Weinheim, Germany, 1989.

The single-crystal Raman spectra of nearly opaque materials-iron (III) oxide and chromium (III) oxide
Beattie I.R., Gilson T.R.
Journal of the Chemical Society, A5, 1970, p.980 – 986.

Micro-Raman investigation of iron oxide films and powders produced by sol-gel syntheses
Bersani D., Lottici P.P., Montenero A.
Journal of Raman Spectroscopy, Vol.30, 1999, p.355 – 360.

Influence of cooling rate on the structure and formation of oxide scale in low carbon steel wire rods during hot rolling
Bhattacharya R., Jha G., Kunda S., Shankar R., Gope N.
Surface & Coatings Technology, Vol.201, 2006, p.526 – 532.

Introduction to the high temperature oxidation of metals
Birks N., Meier G.H., Pettit F.S.
Cambridge University Press, New York, USA, 2006.

Raman studies of corrosion films grown on Fe and Fe-6Mo in pitting conditions
Boucherit N., Goff A.H., Joiret S.
Corrosion Science, Vol.32, 1991, p.497 – 507.

[C]

Infrared- and Raman-active phonons of magnetite, maghemite, and hematite: A computer simulation and spectroscopic study
Chamritski I., Burns G.
Journal of Physical Chemistry B, Vol.109, 2005, p.4965 – 4968.

Reactivity and surface modification of stainless steels used as electric interconnectors in high temperature solid oxide fuel cells
Chandra-ambhorn S.
Ph.D. Thesis, Institut polytechnique de Grenoble (Grenoble INP), France, 2006 (in English).

Effect of process parameters on mechanical adhesion of thermal oxide scale on hot-rolled low carbon steels
Chandra-ambhorn S., Ngamkham K., Jiratthanakul N.
Oxidation of Metals, Vol.80, Issue 1 – 2, 2013, p.61 – 72.

Application of the micro-tensile testing to investigate the adhesion of thermal oxide scales grown on AISI 441 stainless steel sheet oxidised in air and water vapour
Chandra-ambhorn S., Nilsonthi T., Madi Y., Galerie A.
Key Engineering Materials, Vol.410 – 411, 2009, p.187 – 193.

Oxidation kinetics, mechanical adhesion and pickling behaviour of thermal oxide scales on hot-rolled conventional and recycled steels
Chandra-ambhorn S., Nilsonthi T., Wouters Y., Galerie A.
Steel Research International, Vol.81, No.9, 2010, p.130 – 133.

Comments on the quantification of mechanical adhesion energy of thermal oxide scale on metallic substrate using tensile test
Chandra-amphorn S., Promdirek P., Lothongkum G., Wouters Y., Galerie A.
Materials Science Forum, Vol.595 – 598, 2008, p.907 – 914.

Determination of mechanical adhesion energy of thermal oxide scales on AISI 430Ti alloy using tensile test
Chandra-ambhorm S., Roussel-Dherbey F., Toscan F., Wouters Y., Galerie A., Dupeux M.
Materials Science and Technology, Vol.23, No.4, 2007, p.497 – 501.

Characterisation and pickling behaviour of thermal oxide scales on hot-rolled carbon steel strips produced from medium slabs
Chandra-Ambhorn S., Tungtrongpairoj J., Nilsonthi T., Somrak A.
Proceedings on the 216th ECS Meeting, The Electrochemical Society, Vienna, Austria, 2009.

Adhesion of oxide scales grown on ferritic stainless steels in solid oxide fuel cells temperature and atmosphere conditions
Chandra-Ambhorn S., Wouters Y., Antoni L., Toscan F., Galerie A.
Journal of Power Sources, Vol.171, 2007, p.688 – 695.

Oxide scale characterization of hot rolled coils by Raman spectroscopy technique
Chattopadhyay A., Bandyopadhyay N., Das A.K., Panigrahi M.K.
Scripta Materialia, Vol.52, 2005, p.211 – 215.

Role of silicon on oxide morphology and pickling behaviour of automotive steels
Chattopadhyay A., Chanda T.
Scripta Materialia, Vol.58, 2008, p.882 – 885.

A study of the scale structure of hot-rolled steel strip by simulated coiling and cooling
Chen R.Y., Yuen W.Y.D.
Oxidation of Metals, Vol.53, Nos.5/6, 2000, p.539 – 560.

Oxide-scale structures formed on commercial hot-rolled steel strip and their formation mechanisms
Chen R.Y., Yuen W.Y.D.
Oxidation of Metals, Vol.56, Nos.1/2, 2001, p.89 – 118.

Oxidation of low-carbon, low-silicon mild steel at 450 – 900°C under conditions relevant to hot-strip processing
Chen R.Y., Yuen W.Y.D.
Oxidation of Metals, Vol.57, Nos.1/2, 2002, p.53 – 79.

Review of the high-temperature oxidation of iron and carbon steels in air or oxygen
Chen R.Y., Yuen W.Y.D.
Oxidation of Metals, Vol.59, Nos.5/6, 2003, p.433 – 468.

Examination of oxide scales of hot rolled steel products
Chen R.Y., Yuen W.Y.D.
The Iron and Steel Institute of Japan (ISIJ) International, Vol.45, No.1, 2005, p.52 – 59.

Isothermal and step isothermal oxidation of copper-containing steels in air at 980 – 1220°C
Chen R.Y., Yuen W.Y.D.
Oxidation of Metals, Vol.63, Nos.3/4, 2005, p.145 – 168.

Oxide scales on hot-rolled steel strips
Chen R.Y., Yuen W.Y.D.
Publish in developments in high temperature corrosion and protection of materials book, Editor by W. Gao and Z. Li, Woodhead Publishing Limited, Cambridge, UK, 2008.

Mechanical properties of magnetite (Fe_3O_4), hematite (α-Fe_2O_3) and goethite (α-$FeO{\cdot}OH$) by instrumented indentation and molecular dynamics analysis
Chicot D., Mendoza J., Zaoui A., Louis G., Lepingle V., Roudet F., Lesage J.
Materials Chemistry and Physics, Vol.129, 2011, p.862 – 870.

Surface hot shortness due to copper in IF steel and effect of boron and phosphorus
Chihiro N., Hiroshi U., Koji S., Kentaro A., Masaharu H.
Tetsu to Hagane, The Iron and Steel Institute of Japan (ISIJ), Vol.89, No.3, 2003, p.322 – 328.

High-temperature tensile and creep properties of a ferritic stainless steel for interconnect in solid oxide fuel cell
Chiu Y.-T., Lin C.-K., Wu J.-C.
Journal of Power Sources, Vol.196, 2011, p.2005 – 2012.

CIT, Michigan, USA
Web site http://rruff.info/. Accessed 19 Mar 2010.

Single crystal Raman spectra of forsterite, fayalite, and monticellite
Cnopnras A.
American Mineralogist, Vol.76, 1991, p.1101 – 1109.

The iron oxides: Structure, properties, reactions, occurrences and uses
Cornell R.M., Schwertmann U.
2nd edition, Federal Republic of Germany, 2003.

Currier R., Cerro Huañaquino, Potosi Department, Bolivia
Web site http://rruff.info/. Accessed 19 Mar 2010.

[D]

Oxydation du fer pur dans les atmosphères diluées (Etude expérimentale et théorique)
Dauzat M., Henry P.
SCA 91/102, C.A. : G 0301, Fiche de Recherche : FOU 3, St Germain, avril 1991.

Dave Bunk Minerals, Park County, Colorado, USA
Web site http://rruff.info/. Accessed 5 Apr 2010.

Magnetite: Phonon modes and the Verwey transition
Degiorgi L., Blatter-Mörke I., Wachter P.
Physical Review B, Vol.35, 1987, p.5421 – 5424.

An investigation of phase transitions in rush layers using Raman spectroscopy
Dunnwald J., Otto A.
Corrosion Science, Vol.29, 1989, p.1167 – 1176.

[E]

Stress effects in high temperature oxidation of metals
Evans H.E.
International Materials Reviews, Vol.40, No.1, 1995, p.1 – 40.

[F]

Raman microspectroscopy of some iron oxides and oxyhydroxides
Faria D.L.A., Silva S.V., Oliveira M.T.
Journal of Raman Spectroscopy, Vol.28, 1997, p.873 – 878.

The influence of surface conditions in hot forming determined by ring upsetting: a numerical and experimental investigation
Fletcher J.D., Li Y.H., Beynon J.H., Sellars C.M.
Proceedings of the Institution of Mechanical Engineers, Vol.212J, 1998, p.453 – 465.

A Raman spectroscopic study of synthetic giniite
Frost R.L., Wills R.-A., Martens W.N.
Spectrochimica Acta Part A: Molecular and Biomolecular Spectroscopy, Vol.66, 2007, p.42 – 47.

The making, shaping and treating of steel
Fruehan R.J.
11th edition, Steelmaking and refining volume, The AISE Foundation, USA, 1998.

Effect of water vapor on the oxidation behavior of Fe-1.5Si in air at 1073 and 1273 K
Fukumoto M., Maeda S., Hayashi S., Narita T.
Oxidation of Metals, Vol.55, Num.5 – 6, 2001, p.401 – 422.

[G]

Measuring adhesion of Cr_2O_3 and Al_2O_3 scales on Fe-based alloys
Galerie A., Toscan F., N'Dah E., Przybylski K., Wouters Y., Dupeux M.
Materials Science Forum, Vol.461 – 464, 2004, p.631 – 638.

Distribution and characterization of high temperature air corrosion products on iron-chromium alloys by Raman microscopy
Gardiner D.J., Littleton C.J., Thomas K.M., Stratford K.N.
Oxidation of Metals, Vol.27, No.1 – 2, 1987, p.57 – 72.

Garske D., Bisbee, Cochise County, Arizona, USA
Web site http://rruff.info/. Accessed 5 Apr 2010.

Introduction to metallurgical thermodynamics
Gaskell D.R.
2nd edition, Taylor & Francis, London, UK, 1981.

Introduction to the thermodynamics of materials
Gaskell D.R.
4th edition, Taylor & Francis, New York, USA, 2009.

Infrared and Raman studies of the Verwey transition in magnetite
Gasparov L.V., Tanner D.B., Romero D.B., Berger H., Margaritondo G., Forró L.
Physical Review B, Vol.62, 2000, p.7939 – 7944.

Descaling ability of low-alloy steel wires depending on composition and rolling process
Genève D., Rouxel D., Pigeat P., Confente M.
Corrosion Science, Vol.52, 2010, p.1155 – 1166.

Review Poisson's ratio values for rocks
Gercek H.
International Journal of Rock Mechanics & Mining Sciences, Vol.44, 2007, p.1 – 13.

High-pressure studies of magnetite and magnesio-ferrite using synchrotron radiation
Gerward L., Olsen J.S.
Applied Radiation Isotopes, Vol.46, 1995, p.553 – 554.

Ironmaking and steelmaking: Theory and practice
Ghosh A., Chatterjee A.
Prentice Hall of India, New Delhi, India, 2008.

Study of the picklability of 1.8 mm hot-rolled steel strip in hydrochloric acid
Gines M.J.L., Benitez G.J., Perez T., Merli E., Firpo M.A., Egli W.
Latin American Applied Research, 2002, p.281 – 288.

Pressure-temperature stability studies of FeOOH using X-ray diffraction
Gleason A.E., Jeanloz R., Kunz M.
American Mineralogist, November-December, Vol.93, 2008, p.1882 – 1885.

Raman scattering in spinel structure ferrites
Graves P.R., Johnston C., Campaniello J.J.
Materials Research Bulletin, Vol.23, 1988, p.1651 – 1660.

[H]

Raman spectra of single crystal CuO
Hagemann H., Bill H., Sadowski W., Walker E., François M.
Solid State Communications, Vol.73, No.6, 1990, p.447 – 451.

The influence of small amounts of chromium and copper on the oxidation properties of iron
Hammar B., Vannerberg N.G.
Scandinavian Journal of Metallurgy, Vol.3, 1974, p.123 – 128.

Raman spectroscopy of iron oxides and (oxy)hydroxides at low laser power and possible applications in environmental magnetic studies
Hanesch M.
Geophysical Journal International, Vol.177, 2009, p.941 – 948.

Proceedings of the 3rd international conference on light scattering in solids, edited by M. Balkanski, R.C.C. Leite, S.P.S. Porto
Hart T.R., Adams S.B., Tempkin H.
Flammarion Sciences, Paris, 1976, p.254 – 259.

The elastic constants of crystals and other anisotropic materials
Hearmon R.F.S.
K.H. Hellwege, A.M. Hellwege (Eds.), Landolt-Börnstein Tables.(Eds.), Group III, vol.18, Springer-Verlag, Berlin, 1979, p.1 – 244.

[I]

Overview of steel industry in Thailand reported
Iron and Steel Institute of Thailand (ISIT)
2006, (Web site http://asiaeec-col.eccj.or.jp/. Accessed 27 Mar 2012).

Measurement of mechanical properties of oxide scales formed at high temperatures by resonance spectroscopy
Isao S., Shigenari H., Toshio N.
Division of Influence of Scale Properties on Surface Characteristics of Steels, The Iron and Steel Institute of Japan (ISIJ), 2005, p.19 – 26.

Effect of silicon on the steam oxidation resistance of a 9%Cr heat resistant steel
Ishitsuka T., Inoue Y., Ogawa H.
Oxidation of Metals, Vol.61, Nos.1/2, 2004, p.125 – 142.

Comportement des aciers inoxydables ferritiques stabilisés lors des étapes de recuit et décapage
Issartel J.
Thèse de Doctorat, Institut polytechnique de Grenoble (Grenoble INP), France, 2012 (in French).

[J]

Chemical imaging of iron oxides and oxyhydroxides using near infrared Raman imaging microscopy
Jallad K.N., Ben-Amotz D.
Materials Science and Technology, Vol.17, 2001, p.1479 – 1486.

Spectroscopic characterization of geological materials from the United Arab Emirates
Jallad K.N., Espada-Jallad C.
Arabian Journal of Geosciences, Vol.1, 2008, p.119 – 127.

Pickling kinetics of tertiary oxide scale formed on hot-rolled steel strip
Jatuphaksamphan Y.
Master Thesis, Chulalongkorn University (CU), Thailand, 2006 (in Thai).

Pickling kinetics of tertiary oxide scale formed on hot-rolled steel strip
Jatuphaksamphan Y., Phinichka N., Prapakorn K., Supradist M.
Journal of Metals, Materials and Minerals, Vol.20, No.1, 2010, p.33 – 39.

Enhanced bulk modulus and reduced transition pressure in γ-Fe_2O_3 nanocrystals
Jiang J.Z., Olsen J.S., Gerward L., Mørup S.
Europhysics Letters, Vol.44, No.5, 1998, p.620 – 626.

Characterisation of thin oxide scale and its surface roughness in hot metal rolling
Jiang Z.Y., Tieu A.K., Sun W.H., Tang J.N., Wei D.B.
Materials Science and Engineering A, Vol.435 – 436, 2006, p.434 – 438.

Reduction of oxide scale on hot-rolled strip steels by carbon monoxide
Jie S., De-ren W., Ye-dong H., Hui-bin Q., Gao W.
Materials Letters, Vol.62, 2008, p.3500 – 3502.

Evolution of microstructure and internal stresses in multi-phase oxide scales grown on (110) surfaces of iron single crystals at 650°C
Juricic C., Pinto H., Cardinali D., Klaus M., Genzel Ch., Pyzalla A.R.
Oxidation of Metals, Vol.73, 2010, p.115 – 138.

In-situ phase analysis and residual stresses of iron oxides grown during the early stages of oxidation on iron polycrystals and single crystals
Juricic C., Pinto H., Paulmann C., Rothkirch A., Wroblewski T., Pyzalla A.
Present status and future perspectives of SAXS and GISAXS experiments at HASYLAB, Hamburg, Germany, 2007, p.577 – 578.

Dependence of oxidation behavior and residual stresses in oxide layers on armco iron substrate surface condition
Juricic C., Pinto H., Wroblewski T., Pyzalla A.
Materials Science Forum, Vol.524 – 525, 2006, p.963 – 968.

[K]

Introduction to high temperature oxidation and corrosion
Khanna A.S.
ASM International, USA, 2002.

High temperature oxidation of low carbon steel
Kim B.-K.
Ph.D. Thesis, McGill University, Canada, 2003 (in English).

High temperature corrosion
Kofstad P.
Elsevier Applied Science, London, UK, 1988.

Behaviour of copper and nickel during high temperature oxidation of steel containing them
Kondo Y.
Materials Science Forum, Vol.522 – 523, 2006, p.53 – 60.

Suppression of surface hot shortness caused by copper during hot rolling
Kondo Y.
Materials Science Forum, Vol.696, 2011, p.183 – 188.

The tensile failure of mild steel oxides under hot rolling conditions
Krzyzanowski M., Beynon J.H.
Steel Research, Vol.70, 1999, p.22 – 27.

Finite element model of steel oxide failure during tensile testing under hot rolling conditions
Krzyzanowski M., Beynon J.H.
Materials Science and Technology, Vol.15, No.10, 1999, p.1191 – 1198.

Measurement of oxide properties for numerical evaluation of their failure under hot rolling conditions
Krzyzanowski M., Beynon J.H.
Journal of Materials Processing Technology, Vol.125 – 126, 2002, p.398 – 404.

Oxide scale behavior in high temperature metal processing
Krzyzanowski M., Beynon J.H., Farrugia D.C.J.
Wiley-VCH, Printed in the Federal Republic of Germany, 2010.

Analysis of secondary oxide-scale failure at entry into the roll gap
Krzyzanowski M., Beynon J.H., Sellars C.M.
Metallurgical and Materials Transactions B, Vol.31, Issue 6, 2000, p.1483 – 1490.

Metallurgical thermochemistry
Kubaschewski O., Evans E.Ll.
1st edition, Butterworth-Springer, 1951.

Surface hot-shortness of steels induced by a small amount of copper and tin from scrap steels and its suppression methods
Kunishige K., Hatano M.
Materials Science Forum, Vol.539 – 543, 2007, p.4113 – 4118.

[L]

Corrosion et chimie de surfaces des métaux
Landolt D.
Presses Polytechniques et Universitaires Romandes (PPUR), 1997.

Interface effects on magnetoresistance and magnetic-field-reduced Raman scattering in magnetite
Li J.-M., Huan A.C.H., Wang L., Du Y.-W., Feng D.
Physical Review B, Vol.61, 2000, p.6876 – 6878.

[M]

Isothermal compression of magnetite to 320 kbar and pressure-induced phase transformation
Mao H.-K., Takahashi T., Bassett W.A., Kinsland G.L., Merrill L.
Journal of Geophysical Research, Vol.79, No.8, 1974, P.1165 – 1170.

Effects of pressure and isotopic substitution on the Raman spectrum of α-Fe_2O_3: Identification of two-magnon scattering
Massey M.J., Baier U., Merlin R., Weber W.H.
Physical Review B, Vol.41, 1990, p.7822 – 7827.

A Raman study of the systems $Fe_{3-x}Cr_xO_4$ and $Fe_{2-x}Cr_xO_3$
McCarty K.F., Boehme D.R.
Journal of Solid State Chemistry, Vol.79, 1989, p.19 – 27.

Phénomènes d'oxydation à la tôlerie forte de Dunkerque (GTSI) I. Caractérisation des calamines formées au cours de réchauffage
Métivier J., Lanteri V.
SCA 91/43, Fiche de Recherche PPF105, Note intermédiaire n°1, St Germain, Février 1991.

Cover cracking as a function of rebar corrosion: Part 2-Numerical model
Molina F.J., Alonso C., Andrade C.
Materials and Structures, Vol.26, 1993, p.532 – 548.

Blast cleaning technology
Momber A.
1st edition, Springer, 2008.

The effect water vapour on the oxidation of high speed steel, kinetics and scale adhesion
Monteiro M.J., Saunders S.R.J., Rizzo F.C.
Oxidation of Metals, Vol.75, No.1 – 2, 2011, p.57 – 76.

Properties of technical and engineering ceramics
Morrel R.
Handbook, HSMO, London, 1987.

Adhesion of thermal oxide scales grown on ferritic stainless steels measured using the inverted blister test
Mougin J., Dupeux M., Antoni L., Galerie A.
Materials Science and Engineering A, Vol.359, 2003, p.44 – 51.

Inverted blister test to measure adhesion energy of thermal oxide scales on metals or alloys
Mougin J., Dupeux M., Galerie A., Antoni L.
Materials Science and Technology, Vol.18, No.10, 2002, p.1217 – 1220.

Influence of cooling rate and initial surface roughness on the residual stresses in chromia scales thermally grown on pure chromium
Mougin J., Lucazeau G., Galerie A., Dupeux M.
Materials Science and Engineering A, Vol.308, 2001, p.118 – 123.

[N]

The tensile failure of nickel oxide scales at ambient and at growth temperature
Nagl M.M., Saunders S.R.J., Evans W.T., Hall D.J.
Corrosion Science, Vol.35, No.5 – 8, 1993, p.965 – 977.

Failure characteristics of scales formed on Si-containing low carbon steels during cooling -influences of cooling rate and water vapor-
Nakata H., Yamauchi A., Taniguchi S., Shon II.-R., Choi J.-W., Kurokawa K.
Materials Science Forum, Vol.696, 2011, p.101 – 106.

Development of tensile test to investigate mechanical adhesion of thermal oxide scales on hot-rolled steel strips produced using different finishing temperatures
Ngamkham K., Niltawach S., Chandra-ambhorn S.
Key Engineering Materials, Vol.462 – 463, 2011, p.407 – 412.

Adhesion of thermal oxide scales on hot-rolled conventional and recycled steels
Nilsonthi T., Chandra-ambhorn S., Wouters Y., Galerie A.
Oxidation of Metals, Vol.79, Issue 3 – 4, 2013, p.325 – 335.

Effect of silicon on formation and mechanical adhesion of thermal oxide scale grown on low carbon steels in a hot-rolling line
Nilsonthi T., Tungtrongpairoj J., Chandra-ambhorn S., Wouters Y., Galerie A.
Steel Research International, 2012, p.987 – 990.

Effects of Si content on the oxidation behavior of Fe-Si alloys in air
Nishimoto T., Honda K., Kondo Y., Uemura K.
Materials Science Forum, Vol.696, 2011, p.126 – 131.

[O]

Characterization of iron oxides commonly formed as corrosion products on steel
Oh S.J., Cook D.C., Townsend H.E.
Hyperfine Interactions, Vol.112, 1998, p.59 – 65.

Raman spectroscopy of thin corrosion films on iron at 100 to 150C in air
Ohtsuka T., Kubo K., Sato N.
Corrosion, Vol.42, 1986, p.476 – 481.

A study of the crystal structure of Fe_2O_3 in the pressure range up to 65 GPa using synchrotron radiation
Olsen J.S., Cousins C.S.G., Gerward L., Jhans H., Sheldon B.J.
Physica Scripta, Vol.43, 1991, p.327 – 330.

An investigation of surface hot shortness in low carbon steel
O'Neill D.S.
Ph.D. Thesis, The University of New South Wales, Australia, 2002 (in English).

Pickling of hot rollered austenitic stainless steel AISI 304
Onsanit P.
Master Thesis, King Mongkut's Institute of Technology North Bangkok (KMITNB), Thailand, 2006 (in Thai).

Mechanical properties of an iron oxide formed by corrosion in reinforced concrete structures
Ouglova A., Berthaud Y., Francois M., Foct F.
Corrosion Science, Vol.48, 2006, p.3988 – 4000.

[P]

Comparison of growth stress measurements with modelling in thin iron oxide films
Panicaud B., Grosseau-Poussard J.L., Girault P., Dinhut J.F., Thiaudière D.
Applied Surface Science, Vol.252, 2006, p.8414 – 8420.

In-situ stress determination in thermally-grown iron oxide scales using X-ray diffraction of synchrotron radiation
Panicaud B., Grosseau-Poussard J.L., Renault P.O., Dinhut J.F., Thiaudière D., Gailhanou M.
Journal of Neutron Research, Vol.12 (1 – 3), 2004, p.57 – 61.

Measurement of stress in phosphated-iron oxide layers by In-situ diffraction of synchrotron radiation
Panicaud B., Renault P.O., Grosseau-Poussard J.L., Dinhut J.F., Thiaudière D., Gailhanou M.
Materials Science Forum, Vol.404 – 407, 2002, p.809 – 816.

Corrosion behaviour of different hot rolled steels
Pérez F.J., Martínez L., Hierro M.P., Gómez C., Portela A.L., Pucci G.N., Duday D., Lecomte-Beckers J., Greday Y.
Corrosion Science, Vol.48, 2006, p.472 – 480.

Experimental study and numerical simulation of iron oxide scales mechanical behaviour in hot rolling
Picqué B.
Ph.D. Thesis, Ecole des Mines de Paris, France, 2004 (in English).

Mechanical behaviour of iron oxide scale: Experimental and numerical study
Picqué B., Bouchard P.-O., Montmitonnet P., Picard M.
Wear, Vol.260, 2006, p.231 – 242.

Pinch W.W., Zinc Corporation of America mine, Balmat, New York, USA
Web site http://rruff.info/. Accessed 5 Apr 2010.

Prewitt C.
Web site http://rruff.info/. Accessed 5 Mar 2010.

Fragmentation of diffusion zone in high-temperature oxidation of copper
Prisedsky V.V., Vinogradov V.M.
Journal of Solid State Chemistry, Vol.177, 2004, p.4258 – 4268.

[R]

Thermodynamics of materials: Volume II
Ragone D.V.
MIT Series in Materials Science and Engineering, John Wiley & Sons, 1995.

Characterisation of 'rolled-in', 'fragmented' and 'red' scale formation during secondary processing of steels
Raman R.K.S.
Engineering Failure Analysis, Vol.13, 2006, p.1044 – 1050.

Transient oxidation in Fe-Cr-Ni alloys: A Raman-scattering study
Renusch D., Veal B., Natesan K., Grimsditch M.
Oxidation of Metals, Vol.46, No.5 – 6, 1996, p.365 – 381.

Rossman G.R.
Web site http://rruff.info/. Accessed 9 Mar 2010.

Rossman G.R., Kimberly, South Africa
Web site http://rruff.info/. Accessed 5 Mar 2010.

[S]

In situ measurement of Young's modulus of FeO scale formed on pure iron at 973 – 1273 K by acoustic resonance method
Saeki I., Ohno T., Sakai O., Niya T., Sato T.
Corrosion Science, Vol.53, 2011, p.458 – 463.

The oxide handbook
Samsonov G.V.
New York, IFI/Plenum, 1973.

Les mécanismes de la corrosion sèche: une approche cinétique
Sarrazin P., Galerie A., Fouletier J.
EDP Science, France, 2000.

Mechanisms of high temperature corrosion: a kinetic approach
Sarrazin P., Galerie A., Fouletier J.
Materials Science Foundations, 36 – 37, Trans Tech Publications, Stafa-Zürich, CH, Switzerland, 2008.

Measurements of Raman lines in silica, dimethyl-methylphosphonate and methyl salicylate
Schönbächler N., Lüthy W.
Institute of Applied Physics, University of Bern, Switzerland, 2011.

Schlepp E.
Web site http://rruff.info/. Accessed 5 Mar 2010.

Schlepp E., Argentina
Web site http://rruff.info/. Accessed 19 Mar 2010.

Scott M., Little Lake, Lake County, California, USA
Web site http://rruff.info/. Accessed 9 Mar 2010.

Scott M., Pike's Peak, Teller County, Colorado, USA
Web site http://rruff.info/. Accessed 12 Mar 2010.

Scott M., Jacupiranga Pegmatite, Sao Paulo State, Brazil
Web site http://rruff.info/. Accessed 24 Mar 2010.

Scott M., Barberton Mountain, Transvaal, South Africa
Web site http://rruff.info/. Accessed 24 Mar 2010.

Reproduction and deformation characteristics of oxide scale in hot rolling using vacuum rolling mill
Segawa A.
Materials Science Forum, Vol.696, 2011, p.150 – 155.

Nano-mechano-electrochemistry of passive metal surfaces
Seo M., Chiba M.
Electrochimica Acta, Vol.47, 2001, p.319 – 325.

Shannon R.D.
Web site http://rruff.info/. Accessed 5 Mar 2010.

Raman spectroscopic study of magnetite ($FeFe_2O_4$): A new assignment for the vibrational spectrum
Shebanova O.N., Lazor P.
Journal of Solid State Chemistry, Vol.174, 2003, p.424 – 430.

Raman study of magnetite (Fe_3O_4): Laser-induced thermal effects and oxidation
Shebanova O.N., Lazor P.
Journal of Raman Spectroscopy, Vol.34, 2003, p.845 – 852.

Suppression of surface hot shortness due to Cu in recycled steels
Shibata K., Seo S-J., Kaga M., Uchino H., Sasanuma A., Asakura K., Nagasaki C.
Materials Transactions, Vol.43, No.3, 2002, p.292 – 300.

Shigley J., Coso Hot Springs, Inyo County, California, USA
Web site http://rruff.info/. Accessed 5 Mar 2010.

Raman spectroscopy of Fe_2O_3 to 62 GPa
Shim S.H., Duffy T.S.
American Mineralogist, Vol.87, 2001, p.318 – 326.

Raman scattering and photoluminescence studies on Cu_2O
Solache-Carranco H., Juárez-Díaz G., Galván-Arellano M., Martínez-Juárez J., Romero-Paredes G., Peña-Sierra R.
5th International Conference on Electrical Engineering, Computing Science and Automatic Control (CCE), 2008, p.421 – 424.

A study of structure and picklability of thermal oxide scale on hot-rolled steel strip produced from a recycled slab
Somphakdee T., Nilsonthi T., Chandra-ambhorn S.
The 4th Thailand Metallurgy Conference, Nakhon Ratchasima, Thailand, 2010.

Texture evolution of tertiary oxide scale during steel plate finishing hot rolling simulation tests
Suárez L., Petrov R., Kestens L., Lamberigts M., Houbaert Y.
Materials Science Forum, Vol.550, 2007, p.557 – 562.

Oxidation of ultra low carbon and silicon bearing steels
Suárez L., Rodríguez-Calvillo P., Houbaert Y., Colás R.
Corrosion Science, Vol.52, 2010, p.2044 – 2049.

[T]

Oxidation behavior and scale properties on the Si containing steels
Takeda M., Onishi T.
Materials Science Forum, Vol.522 – 523, 2006, p.477 – 488.

Physical properties of iron-oxide scales on Si-containing steels at high temperature
Takeda M., Onishi T., Nakakubo S., Fujimoto S.
Materials Transactions, Vol.50, No.9, 2009, p.2242 – 2246.

Characteristics of scale/substrate interface area of Si-containing low-carbon steels at high temperatures
Taniguchi S., Yamamoto K., Megumi D., Shibata T.
Materials Science and Engineering A, Vol.308, 2001, p.250 – 257.

Private communication
Thai steelmakers
2009.

Investigations of cycle behaviour of the contact mass in the RESC process for hydrogen production
Thaler M., Hacker V., Anilkumar M., Albering J., Besenhard J.O., Schröttner H., Schmied M.
International Journal of Hydrogen Energy, Vol.31, 2006, p.2025 – 2031.

Raman spectra of possible corrosion products of iron
Thibeau R.J., Brown C.W., Heidersbach R.H.
Applied Spectroscopy, Vol.32, No.6, 1978, p.532 – 535.

Raman spectroscopy and XPS investigations of anodic corrosion films formed on Fe-Mo alloys in alkaline solutions
Thierry D., Persson D., Leygraf C., Boucherit N., Goff A.H.
Corrosion Science, Vol.32, 1991, p.273 – 284.

Laser Raman spectroscopic studies of the surface oxides formed on iron chromium alloys at elevated temperatures
Tjong S.C.
Materials Research Bulletin, Vol.18, 1983, p.157 – 165.

Optimisation conjointe de l'adhérence des couches d'oxydes et des cinétiques d'oxydation thermique sur aciers inoxydables
Toscan F.
Thèse de Doctorat, Institut polytechnique de Grenoble (Grenoble INP), France, 2004 (in French).

Oxidation kinetics and scale spallation of iron-chromium alloys with different titanium contents
Toscan F., Antoni L., Wouters Y., Dupeux M., Galerie A.
Materials Science Forum, Vol.461 – 464, 2004, p.705 – 712.

Study of thermal oxide scales on hot rolled carbon steel strips produced from EAF-type slab and different Si containing BF-type slabs
Tungtrongpairoj J.
Master Thesis, King Mongkut's University of Technology North Bangkok (KMUTNB), Thailand, 2009 (in English).

Twaites L., Florence mine, Egremont, Cumbria, England
Web site http://rruff.info/. Accessed 19 Mar 2010.

Twaites L., Merrry Widow mine, Vancouver Island, British Columbia, Canada
Web site http://rruff.info/. Accessed 19 Mar 2010.

[U]

Effects of C and P on surface hot shortness of steel due to Cu mixed from steel scrap
Uchino H., Nagasaki C., Kaga M., Seo S-J., Asakura K., Shibata K.
Journal of Advanced Science, Vol.13, No.3, 2001, p.260 – 264.

University of Arizona Mineral Museum, Lavender Pit, Bisbee, Warren District, Cochise County, Arizona, USA
Web site http://rruff.info/. Accessed 5 Mar 2010.

University of Arizona Mineral Museum, Papago Indian Reservation, Arizona, USA
Web site http://rruff.info/. Accessed 19 Mar 2010.

University of Arizona Mineral Museum, Itabira, Minas Gerais, Brazil
Web site http://rruff.info/. Accessed 19 Mar 2010.

[V]

Temperature-dependent light-scattering studies of the Verwey transition and electronic disorder in magnetite
Verble J.L.
Physical Review, Vol.9, 1974, p.5236 – 5248.

[W]

Oxidation behavior of pure copper in oxygen and/or water vapor at intermediate temperature
Wang J.-P., Cho W.D.
ISIJ International, Vol.49, No.12, 2009, p.1926 – 1931.

X-ray diffraction and Raman spectroscopic study of nanocrystalline CuO under pressures
Wang Z., Pischedda V., Saxena S.K., Lazor P.
Solid State Communications, Vol.121, Issue 5, 2002, p.275 – 279.

Web site http://hytechcontrols.com/. Accessed 22 Mar 2012.

Web site http://ssi-steel.com/. Accessed 22 Mar 2012.

Web site http://g-steel.com/. Accessed 22 Mar 2012.

Web site http://pvd-coatings.co.uk/. Accessed 3 April 2012.

Web site http://courses.chem.indiana.edu/c360/documents/thermodynamicdata.pdf/. Accessed 11 May 2012.

[Y]

Crystal structures of spinel polymorphs of Fe_2SiO_4 and Ni_2SiO_4
Yagi T., Marumo F., Akimoto S.I.
American Minerulogist, Vol.59, 1974, p.486 – 490.

Effects of Si and its content on the scale formation on hot-rolled steel strips
Yang Y.-L., Yang C.-H., Lin S.-N., Chen C.-H., Tsai W.-T.
Materials Chemistry and Physics, Vol.112, 2008, p.566 – 571.

High temperature oxidation and corrosion of metals
Young D.J.
Elsevier Science, Great Britain, 2008.

[Z]

Characterization and properties of oxide scales on hot-rolled strips
Zhang M., Shao G.
Materials Science and Engineering A, Vol.452 – 453, 2007, p.189 – 193.

A study of the initial oxidation of copper in 0.1 MPa oxygen and the effect of purity by metallographic methods
Zhu Y., Mimura K., Isshiki M.
Corrosion Science, Vol.46, 2004, p.2445 – 2454.

A study of the formation and penetration of the molten copper-rich phase in iron with the addition of nickel and tin
Zou Y., Langer E.W.
Materials Science and Engineering, Vol.A110, 1989, p.203 – 208.

APPENDIX I

X-RAY DIFFRACTION (XRD)

Hematite (Fe_2O_3)

89-0599 Quality: C
CAS Number:
Molecular Weight: 159.69
Volume[CD]: 301.15
Dx: 5.283 Dm:
Sys: Rhombohedral
Lattice: Rhomb-centered
S.G.: R$\bar{3}$c (167)
Cell Parameters:
a 5.032 b c 13.733
α β γ

I/Icor: 3.09
Rad: CuKa1
Lambda: 1.54060
Filter:
d-sp: calculated
ICSD #: 082137
Mineral Name:
Hematite, syn

Fe2 O3
Iron Oxide
Ref: Calculated from ICSD using POWD-12++
Ref: Sadykov, V.A et al., J. Solid State Chem., 123, 191 (1996)

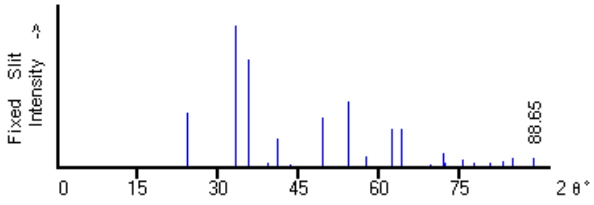

2θ	Int-f	h	k	l	2θ	Int-f	h	k	l	2θ	Int-f	h	k	l
24.169	375	0	1	2	57.670	75	0	1	8	78.843	10	2	2	3
33.193	999 *	1	0	4	62.491	264	2	1	4	79.552	1	1	3	1
35.656	750	1	1	0	64.050	266	3	0	0	80.650	16	3	1	2
39.333	25	0	0	6	66.092	3	1	2	5	80.801	28	1	2	8
40.896	203	1	1	3	69.676	19	2	0	8	83.062	45	0	2	10
43.542	22	2	0	2	72.045	94	1	0	10	84.612	3	0	0	12
49.506	347	0	2	4	72.371	23	1	1	9	85.012	62	1	3	4
54.126	460	1	1	6	75.271	3	2	1	7	88.648	65	2	2	6
56.201	6	2	1	1	75.515	55	2	2	0					
57.493	27	1	2	2	77.815	23	0	3	6					

Magnetite (Fe_3O_4)

87-2334 Quality: C
CAS Number:
Molecular Weight: 231.54
Volume[CD]: 592.28
Dx: 5.193 Dm:
Sys: Cubic
Lattice: Face-centered
S.G.: Fd$\bar{3}$m (227)
Cell Parameters:
a 8.398 b c
α β γ

I/Icor: 5.08
Rad: CuKa1
Lambda: 1.54060
Filter:
d-sp: calculated
ICSD #: 084098
Mineral Name:
Magnetite, syn

Fe3 O4
Iron Oxide
Ref: Calculated from ICSD using POWD-12++
Ref: Tsukimura, K., Sasaki, S., Kimizuka, N., Jpn. J. Appl. Phys. Part 1, 36, 3609 (1997)

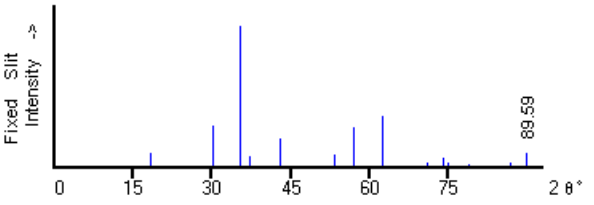

2θ	Int-f	h	k	l	2θ	Int-f	h	k	l	2θ	Int-f	h	k	l
18.283	100	1	1	1	53.405	84	4	2	2	74.952	28	6	2	2
30.073	295	2	2	0	56.929	278	5	1	1	78.912	21	4	4	4
35.422	999 *	3	1	1	62.513	360	4	4	0	81.845	4	5	5	1
37.053	77	2	2	2	65.728	7	5	3	1	86.692	28	6	4	2
43.049	204	4	0	0	70.917	27	6	2	0	89.586	96	7	3	1
47.134	5	3	3	1	73.952	67	5	3	3					

Wüestite (FeO)

89-0687 Quality: C
CAS Number:
Molecular Weight: 71.85
Volume[CD]: 80.96
Dx: 5.895 Dm:
Sys: Cubic
Lattice: Face-centered
S.G.: Fm3m (225)
Cell Parameters:
a 4.326 b c
α β γ

I/Icor: 5.01
Rad: CuKa1
Lambda: 1.54060
Filter:
d-sp: calculated
ICSD #: 082233

Fe O
Iron Oxide
Ref: Calculated from ICSD using POWD-12++
Ref: Fjellvag, H et al., J. Solid State Chem., 124, 52 (1996)

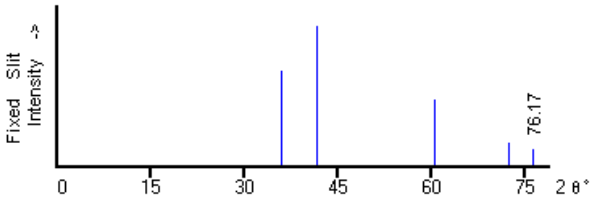

2θ	Int-f	h	k	l	2θ	Int-f	h	k	l	2θ	Int-f	h	k	l
35.927	680	1	1	1	60.482	466	2	2	0	76.170	115	2	2	2
41.725	999 *	2	0	0	72.395	165	3	1	1					

Iron (Fe)

87-0721 Quality: C
CAS Number:
Molecular Weight: 55.85
Volume[CD]: 23.55
Dx: 7.877 Dm: 7.870
Sys: Cubic
Lattice: Body-centered
S.G.: Im3m (229)
Cell Parameters:
a 2.866 b c
α β γ

I/Icor: 10.77
Rad: CuKa1
Lambda: 1.54060
Filter:
d-sp: calculated
ICSD #: 064998
Mineral Name:
Iron

Fe
Iron
Ref: Calculated from ICSD using POWD-12++, (1997)
Ref: Owen, E.A., Williams, G.I., J. Sci. Instrum., 31, 49 (1954)

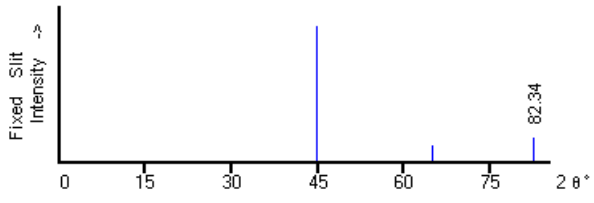

2θ	Int-f	h	k	l	2θ	Int-f	h	k	l	2θ	Int-f	h	k	l
44.677	999 *	1	1	0	65.028	115	2	0	0	82.342	174	2	1	1

87-0320 Quality: C

CAS Number:

Molecular Weight: 203.78
Volume[CD]: 280.48
Dx: 4.826 Dm:

Sys: Orthorhombic
Lattice: Primitive
S.G.: Pbnm (62)
Cell Parameters:
a 4.739 b 9.899 c 5.979
α β γ

I/Icor: 1.52
Rad: CuKa1
Lambda: 1.54060
Filter:
d-sp: calculated

ICSD #: 054034

Mineral Name:
Fayalite, syn

Non-Ambient Pressure

Fe2 (Si O4)
Iron Silicate
Ref: Calculated from ICSD using POWD-12++
Ref: Kudoh, Y., Takeda, H., Physica B+C (Amsterdam), 139, 333 (1986)

Fayalite (Fe_2SiO_4)

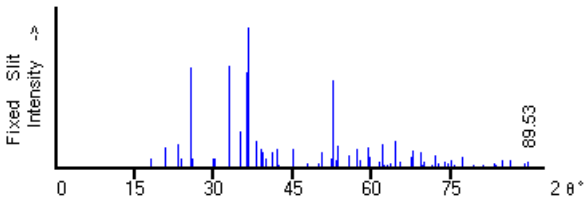

2θ	Int-f	h	k	l	2θ	Int-f	h	k	l	2θ	Int-f	h	k	l
17.907	59	0	2	0	59.229	140	1	6	0	78.743	3	2	7	0
20.764	137	1	1	0	59.505	76	0	4	3	78.947	2	0	8	1
23.312	163	0	2	1	60.579	1	3	0	1	79.216	20	2	5	3
23.941	58	1	0	1	60.931	1	2	5	0	79.792	5	3	2	3
25.598	706	1	1	1	61.372	43	3	1	1	80.091	3	1	8	0
26.010	62	1	2	0	61.461	31	1	6	1	80.676	1	2	7	1
29.864	66	0	0	2	61.461	31	2	1	3	81.110	19	4	0	0
30.058	57	1	2	1	61.577	32	3	2	0	81.812	2	4	1	0
33.053	717	1	3	0	62.040	166	0	0	4	82.017	2	1	8	1
35.038	254	0	2	2	62.479	21	2	4	2	83.013	6	0	2	5
36.271	285	0	4	0	63.085	21	2	5	1	83.301	27	1	0	5
36.393	672	1	3	1	63.718	24	3	2	1	83.301	27	3	3	3
36.653	999 *	1	1	2	64.455	191	0	6	2	83.498	22	1	5	4
37.942	189	2	0	0	65.139	10	0	2	4	83.729	8	4	1	1
39.057	131	2	1	0	65.454	41	3	3	0	83.966	6	4	2	0
39.373	103	0	4	1	66.177	10	1	1	4	83.966	6	1	1	5
40.010	60	1	2	2	67.528	73	3	3	1	84.714	7	0	8	2
41.115	103	1	4	0	67.696	116	3	1	2	84.901	54	3	5	2
41.984	128	2	1	1	67.696	116	1	6	2	84.901	54	3	6	0
42.252	20	2	2	0	68.434	2	1	2	4	85.820	3	4	2	1
43.930	1	1	4	1	69.284	107	1	7	0	86.346	50	2	4	4
45.140	132	1	3	2	69.284	107	2	5	2	86.346	50	2	7	2
47.185	1	2	3	0	69.780	16	1	5	3	86.833	8	3	6	1
47.667	26	0	4	2	69.928	38	3	2	2	86.833	8	1	7	3
49.016	5	2	0	2	70.691	9	3	4	0	87.390	2	4	3	0
49.580	6	1	0	3	71.370	17	1	7	1	87.748	4	1	8	2
49.726	6	2	3	1	71.370	17	2	6	1	88.173	11	0	6	4
49.880	28	1	5	0	72.120	82	1	3	4	88.173	11	3	4	3
49.880	28	2	1	2	72.695	23	3	4	1	88.754	4	4	0	2
50.485	108	1	1	3	73.582	2	3	3	2	89.223	26	2	8	0
51.640	7	1	4	2	74.033	35	0	4	4	89.223	26	4	3	1
52.324	65	1	5	1	74.618	31	0	6	3	89.527	41	1	3	5
52.598	616	2	2	2	75.079	53	2	0	4	89.527	41	4	1	2
53.134	54	1	2	3	75.796	12	2	1	4					
53.497	150	2	4	0	77.002	7	3	0	3					
55.829	85	2	4	1	77.002	7	0	8	0					
56.849	10	2	3	2	77.299	75	1	7	2					
57.358	134	1	3	3	77.299	75	2	6	2					
57.939	51	0	6	1	77.933	6	2	2	4					
59.229	140	1	5	2	78.588	1	3	4	2					

89-5416 Quality: C

CAS Number:

Molecular Weight: 60.08
Volume[CD]: 1853.97
Dx: 1.722 Dm: 1.662

Sys: Anorthic
Lattice: Body-centered
S.G.: I$\bar{1}$
Cell Parameters:

a 14.76	b 18.17	c 7.382
α 89.140	β 110.67	γ 90.945

I/Icor: 3.71
Rad: CuKa1
Lambda: 1.54060
Filter:
d-sp: calculated

ICSD #: 086637

Also called:
Silica ITQ-9, syn

Si O2
Silicon Oxide

Silicon Oxide (SiO_2)

Ref: Calculated from ICSD using POWD-12++
Ref: Villaescusa, L.A., Barrett, P.A., Camblor, M.A., Chem. Commun. (Cambridge), 1998, 2329 (1998)

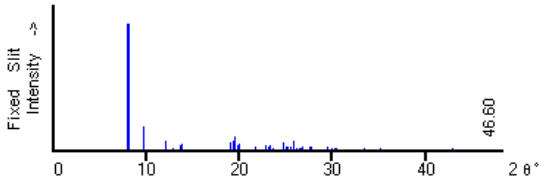

2θ	Int-f	h	k	l	2θ	Int-f	h	k	l	2θ	Int-f	h	k	l
7.985	992	$\bar{1}$	1	0	28.315	3	$\bar{2}$	5	1	37.088	3	0	$\bar{7}$	1
8.078	999 *	1	1	0	28.580	3	3	$\bar{2}$	1	37.088	3	$\bar{5}$	3	2
9.724	189	0	2	0	28.580	3	$\bar{1}$	$\bar{3}$	2	37.231	8	$\bar{1}$	0	3
12.127	76	$\bar{1}$	0	1	28.843	1	$\bar{2}$	$\bar{5}$	1	37.375	5	$\bar{2}$	7	1
12.805	14	2	0	0	29.148	4	1	1	2	37.983	1	3	$\bar{1}$	2
13.660	45	0	1	1	29.208	4	1	$\bar{1}$	2	37.983	1	1	5	2
13.750	56	0	$\bar{1}$	1	29.462	32	$\bar{4}$	0	2	38.134	1	$\bar{3}$	2	3
15.284	4	$\bar{2}$	1	1	29.462	32	0	6	0	38.223	2	1	$\bar{5}$	2
15.440	11	$\bar{1}$	2	1	29.887	12	$\bar{3}$	3	2	38.223	2	$\bar{2}$	6	2
15.440	11	2	$\bar{1}$	1	30.278	22	$\bar{5}$	0	1	38.448	2	$\bar{1}$	2	3
15.695	7	$\bar{1}$	2	1	30.374	21	$\bar{3}$	$\bar{3}$	2	38.448	2	3	$\bar{2}$	3
15.889	5	$\bar{1}$	3	0	30.849	1	$\bar{4}$	2	2	38.554	2	2	$\bar{4}$	2
16.031	5	$\bar{2}$	2	0	31.136	2	$\bar{3}$	5	0	38.554	2	$\bar{6}$	0	2
16.031	5	1	3	0	31.136	2	$\bar{2}$	$\bar{4}$	2	38.796	1	$\bar{4}$	1	3
16.196	2	2	2	0	31.215	1	$\bar{4}$	$\bar{2}$	2	38.938	1	$\bar{2}$	$\bar{6}$	2
16.196	2	1	0	1	31.510	2	$\bar{3}$	5	0	38.938	1	$\bar{4}$	$\bar{1}$	3
19.002	67	1	$\bar{2}$	1	31.771	2	$\bar{5}$	2	1	39.123	3	6	0	0
19.002	67	$\bar{3}$	0	1	31.771	2	$\bar{1}$	6	1	39.123	3	5	0	1
19.379	73	0	3	1	32.159	5	$\bar{2}$	$\bar{6}$	0	39.263	2	$\bar{6}$	3	1
19.570	113	0	$\bar{4}$	0	32.159	5	$\bar{1}$	$\bar{6}$	1	39.294	2	2	3	3
19.570	113	0	$\bar{3}$	1	32.343	9	$\bar{4}$	4	0	39.294	2	0	$\bar{6}$	2
19.815	37	$\bar{3}$	1	0	32.343	9	2	$\bar{6}$	0	39.473	3	0	$\bar{1}$	3
19.929	52	3	1	0	32.728	7	0	$\bar{4}$	2	39.610	1	$\bar{3}$	7	0
20.493	2	$\bar{2}$	3	1	32.728	7	4	4	0	39.610	1	0	8	0
20.893	1	$\bar{2}$	$\bar{3}$	1	32.808	8	2	0	2	39.717	1	$\bar{2}$	$\bar{3}$	3
21.222	1	$\bar{3}$	$\bar{2}$	1	32.808	8	5	1	0	39.717	1	0	$\bar{6}$	2
21.711	24	2	$\bar{1}$	1	33.154	3	4	$\bar{1}$	1	40.044	1	$\bar{3}$	7	0
21.711	24	$\bar{2}$	1	1	33.283	6	4	1	1	40.044	1	$\bar{6}$	$\bar{2}$	2
22.868	45	$\bar{1}$	$\bar{4}$	1	33.283	6	3	$\bar{4}$	1	40.144	1	$\bar{3}$	$\bar{6}$	1
23.218	34	$\bar{1}$	$\bar{4}$	1	33.411	13	3	$\bar{4}$	1	40.255	1	$\bar{6}$	2	0
23.283	37	$\bar{2}$	4	0	33.863	9	1	$\bar{6}$	1	40.343	1	3	$\bar{6}$	1
23.544	17	$\bar{2}$	4	0	33.863	9	$\bar{5}$	1	2	40.343	1	5	$\bar{2}$	1
24.114	4	$\bar{3}$	3	0	34.073	1	$\bar{5}$	$\bar{1}$	2	40.477	1	5	2	1
24.398	10	$\bar{2}$	0	2	34.327	1	2	$\bar{2}$	2	40.477	1	6	2	0
24.398	10	3	3	0	34.327	1	$\bar{2}$	$\bar{2}$	2	40.587	2	3	$\bar{3}$	2
24.672	31	$\bar{1}$	1	2	34.497	3	$\bar{1}$	5	2	40.587	2	$\bar{3}$	$\bar{3}$	2
24.795	57	$\bar{4}$	1	1	34.497	3	$\bar{4}$	$\bar{5}$	1	40.747	2	$\bar{5}$	$\bar{5}$	0
24.795	57	$\bar{1}$	$\bar{1}$	2	34.955	5	$\bar{1}$	$\bar{5}$	2	40.747	2	2	$\bar{7}$	1
24.969	23	$\bar{4}$	$\bar{1}$	1	34.955	5	$\bar{3}$	6	1	40.853	2	$\bar{2}$	7	1
25.238	25	$\bar{1}$	5	0	35.059	5	$\bar{1}$	7	0	41.241	2	$\bar{5}$	0	3
25.453	30	1	5	0	35.208	12	$\bar{4}$	4	2	41.241	2	$\bar{5}$	5	0
25.453	30	1	$\bar{4}$	1	35.208	12	1	7	0	41.394	3	$\bar{1}$	8	1
25.530	27	1	$\bar{4}$	1	35.517	1	$\bar{5}$	3	0	41.463	3	4	5	1
25.773	72	4	0	0	35.606	1	$\bar{3}$	$\bar{6}$	1	41.606	2	$\bar{5}$	5	2
25.773	72	$\bar{2}$	3	1	35.857	3	$\bar{5}$	3	0	41.665	3	$\bar{2}$	8	0
26.161	12	$\bar{2}$	$\bar{2}$	2	35.857	3	$\bar{4}$	$\bar{4}$	2	41.665	3	$\bar{4}$	$\bar{3}$	3
26.470	16	$\bar{2}$	$\bar{2}$	2	35.990	5	$\bar{5}$	$\bar{4}$	1	41.807	5	$\bar{1}$	$\bar{8}$	1
26.578	19	$\bar{3}$	1	2	35.990	5	4	$\bar{3}$	1	41.807	5	$\bar{3}$	4	3
26.769	26	$\bar{3}$	$\bar{1}$	2	36.158	3	4	3	1	41.976	3	1	0	3
26.769	26	3	0	1	36.572	5	$\bar{5}$	$\bar{3}$	2	41.976	3	2	$\bar{8}$	0
27.110	2	$\bar{3}$	4	1	36.572	5	$\bar{5}$	$\bar{4}$	1	42.149	2	0	$\bar{3}$	3
27.520	30	0	2	2	36.767	3	$\bar{6}$	1	1	42.149	2	$\bar{1}$	4	3
27.520	30	0	$\bar{5}$	1	36.767	3	$\bar{2}$	1	3	42.249	1	$\bar{5}$	2	3
27.703	27	0	$\bar{2}$	2	36.831	3	0	$\bar{7}$	1	42.431	3	$\bar{5}$	$\bar{5}$	2
27.703	27	$\bar{4}$	2	0	36.952	5	$\bar{2}$	$\bar{1}$	3	42.431	3	$\bar{3}$	$\bar{4}$	3
28.315	3	$\bar{4}$	3	1	36.952	5	$\bar{3}$	0	3	42.525	2	$\bar{4}$	$\bar{6}$	2
28.315	3	4	3	1	36.952	5	3	0	3	42.525	2	4	6	2
28.315	3	$\bar{2}$	5	1	37.088	3	0	$\bar{7}$	1	42.630	1	$\bar{1}$	$\bar{4}$	3
28.580	3	3	$\bar{2}$	1	37.088	3	$\bar{5}$	$\bar{3}$	2	42.630	1	$\bar{5}$	$\bar{2}$	3
28.580	3	$\bar{1}$	$\bar{3}$	2	37.231	8	$\bar{1}$	0	3	42.950	14	$\bar{1}$	$\bar{7}$	2
28.843	1	$\bar{2}$	$\bar{5}$	1	37.375	5	$\bar{2}$	$\bar{7}$	1	42.950	14	$\bar{7}$	0	1
29.148	4	1	1	2	37.983	1	3	$\bar{1}$	2	43.049	9	$\bar{4}$	0	2
29.208	4	1	$\bar{1}$	2	37.983	1	1	5	2	43.049	9	$\bar{4}$	$\bar{7}$	1
29.462	32	$\bar{4}$	0	2	38.134	1	$\bar{3}$	2	3	43.259	2	1	$\bar{2}$	3
29.462	32	0	6	0	38.223	2	1	$\bar{5}$	2	43.434	1	$\bar{3}$	7	2
29.887	12	$\bar{3}$	3	2	38.223	2	$\bar{2}$	6	2	44.069	5	$\bar{6}$	5	1
30.278	22	$\bar{5}$	0	1	38.448	2	$\bar{1}$	2	3	44.069	5	$\bar{2}$	5	3
30.374	21	$\bar{3}$	$\bar{3}$	2	38.448	2	$\bar{3}$	$\bar{2}$	3	44.247	4	$\bar{7}$	1	2

89-5899 Quality: C

CAS Number:

Molecular Weight: 79.55
Volume[CD]: 81.12
Dx: 6.513 Dm:

Sys: Monoclinic
Lattice: End-centered
S.G.: Cc (9)
Cell Parameters:
a 4.689 b 3.420 c 5.130
α β 99.570 γ

I/Icor: 3.72
Rad: CuKa1
Lambda: 1.54060
Filter:
d-sp: calculated

ICSD #: 087126

Cu O
Copper Oxide
Ref: Calculated from ICSD using POWD-12++
Ref: Massarotti, V et al., Z. Kristallogr., 213, 259 (1998)

Tenorite (CuO)

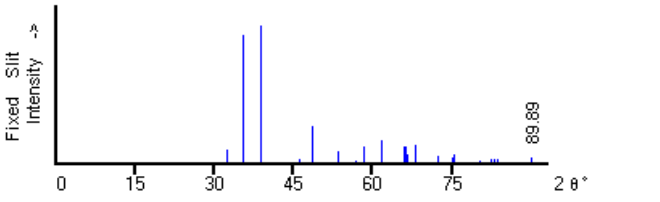

2θ	Int-f	h	k	l	2θ	Int-f	h	k	l	2θ	Int-f	h	k	l
32.538	102	1	1	0	61.559	167	$\bar{1}$	1	3	75.280	65	$\bar{2}$	2	2
35.462	386	0	0	2	65.880	119	0	2	2	79.818	5	0	2	3
35.558	924	$\bar{1}$	1	1	66.222	124	$\bar{3}$	1	1	80.159	14	$\bar{2}$	0	4
38.759	999 *	1	1	1	66.487	65	3	1	0	82.333	31	$\bar{3}$	1	3
38.925	617	2	0	0	67.973	75	1	1	3	83.158	31	2	2	2
46.269	24	$\bar{1}$	1	2	68.154	136	2	2	0	83.577	29	3	1	2
48.704	263	$\bar{2}$	0	2	68.931	6	$\bar{2}$	2	1	83.577	29	4	0	0
51.407	10	1	1	2	71.658	4	$\bar{3}$	1	2	86.484	11	$\bar{4}$	0	2
53.547	90	0	2	0	72.424	55	3	1	1	86.792	8	$\bar{2}$	2	3
56.785	16	0	2	1	73.022	8	2	2	1	88.078	2	1	1	4
58.333	122	2	0	2	75.049	43	0	0	4	88.204	4	1	3	0

78-2076 Quality: C

CAS Number:

Molecular Weight: 143.09
Volume[CD]: 77.69
Dx: 6.117 Dm:

Sys: Cubic
Lattice: Primitive
S.G.: Pn$\bar{3}$m (224)
Cell Parameters:
a 4.267 b c
α β γ

I/Icor: 8.28
Rad: CuKa1
Lambda: 1.54060
Filter:
d-sp: calculated

ICSD #: 063281

Mineral Name:
Cuprite

Non-Ambient Temperature

Cu2 O
Copper Oxide
Ref: Calculated from ICSD using POWD-12++, (1997)
Ref: Restori, R., Schwarzenbach, D., Acta Crystallogr., Sec. B: Structural Science, 42, 201 (1986)

Cuprite (Cu_2O)

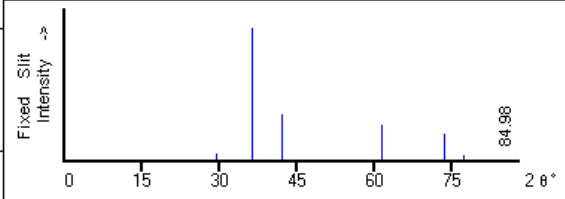

2θ	Int-f	h	k	l	2θ	Int-f	h	k	l	2θ	Int-f	h	k	l
29.583	53	1	1	0	73.558	198	3	1	1					
36.442	999 *	1	1	1	77.417	43	2	2	2					
42.329	347	2	0	0	84.981	2	3	2	1					
52.488	11	2	1	1										
61.408	265	2	2	0										
65.582	1	2	2	1										
69.622	3	3	1	0										

APPENDIX II

RAMAN SPECTROSCOPY

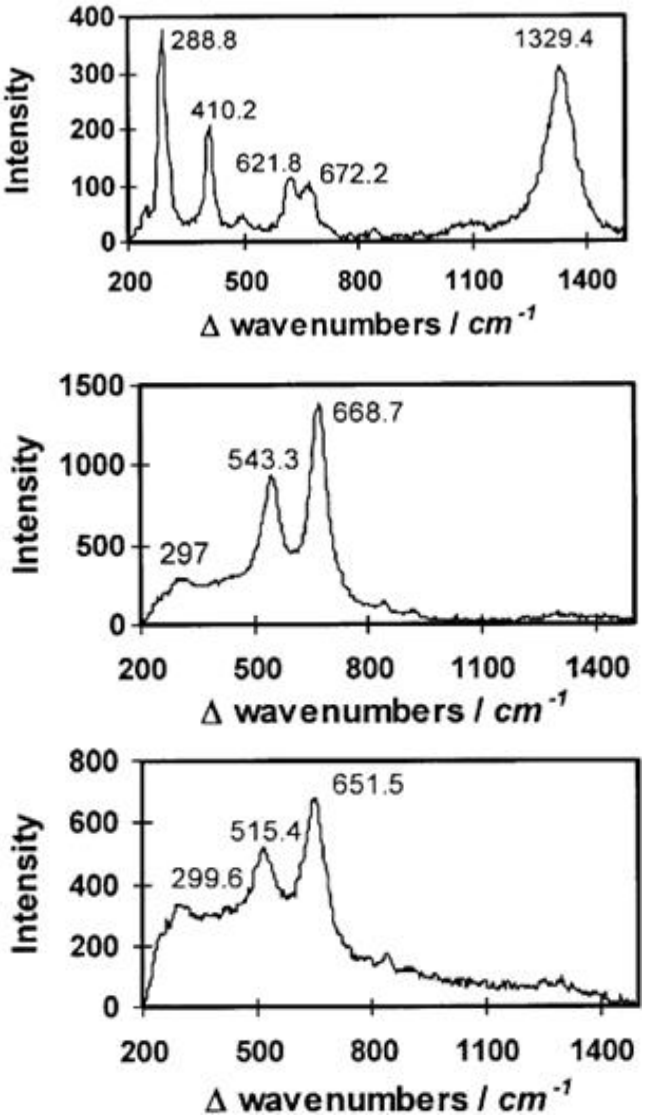

Figure A2.1: Standard Raman spectra for layers of different iron oxides [Raman (2006)].

Table A2.1: Raman spectra of reference Fe_2O_3 oxides formed.

Nature of oxide	Raman peak positions (cm^{-1})								Reference
Hematite (Fe_2O_3)	227		**298**		414	501	612	665	[Tjong (1983)]
	225	245	**295**		415	500	615		[Ohtsuka (1986)]
	226	245	**293**	298	413	500	612		[Beattie (1970)]
	227	245	**293**	298	414	501	612		[Thibeau (1978)]
	220	238	**288**		408	498	608		[Gardiner (1987)]
	236	253	**298**		413	502	616		[McCarty (1989)]
	228	248	**296**		413	500	612	663	[Massey (1990)]
	225	247	**299**		412	500	613		[Thierry (1991)]
	225	250	**300**		410	500	610		[Renusch (1996)]
	227	246	**293**	299	411	497	612		[Faria (1997)]
	226	245	**292**		411	497	612		[Oh (1998)]
	227	246	**294**	300	413	499	613	659	[Bersani (1999)]
	222		**290**		415	496	610		[Jallad (2001)]
	224	243	**290**	297	408	496	609	659	[Shim (2001)]
	228		**294**	310	391	466			[Chamritski (2005)]
	225	247	**299**		412	500	613		[Chattopadhyay (2005)]
			289		410		622	672	[Raman (2006)]
	224		**290**		410				[Thaler (2006)]
	225	245	**290**	300	412				[Hanesch (2009)]
	226	247	**293**		411	499	614		[CIT (2010)]
	228	247	**293**		411	500	614	665	[Schlepp (2010)]
	226	246	**292**		410	500	611		[Twaites (2010)]
	227	247	**294**		413	503	615	666	[U. of Arizona (2010)]
	225	248	**299**		410	502	612	663	[U. of Arizona (2010)]
	226		**292**		409	499	612	660	[Chicot (2011)]

Table A2.2: Raman spectra of reference Fe_3O_4 oxides formed.

Nature of oxide	Raman peak positions (cm^{-1})								Reference
Magnetite (Fe_3O_4)		300	320	420		560		**680**	[Verble (1974)]
		298	320	420	472	550		**676**	[Hart (1976)]
							616	**663**	[Thibeau (1978)]
				425			612	**667**	[Tjong (1983)]
						540		**665**	[Ohtsuka (1986)]
	160		318	410	462	542		**672**	[Degiorgi (1987)]
								662	[Gardiner (1987)]
	226		336	490			570		[Graves (1988)]
		298	319	418	470	550		**676**	[Dunnwald (1989)]
						542		**671**	[McCarty (1989)]
						550		**670**	[Boucherit (1991)]
						550		**670**	[Thierry (1991)]
		300		410		550		**660**	[Renusch (1996)]
		302		513		534		**663**	[Faria (1997)]
						532		**667**	[Oh (1998)]
			311			541		**666**	[Bersani (1999)]
	193		308			540		**670**	[Gasparov (2000)]
			311			540		**665**	[Li (2000)]
	217	288		403	487			**660**	[Jallad (2001)]
						535		**662**	[Antunesa (2003)]
	193	306				538		**668**	[Shebanova (2003)]
	220			400			600		[Shebanova (2003)]
		296	326	360	491		581	**666**	[Chamritski (2005)]
						550		**676**	[Chattopadhyay (2005)]
		297				543		**669**	[Raman (2006)]
			310			540		**670**	[Hanesch (2009)]
	203	300				569		**673**	[Currier (2010)]
	195		310			536		**665**	[Pinch (2010)]
	203		325		472	560		**679**	[Scott (2010)]
	203		315			568		**671**	[Scott (2010)]
	200	303				566		**672**	[Twaites (2010)]
			307			550		**670**	[Chicot (2011)]

Table A2.3: Raman spectra of reference FeO, Fe_2SiO_4, SiO_2, CuO, Cu_2O oxides formed.

Nature of oxide	Raman peak positions (cm^{-1})								Reference
Wüstite (FeO)						616	**663**		[Thibeau (1978)]
							652		[Faria (1997)]
		290					**656**		[Jallad (2001)]
	250	300	385	470	560				[Chattopadhyay (2005)]
		300			515		**652**		[Raman (2006)]
	234	346	396						[Frost (2007)]
						595			[Hanesch (2009)]
	197	249	403	486	553			688	[Dave Bunk (2010)]
	248	300	388		551			688	[Chicot (2011)]
Fayalite (Fe_2SiO_4)				334		672	779	**845**	[Yagi (1974)]
	119	171	289	369	505	562	814	**840**	[Cnopnras (1991)]
		189					818	**846**	[American (2010)]
	166	242	282	303	380			**812**	[American (2010)]
	157	174	242	293	380	509		**815**	[American (2010)]
	158	198	296	316	384	508	566	**820**	[Rossman (2010)]
	115	172	200	239	400	573	817	**843**	[Scott (2010)]
	119		290	370		565		**815**	[Scott (2010)]
		238	292	374		560		**814**	[Shannon (2010)]
			289	374		566		**814**	[Shigley (2010)]
	158		293	374		559		**820**	[Shigley (2010)]
Coesite (SiO_2)	205			353		459		806	[Jallad (2008)]
	204	270	325	355	426	466	**520**	815	[Prewitt (2010)]
	120	180	206	271	427	465	**523**	790	[Rossman (2010)]
				496	749	1052	1179	1581	[Schönbächler (2011)]
Tenorite (CuO)				**297**	344			629	[Hagemann (1990)]
				298	330			602	[Wang (2002)]
	105	146	190	217	309	423	488	641	[Garske (2010)]
Cuprite (Cu_2O)	109	154	**218**	308	436	515	635	665	[Solache-C. (2008)]
	108	144	**215**				409		[Schlepp (2010)]
	108	143	**217**				409		[U. of Arizona (2010)]

APPENDIX III

PARAMETERS OF OXIDE

Table A3.1: Yong's modulus (E) of reference various oxides formed.

Type of oxide	Temperature of properties testing (°C)	Values obtained (GPa)	Reference
Hematite (Fe_2O_3)	Room temperature	214 to 350	[Samsonov (1973)]
	20	220	[Nagl (1993)]
	20	122, 205 to 266	
	Room temperature	210	[Krzyzanowski (2002)]
	Room temperature	350	[Ouglova (2006)]
	Room temperature	359	[Chicot (2011)]
Magnetite (Fe_3O_4)	Room temperature	214 to 350	[Samsonov (1973)]
	Room temperature	230.33	[Hearmon (1979)]
	20	210	[Nagl (1993)]
	20	140 to 260	
	Room temperature	175	[Seo (2001)]
	Room temperature	215	[Ouglova (2006)]
	Room temperature	175	[Chicot (2011)]
Wüstite (FeO)	20	130	[Nagl (1993)]
	Room temperature	152	[Krzyzanowski (2002)]
	Room temperature	358	[Chicot (2011)]
	700	98.6	[Saeki (2011)]
	900	75.9	
	1000	83.4	
Iron (Fe)	570 to 800	190 to 120	[Nagl (1993)]
	20	128	
	600 to 900	75	
	Room temperature	200	[Momber (2008)]
	570	155	
	674	150	
	743	135	
	800	125	
	25	213	[Saeki (2011)]
Fe_3O_4 + 20% Fe_2O_3	20	61 to 84	[Nagl (1993)]

Table A3.1: Yong's modulus (E) of reference various oxides formed (continued).

Type of oxide	Temperature of properties testing (°C)	Values obtained (GPa)	Reference
Iron oxide (non-specific)	600	175	[Morrel (1987)]
	700	164	
	800	153	
	900	141	
	900	145	[Picqué (2004)]
	570	182	[Momber (2008)]
	674	168	
	743	158	
	800	151	
	550	160	[Isao (2005)]
	700	135	
	Room temperature	240	[Krzyzanowski (2010)]
Carbon steel	600	170	[Fletcher (1998)]
	700	150	
	800	130	
	900	110	
	900	145	[Picqué (2004)]
	600	95	[Picqué (2006)]
	25	220	[Momber (2008)]

Table A3.2: Residual stress (σ_{res}) of reference various oxides formed.

Type of oxide	Temperature of properties testing (°C)	Values obtained (GPa)	Reference
Hematite (Fe_2O_3)	25	– 0.760 to – 0.350	[Panicaud (2002)]
	25	– 0.381 to – 0.315	[Kim (2003)]
	25	– 0.387 to – 0.300	
	25	– 0.821	[Panicaud (2006)]
	25	– 0.451	[Juricic (2007)]
	25	– 0.438	
	25	– 0.100	[Juricic (2010)]
Magnetite (Fe_3O_4)	25	– 0.250 to – 0.010	[Panicaud (2002)]
	25	0.025 to 0.054	[Kim (2003)]
	25	– 0.400 to – 0.300	[Panicaud (2004)]
	25	– 0.206	[Juricic (2006)]
	25	– 0.184	
	25	– 0.212	
	25	– 0.255	
	25	– 0.215	
	25	– 0.391	[Panicaud (2006)]
	25	– 0.247	
	25	– 0.210	[Juricic (2007)]
	25	– 0.195	
	25	– 0.251	
	25	– 0.231	
	25	– 0.240	
Wüstite (FeO)	25	– 0.733 to – 0.645	[Kim (2003)]
	25	0.365	[Juricic (2010)]
Iron (Fe)	25	– 0.084 to 0.051	[Kim (2003)]

Table A3.3: Poisson's ratio (υ) of reference various oxides formed.

Type of oxide	Temperature of properties testing (°C)	Values obtained (GPa)	Reference
Hematite (Fe_2O_3)	Room temperature	0.19	[Krzyzanowski (2002)]
	Room temperature	0.12	[Chicot (2011)]
Magnetite (Fe_3O_4)	Room temperature	0.262	[Gercek (2007)]
	Room temperature	0.37	[Chicot (2011)]
Wüstite (FeO)	Room temperature	0.36	[Krzyzanowski (2002)]
	Room temperature	0.22	[Chicot (2011)]
Iron (Fe)	570	0.34	[Momber (2008)]
	674	0.34	
	743	0.34	
	800	0.34	
Iron oxide (non-specific)	Room temperature	0.33	[Taniguchi (2001)]
	900	0.30	[Picqué (2004)]
	570	0.34	[Momber (2008)]
	674	0.34	
	743	0.34	
	800	0.34	
	Room temperature	0.30	[Krzyzanowski (2010)]
Carbon steel	Room temperature	0.50	[Molina (1993)]
	900	0.33	[Picqué (2004)]
	Room temperature	0.30	[Picqué (2006)]
For most metals and oxides	elastic deformation	0.30	[Nagl (1993)]
	plastic deformation	0.50	

Table A3.4: Thermal stress, bulk modulus and fracture stress of reference various oxides formed.

Parameter	Type of oxide	Temperature of properties testing (°C)	Values obtained (GPa)	Reference
Thermal stress	Hematite (Fe_2O_3)	25	– 0.664	[Kim (2003)]
	Magnetite (Fe_3O_4)	25	0.744	
	Wüstite (FeO)	25	– 0.277	
	Iron oxide (non-specific)	1143 to 1203	1 to 1.4	[Taniguchi (2001)]
Bulk modulus	Hematite (Fe_2O_3)	Room temperature	230 ± 5	[Olsen (1991)]
		Room temperature	203 to 305	[Jiang (1998)]
	Magnetite (Fe_3O_4)	Room temperature	183 ± 10	[Mao (1974)]
		Room temperature	215 ± 25	[Gerward (1995)]
	Wüstite (FeO)	Room temperature	100 to 160	[Gleason (2008)]
Fracture stress	Iron oxide (non-specific)	570	0.0380	[Momber (2008)]
		674	0.0024	
		743	0.0019	
		800	0.0049	

Table A3.5: Hardness of reference various oxides formed.

Type of oxide	Temperature of properties testing (°C)	Values obtained	Reference
Hematite (Fe_2O_3)	Room temperature	600 $kg.mm^{-2}$ (6 GPa)	[Momber (2008)]
	25	670 $kg.mm^{-2}$ (6.70 GPa)	[Takeda (2009)]
	1000	530 $kg.mm^{-2}$ (0.53 GPa)	
Hematite (α-Fe_2O_3)	Room temperature	986 to 1219 $kg.mm^{-2}$ (9.86 to 12.19 GPa)	[Momber (2008)]
Magnetite (Fe_3O_4)	Room temperature	420 to 500 $kg.mm^{-2}$ (4.20 to 5.00 GPa)	[Momber (2008)]
	25	400 $kg.mm^{-2}$ (4.00 GPa)	[Takeda (2009)]
	1000	8 $kg.mm^{-2}$ (0.08 GPa)	
Wüstite (FeO)	Room temperature	270 to 390 $kg.mm^{-2}$ (2.70 to 3.90 GPa)	[Momber (2008)]
	25	350 $kg.mm^{-2}$ (3.50 GPa)	[Takeda (2009)]
	1000	5 $kg.mm^{-2}$ (0.05 GPa)	
Fayalite (Fe_2SiO_4)	25	550 $kg.mm^{-2}$ (5.50 GPa)	[Takeda (2009)]
	1000	63 $kg.mm^{-2}$ (0.63 GPa)	

Table A3.6: Physical properties of iron oxide [Cornell (2003)].

Type of oxide	Structure	Molar mass ($g.mol^{-1}$)	Density ($g.cm^{-3}$)	Colour
Hematite (Fe_2O_3)	Hexagonal (Rhombohedral) α = 5.0356 Å c = 13.7489 Å n-type	159.690	5.260	Red
Magnetite (Fe_3O_4)	Cubic α = 8.396 Å p-type	231.533	5.180	Black
Wüstite (FeO)	Cubic α = 4.302 – 4.275 Å p-type	71.844	5.900 to 5.990	Black

Table A3.6: Physical properties of iron oxide (continued).

Type of oxide	Melting point (°C)	Boiling point (°C)	Heat of fusion ($kJ.mol^{-1}$)	Heat of decomposition ($kJ.mol^{-1}$)	Heat of vaporization ($kJ.mol^{-1}$)
Hematite (Fe_2O_3)	1562	-	-	461.40	-
Magnetite (Fe_3O_4)	1583 to 1597	2623	138.16	605.00	298 at 2623°C
Wüstite (FeO)	1377	2512	31.40 (for $Fe_{0.97}O$)	529.60	230.3 at 2517°C (for $Fe_{0.97}O$)

Effect of oxide structure on oxidation.

General of oxides are not ideal. Their compositions are different from the stoichiometric ratios. The oxide structure may be divided into two groups.

1. n-type oxides structure with anion deficiency (e.g. ZnO, ZrO_2, MgO, Al_2O_3, SiO_2, SnO_2, PbO_2).
   Anion: Negatively charged ion (oxygen).

2. p-type oxides structure with cation deficiency (e.g. NiO, CoO, FeO, PbO, MnO, Cu_2O).
   Cation: Positively charged ion (metal).

Effects of alloying elements on the oxidation rate of metal.

1. n-type oxides structure.
   Addition of a higher valency cation (e.g. Al to Zn) resulted in a lower oxidation rate.
   Addition of a lower valency cation (e.g. Li to Zn) resulted in a higher oxidation rate.

2. p-type oxides structure.
   Addition of a higher valency cation (e.g. Cr to Ni) resulted in a higher oxidation rate.
   Addition of a lower valency cation (e.g. Ni to Cr) resulted in a lower oxidation rate.

Table A3.7: Standard thermodynamic properties of iron oxide [Web site http://courses.chem.indiana.edu (2012)].

Type of oxide	Standard molar enthalpy (heat) of formation, $\Delta_f H^\circ_{298}$ ($kJ.mol^{-1}$)	Standard molar Gibbs energy of formation, $\Delta_f G^\circ_{298}$ ($kJ.mol^{-1}$)	Standard molar entropy, S°_{298} ($J.mol^{-1}.K^{-1}$)	Molar heat capacity at constant pressure, C_p ($J.mol^{-1}.K^{-1}$)
Hematite (Fe_2O_3)	– 824.2	– 742.2	87.4	103.9
Magnetite (Fe_3O_4)	– 1118.4	– 1015.4	146.4	143.4
Wüstite (FeO)	– 272.0	-	-	-

Table A3.8: Types of iron oxide [Cornell (2003)].

Oxide-hydroxides and hydroxides	Oxides
Goethite α-FeOOH	Hematite α-Fe_2O_3
Lepidocrocite γ-FeOOH	Magnetite Fe_3O_4 ($Fe^{"}Fe^{'''}_2O_4$)
Akaganéite β-FeOOH	Maghemite γ-Fe_2O_3
Schwertmannite $Fe_{16}O_{16}(OH)_y(SO_4)_z \cdot n\ H_2O$	β-Fe_2O_3
δ-FeOOH	ε-Fe_2O_3
Feroxyhyte δ′·FeOOH	Wüstite FeO
High pressure FeOOH	
Ferrihydrite $Fe_5HO_8 \cdot 4\ H_2O$	
Bernalite $Fe(OH)_3$	
$Fe(OH)_2$	
Green Rusts $Fe^{'''}_x Fe^{"}_y (OH)_{3x+2y-z}(A^-)_z; A^- = Cl^-; \frac{1}{2}SO_4^{2-}$	

Calculation of the standard Gibbs free energy change and partial pressure participating in oxidation of metals.

Calculate the standard Gibbs free energy change (ΔG°) and partial pressure of di-oxygen gas molecule in equilibrium ($P_{O_2,eq}$) with the possible oxidation products of metallic elements as follow.

1. Oxidation of Fe to FeO (marked as Fe/FeO) of reaction $Fe_{(s)} + \frac{1}{2}O_{2(g)} = FeO_{(s)}$ given as

$$\Delta G^\circ_{FeO} = -RT \ln\left(\frac{a_{FeO}}{a_{Fe} \cdot P^{1/2}_{O_2,eq}}\right) \qquad (A3-1)$$

Assuming the unit activity of the solid phases, then

$$P_{O_2,eq} = \exp\left(\frac{2 \cdot \Delta G^{\circ}_{FeO}}{RT}\right) \quad \text{(A3 – 2)}$$

With ΔG°_{FeO} of reaction given as [Young (2008)]

$$\Delta G^{\circ}_{FeO}\ (J.mol^{-1}) = -264\ 890 + 65.40T \quad \text{(A3 – 3)}$$

2. Oxidation of Fe to Fe_3O_4 (marked as Fe/Fe_3O_4) of reaction $3FeO_{(s)} + \frac{1}{2}O_{2(g)} = Fe_3O_{4(s)}$ given as

$$\Delta G^{\circ}_{Fe_3O_4} = -RT \ln\left(\frac{a_{Fe_3O_4}}{a^3_{FeO} \cdot P^{1/2}_{O_2,eq}}\right) \quad \text{(A3 – 4)}$$

Assuming the unit activity of the solid phases, then

$$P_{O_2,eq} = \exp\left(\frac{2 \cdot \Delta G^{\circ}_{Fe_3O_4}}{RT}\right) \quad \text{(A3 – 5)}$$

With $\Delta G^{\circ}_{Fe_3O_4}$ of reaction given as [Young (2008)]

$$\Delta G^{\circ}_{Fe_3O_4}\ (J.mol^{-1}) = -312\ 210 + 125.10T \quad \text{(A3 – 6)}$$

3. Oxidation of Fe to Fe_2O_3 (marked as Fe/Fe_2O_3) of reaction $2Fe_3O_{4(s)} + \frac{1}{2}O_{2(g)} = 3Fe_2O_{3(s)}$ given as

$$\Delta G^{\circ}_{Fe_2O_3} = -RT \ln\left(\frac{a^3_{Fe_2O_3}}{a^2_{Fe_3O_4} \cdot P^{1/2}_{O_2,eq}}\right) \quad \text{(A3 – 7)}$$

Assuming the unit activity of the solid phases, then

$$P_{O_2,eq} = \exp\left(\frac{2 \cdot \Delta G^{\circ}_{Fe_2O_3}}{RT}\right) \quad \text{(A3 – 8)}$$

With $\Delta G^{\circ}_{Fe_2O_3}$ of reaction given as [Young (2008)]

$$\Delta G^{\circ}_{Fe_2O_3}\ (J.mol^{-1}) = -249\ 450 + 140.70T \quad \text{(A3 – 9)}$$

These ΔG° and $P_{O_2,eq}$ of iron oxide will be appeared in Table A3.9 and Table A3.10 respectively.

Table A3.9: The standard Gibbs free energy change (ΔG°) of the oxidation of iron oxide at 600°C (873 K), 700°C (973 K), 800°C (1073 K) and 900°C (1173 K).

Temperature (K)	$\Delta G^{\circ}(J.mol^{-1})$		
	Fe/FeO (Wüstite)	Fe/Fe_3O_4 (Magnetite)	Fe/Fe_2O_3 (Hematite)
873	– 207 796	– 202 998	– 126 619
973	– 201 256	– 190 488	– 112 549
1073	– 194 716	– 177 978	– 98 479
1173	– 188 176	– 165 468	– 84 409

Table A3.10: Partial pressure of di-oxygen gas molecule in equilibrium ($P_{O_2,eq}$) of the oxidation of iron oxide at 600°C (873 K), 700°C (973 K), 800°C (1073 K) and 900°C (1173 K).

Temperature (K)	$P_{O_2,eq}(bar)$		
	Fe/FeO (Wüstite)	Fe/Fe_3O_4 (Magnetite)	Fe/Fe_2O_3 (Hematite)
873	1.36×10^{-25}	5.09×10^{-25}	7.04×10^{-16}
973	2.46×10^{-22}	3.52×10^{-21}	8.23×10^{-13}
1073	1.10×10^{-19}	4.69×10^{-18}	2.58×10^{-10}
1173	1.74×10^{-17}	1.83×10^{-15}	3.04×10^{-8}

4. Oxidation of Cu to Cu_2O (marked as Cu/Cu_2O) of reaction $2Cu_{(s)} + \frac{1}{2}O_{2(g)} = Cu_2O_{(s)}$ given as

$$\Delta G^{\circ}_{Cu_2O} = -RT \ln\left(\frac{a_{Cu_2O}}{a^2_{Cu} \cdot P^{1/2}_{O_2,eq}}\right) \qquad \text{(A3 – 10)}$$

Assuming the unit activity of the solid phases, then

$$P_{O_2,eq} = \exp\left(\frac{2 \cdot \Delta G^{\circ}_{Cu_2O}}{RT}\right) \qquad \text{(A3 – 11)}$$

With $\Delta G^{\circ}_{Cu_2O}$ of reaction given as [Gaskell (2009)]

$$\Delta G^{\circ}_{Cu_2O}(J.mol^{-1}) = -162\,200 + 69.24T \qquad \text{(A3 – 12)}$$

5. Oxidation of Si to SiO_2 (marked as Si/SiO_2) of reaction $Si_{(s)} + O_{2(g)} = SiO_{2(s)}$ given as

$$\Delta G^{\circ}_{SiO_2} = -RT \ln\left(\frac{a_{SiO_2}}{a_{Si} \cdot P_{O_2,eq}}\right) \qquad \text{(A3 – 13)}$$

Assuming the unit activity of the solid phases, then

$$P_{O_2,eq} = \exp\left(\frac{\Delta G^{\circ}_{SiO_2}}{RT}\right) \quad \text{(A3 – 14)}$$

With $\Delta G^{\circ}_{SiO_2}$ of reaction given as [Gaskell (2009)]

$$\Delta G^{\circ}_{SiO_2}\ (J.mol^{-1}) = -907\,100 + 175.00T \quad \text{(A3 – 15)}$$

6. Oxidation to form Fe_2SiO_4 (marked as $Fe/SiO_2/ Fe_2SiO_4$) of reaction $2Fe_{(s)} + SiO_{2(s)} + O_{2(g)} = Fe_2SiO_{4(s)}$ given as

$$\Delta G^{\circ}_{Fe_2SiO_4} = -RT\ln\left(\frac{a_{Fe_2SiO_4}}{a^2_{Fe}\cdot a_{SiO_2}\cdot P_{O_2,eq}}\right) \quad \text{(A3 – 16)}$$

Assuming the unit activity of the solid phases, then

$$P_{O_2,eq} = \exp\left(\frac{\Delta G^{\circ}_{Fe_2SiO_4}}{RT}\right) \quad \text{(A3 – 17)}$$

With $\Delta G^{\circ}_{Fe_2SiO_4}$ of reaction given as [Kubaschewski (1951)]

$$\Delta G^{\circ}_{Fe_2SiO_4}\ (J.mol^{-1}) = -566\,366 + 144.00T \quad \text{(A3 – 18)}$$

7. Oxidation to form $Fe_2SiO_4 + O_2$ (marked as $Fe_3O_4/SiO_2/ Fe_2SiO_4$) of reaction $2Fe_3O_{4(s)} + 3SiO_{2(s)} = 3Fe_2SiO_{4(s)} + O_{2(g)}$ given as

$$\Delta G^{\circ}_{Fe_2SiO_4+O_2} = -RT\ln\left(\frac{a^3_{Fe_2SiO_4}\cdot P_{O_2,eq}}{a^3_{SiO_2}\cdot a^2_{Fe_3O_4}}\right) \quad \text{(A3 – 19)}$$

Assuming the unit activity of the solid phases, then

$$P_{O_2,eq} = \exp\left(-\frac{\Delta G^{\circ}_{Fe_2SiO_4+O_2}}{RT}\right) \quad \text{(A3 – 20)}$$

With $\Delta G^{\circ}_{Fe_2SiO_4+O_2}$ of reaction given as [Kubaschewski (1951)]

$$\Delta G^{\circ}_{Fe_2SiO_4+O_2}\ (J.mol^{-1}) = 115\,640 + 23.30T \quad \text{(A3 – 21)}$$

These ΔG° and $P_{O_2,eq}$ of copper oxide, silicon oxide and fayalite will be appeared in Table A3.11 and Table A3.12 respectively.

Table A3.11: The standard Gibbs free energy change (ΔG°) of the oxidation of copper oxide, silicon oxide and fayalite at 600°C (873 K), 700°C (973 K), 800°C (1073 K) and 900°C (1173 K).

Temperature (K)	$\Delta G^{\circ}(J.mol^{-1})$			
	Cu_2O	SiO_2	Fe_2SiO_4	$Fe_2SiO_4 + O_2$
873	– 101 754	– 754 325	– 440 655	95 299
973	– 94 830	– 736 825	– 426 255	92 969
1073	– 87 906	– 719 325	– 411 856	90 639
1173	– 80 982	– 701 825	– 397 456	88 309

Table A3.12: Partial pressure of di-oxygen gas molecule in equilibrium ($P_{O_2,eq}$) of the oxidation of copper oxide, silicon oxide and fayalite at 600°C (873 K), 700°C (973 K), 800°C (1073 K) and 900°C (1173 K).

Temperature (K)	$P_{O_2,eq}(bar)$			
	Cu_2O	SiO_2	Fe_2SiO_4	$Fe_2SiO_4 + O_2$
873	6.64×10^{-13}	7.31×10^{-46}	4.31×10^{-27}	1.99×10^{-6}
973	6.54×10^{-11}	2.78×10^{-40}	1.31×10^{-23}	1.02×10^{-5}
1073	2.76×10^{-9}	9.61×10^{-36}	8.88×10^{-21}	3.87×10^{-5}
1173	6.12×10^{-8}	5.54×10^{-32}	1.99×10^{-18}	1.16×10^{-4}

8. A $P_{O_2,eq}$ is in studied atmosphere which was 20%H_2O/Ar (marked as 20%H_2O). In equilibrium of this atmosphere will be consist of $H_2O_{(g)}$, $H_{2(g)}$, and $O_{2(g)}$. The level of oxygen generated is determined by the thermodynamic equilibrium as the following reaction $H_2O_{(g)} = H_{2(g)} + \frac{1}{2}O_{2(g)}$. The standard free energy of formation ($\Delta G^{\circ}_{H_2O}$) of this reaction given as [Gaskell (1981)]

$$\Delta G^{\circ}_{H_2O}(J.mol^{-1}) = 246\,000 + 54.8T \qquad (A3-22)$$

Assuming that x is the water vapour dissociated, the remaining amount of water vapour is (20-x)%, the amount of hydrogen is x%, and the amount of oxygen is 1/2x%. The standard free energy of formation may be given as

$$\Delta G^{\circ}_{H_2O} = -RT\ln\left(\frac{\left(\frac{x}{2}\right)^{1/2}\cdot x}{(20-x)}\right) \qquad (A3-23)$$

The ΔG° and $P_{O_2,eq}$ of water vapour will be appeared in Table A3.13

Table A3.13: The standard Gibbs free energy change (ΔG°) and partial pressure of di-oxygen gas molecule in equilibrium ($P_{O_2,eq}$) of the water vapour at 600°C (873 K), 700°C (973 K), 800°C (1073 K) and 900°C (1173 K).

Temperature (K)	Water vapour (H_2O)	
	$\Delta G^{\circ}(J.mol^{-1})$	$P_{O_2,eq}(bar)$
873	198 160	5.83×10^{-8}
973	192 680	5.98×10^{-7}
1073	187 200	3.95×10^{-6}
1173	181 720	1.94×10^{-5}

The $P_{O_2,eq}$ of their oxides can be plots in Fig. A3.1.

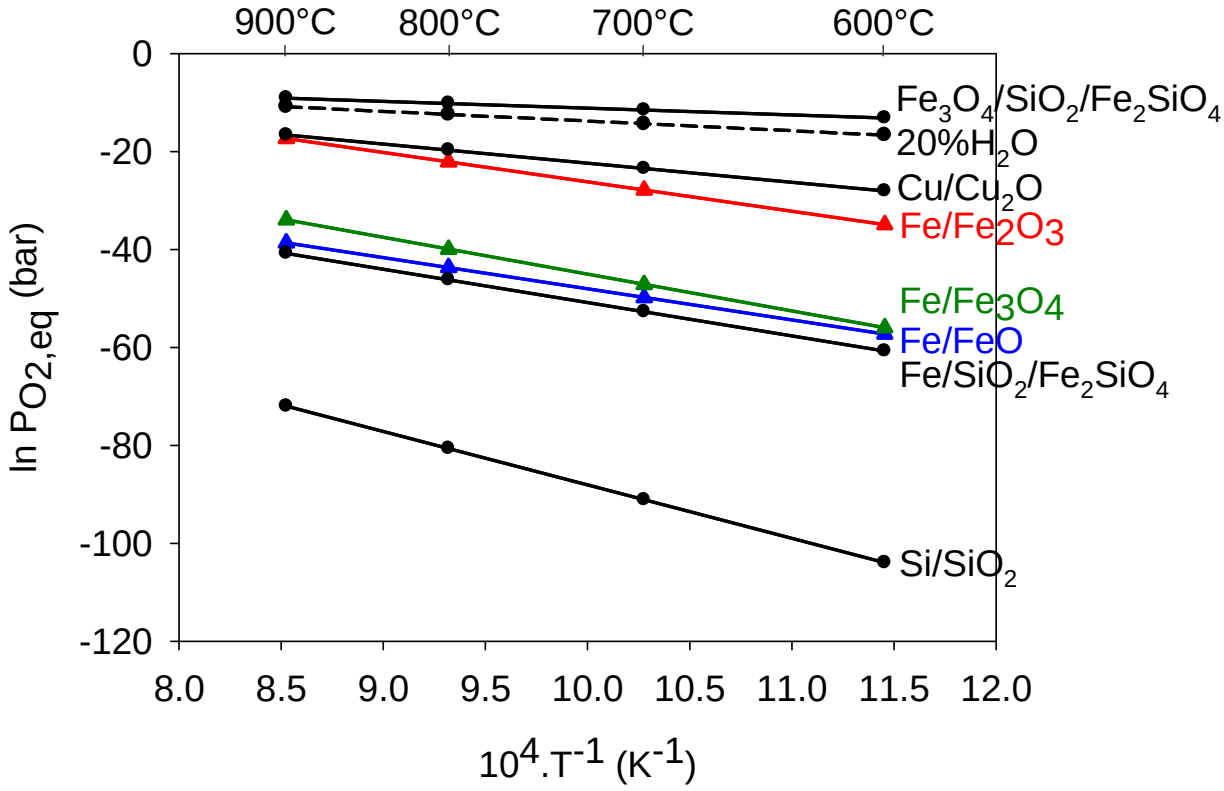

Figure A3.1: The equilibrium of oxygen partial pressure of iron oxides, copper oxide, silicon oxide and fayalite (It may be noted that the mole of di-oxygen gas molecule of various reaction are an inequality).

The vapour pressure of water will be appeared in Table A3.14, also can be plots in Fig. A3.2.

Table A3.14: Vapour pressure of water at various temperatures.

T (°C)	P (mbar)	T (°C)	P (mbar)	T (°C)	P (mbar)
– 10	2.76	32	46.97	74	364.74
– 9	3.03	33	49.61	75	380.39
– 8	3.29	34	52.50	76	396.58
– 7	3.55	35	55.53	77	413.29
– 6	3.82	36	58.68	78	430.66
– 5	4.21	37	61.97	79	448.68
– 4	4.47	38	65.39	80	467.24
– 3	4.87	39	68.95	81	486.45
– 2	5.26	40	72.76	82	506.45
– 1	5.66	41	76.71	83	527.11
0	6.05	42	80.92	84	548.42
1	6.45	43	85.26	85	570.53
2	6.97	44	89.87	86	593.29
3	7.50	45	94.61	87	616.71
4	8.03	46	99.61	88	640.92
5	8.55	47	104.74	89	665.92
6	9.21	48	110.13	90	691.84
7	9.87	49	115.79	91	718.55
8	10.53	50	121.71	92	746.05
9	11.32	51	127.89	93	774.47
10	12.11	52	134.34	94	803.82
11	12.89	53	141.05	95	834.08
12	13.82	54	148.03	96	865.26
13	14.74	55	155.26	97	897.50
14	15.79	56	162.89	98	930.66
15	16.84	57	170.79	99	964.74
16	17.89	58	179.08	100	1000.00
17	19.08	59	187.63		
18	20.39	60	196.58	102	1073.55
19	21.71	61	205.79		
20	23.03	62	215.53	104	1151.45
21	24.61	63	225.53		
22	26.05	64	235.92	106	1234.08
23	27.76	65	246.71		
24	29.47	66	258.03	108	1321.05
25	31.32	67	269.74		
26	33.16	68	281.84	110	1414.47
27	35.13	69	294.34		
28	37.24	70	307.50	112	1511.84
29	39.47	71	320.92		
30	41.84	72	335.00	114	1614.47
31	44.34	73	349.61		

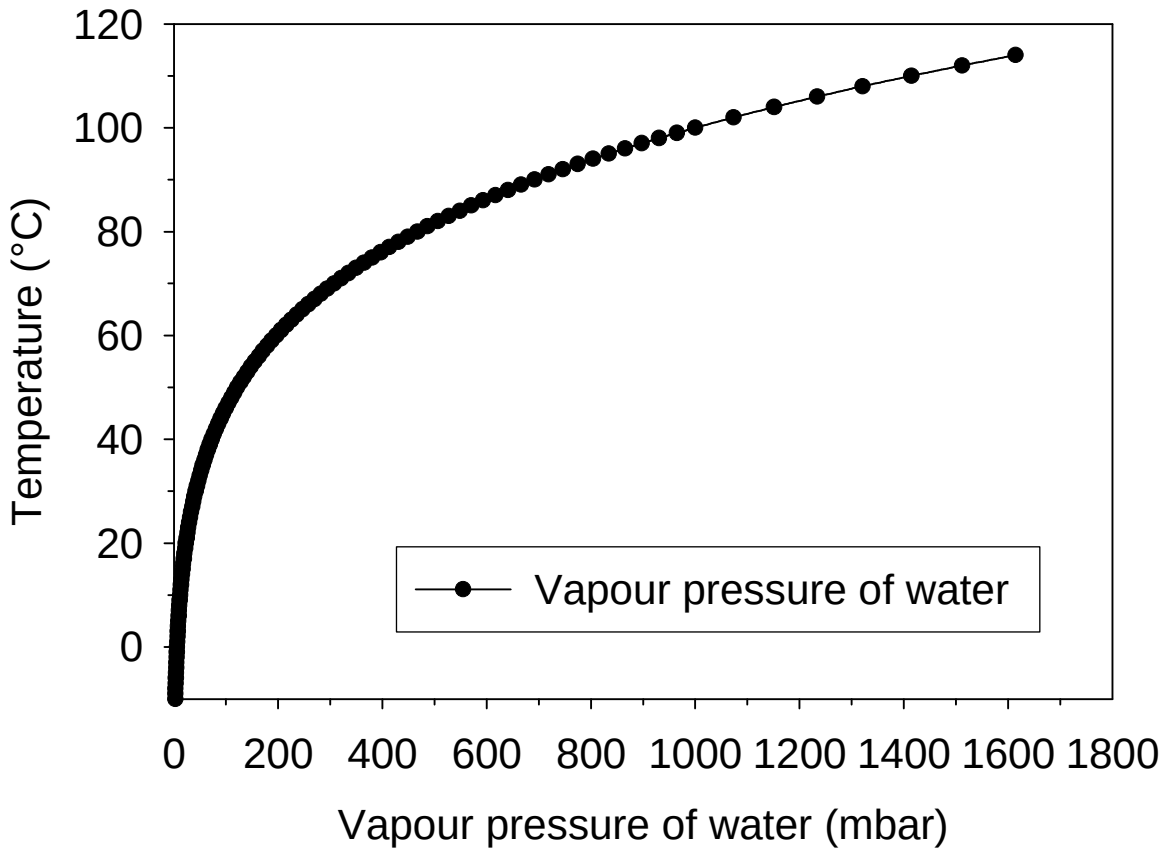

Figure A3.2: Graph of vapour pressure of water.

RESUME IN FRENCH

« Caractérisation physico-chimique et adhérence des couches d'oxydes thermiques formées sur aciers recyclés »

Introduction

Le développement de l'industrie métallurgique en Thaïlande s'appuie naturellement sur les procédés classiques, tels la réduction du minerai en haut-fourneau et l'affinage de la fonte au convertisseur, mais mise aussi de façon importante sur les filières de recyclage, en particulier l'utilisation de rebuts métalliques, collectés puis refondus au four électrique. L'intérêt de cette voie est de réduire la production de gaz à effet de serre et de maintenir un coût attractif. Son désavantage réside dans la composition variable des matières ferreuses recyclées et dans le contrôle de la teneur de certains éléments résiduels, en particulier le silicium et le cuivre. Ces éléments ont la propriété de se concentrer à l'interface entre l'acier et la calamine qui se forme au cours des process chauds (réchauffage, laminage), sous forme métallique (Cu) ou oxydée (SiO_2). Cette concentration influe sur l'aptitude de l'acier au décapage et conduit à des produits finaux de mauvaise qualité.

L'objectif de l'étude est de quantifier l'influence du silicium et du cuivre sur l'adhérence des calamines et, pour ce faire, nous avons opté pour la détermination de l'adhérence de ces dernières par un test mécanique : la traction uniaxiale à température ambiante. Pour faire progresser la connaissance de ce test, nous avons décidé d'utiliser un dispositif existant au Laboratoire SIMaP de Grenoble, et de mettre en place un dispositif nouveau à Supanburi en Thaïlande. L'intérêt de ce nouveau test est qu'il utilise une machine de traction conventionnelle et qu'il devrait permettre d'étudier l'influence de la vitesse de déformation sur les résultats d'adhérence obtenus.

Parallèlement, un test d'immersion acide a été mis en place pour mesurer la vitesse de décapage et évaluer la relation qui devrait exister entre cette vitesse et l'adhérence des calamines.

Matériaux utilisés et procédures expérimentales

L'influence de la voie d'élaboration des aciers sur la cinétique d'oxydation et l'adhérence des calamines a été conduite en utilisant deux nuances d'aciers. La première, dite « conventionnelle » a été fournie par Sahaviriya Steel Industries (SSI), un des aciéristes Thaïlandais et élaborée par la voie classique (haut-fourneau + convertisseur). La seconde nuance, fournie par l'aciériste Thaïlandais G Steel Company, appelée dans la suite « acier recyclé » est élaborée par fusion au four électrique d'aciers de récupération. La composition de ces aciers est fournie dans le Tableau 1.

Tableau 1: composition des nuances conventionnelle et recyclée (pds.%).

Acier	C	Si	Cu	Mn	Al	P	S	Fe
Conventionnel	0,033	**0,013**	**0,059**	0,232	0,043	0,006	0,009	Bal.
Recyclé	0,058	**0,267**	**0,168**	0,347	0,020	0,013	0,004	Bal.

Pour ces deux nuances, en sus des compositions, les températures de process sont légèrement différentes, en particulier la température de sortie du laminoir chaud et celle de bobinage (910 et 660°C pour l'acier conventionnel, 880 et 580°C pour l'acier recyclé). L'épaisseur des bandes est également différente : 3,2 mm et 6 mm.

Nous avons aussi étudié l'influence particulière du silicium sur deux nuances conventionnelles, fournies par SSI (Tableau 2).

Tableau 2: composition des deux nuances conventionnelles au silicium (pds.%).

Acier	C	Si	Cu	Mn	Al	P	S	Fe
0,026-pds% Si	0,193	**0,026**	0,040	0,521	0,039	0,008	0,008	Bal.
0,193-pds% Si	0,165	**0,193**	0,047	0,542	0,036	0,011	0,007	Bal.

Une série d'expériences a été, de plus, effectuée sur des aciers modèles au silicium et au cuivre élaborés à partir de fer pur par ArcelorMittal (Maizière-les-Metz, France). Leur composition est donnée au Tableau 3.

Tableau 3: composition des aciers modèles (pds.%).

Acier	Nuance	
Fe référence	(Fe avec un très faible niveau d'impuretés)	
Alliages au Si (pds% Si)	0,25	0,84
Alliages au Cu (pds% Cu)	0,08	0,39

La plupart des échantillons sont étudiés « as-received », c'est-à-dire oxydés pendant le laminage à chaud. Certains sont oxydés en thermobalance ou en four horizontal après un polissage soigneux de surface. La température d'oxydation isotherme est alors comprise entre 600 et 900°C ; l'atmosphère dynamique utilisée est 20%H_2O dans Ar.

Sur les échantillons industriels et sur ceux oxydés en laboratoire, les techniques de caractérisation usuelles sont appliquées : diffraction des rayons X, spectroscopie Raman, MEB avec EDX, Calotest.

La détermination de l'énergie d'adhérence mécanique des couches de calamine est effectuée par traction uniaxiale et observation de l'écaillage qui en résulte. Deux machines on été utilisées dans cette étude : une micro-machine insérée dans la chambre du Microscope Electronique à Balayage (Grenoble, France) et une macro-machine classique (Supanburi, Thaïlande). Le dispositif de repérage de l'écaillage est de type électrons rétrodiffusés pour la micro-machine et de type optique pour la macro-machine. La vitesse de déformation est unique pour la micro-machine (7×10^{-5} s^{-1}), ajustable pour la macro-machine (0,08; 0,33 et 0,83 s^{-1}). Les caractéristiques mécaniques particulières de la micromachine rendent nécessaire une correction des valeurs d'élongation mesurées. Cette correction est largement décrite dans le manuscrit.

L'adhérence G_i est calculée à partir de l'épaisseur e de la calamine étudiée et de l'énergie mécanique W_{total} qui y est emmagasinée à l'instant du premier écaillage par :

$$G_i = W_{total} \cdot e$$

Cette énergie d'adhérence correspond donc à celle de la calamine la moins adhérente. Le calcul prend en compte la contrainte résiduelle compressive de l'oxyde (croissance + thermique), la traction uniaxiale subie par le film d'oxyde, mais aussi la compression transverse Poisson élastique et surtout la compression transverse plastique. Les figures 1 et 2 montrent l'évolution du couple déformation-contrainte selon *x* (axe de traction) et *y* (axe transverse).

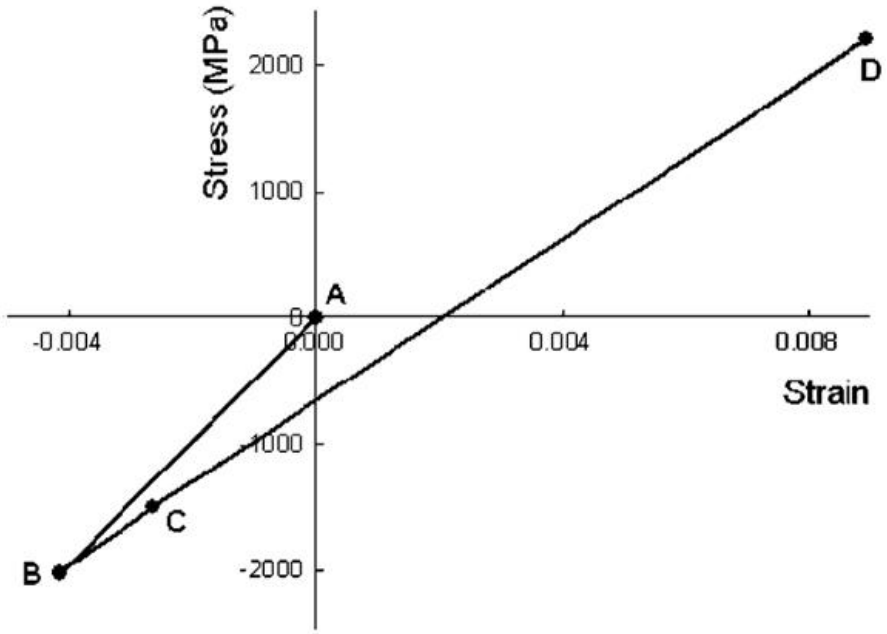

Figure 1: évolution du couple déformation-contrainte selon l'axe de traction. De A à B : refroidissement, de B à C : métal élastique, de C à D : métal plastique.

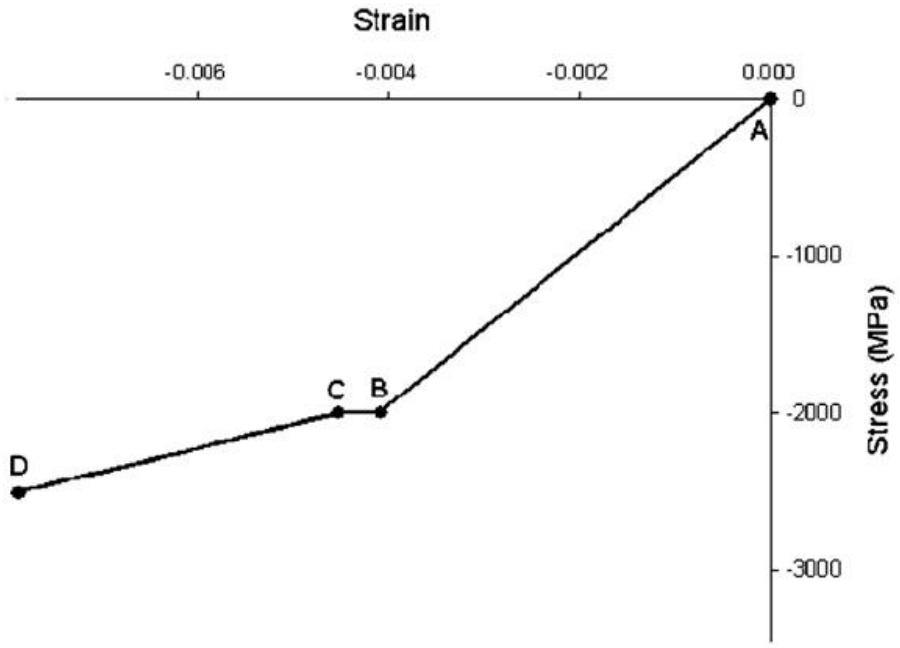

Figure 2: évolution du couple déformation-contrainte selon l'axe transverse. De A à B : refroidissement, de B à C : métal élastique, de C à D : métal plastique.

Pour rapprocher les résultats d'adhérence des observations de décapage effectuées sur les lignes industrielles, un test de décapage simple a été utilisé. Il consiste à immerger les échantillons oxydés dans une solution d'acide chlorhydrique à 10% en masses maintenue à 80°C. Le temps d'immersion peut varier entre 1 et 60 s. Après rinçage et séchage, la perte de masse des échantillons est mesurée.

Adhérence des calamines en fonction du process de production

L'acier conventionnel et l'acier recyclé sont ici étudiés comparativement. En termes de composition, les calamines formées pendant le process sont très proches : présence de magnétite et de fer métallique (résultat de la décomposition eutectoïde de la wüstite au refroidissement. Seule différence, la présence de raies de diffraction d'hématite sur l'acier recyclé, en raison probable du refroidissement plus lent de cette tôle plus épaisse (Figs. 3 et 4).

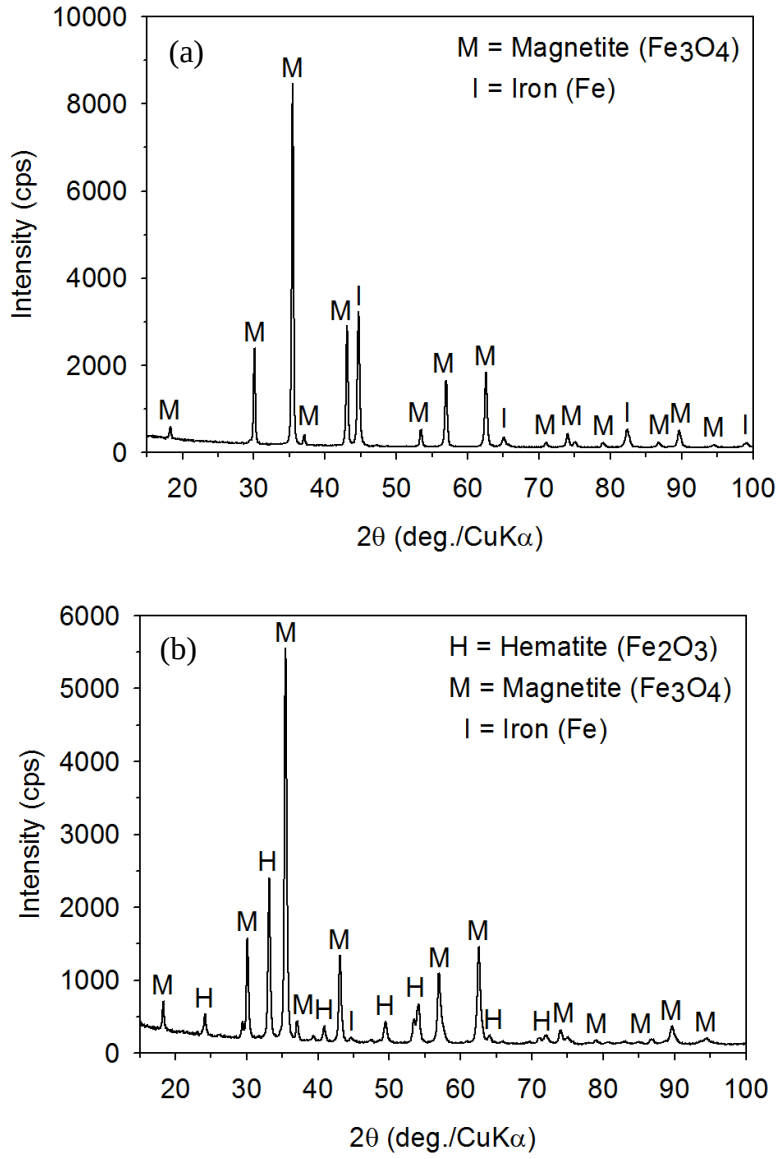

Figure 3: diffractogrammes des aciers conventionnel (a) et recyclé (b).

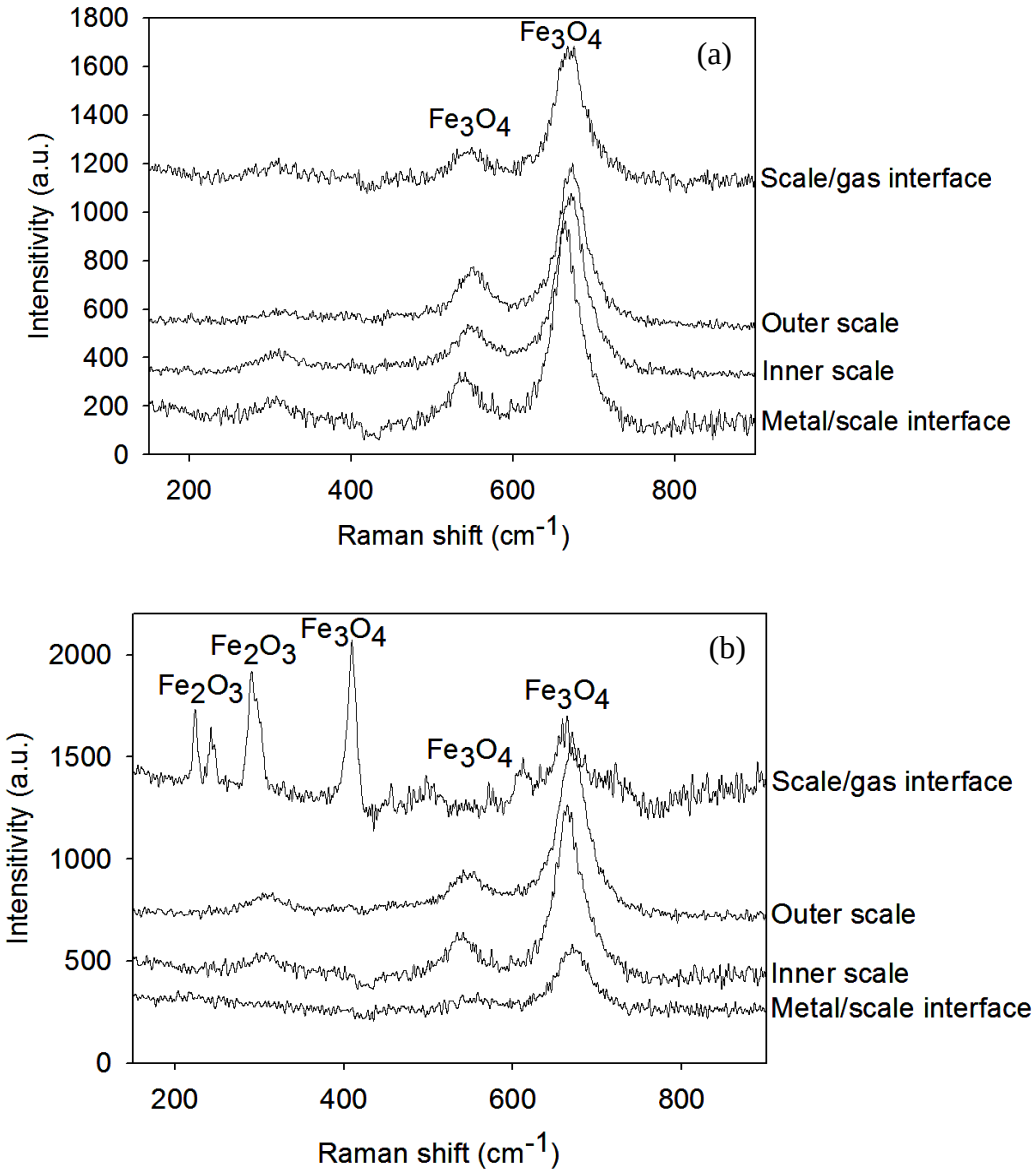

Figure 4: spectroscopie Raman des oxydes sur aciers conventionnel (a) et recyclé (b).

Les résultats des tests de traction sur micro-machine et sur macro-machine apparaissent sur les Figures 5 et 6. La Figure 5 décrit les observations microscopiques de l'écaillage de la calamine en fonction de la déformation pour les différentes vitesses de déformation utilisées. La Figure 6 quantifie l'aire écaillée en fonction de la déformation.

A partir de ces valeurs, nous avons obtenu l'énergie mécanique stockée dans la calamine au premier écaillage, en tenant compte de la présence de fissures qui réduisent la contrainte résiduelle calculée. Puis, l'adhérence des calamines est déterminée (Fig. 7). On observe sur cette figure que l'énergie d'adhérence est une fonction décroissante de la vitesse de déformation, ce qui s'explique par la possibilité de relaxation offerte au système quand le temps d'expérience est grand.

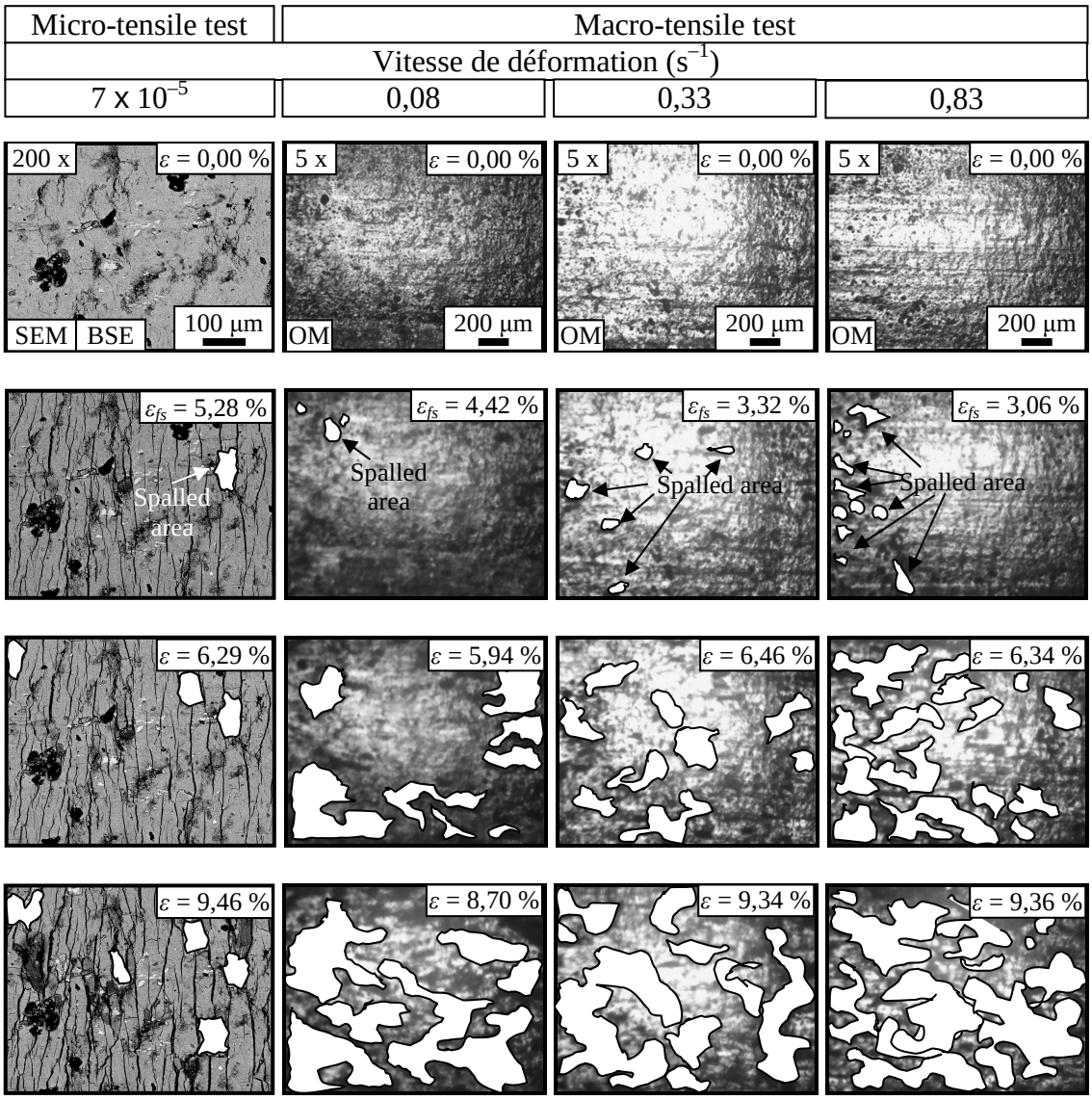

Figure 5: évolution de l'écaillage en fonction de la déformation pour l'acier recyclé (ε = déformation).

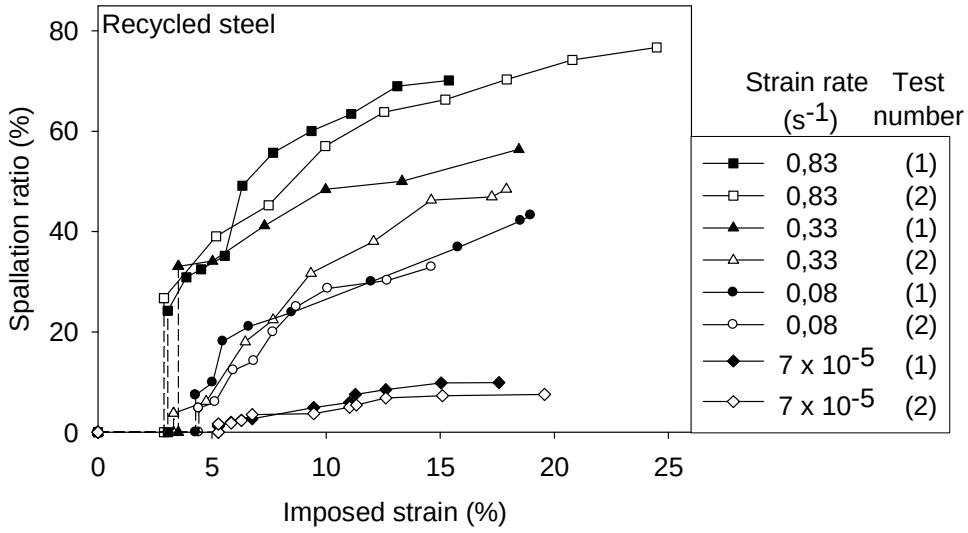

Figure 6: fraction écaillée de la calamine sur l'acier recyclé en fonction de la déformation pour les quatre vitesses de déformation utilisées.

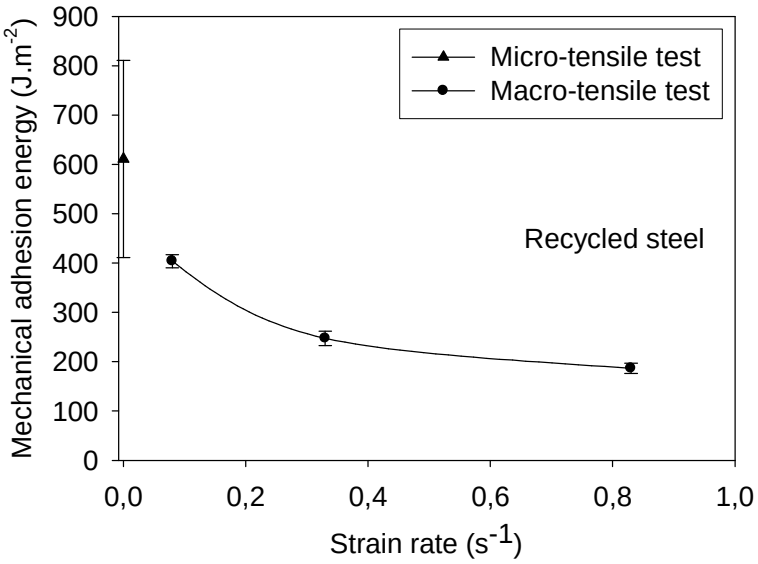

Figure 7: adhérence des calamines sur l'acier recyclé en fonction de la vitesse de déformation.

En comparant alors les résultats obtenus sur l'acier conventionnel et sur l'acier recyclé, il apparait que les calamines formées au cours du process sur l'acier recyclé sont plus adhérentes que celles formées sur l'acier conventionnel, quelle que soit la vitesse de déformation utilisée 7.10^{-5} ou 0,83 s^{-1} (Fig. 8). La raison principale de cette adhérence plus élevée réside certainement en la présence de silice ou de fayalite (Fe_2SiO_4) à l'interface entre l'acier et la calamine, comme le montrent les observations de microanalyse locale de la Figure 9. La silice qui se forme au début de l'oxydation est ancrée dans le métal (oxydation interne), la fayalite qui en résulte provient de sa réaction avec la calamine. On comprend alors que la présence de silicium en quantités importantes ancre la calamine au métal. Les phases oxydées du silicium stoppent la propagation des fissures interfaciales au cours du test de traction.

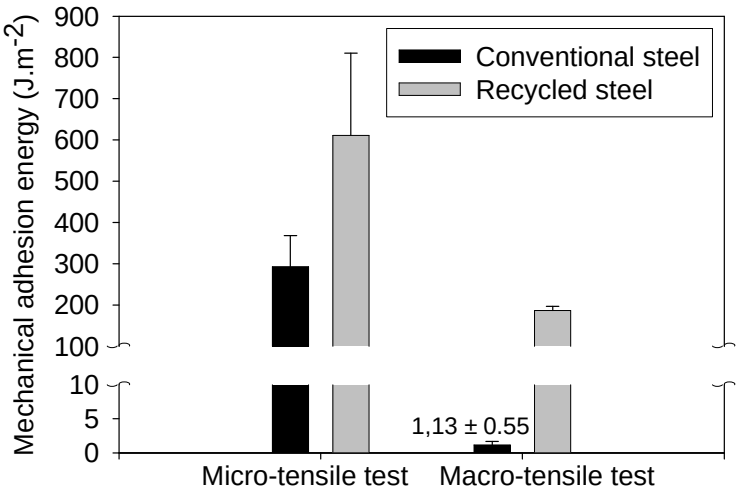

Figure 8: adhérence des calamines formées sur les deux types d'acier. Micro test : 7.10^{-5} s^{-1}, macro test : 0,83 s^{-1}.

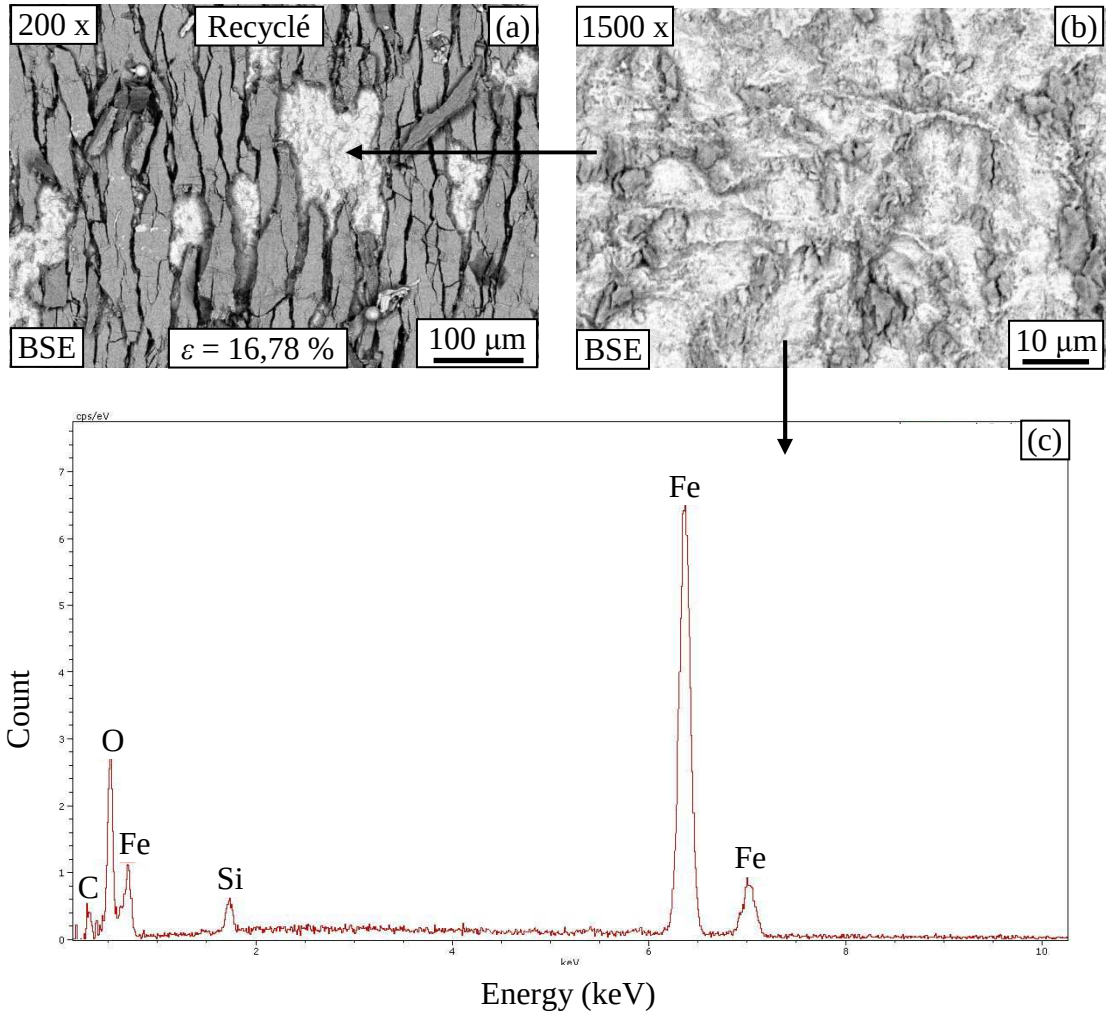

Figure 9: (a) analyse EDS de la calamine sur l'acier recyclé au cours du test de traction, (b) zone interfaciale décollée agrandie de (a), (c) spectre EDS de la partie du métal nue de (b).

L'utilisation du test de décapage acide permet de visualiser l'efficacité de cette opération (Fig. 10). De ces expériences, on déduit la vitesse de décapage (Fig. 11) qu'on observe inférieure sur l'acier recyclé en raison de la présence des phases oxydées du silicium à l'interface interne.

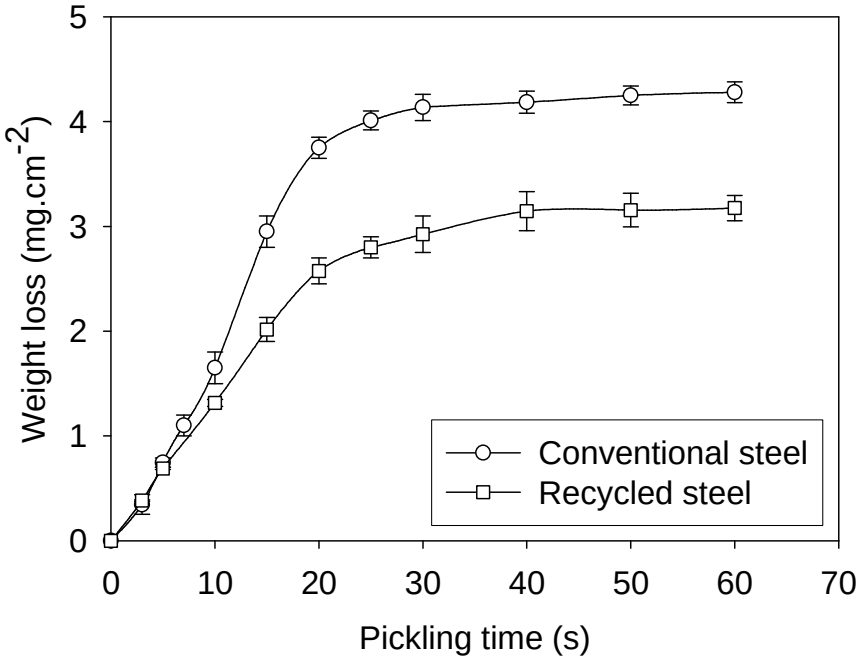

Figure 10: perte de masse au cours du décapage des deux nuances dans 10%v/v HCl à 80°C.

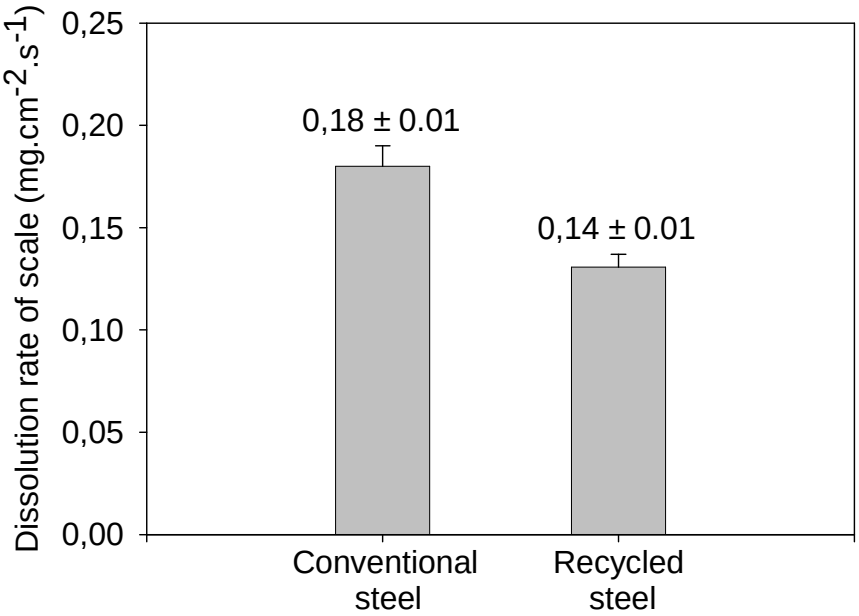

Figure 11: vitesse de dissolution de la calamine sur les deux nuances étudiées (10%v/v HCl à 80°C).

Adhérence des calamines en fonction de la teneur en silicium

Les deux nuances identiques en tous points (composition, process et épaisseur du métal) excepté la teneur en silicium (bas Si : 0,026%, haut Si : 0,193%) sont comparativement étudiés de façon identique à celles présentées ci-dessus. Les résultats de caractérisation montrent que leurs calamines de surface sont identiques (également similaires à celle présente sur l'acier conventionnel ci-dessus) ; seul l'enrichissement en silicium de l'interface acier haut Si/calamine les différencie, ainsi qu'une épaisseur moindre sur la nuance à haut Si (cinétique freinée par la silice interfaciale).

Au vu des résultats d'adhérence (Tableau 4), il apparaît que les calamines sont plus adhérentes quand la teneur en silicium de l'acier est plus élevée. Ceci confirme les observations du chapitre précédent, sans toutefois montrer une différence si grande. On peut en conclure que d'autres paramètres influencent la forte adhérence sur l'acier recyclé, probablement liées au process différents de ces deux nuances.

Tableau 4: adhérence des calamines sur les aciers à teneur en silicium différentes (0,026-pds% Si et 0,193-pds% Si.

	Micro-tensile test ($\dot{\varepsilon}$ = 7 x 10^{-5} s^{-1})		Macro-tensile test ($\dot{\varepsilon}$ = 0,83 s^{-1})	
	0,026-pds% Si	0,193-pds% Si	0,026-pds% Si	0,193-pds% Si
Epaisseur d'oxyde (µm)	9,08	7,55	9,08	7,55
Energie d'adhérence ($J.m^{-2}$)	306 ± 17	401 ± 9	3,6 ± 1,5	10,7 ± 1,3

Oxydation d'aciers modèles au silicium et au cuivre

Dans ces chapitres (Chaps. 5 et 6), nous avons mené l'étude d'aciers modèles en termes de cinétique d'oxydation dans la vapeur d'eau et de caractérisation des produits formés.

Pour les aciers contenant 0,25 et 0,84% Si, l'oxydation linéaire-parabolique du fer pur s'applique. On observe une diminution de la cinétique d'oxydation quand la teneur en silicium augmente, mais pas de modification notable de l'énergie d'activation sur k_p, come le montre la Figure 12. Cette énergie d'activation est d'ailleurs faible (~ 150 kJ/mol), plus faible qu'au cours de l'oxydation dans l'air sec ou l'oxygène.

La morphologie particulière des couches de calamine est décrite en termes de 3 sous-couches oxydées. L'évolution de l'oxyde contenant le silicium, de SiO_2 à Fe_2SiO_4 semble jouer un rôle important.

Pour les aciers contenant 0,08 et 0,39% Cu, l'étude est menée de la même façon. La présence de cuivre diminue la cinétique d'oxydation, surtout aux plus hautes températures. Contrairement au cas du silicium, on observe ici une diminution de l'énergie d'activation sur la constante parabolique quand la teneur en cuivre augmente (155, 140, 124 kJ/mol). La description en trois couches présentée pour les aciers au silicium est encore valable ici, suele diffère la présence du cuivre métallique dans la couche interne.

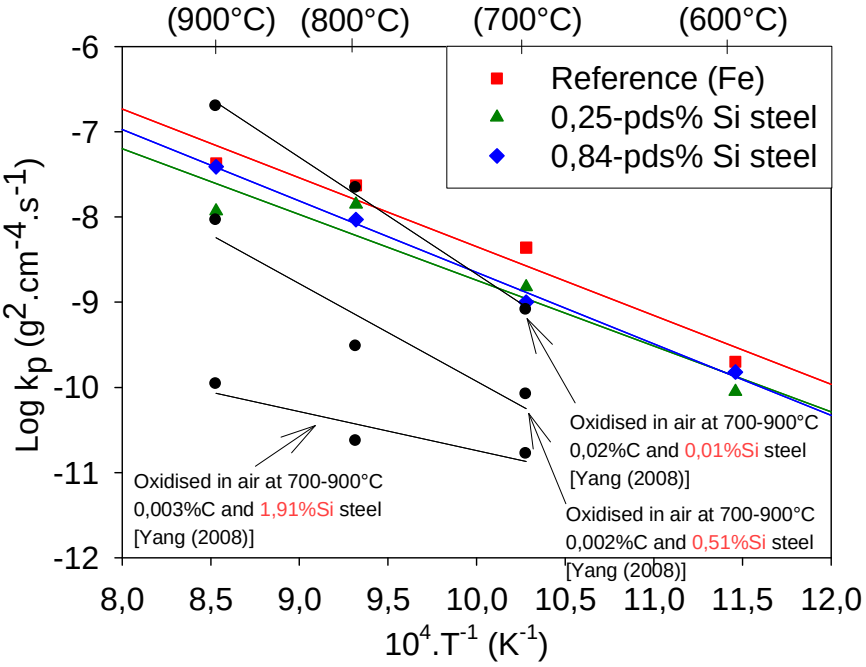

Figure 12: diagramme d'Arrhenius de l'oxydation parabolique des divers matériaux contenant du silicium et comparaison avec la littérature.

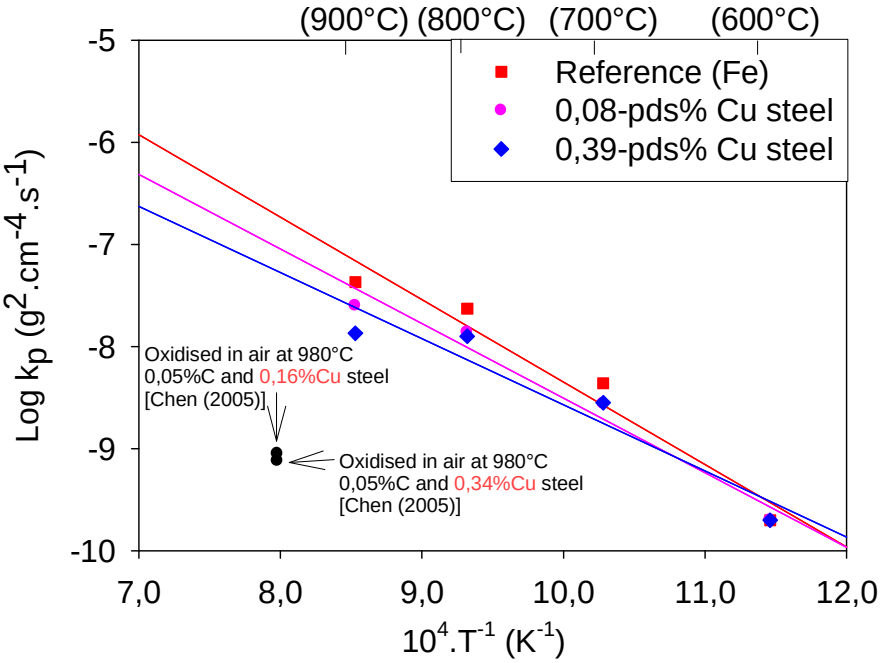

Figure 13: diagramme d'Arrhenius de l'oxydation parabolique des divers matériaux contenant du cuivre et comparaison avec la littérature.

Physico-chemical characterisation and adhesion behaviour of thermal oxide scales formed on recycled steels

Abstract:
The purpose of this study was first to develop in Thailand a "macroscopic" adhesion test using a conventional tensile machine, to compare it to the micro-tensile test used in Grenoble and sitting in the SEM chamber, and to use it for measuring adhesion of scales grown during processing on industrial steels. Parameters affecting the test, i.e. strain rate and Si content of steels were investigated. The results showed that spallation of scales during straining increased with increasing tensile strain rate. A higher strain rate resulted in lower strain initiating the first spallation and lower mechanical adhesion of scales, which could be explained by a relaxation effect. Oxide containing Si existed at the steel-scale interface and promoted adhesion of scales. Oxidation studies were also performed, and the behaviour in water vapour of steels with different contents of Si and Cu was investigated. Increasing Si content tended to decrease oxidation rate. It also resulted in the thickening of the wüstite and fayalite layers which formed by internal oxidation. When Si in steel increased, the intermediate ($FeO + Fe_3O_4$) and outermost (Fe_2O_3 sitting on Fe_3O_4) layers formed by external oxidation were thinner. For Cu containing steel, increasing Cu content tended to decrease the oxidation rate. It also decreased the innermost and intermediate layers and resulted in more Cu precipitates along steel-scale interface.

Keywords: Oxide scale, Adhesion, Tensile test, Oxidation kinetics, Hot-rolled steels, Recycled steels, Silicon-containing steel, Copper-containing steel.

Caractérisation physico-chimique et adhérence des couches d'oxydes thermiques formées sur aciers recyclés

Résumé:
L'objectif de cette étude était, en premier lieu, de mettre en place en Thaïlande un test d'adhésion par traction-écaillage sur une machine de traction classique (test « macroscopique »), de le comparer au test « microscopique » Grenoblois fonctionnant dans la chambre du MEB et de l'utiliser pour évaluer l'adhérence des calamines de process sur des aciers industriels. Deux paramètres ont été étudiés, la vitesse de déformation et la teneur des aciers en silicium. Il apparaît que l'écaillage des calamines au cours du test augmente quand augmente la vitesse de déformation. Une vitesse de déformation élevée entraîne une déformation au premier écaillage plus faible, donc une adhérence mesurée plus faible. Cet effet est lié aux phénomènes de relaxation. On a pu alors montrer que la présence d'oxyde(s) contenant Si, situé(s) à l'interface avec le métal, augmentait l'adhérence. Les études d'oxydation dans la vapeur d'eau qui ont aussi été réalisées ont révélé que la présence de silicium réduisait la vitesse d'oxydation. En augmentant la teneur en Si, les couches de fayalite et de wüstite s'épaississent ; par contre, les couches externes s'amincissent. Pour les aciers contenant du cuivre, la vitesse d'oxydation est réduite quand la teneur en Cu est augmentée. De la même façon, les couches internes sont plus épaisses et on observe une augmentation du nombre de précipités de Cu quand la teneur en cet élément augmente.

Mots-clés: Couches d'oxyde, Adhérence, Test de traction, Cinétique d'oxydation, Aciers au carbone, Aciers recyclés, Aciers au silicium, Aciers au cuivre.